



Kapetanaki, Anna-Maria (2025) High throughput characterisation of calcium dynamics for single cell functional phenotyping. PhD thesis.

<https://theses.gla.ac.uk/85309/>

Copyright and moral rights for this work are retained by the author

A copy can be downloaded for personal non-commercial research or study, without prior permission or charge

This work cannot be reproduced or quoted extensively from without first obtaining permission from the author

The content must not be changed in any way or sold commercially in any format or medium without the formal permission of the author

When referring to this work, full bibliographic details including the author, title, awarding institution and date of the thesis must be given

Enlighten: Theses

<https://theses.gla.ac.uk/>
research-enlighten@glasgow.ac.uk

High throughput characterisation of calcium dynamics for single cell functional phenotyping

Anna-Maria Kapetanaki
BSc, MSc

Submitted in fulfilment of the requirements for the
Degree of Doctor of Philosophy



School of Engineering
College of Science and Engineering
Department of Biomedical Engineering
University of Glasgow



April 2025

Abstract

Cell mechanosensitivity is the ability of cells to feel and respond to their surrounding environment, and it plays a crucial role in regulating various physiological processes, including proliferation, differentiation, migration, and apoptosis. Mechanosensitive ion channels are key players in the cellular response to mechanical stimuli. Upon their activation, Ca^{2+} ions enter the cell and trigger downstream signalling pathways. Therefore, tracking of Ca^{2+} signalling appears to be a reliable readout of mechanosensitive activity.

However, current methods for mechanosensitivity assessment have low throughput and are not easily applied to large studies or clinical settings. This thesis aimed to address this limitation by creating a device for real-time monitoring of Ca^{2+} signalling in high-throughput. For this purpose, microfluidics were used as a platform for the device development and cells were stained with a calcium-sensitive dye to facilitate the detection of the calcium influx upon stimulation.

Initially, to understand the operational parameters, the device was tested by chemically stimulating a cell line. Both the chemical stimulant and the cell sample were inserted into the microfluidic device by syringe pumps with a constant flow rate. Upon contact with the chemical stimulant, the cells were probed in different areas of the microfluidic device with a laser source. It was shown that the flow rate and the laser power affect the produced signal, so both experimental parameters should be carefully chosen.

After confirming that Ca^{2+} signalling could be tracked in real time and with high throughput using microfluidics, newly designed devices were introduced to apply mechanical stimulation to the cells. These microfluidic devices featured constrictions within the channels, allowing cells to be mechanically compressed as they passed through. To assess cellular responses, cells were labelled with a calcium-sensitive dye and exposed to a laser source to enable fluorescence-based detection of Ca^{2+} signalling. The results showed that both the magnitude and type of mechanical force influenced the cellular response, with those subjected to gentler constrictions exhibiting significantly higher responses than those subjected to more extreme compression.

Finally, stem cell mechanosensitivity and how this is affected by ageing was investigated. Hu-

man mesenchymal stem cells were aged on purpose using either physical or chemical methods. Senescent markers confirmed the ageing induction since all senescent cells are aged. Then, the aged stem cells were subjected to mechanical and chemical stimulation to assess their responsiveness. Real-time qPCR and in-cell western tests showed decreased responsiveness to either stimulation. However, some compensatory mechanisms were observed at the post-transcriptional level.

Overall, this study demonstrates that high-throughput microfluidic platforms can effectively monitor cellular mechanosensitivity through Ca^{2+} signalling. It was shown that both chemical and mechanical stimulations produce measurable responses in cells. The modified responsiveness observed in aged stem cells highlights the critical contribution of mechanosensitive pathways to cellular ageing.

Contents

Abstract	i
Acknowledgements	xi
Declaration	xiv
Abbreviations	xv
Thesis Outline	xvi
1 Introduction	1
1.1 Mechanosensitivity	1
1.1.1 Mechanosensors	3
1.1.2 Mechanosensitivity dysregulation	4
1.2 Stem cells	5
1.2.1 Stem cell mechanosensitivity	7
1.3 Mechanosensitivity assessment	8
1.3.1 Limitations	13
1.4 Towards High-Throughput	13
1.4.1 Flow cytometry principle	13
1.4.2 Limitations	17
1.4.3 Microfluidics	17
1.5 Aims and Objectives of the project	22
2 Methodology	23
2.1 Materials	23
2.2 Cells	24
2.2.1 HEK293T cells	25
2.2.2 Human mesenchymal stem cells (hMSCs)	26
2.2.3 Cell staining with calcium-sensitive dye	26
2.3 Cell-based analytical techniques	26
2.3.1 Alamar blue	26

2.3.2	Flow cytometry - cell cycle	27
2.3.3	Quantitative Polymerase Chain Reaction	29
2.3.4	In Cell Western	35
2.4	Microfluidics	38
2.4.1	Design	38
2.4.2	Fabrication	40
2.5	Statistical analysis	42
3	Calcium Signalling Tracking with High-Throughput	43
3.1	Introduction	43
3.1.1	Ca ²⁺ signalling as a tracking tool	43
3.1.2	Ca ²⁺ signalling in disease	44
3.2	Materials and methods	45
3.2.1	Stimulation of adherent and suspended cells	45
3.2.2	Sedimentation test	47
3.2.3	Investigation of laser power and flow rate effect on the signal	47
3.2.4	Stimulation of suspended HEK293T cells with ATP in a microfluidic device	48
3.3	Results	48
3.3.1	Stimulation of adherent and suspended cells	48
3.3.2	Sedimentation test	50
3.3.3	Characterisation of experimental parameters	52
3.3.4	Stimulation of suspended HEK293T cells in microfluidic devices	57
3.4	Discussion	66
3.4.1	Proof of concept: Stimulation of adherent and suspended cells	66
3.4.2	Sedimentation test: optimising cell sample solution	67
3.4.3	Signal profile: effect of laser power and flow rate	67
3.4.4	Chemical stimulation experiments	67
3.4.5	Suspension Format vs. Adherent Assays	68
3.4.6	Influence of Mechanical Stimulus (Shear Stress)	68
3.4.7	Relevance of Suspension-Based Assays and Limitations	69
3.5	Conclusion	69
4	Mechanical Stimulation of HEK293T Cells with Microfluidics	71
4.1	Introduction	71
4.1.1	Piezo1 structure and function	71
4.1.2	Yoda1 as Piezo1 activator	73
4.1.3	Piezo1 response	73
4.2	Materials and methods	74

4.2.1	Microfluidic device	74
4.2.2	Confocal microscope	75
4.2.3	Data filtering	76
4.2.4	Chemical stimulation	78
4.2.5	Mechanical stimulation	78
4.3	Results	81
4.3.1	Chemical stimulation	81
4.3.2	Mechanical stimulation	83
4.4	Discussion	86
4.4.1	Biological Interpretation and Comparison with Literature	86
4.4.2	Technical Limitations and Drawbacks	87
4.4.3	Suggested Improvements and Future Directions	87
4.5	Conclusion	88
5	Stem Cell Ageing and Mechanosensitivity	90
5.1	Introduction	90
5.1.1	Ageing	90
5.1.2	Stem cell ageing and consequences	91
5.1.3	Ageing indicators	92
5.1.4	Nanokicking	92
5.2	Materials and methods	93
5.2.1	Physical methods for ageing induction	93
5.2.2	Chemical methods for ageing induction	94
5.2.3	Nanokicking bioreactor	94
5.3	Results	97
5.3.1	Physical methods for ageing induction	97
5.3.2	Chemical methods for ageing induction	101
5.4	Discussion	114
5.4.1	Summary of Findings and Context	114
5.4.2	Methodological Reflections and Limitations	115
5.4.3	Suggestions for Future Optimisation	116
5.4.4	Applicability and Potential Impact	116
5.5	Conclusion	116
6	Conclusions and Future Work	118
6.1	Experimental Findings	118
6.1.1	Combining findings towards a common goal	119
6.1.2	Limitations	120
6.2	Future work	121

6.3 Conclusion	121
A Microfluidic devices	123
B Python code for confocal data processing	125

List of Tables

2.1	Microfluidics materials.	23
2.2	Reagents used in cell culturing and testing	24
2.3	Master Mix recipe	32
2.4	Thermal cycling of the qPCR	35
2.5	Microfluidics materials UoG.	38
2.6	Microfluidics materials Cytonome.	39
5.1	Measurement of vibration displacement	97

List of Figures

1.1	Mechanical forces	2
1.2	Ca ²⁺ involvement in cellular response to mechanical stimulations	3
1.3	Stem Cells classification based on their origin and differentiation potency.	6
1.4	Illustration of systems applying shear stress to cells.	9
1.5	Experimental setup for applying and measuring compression forces on cells.	11
1.6	Experimental setup for applying and measuring tensile forces in cells.	12
1.7	Flow Cytometry	14
1.8	FSC and SSC overview	14
1.9	Fluorescence along with FSC and SSC	15
1.10	Fluorescence Activated Cell Sorting (FACS)	16
1.11	Laminar Flow Velocity Profile in a Rectangular Channel	20
2.1	Cell population gating	29
2.2	Cell Cycle phases	29
2.3	Nanodrop Device	32
2.4	qPCR device and reaction mix.	33
2.5	PBS and Formaldehyde recipes	36
2.6	Permeable, Blocking and Washing Buffer Recipes	37
2.7	Li-COR device	37
2.8	Microfluidic devices developed in UoG.	39
2.9	Microfluidic devices developed by me.	40
3.1	Physiological Solution recipe	46
3.2	Setup for the stimulation of adherent and suspended HEK293T cells	46
3.3	Response of adherent and suspended cells on chemical stimulation.	49
3.4	Sedimentation test	51
3.5	Sedimentation test results.	51
3.6	Complete experimental setup for fluorescence-based calcium signalling detection in a microfluidic device.	52
3.7	Spot characterisation for single-cell fluorescence detection in a microfluidic device.	53

3.8	Signal analysis of cell responses in the microfluidic device.	54
3.9	Effect of Laser Power on Vmax and Peak Duration.	55
3.10	Effect of Flow Rate on Peak Duration and Vmax.	56
3.11	Characterisation of mixing within the microfluidic meander.	57
3.12	Meander of the microfluidic device no1	58
3.13	Representations of the peak durations (ms) distribution.	59
3.14	Maximum Voltage of unstimulated cells' response in different positions. The total flow rate in the device is 100 $\mu\text{L/hr}$, since it is the sum of the flow rate of the two inlets (50 $\mu\text{L/hr}$ each)	59
3.15	Maximum Voltage of stimulated cells' response in different positions.	60
3.16	Measurement of cell response to stimulation.	61
3.17	Meander of the device no2	64
3.18	Maximum Voltage of unstimulated cells' response	64
3.19	Maximum Voltage of stimulated cells' response	65
3.20	Cells' response to different concentrations of ATP	66
4.1	Piezo1 structure and function	72
4.2	Mixing profile of the Chemical stimulation device 3	75
4.3	Confocal Signal Output	76
4.4	Data filtering for the confocal microscope LSM980.	77
4.5	Positions of the chemical stimulation device that was used in the plots.	78
4.6	Mechanical stimulation device with sheath and positions used in the plot	79
4.7	Mechanical stimulation device with focusing meander and positions used in the plot.	80
4.8	Mechanical stimulation device with sheath flow perpendicular to the cell sample flow and positions used in the plot.	81
4.9	Cells' response to ATP stimulation	81
4.10	Cells' response to Yoda1 stimulation	82
4.11	Dose-dependent response to Yoda1	83
4.12	Cells' response to mechanical stimulation (10 μm constrictions)	84
4.13	Cells' response to mechanical stimulation (15 μm constrictions)	84
4.14	Cells' response to mechanical stimulation (cell compression by the sheath flow)	85
5.1	Nanokicking bioreactor	95
5.2	Laser Interferometry	96
5.3	Cell Cycle results for prolonged cultured cells	98
5.4	S-Phase under various culturing periods	99
5.5	Alamar blue results	100
5.6	Cell Cycle results	101

5.7	S-Phase under various culturing periods	102
5.8	qPCR results for ageing treatments	102
5.9	ICW results for ageing treatments	103
5.10	qPCR results for day0	105
5.11	ICW results for day0	105
5.12	qPCR results for day3	106
5.13	ICW results for day3	107
5.14	qPCR results for MS-275-treated cells	108
5.15	ICW results for MS-275-treated cells	109
5.16	qPCR results for TNF- α -treated cells	110
5.17	ICW results for TNF- α -treated cells	110
5.18	qPCR results for day28	112
5.19	ICW results for day28	113
A.1	Mechanical stimulation with sheath and one constriction	123
A.2	Mechanical stimulation without sheath and one constriction	124

Acknowledgements

I would like to acknowledge and thank my supervisors, Professor Massimo Vassalli and Professor Matthew Dalby, for giving me the opportunity to pursue my PhD under their guidance. I am especially thankful to Massimo for his support, thoughtful discussions, and the many opportunities he has provided me over the course of this project.

In addition, I would like to extend my deep appreciation to Matthew for offering me the opportunity to undertake this PhD within the lifETIME Centre for Doctoral Training (CDT). Throughout this journey, I have developed valuable skills and gained insights that will shape my future path.

I would also like to acknowledge the Engineering and Physical Sciences Research Council (EPSRC) for funding this PhD project and supporting my research throughout these years.

There are not enough words to express my gratitude to Dr. Monica Tsimbouri for introducing me to the world of biology and opening that door for me. Thank you, Monica, for dedicating so much time to sharing your expertise in stem cell biology. Your unwavering support has been invaluable, and I could not have explored this field without you.

A heartfelt thank you to my industrial supervisor, Dr. John Sharpe, and to Cytonome, the industrial partner of my PhD project, for offering me the opportunity to complete a three-month placement at their company. It was an incredibly enriching experience through which I gained hands-on knowledge and practical experience and had the pleasure of working alongside some truly inspiring individuals. I am especially grateful to Pascal Spink and Ekaterina Protozanova for their guidance and support during my time at Cytonome. Their advice, expertise, and encouragement played a key role in making the placement both productive and enjoyable.

I am also thankful to Professor Thomas Franke and his group for generously sharing their expertise in microfluidics. A special thanks goes to Matt Woods, Thomas' PhD student, for our collaboration and the many hours we spent together in the dark microscopy room during our first microfluidics experiments. Stepping into the unfamiliar world of microfluidics alongside you made the journey feel less daunting and less lonely.

I would also like to thank all the members of the Centre for the Cellular Microenvironment for their help and support throughout my PhD journey. I am especially thankful to Marta for patiently training me in cell culture techniques and for our collaboration on the writing of our first review paper. A huge thank you to Eva, my office mate, for your friendship, unwavering support, and constant encouragement throughout the last—and most challenging—two years of my PhD. Your company, our endless conversations, and shared laughter were a true source of strength and kept me going when things got tough.

Speaking of friendship, I want to thank Vaios and Demmi, who have been by my side since the very beginning of my PhD. Thank you for always being there, for all the chats that helped quiet my imposter syndrome, for the countless cooking nights and food adventures (I definitely owe you more than a few kilos!) and for all the laughter that brought tears to my eyes. You both have a special place in my heart, and I honestly think of you more as family than friends.

I am forever grateful to my family, especially to my mum, Areti, and my dad, Giannis, for their unconditional love and support. I owe you both so much for encouraging me to move to Glasgow and chase my dreams. From that moment on, you have been by my side, supporting me at every step of this journey. Thank you for always being there to listen to my doubts and fears, and for helping me feel strong and safe. To my sister, Ria, thank you for sharing the countless funny stories of my nieces, which never failed to bring me mentally back home. You've always been my anchor, and your belief in me has meant everything. Thank you for being there and for always having faith in me.

Last, but not least, I want to thank my soul mate, my best friend, my husband, Georgios. Your unwavering love and support have been my greatest strength throughout this entire journey. You have stood by me through every challenge, celebrated every milestone, and offered your endless encouragement when the path seemed unclear. Believing in me, even when I doubted myself, has been my source of motivation. Thank you for your patience and understanding, for staying up with me through countless late nights to offer your comfort and encouragement, and for always making our home a place of peace and love, even in the most stressful moments. I am incredibly grateful for you, and for the shared life and dreams that we continue to build together.

To my family.

Declaration

University of Glasgow
College of Science and Engineering

Statement of Originality to Accompany Thesis Submission

I certify that the thesis presented here for examination for PhD degree of the University of Glasgow is solely my own work other than where I have clearly indicated that it is the work of others (in which case the extent of any work carried out jointly by me and any other person is clearly identified in it).

The copyright of this thesis rests with the author. No quotation from it is permitted without full acknowledgement.

I declare that the thesis does not include work forming part of a thesis presented successfully for another degree (unless explicitly identified and as noted below).

Abbreviations

AFM	Atomic Force Microscope
ASCs	Adult Stem Cells
BMP2	Bone Morphogenic Protein 2
DMEM	Dulbecco's Modified Eagle's Medium
DNA	DeoxyriboNucleic Acid
ECM	ExctraCellular Matrix
ESCs	Embryonic Stem Cells
FACS	Fluorescent Activated Cell Sorting
FBS	Foetal Bovine Serum
FC	Flow Cytometry
FRET	Fluorescence Resonance Energy Transfer
FSC	Forward SCatter
HEK	Human Embryonic Kidney
HSCs	Hematopoietic Stem Cells
HT	High Throughput
HP	Hydrostatic Pressure
HUVECs	Human Umbilical Vein Endothelial Cells
IPA	IsoPropyl Alcohol
iPSCs	induced Pluripotent Stem Cells
ICW	In Cell Western
LSSE	Linear Strain Single-cell Electrophysiology
mRNA	messenger RiboNucleic Acid
MSCs	Mesenchymal Stem Cells
MuSCs	Muscle Stem Cells
PBS	Phosphate-Bafferred Saline
PDMS	PolyDiMethylSiloxane
PMT	PhotoMultiplier Tube
RhoA	Ras homolog family member A
ROS	Riactive Oxygen Species
SASP	Senescence Associated Secretory Phenotype
SSC	Side SCatter
TRPV	Transient Receptor Potential Vanilloid
qPCR	quantitative Polymerase Chain Reaction

Thesis Outline

This thesis begins by providing the motivation and the aims of this project, as well as the theoretical background and the key scientific concepts underpinning this research (Chapter 1). This includes a discussion on mechanosensitivity, focusing on potential mechanosensors and mechanosensitivity assessment methods. Additionally, the fundamental properties of stem cells are explored with emphasis on their mechanosensitivity and relevance to this work. The chapter also introduces microfluidics, detailing how microscale fluid dynamics can be used to study cellular behaviour under controlled conditions. This theoretical background knowledge is essential for understanding the experimental techniques used in this project.

The following chapter (Chapter 2) presents the general methodology employed throughout this study. It includes details on the materials used, such as chemicals, reagents, and microfluidic devices, as well as the instruments utilised for data acquisition and analysis. The chapter also outlines the general experimental techniques, including cell culture protocols and microfluidic device fabrication. Furthermore, the statistical analysis approach used to interpret the acquired data is presented.

The experimental work in this chapter was divided into three main stages. First, it was essential to verify that the selected cells could respond to chemical and mechanical stimuli—both in adherent and suspended states—and generate observable calcium signals. Once this was confirmed, the cell preparation protocol was optimised to address issues related to aggregation and sedimentation. In the final stage, ATP was introduced as a chemical stimulant within the microfluidic device to investigate the effects of laser power and flow rate on the resulting calcium signal. Additionally, a dose-dependent cellular response to ATP was demonstrated (Chapter 3).

Next, Yoda1 was employed for chemical stimulation within the microfluidic device as a precursor to mechanical stimulation. Through these experiments, the response of the Piezo1 mechanosensor to stimulation while the cell was in motion was assessed. A dose-dependent cellular response to Yoda1 was provided. Finally, experiments were conducted in which the cells experienced mechanical stimulation derived from the geometry of the microfluidic channel. Different channel designs were utilised for this purpose. The microfluidic devices used in these experiments were

designed and fabricated in Boston during my industrial placement at the stakeholder company Cytonome (Chapter 4).

Some preliminary experiments were performed for the potential application of our device (sorting of aged stem cells based on their mechanosensitivity). Initially, ageing was induced in hMSCs using two different methods (chemical and physical). Since all senescent cells are aged, the induction of ageing was confirmed by checking the expression of senescent markers (P16, P21, cell cycle, arrest, etc). From this point forward, all hMSCs that have undergone the above-mentioned treatments and exhibit senescence markers will be referred to as aged hMSCs. The effects of ageing on mechanosensitivity markers were examined in comparison to non-aged cells. Subsequently, both aged and non-aged cells were stimulated chemically and mechanically, and changes were observed in both mechanosensitivity and ageing markers (Chapter 5).

Finally, Chapter 6 presents the conclusions and discusses their broader implications. The key findings are summarised in the context of cell mechanosensitivity assessment, stem cell behaviour during ageing, and the utilisation of microfluidic platforms as a tool for studying cellular response. Furthermore, limitations of the current approach are considered, along with potential refinements and improvements that could enhance future studies. The chapter concludes by proposing directions for future research, including further investigations into mechanosensitivity-based sorting techniques and the translational potential of this work in regenerative medicine and stem cell therapies.

Chapter 1

Introduction

This chapter introduces the motivation and objectives of the project and provides a brief overview of the scientific background.

1.1 Mechanosensitivity

Mechanosensitivity, or mechanosensation, refers to the ability of cells to detect mechanical stimuli from their surrounding environment, like shear stress [17], compression or tension [163] (Figure 1.1). This process is followed by mechanotransduction, where the mechanical stimulus is converted into biochemical signals [11, 95]. These mechanisms are essential in determining cell fate [50], allowing cells to adapt to their physical surroundings by remodelling the cytoskeleton, activating various signalling pathways, and influencing gene expression. This regulation impacts key cellular processes such as proliferation, apoptosis [81, 146], differentiation [208], migration [112, 120, 125], and collective organisation, ultimately leading to organogenesis [125].

Mechanosensation plays a vital role in numerous physiological processes, including hearing [158] and touch [82]. A clear example of mechanotransduction occurs when a ship travels through waves at night, creating a visible wake due to the bioluminescence of unicellular dinoflagellates. [91]. This bioluminescence, triggered by the stress exerted by the ship's bow, serves as a defence mechanism against predators and depends on the magnitude and velocity of the applied forces [177].

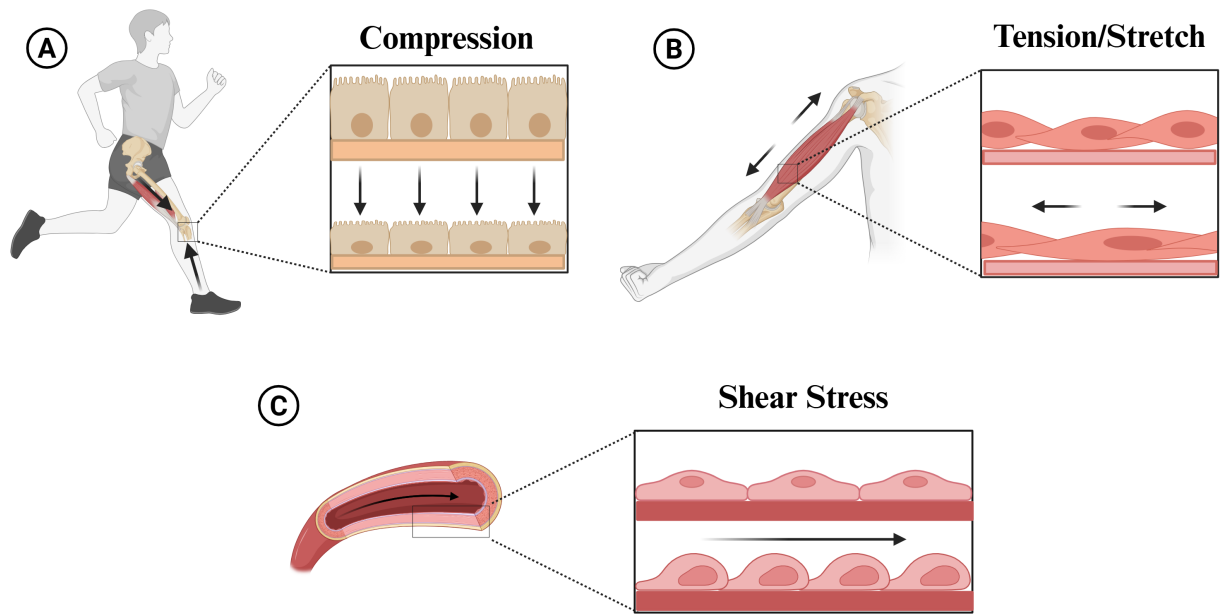


Figure 1.1: An illustration of the different types of mechanical forces that cells can experience. (A) Bone cells under compression forces. (B) Muscle cells under tension due to the muscle stretching. (C) Endothelial cells at the inner surface of a blood vessel under shear stress induced by the blood flow. (Created in BioRender.com).

Moreover, mechanosensation is not limited to specialised sensory cells but is a common feature across nearly all cell types. Most cells have specialised receptors that enable them to detect and respond to mechanical forces and stresses within their microenvironment [134].

Mechanical stimulation of cells, such as stretch, shear stress, or compression, initiates a rapid cellular response mediated mainly by calcium signalling [50]. The first step of this process is the activation of mechanosensitive ion channels embedded in the plasma membrane (Subsection 1.1.1), with Piezo1 (subsection 4.1.1) being one of the most important among them. Upon mechanical deformation of the cell membrane, these channels open to allow the influx of extracellular calcium ions into the cytosol. This calcium entry is an initial signal that can trigger a cascade of downstream processes essential for cellular adaptation and survival [51]. Following calcium influx, the elevated cytosolic Ca^{2+} levels serve as a second messenger that propagates the mechanical signal internally (Figure 1.2). One key mechanism amplifying this signal is calcium-induced calcium release (CICR), in which the initial rise in calcium activates receptors located on the endoplasmic reticulum, leading to further release of calcium from intracellular stores [26]. Therefore, tracking the (Ca^{2+}) signalling in HT was a reliable way to measure how cells respond to mechanical stimulation.

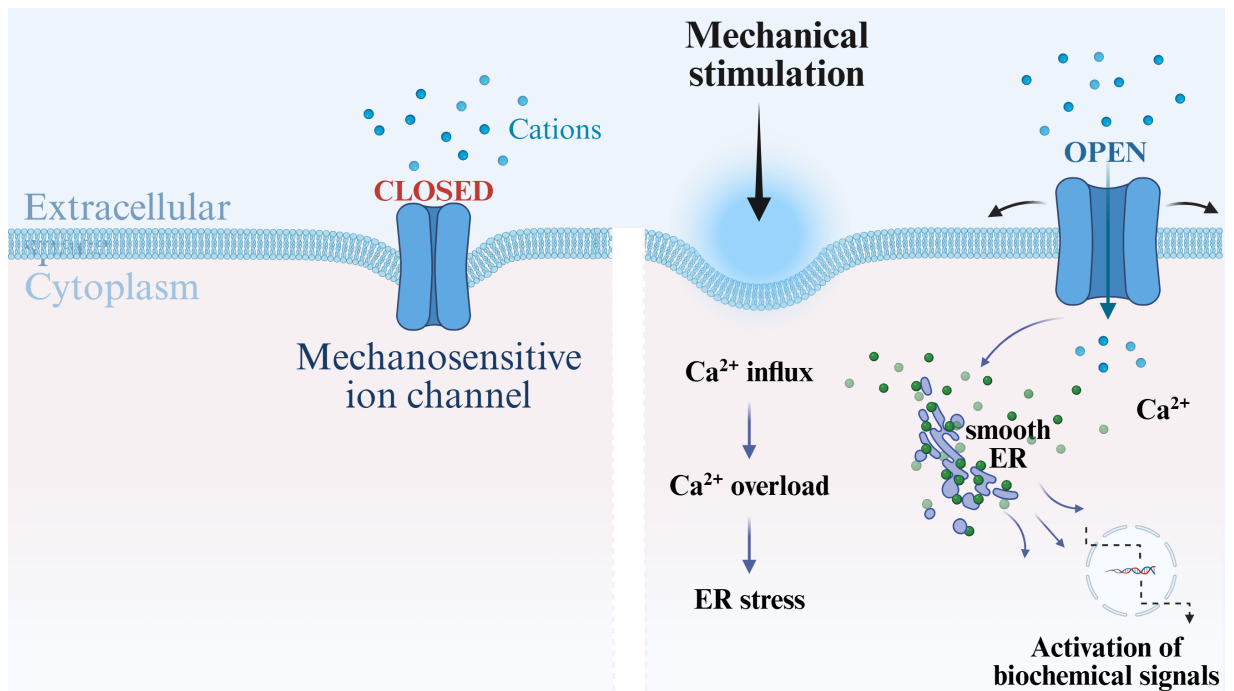


Figure 1.2: A schematic illustration of Ca^{2+} influx into the cytosol. Following the mechanical deformation of the cell membrane, the mechanosensitive ion channel opens to allow the influx of extracellular Ca^{2+} ions into the cytosol. The initial rise in Ca^{2+} (Created in BioRender.com).

1.1.1 Mechanosensors

Cells possess a variety of mechanosensors that enable them to detect mechanical stimuli in their environment and convert them into intracellular signals. Among these are membrane proteins like integrins, which link the extracellular matrix (ECM) to the cytoskeleton, transmitting mechanical signals from the outside to the inside of the cell [64, 141]. Cadherins, another class of transmembrane proteins, mediate cell-cell adhesion and participate in mechanotransduction by transmitting mechanical forces between neighbouring cells. Additionally, mechanosensitive ion channels such as Piezo channels [50, 85, 155] and particular Transient Receptor Potential (TRP) channels respond to mechanical stimuli like stretch and pressure, facilitating processes such as touch sensation and vascular development [141]. Intracellular structures like the actin cytoskeleton [52] and focal adhesions [28] play vital roles in sensing and transmitting mechanical forces throughout the cell, influencing various signalling pathways in response to mechanical stimuli [55]. Moreover, primary cilia, microtubule-based cellular protrusions, contain mechanosensitive ion channels that allow them to detect fluid flow and mechanical changes in the cellular environment.

While not a mechanosensor itself, the ECM significantly contributes to cellular mechanosensing [76, 109]. The ECM is a complex network of proteins and polysaccharides, including fibronectin, collagen, and elastin, which provide structural support to tissues. These ECM com-

ponents can undergo conformational changes in response to mechanical forces, thereby altering the presentation of binding sites for cell surface receptors [86]. A good example of this is the study by Lai et al. ([109]), which demonstrated that while Piezo1 sensitivity is inherently independent of the ECM, ECM proteins can still modulate Piezo1 sensitivity when exposed to varying levels of shear stress. More precisely, it was shown that under high shear stress, fibronectin enhances Piezo1 sensitivity. In contrast, under low shear stress, the ECM proteins that improve Piezo1 mechanosensitivity are collagen types I and IV and laminin [109] (Piezo1 is a mechanosensor of interest in this study, and it will be further discussed in Chapter 4). The ECM plays a crucial role in transmitting mechanical signals to the cell interior through interactions with integrins and other cell surface receptors. These interactions enable the cells to sense environmental changes, adjust their adhesion, migration, proliferation, and differentiation processes accordingly, and maintain tissue homeostasis. Thus, the ECM is integral to the overall mechanotransduction process, serving as a crucial intermediary that modulates the cell's response to mechanical stimuli.

1.1.2 Mechanosensitivity dysregulation

Dysfunction in cellular mechanosensitivity can lead to serious diseases. For example, in cancer, stiffer surrounding tissue and abnormal force signals help tumour cells grow and spread by strengthening how they stick to their surroundings and respond to growth cues [146]. In blood vessels, when endothelial cells experience irregular shear stress from blood flow, they become inflamed and more likely to form plaques, which drives atherosclerosis [17]. Likewise, heart muscle cells depend on the elasticity of their surrounding matrix to contract and stay alive. As the heart tissue hardens, these cells struggle to work properly and may die, contributing to heart failure [135].

Given the crucial role mechanosensitivity plays in tissue function and disease, it is especially important to consider how stem cells respond to mechanical cues in their microenvironment. Stem cells exhibit a remarkable sensitivity to mechanical signals, which significantly influence their fate decisions, including differentiation, proliferation, and self-renewal [61, 66]. This mechanosensitive behaviour is fundamental not only for normal development and tissue maintenance but also for the success of regenerative medicine and tissue engineering applications [40, 94]. Consequently, classifying stem cells based on their origin and potency, and assessing their mechanosensitive properties, are critical steps toward understanding their behaviour and optimising their use in therapeutic applications.

1.2 Stem cells

Stem cells are defined as unspecialised precursor cells with the exceptional capacity for self-renewal and the ability to generate multiple mature cell types. These cells have the potential to differentiate into various cell types within the body during early development and throughout life, playing a crucial role in growth and tissue repair [41]. This differentiation potential is known as potency and distinguishes the stem cells into five subcategories (see Figure 1.3) [43, 193, 204]:

- **Totipotent**, or omnipotent, are the stem cells that result from the fusion of an egg and a sperm cell. They can differentiate into both embryonic and extra-embryonic cell types, enabling them to form a complete, viable organism. Additionally, the cells resulting from the initial divisions of the fertilised egg also possess totipotency.
- **Pluripotent** are the stem cells derived from the totipotent cells. They can differentiate into nearly all cell types, including cells originating from any of the three germ layers (ectoderm, mesoderm, endoderm).
- **Multipotent** are the stem cells that can differentiate into multiple cell types, given that they are within a closely related family of cells. In this category, for instance, fall the Hematopoietic Stem Cells (HSCs) that can differentiate into various types of blood cells (red blood cells, white blood cells, platelets), the Mesenchymal Stem Cells (MSCs) that can differentiate into osteoblasts, chondroblasts, myoblasts, fibroblast etc.
- **Oligopotent** stem cells can only differentiate into a few specific cell types, such as lymphoid or myeloid stem cells.
- **Unipotent** are the stem cells that can produce only one specific cell type but can self-renew, which sets them apart from non-stem cells.

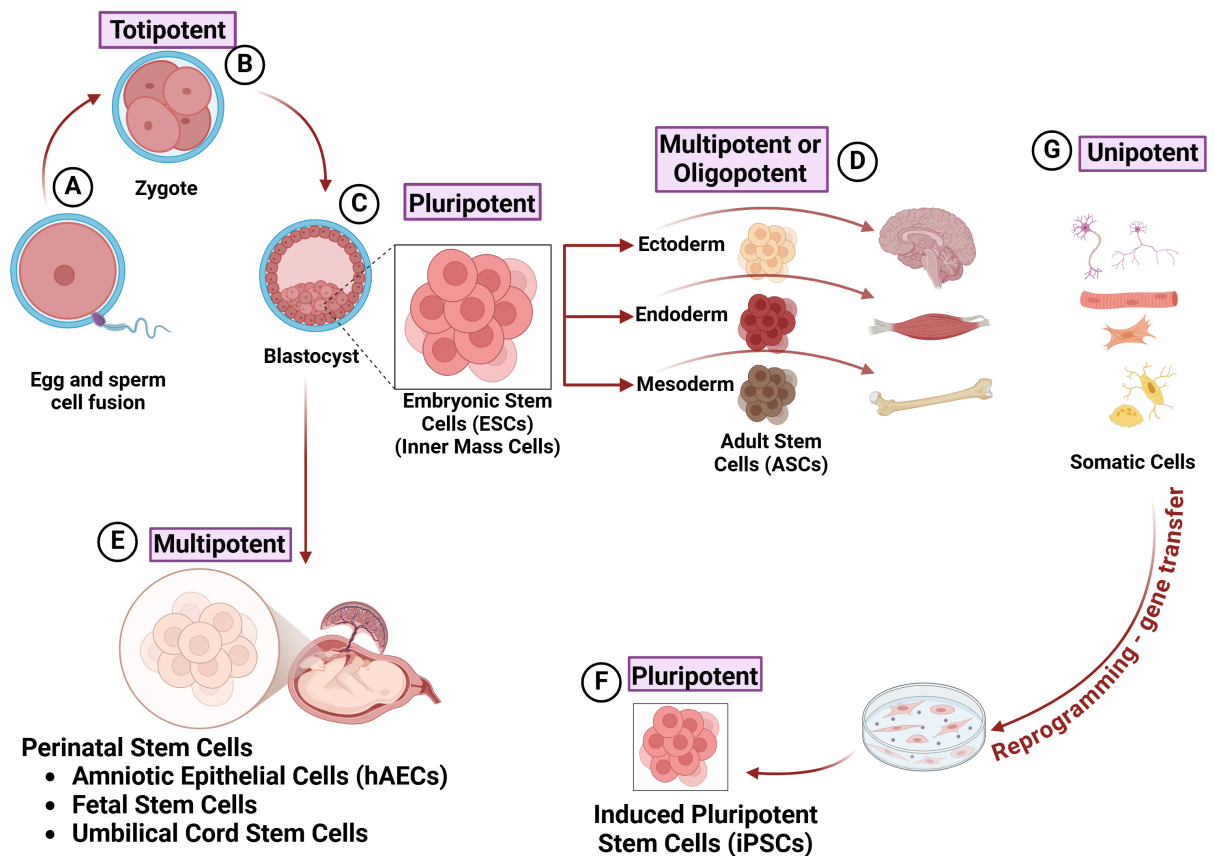


Figure 1.3: Stem Cells classification based on their origin and differentiation potency. Following the fusion of an egg and sperm cell (A), a totipotent zygote is formed (B), which can develop into any cell type. The zygote undergoes division to form a blastocyst containing pluripotent embryonic stem cells (ESCs) within its inner cell mass (C). These pluripotent cells can differentiate into nearly all cell types derived from the three germ layers: ectoderm, mesoderm, and endoderm. Adult stem cells (ASCs), multipotent or oligopotent, arise from these germ layers and can differentiate into a limited range of related cell types (D). Perinatal stem cells, including amniotic epithelial cells, fetal stem cells, and umbilical cord stem cells, are multipotent (E). Additionally, somatic cells can be reprogrammed through gene transfer to create induced pluripotent stem cells (iPSCs), which exhibit pluripotency similar to ESCs (F). Unipotent stem cells, capable of self-renewal, can only differentiate into one specific cell type (G). (Created in BioRender.com).

Stem cells can also be classified based on their origin (Figure 1.3):

- **Embryonic Stem Cells (ESCs)** Embryonic stem cells are derived from the inner cell mass of a blastocyst, an early-stage embryo. These cells are pluripotent, meaning they can differentiate into nearly all body cell types. This high versatility makes them a critical focus of research in regenerative medicine and developmental biology [94, 104].
- **Adult Stem Cells (ASCs)** or somatic stem cells are found in various tissues and organs of the body after development (e.g. bone marrow, peripheral blood, dental pulp, adipose tissue, skeletal muscle, etc). They are typically multipotent, meaning they can differentiate into a limited range of cell types related to their tissue of origin. Examples of adult

stem cells include hematopoietic stem cells (HSCs), which are found in bone marrow and differentiate into various blood cells, and mesenchymal stem cells (MSCs), which are also found in bone marrow, adipose tissue, and other locations, and can differentiate into bone, cartilage, fat, and muscle cells. Neural stem cells, found in the brain, and epithelial stem cells, located in the lining of the gastrointestinal tract and skin, are also types of ASCs. The former can differentiate into neurons, astrocytes, and oligodendrocytes, and the latter into various types of epithelial cells [22, 204].

- **Induced Pluripotent Stem Cells (iPSCs)** are somatic (adult) cells that have been genetically reprogrammed to an ESC-like state. Like embryonic stem cells, iPSCs are pluripotent and can differentiate into nearly all body cell types. This reprogramming provides a valuable tool for research and potential therapeutic applications without the ethical concerns associated with embryonic stem cells [22, 41, 94, 104]
- **Perinatal Stem Cells** are derived from perinatal tissues such as the placenta, umbilical cord blood, and amniotic fluid. These cells are generally multipotent, and compared to MSCs, umbilical cord-derived stem cells are much more readily available. For instance, umbilical cord blood cells contain hematopoietic stem cells that can differentiate into various blood cells. Similarly, amniotic fluid stem cells have the potential to differentiate into a range of cell types, including those of the mesodermal and ectodermal lineages [43, 151]

1.2.1 Stem cell mechanosensitivity

Stem cells are highly responsive to mechanical signals, which can influence their fate and behaviour. Therefore, mechanosensitivity affects them in various ways and plays a crucial role in their differentiation. This phenomenon is a key aspect of tissue engineering, homeostasis, and regeneration [66].

Substrate stiffness is one of the most extensively studied mechanical factors influencing stem cell differentiation. Stem cells are highly sensitive to the rigidity of the ECM, and their shape and size are closely linked to the stiffness of the substrate. Depending on its value, this stiffness can also guide differentiation into specific cell lineages. For example, stem cells cultured on soft substrates with brain-like stiffness tend to adopt a rounded shape and are more likely to differentiate into neuronal or adipogenic (fat) cells. In contrast, when cultured on stiffer substrates, stem cells become elongated or stretched, favouring osteogenic (bone) differentiation. These responses are regulated by mechanosensitive molecules, such as integrins, which connect the ECM to the cytoskeleton, and by signalling pathways, including RhoA, YAP/TAZ, and MAPK, which influence gene expression and drive lineage-specific differentiation. [25, 60, 66, 130, 138, 164, 182, 194].

Since stem cells maintain a dynamic equilibrium between contractile forces from the actin cytoskeleton and the ECM, the mechanical tension within the cell influences the cytoskeletal structure, which regulates stem cell behaviour. For example, high tensile forces are associated with mesodermal differentiation (e.g., muscle or bone cells), while lower tension favours ectodermal differentiation (e.g., neural cells). The mechanotransduction process involves molecules such as focal adhesion kinase (FAK) and paxillin, which transduce mechanical signals from the ECM to the inside of the cell, ultimately affecting gene expression patterns and stem cell fate [125, 130, 138].

Beyond studying disease, exploiting mechanosensitivity has profound implications for regenerative medicine. Tissue-engineering strategies use mechanical conditioning to enhance the maturation and function of engineered constructs: cyclic stretch improves vascular graft performance [61], while compressive loading promotes cartilage formation [128]. Therefore, assessment of cellular mechanosensitivity is essential for both basic research and translational applications.

In the following section, the state of the art in cell mechanosensitivity assessment, along with its limitations, is presented.

1.3 Mechanosensitivity assessment

Since the mechanical forces that a cell can experience vary from shear stress to compressive or tensile forces, the cellular mechanosensitivity assessment is conducted by devices that try to simulate one of the aforementioned natural stimulants. The following subsections will present the fundamental principles of various experimental approaches developed to assess cell mechanosensitivity [173].

In most of the presented methods, Ca^{2+} signalling is used as a tracking tool to observe cells' response. This aspect will be described in detail in Chapter 3, where the development of the Ca^{2+} signalling tracking device is presented.

Shear stress

The primary mechanical stress in blood vessels is shear stress, created by blood flowing along the endothelial layer [44]. Under normal laminar flow (7–20 dyn/cm^2), shear stress aligns endothelial cells with the flow and boosts nitric oxide production to keep vessels healthy [157]. Therefore, studying mechanosensitivity induced by shear stress is important because it governs endothelial function and vascular homeostasis.

In Xu et al. 2018, a novel shear stress simulation assay was described [198]. The device consists of a flat-headed piston powered by an acoustic transducer operated by a signal generator (Figure 1.4 (A)). When in operation, the piston is immersed in a buffer in a transparent-bottom container, moving up and down at a controlled frequency and amplitude to create obstructed fluid motion in an oscillatory fashion. The moving fluid enforces shear stress on the cells seated on the bottom of the container. A detector below the container records the cells' response to the applied shear stress. Following initial testing of the piston-container device, the system was scaled up to a format with a 3D-printed 384-pin stimulation array affixed to a voice coil. The scaled-up system fits inside the molecular device's fluorescence image plate reader. The pins' shape was optimised to prevent the trapping of air bubbles in the plate [198]. The intensity of the induced shear stress was measured through particle image velocimetry, and it was found to be between 0.1 and 2 Pa. This intensity can be raised up to 16.7 Pa by increasing the buffer's viscosity. The above-described device applied shear stress at 6.5 Pa to human umbilical vein endothelial cells (HUVECs). An increase in intracellular calcium levels in HUVECs was observed, and this was completely eliminated by 2.5 mM EGTA. This suggested that the signal was triggered by extracellular calcium entering the cells, which confirms that this high throughput mechanical stimulation system is suitable for simulating shear stress application in a precise, quantitative and reproducible fashion.

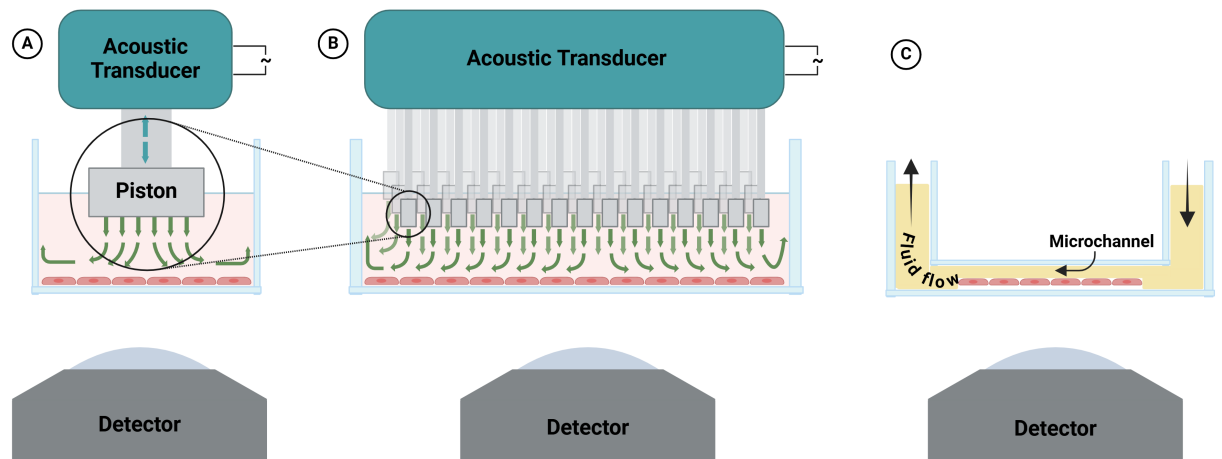


Figure 1.4: Illustration of systems applying shear stress to cells: (A) A single-piston device powered by an acoustic transducer, which is operated by a signal generator. Shear stress is induced by the oscillatory fluid movement. (B) The scaled-up system of the single-piston device comprises a 384-pin stimulation array. (C) Fluid shear stress system. It comprises a microchannel, where the cells are seeded, an inlet for the fluid introduction, and an outlet to allow the fluid to exit the system ([126]). (Created in BioRender.com).

In another study [127], a fluid shear stress system was used to investigate the effect of $A\beta$ peptides on PIEZO1 activation (Figure 1.4 (C)). The cells were dyed with a calcium indicator (Fluo4_AM) and imposed to single square, shear pulses of 10 ms duration at 15 dynes/cm². The

effect of the shear stress on the cells was monitored by genetically encoded optical force probes embedded in actin. It was shown that 22 sec after the first stimulus, the cells exhibited a drastic increase in Ca^{2+} concentration, which was followed by a loss of fluorescence, demonstrating adaption or inactivation after 60 sec.

Compression forces

The predominant form of mechanical stress in our body is compression. Almost all the cells in our body are under constant compression. For instance, osteocytes are under compression when we stand, sit, or walk. Thus, a device imitating this form of mechanical stimuli is of great importance and will significantly facilitate the understanding of cell mechanosensitivity.

He et al studied the response of mammalian cells under mechanical compression. The device used for this purpose consists of an upper and a lower chamber separated by a polydimethylsiloxane (PDMS) layer of 200 μm thickness (Figure 1.5 (A)). When the upper chamber gets inflated by air pressure, the PDMS membrane moves downwards and compresses the mammalian cells, which are cultured in the lower chamber [87]. The applied compression is controlled by micropillars of the same material as the membrane (PDMS). Their role is to support the PDMS membrane and implement a threshold for its downward movement, regulating the degree of compression of the mammalian cells in this way. A fluorescence resonance energy transfer (FRET)-based sensor was used to track the response of RhoA activity in cells under different environments in real time. It was shown that the RhoA (ras homolog gene family member A) activity decreases when mechanical compression is applied and returns to its initial level when it ceases. The fact that the cells respond to a mechanical stimulus generated by the air-driven microfluidic compression device suggests that it is suitable for studying cell mechanosensitivity.

A. Sugimoto et al. 2017 used a custom-made hydrostatic pressure chamber (Figure 1.5(B)) to investigate the effect of hydrostatic pressure (HP) on cell fate determination of mesenchymal stem cells (MSCs) by monitoring their differentiation into osteoblasts [169]. For this study, MSCs and MSC lines (UE7T-13 and SDP11) loaded with Yoda1 (Piezo1 activator) or GsMTx4 (Piezo1 inhibitor) were used. Atmospheric pressure was set as the zero reference point, and hydrostatic pressure was applied by increasing the pressure of either the gas phase or the aqueous medium. BMP2 expression, which is a key indicator of osteoblast differentiation, was measured as the primary outcome. When Piezo1 was inhibited, BMP2 expression was reduced, and osteoblast differentiation was impaired. Similarly, BMP2 blockade prevented the pressure-induced upregulation of osteogenic marker genes. These results indicate that Piezo1, which is upregulated in primary MSCs and MSC lines under hydrostatic pressure, functions as a pressure sensor that drives BMP2 expression and promotes osteoblast differentiation.

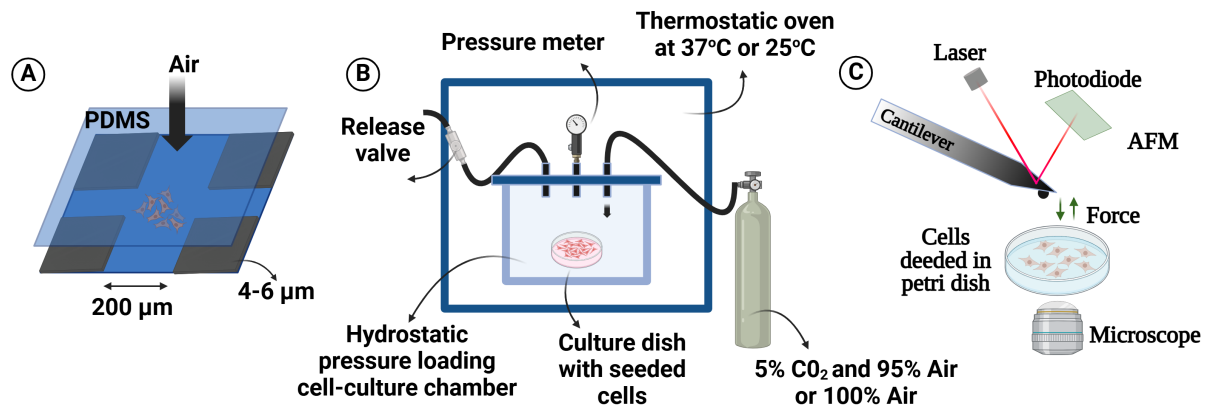


Figure 1.5: Experimental setup for applying and measuring compression forces on cells: (A) Schematic of a PDMS-based microdevice used to confine and apply controlled compression to cells. (B) A hydrostatic pressure loading system within a thermostatic oven (25°C or 37°C) to regulate environmental conditions for cell culture. (C) Atomic Force Microscopy (AFM) setup for measuring mechanical responses, where a laser and photodiode detect cantilever deflection as force is applied to cells seeded on a petri dish. (Created in BioRender.com).

B. Gaub et al. 2017 employed AFM-based force spectroscopy combined with confocal microscopy to mechanically stimulate living mammalian cells and characterise the activation of the Piezo1 receptor. Hence, the receptor activity was monitored by real-time fluorescent calcium imaging. The experimental assay is described in Figure 1.5 (C). The cells (neuroblastoma and human embryonic kidney cells) were loaded with the mechanosensitive receptor Piezo1 co-expressing GFP and the calcium indicator jRCaMP1a. The expression of both was observed by the confocal microscopy following the applied compression stimulus [76].

Tensile forces

The main mechanical stress that stretches cells and their surrounding matrix is tensile force. Cardiomyocytes experience cyclic tension with every heartbeat, which influences their alignment and gap-junction organisation [67], and skin fibroblasts align and alter gene expression when subjected to uniaxial stretch [57]. Therefore, studying mechanosensitivity to tensile forces is important because it reveals how cells detect and adapt to stretching, ensuring proper tissue structure and function.

B Gaub et. al 2017 describe how the same setup, that was used to apply compression forces, was utilised to investigate the Piezo1 receptor response to mechanical pulling instead of compression. For this purpose, the bead and cantilever were fixed with Matrigel, a mix of ECM proteins, and lowered onto the cell until reaching the contact force required for mechanically activating Piezo1 receptors (Figure 1.6 (A)). The cantilever and bead were kept at that position for 60 sec to ensure cell adhesion to the ECM proteins. The cell membrane was stretched locally at the adhesion point by rapidly pulling back the cantilever. This pulling force resulted in a strong calcium signal in the cells.

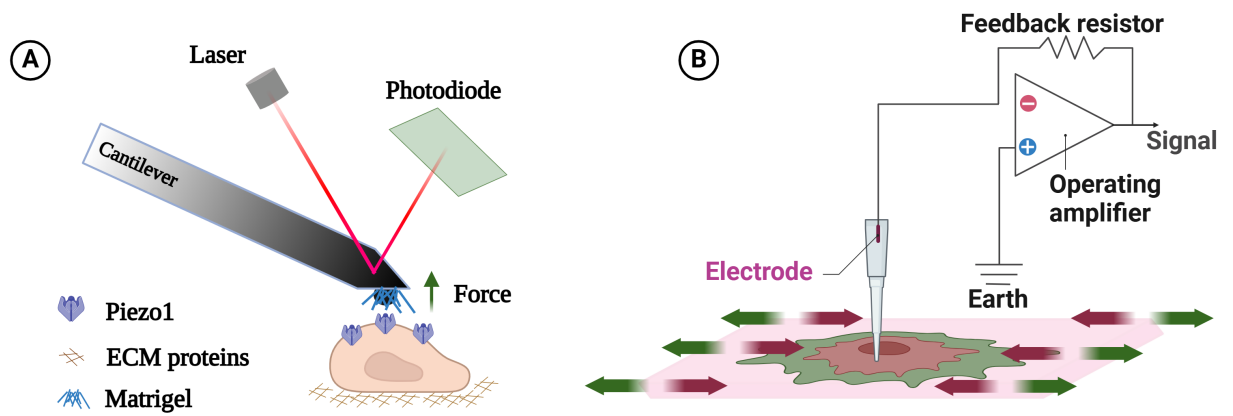


Figure 1.6: Experimental setup for applying and measuring tensile forces in cells: (A) Atomic Force Microscopy (AFM) setup used to apply mechanical force on cells via a cantilever while measuring responses through laser reflection onto a photodiode. Cells are embedded in a matrix containing extracellular matrix (ECM) proteins and Matrigel, with Piezo1 mechanosensitive ion channels indicated. (B) Schematic representation of an electrophysiological setup using an electrode to measure cellular responses to mechanical stimulation. The signal is amplified through an operational amplifier with a feedback resistor while the system is grounded to Earth. (Created in BioRender.com).

For the investigation of the mechano-electrical coupling, E. de Coulon et al 2021 created a linear strain single-cell electrophysiology (LSSE) device to produce unidirectional strain events to adherent cells kept in whole cell patch clamp recording configuration (Figure 1.6 (B)) [56]. The system they developed consists of the strain stage, which produces the required stimulus, and a spatial stabilisation system of high accuracy, vital for maintaining the sealing formed by the patch pipette on the cell surface unharmed during strain-induced cell movements. A flexible cell culture dish is located at the centre of the LSSE system. During the strain application, the cell is kept in place and contact with the micropipette-electrode by 6 μm beads functionalised with black-dyed polystyrene. The culture dish is fixed by a pair of brackets to the piezo-actuated strain stage, which is mechanically fixed to a 3D positioning control system. This system combines a 3-axis nanopositioner to stabilise the cell-micropipette interface in all significant directions during the straining of the patched cells. The patch pipette is fixed to a scanning ion conductance microscope, and the whole LSSE system is fitted on the stage of an inverted microscope equipped for epifluorescence. The cells were marked with a fluorescent cell membrane, and their substrate (flexible culture dish) was subjected to different magnitudes of strain. It was shown that the applied strain stimulus is transmitted effectively to the adherent cells. The effect of the applied strain on the cells was monitored by mounting the cells to whole-cell voltage-clamp recording. The mechanosensitive activated currents increased at higher strain amplitudes, with some of them exhibiting a sigmoidal strain dependence.

1.3.1 Limitations

Yet despite the importance of mechanical signals, our ability to measure how cells respond to mechanical force is still limited to slow, low-throughput methods, such as atomic force microscopy [76] or microchannels [127] for compression force or shear stress application, which can test only dozens to hundreds of cells at a time. To accelerate both basic research and clinical translation, we need new high-throughput, real-time assays that can track mechanosensitive signalling across thousands of cells simultaneously.

1.4 Towards High-Throughput

The gold standard in HT single-cell analysis is flow cytometry (FC). FC is a multi-parametric technique with applications in multiple disciplines, such as immunology, virology, molecular biology, cancer biology and infectious diseases, offering a solid platform for quantifying and analysing particles suspended in a fluid. FC enables researchers to explore cells' or particles' complex physical and chemical characteristics within a biological sample. Through FC, scientists can thoroughly measure and assess various cell properties such as cell size and granularity, as well as the expression patterns of specific cell surface and intracellular molecules, specific messenger Ribonucleic Acid (mRNAs), and the amount of total Deoxyribonucleic Acid (DNA). This information emphasises the FC potential, as it unlocks valuable insights into cellular behaviour and functionality [16, 42, 131].

An evolution of FC is the fluorescent-activated cell sorting (FACS). FACS utilises fluorescent labelling technology to enable the isolation of specific cell subpopulations with precision. This technology relies on the emission of fluorescent signals by labelled cells, allowing researchers to sort and separate distinct cellular subsets based on their unique fluorescence profiles. This approach revolutionises the field, providing a means to isolate and study specific cell types in a targeted manner [42].

In the following subsections, the underlying principles governing both FC and FACS will be presented. Additionally, a focus will be placed on the innovative applications and advancements of these methodologies.

1.4.1 Flow cytometry principle

Traditional flow cytometers are complex devices comprising three basic components: fluidics, optics, and electronics. The fluidics system uses a precisely calibrated pressurised sheath fluid, usually a buffered saline solution, to deliver and accurately focus the sample at a laser beam, where the critical analysis occurs [131].

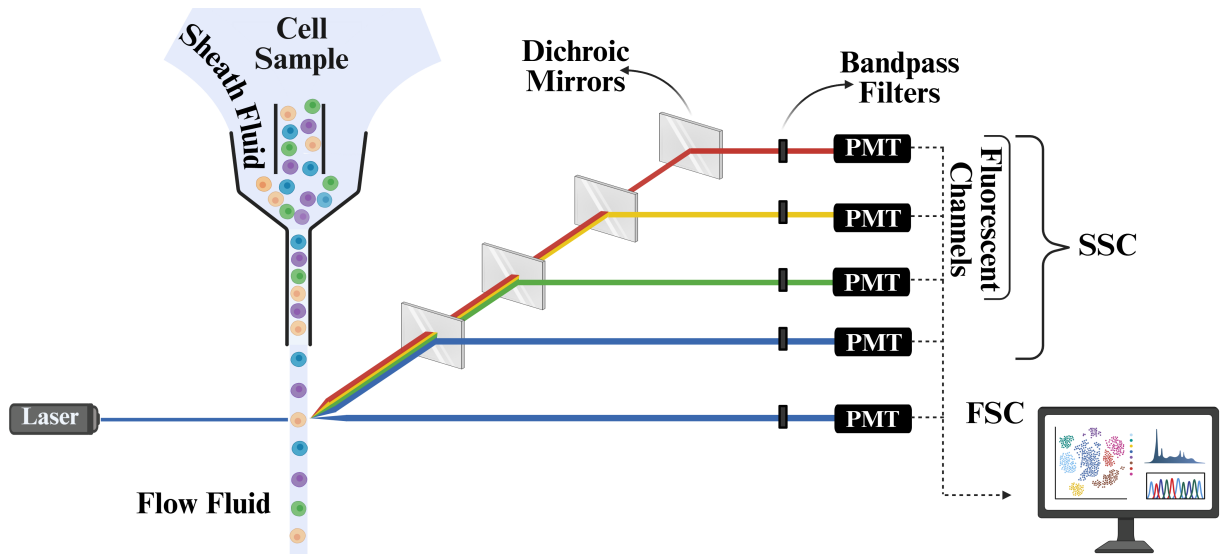


Figure 1.7: A schematic illustration of a flow cytometer (Created in BioRender.com).

Within the optical system of the flow cytometer, excitation sources, such as lasers, and detectors, such as photomultiplier tubes (PMTs) and photodiodes, are responsible for the generation and collection of visible and fluorescent signals, respectively, which are essential for comprehensive sample analysis. As cells pass through the laser beam, scattering occurs in multiple directions, resulting in forward scatter (FSC) and side scatter (SSC) light patterns depending on the positioning of the detector in relation to where the laser interacts with the cells (Figure 1.7).

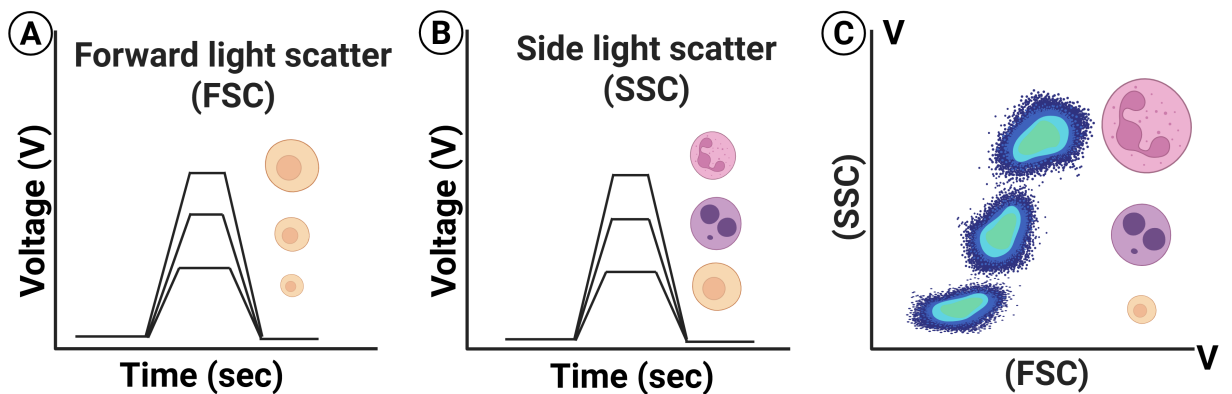


Figure 1.8: (A) The Forward Scatter (FSC) gives information about the cell's size as a function of a measurement voltage, which is proportional to the FSC light. The higher the voltage, the bigger the cell. (B) The Side Scatter (SSC) gives information about the cell's shape and internal complexity as a function of a measurement voltage, which is proportional to the SSC light. (C) By analysing the FSC and SSC together, the researcher can understand a cell's size, shape, and complexity. The FSC and SSC data analysis allows the researcher to divide the heterogeneous population of cells into individual populations with varying sizes, shapes and complexity (Created in BioRender.com).

These patterns offer valuable insights into the cell's size and morphology. More precisely, FSC is proportional to the size of the cell. Larger cells diffract more light in the forward direction

than smaller ones because they have a greater cross-sectional area to interact with the light beam. The detector converts the scattered light into a voltage pulse, which is directly proportional to the amount of the scattered light. The amount of SSC light is detected by a detector located perpendicular to the path of the laser beam. SSC is proportional to the shape and internal complexity of a cell. Like with FSC light, the PMT converts the detected SSC light into a voltage pulse, directly proportional to the amount of SSC light (Figure 1.8) [53, 167].

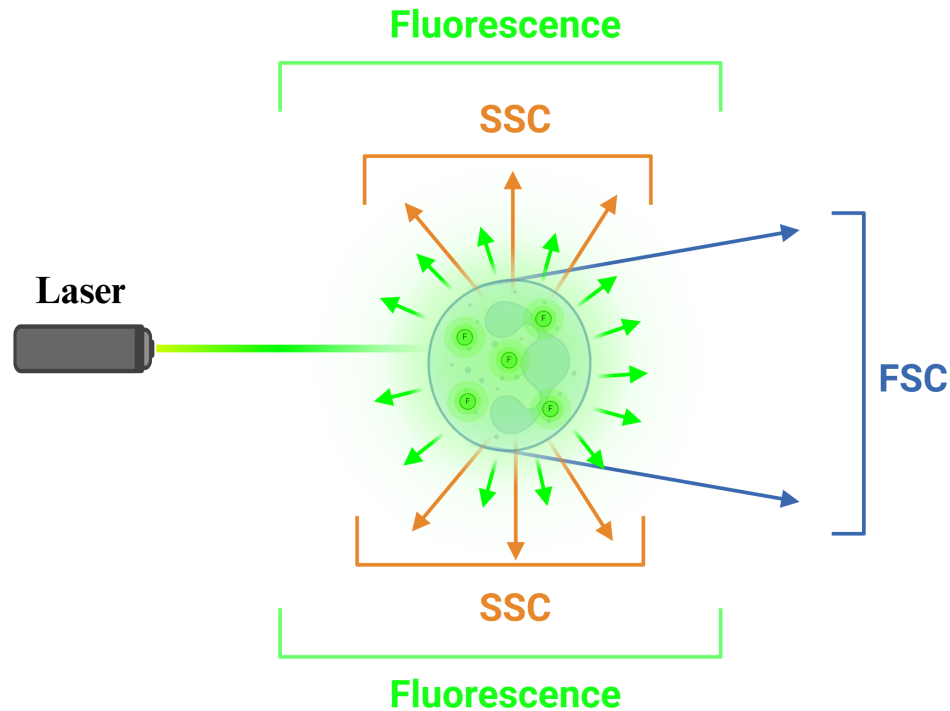


Figure 1.9: Schematic illustration of fluorescence, FSC, SSC in a flow cytometer (Created in BioRender.com).

Apart from the physical characteristics of a cell, FC can give information on the molecular composition of a cell. In particular, to identify specific surface or intracellular molecules, cells need to be marked by fluorescent reagents prior to flow cytometric analysis [42]. These could include fluorescently conjugated antibodies, DNA binding dyes, viability dyes, ion indicator dyes and fluorescent expression proteins. In that case, the laser beam is incident to the cell and excites the fluorescent agent, which emits fluorescent light, along with the scattered light [131]. The fluorescent light from the excited fluorophores can be of various wavelengths, and the scattered light is typically directed at a 90-degree angle (SSC) (see Figure 1.9). Through a lens, the light is guided to a series of dichroic mirrors that focus it onto PMTs. The bandpass filters located in front of the PMTs isolate particular wavelengths of light. This precision in filtering enables the detection and the precise measurement of individual fluorophores utilised in the analysis, as shown in Figure 1.7 [34, 131].

Fluorescence-Activated Cell Sorting (FACS) is an advanced flow cytometry (FC) extension enhanced by fluorescent labelling. In this process, cells are tagged with fluorescent markers that bind to specific intracellular or surface molecules. When these target molecules are present, the labelled cells emit a fluorescent signal, which is detected by a detector. As cells pass through the flow cytometer, they are encapsulated into droplets by a vibrating mechanism at the tube's nozzle. At the end of the nozzle, an electrical charging ring assigns a positive or negative charge to each droplet based on the presence or absence of the target molecule. An electric field then guides the charged droplets towards different containers: positively charged droplets are directed to a container with a negative electrode, negatively charged droplets to a container with a positive electrode, and neutral droplets are collected in a waste container. This precise sorting mechanism allows for the separation and collection of cells based on the specific molecules they express [62, 68, 75, 156].

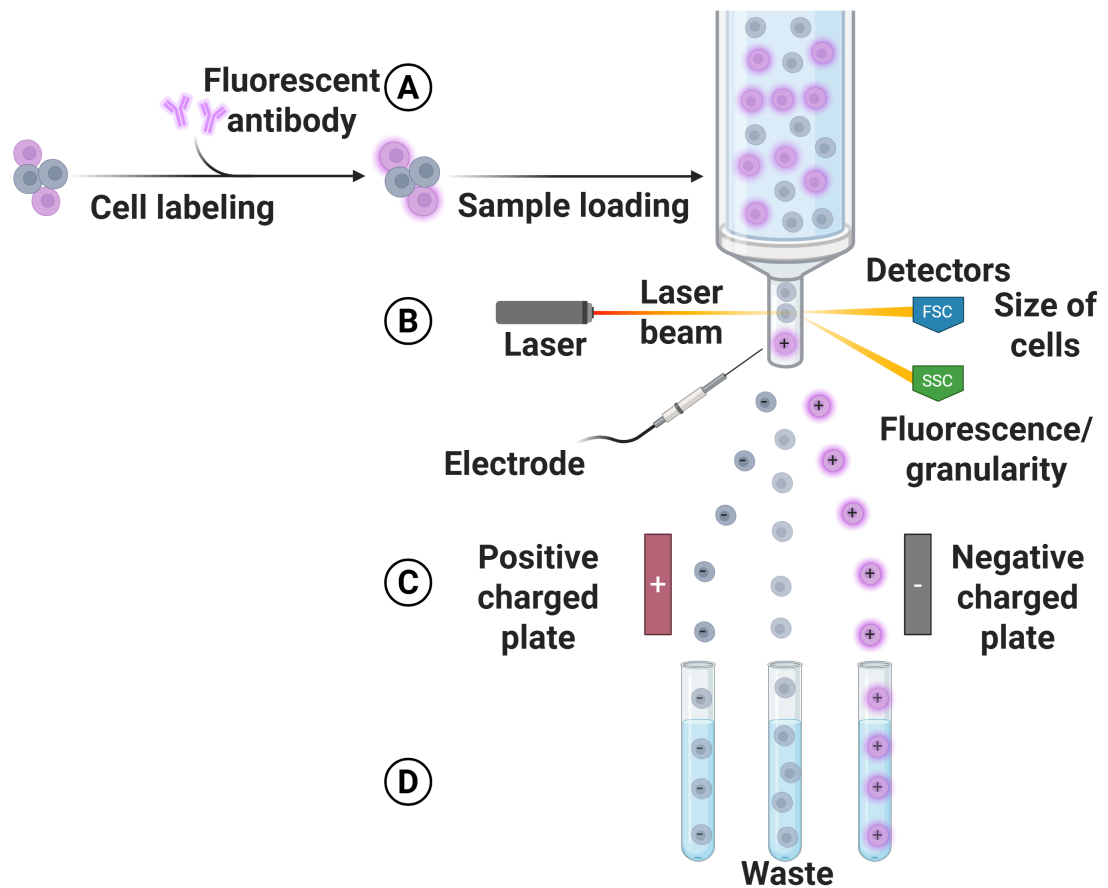


Figure 1.10: Fluorescence Activated Cell Sorting (FACS): (A) A target cell type within a mixture of cells is fluorescently labelled. (B) The cell mixture leaves the nozzle in droplets. A laser beam strikes each droplet. FSC detector identifies cell size. SCC detector identifies fluorescence/granularity. Electrode assigns positive (+) or negative (-) charge. (C) Positively charged cells move closer to the negatively charged (-) plate and vice versa. (D) The separated cells are collected in different collection tubes (Created in BioRender.com).

1.4.2 Limitations

A significant limitation of current technological advancements is the challenge of identifying specific biomarkers for rare cell subpopulations or particular biological conditions. Biomarkers such as specific surface proteins, transcription factors, or secreted factors are essential for distinguishing these cells, yet many physiologically or pathologically important subsets (e.g., cancer stem cells, early progenitors, activated immune cells) lack well-validated markers that can be used for high-throughput sorting. For instance, senescent cells, which accumulate with ageing and disease, express various proteins and surface markers like P16, P21, SA- β -gal etc, but there is no universal surface marker to positively identify all senescent cells for isolation or in vivo tracking [48, 59, 88].

While label-free methods for marking individual cells in high-throughput scenarios show promise, they face a major obstacle: they are not directly compatible with existing cell-sorting processes. This issue complicates the efforts of researchers and healthcare professionals to accurately identify and sort rare cell types or cells with specific biological characteristics. The difficulty in integrating label-free methods with cell-sorting procedures slows the progress of biomedical research and clinical applications.

To address this, scientists are exploring innovative strategies to link label-free marking techniques with cell-sorting methodologies. Overcoming this challenge could significantly enhance our ability to study and isolate rare cell populations, leading to significant advancements in cellular biology research and medical diagnostics. These improvements could result in more effective therapeutic methods and better patient outcomes in various diseases.

While flow cytometry remains the gold standard for HT single-cell analysis due to its speed and multiparametric capabilities [148], it is often limited in terms of assay flexibility, integration with other analysis modalities, and reagent consumption. Microfluidics addresses many of these limitations by offering customisable platforms that can sort, culture, and analyse cells in a controlled microenvironment [159, 190]. Their versatility and compatibility with live-cell analysis make them particularly valuable for stem cell research and mechanobiology [159, 206].

1.4.3 Microfluidics

Microfluidics pertains to the science and technology concerning systems that manipulate or process minute volumes of fluids, typically ranging from 10^{-6} to 10^{-18} litres, utilising channels with dimensions spanning tens to hundreds of micrometres. Typically employed fluids within microfluidic apparatus involve whole blood samples, bacterial cell suspensions, protein or antibody solutions, and assorted buffers ([70]).

Microfluidics' initial applications primarily focused on analysis, capitalising on several advantageous features. Given the minute volumes within these chambers, there's a consequential reduction in the consumption of reagents and analytes, a significant advantage when dealing with costly reagents. On top of that, they facilitate high-resolution separations and detections along with rapid analysis times and compact device footprints[190].

The functionality of microfluidic devices extends to intriguing measurements, spanning molecular diffusion coefficients, fluid viscosity, pH levels, chemical binding coefficients, and enzyme reaction kinetics. Additionally, microfluidic platforms find diverse applications in techniques such as capillary electrophoresis, immunoassays, flow cytometry, sample injection for mass spectrometry analysis, PCR amplification, DNA analysis, cell manipulation, chemical gradient formation and more. These applications' versatility renders great potential particularly valuable in clinical diagnostic settings ([1]).

Principles

The principles governing microfluidics differ significantly from those of macroscale fluid dynamics due to the dominance of surface forces, low Reynolds numbers, and laminar flow conditions.

- **Laminar Flow and Reynolds Number:**

Fluid motion is governed by two key forces: inertial and viscous. Inertial forces arise from the fluid's momentum. They are related to the mass of a fluid and its tendency to keep moving in the same direction unless something stops or redirects it. Inertial forces, when dominant, cause the fluid to create swirls and turbulence [23, 153, 168].

Viscous forces are the resistance of a fluid to being deformed or moved. It can be described as the friction between layers of fluid that are sliding past each other. Viscous forces, when dominant, make flow smooth and controllable [168].

Reynolds number (Re), is a dimensionless parameter relating inertial forces to viscous forces of a flowing fluid, and is mathematically described by the following equation [168, 190]:

$$R_{(e)} = \frac{\rho \times u \times L}{\mu}$$

Where,

ρ : Fluid density

u: velocity

L: Characteristic length (e.g. channel width)

μ : Dynamic viscosity.

The numerator of the Re equation describes the inertial forces while the denominator represents the viscous forces. In microfluidic systems, Re is usually much less than 1, indicating that viscous forces dominate over inertial forces, preventing turbulence and allowing precise control over fluid mixing and transport ([1]).

- **Surface Tension and Capillary Effects:**

Due to the small dimensions of microfluidic channels, surface tension and capillary forces become significant and facilitate the liquid movement through the microchannels. Furthermore, these forces influence droplet formation, fluid interface behaviour, and spontaneous flow in capillary-driven systems ([70]).

- **Diffusion and Mixing:**

Diffusion and mixing are fundamental processes in microfluidic systems, mainly due to the challenges associated with adequate mixing at the microscale. The absence of turbulence necessitates the development of advanced strategies to achieve uniform fluid distribution ([1]).

Molecular diffusion:

Diffusion occurs in a predictable manner governed by concentration gradients. In microfluidic environments, mixing is primarily diffusion-driven, operating over timescales distinct from those in macroscopic systems.

Passive mixing strategies:

Passive approaches, including the use of curved channels and geometric constrictions, enhance mixing by inducing chaotic advection. These methods improve fluid homogenisation without requiring external energy sources or mechanical components.

- **Velocity Profile for a Rectangular Microchannel:**

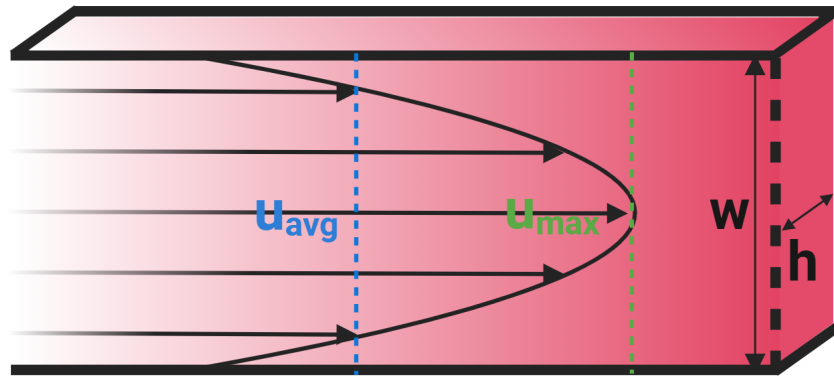


Figure 1.11: Laminar flow velocity profile in a rectangular channel. The schematic illustrates the parabolic velocity distribution, where the maximum velocity (U_{\max}) occurs at the centre of the channel, while the average velocity (U_{avg}) is lower and located closer to the walls. The channel dimensions are represented by width (w) and height (h). (Created in BioRender.com).

For fully developed laminar flow in a rectangular channel, the velocity profile is given by ([2, 99]):

$$v_{(x,y)} = v_{\max} \left(1 - \frac{x^2}{w^2}\right) \left(1 - \frac{y^2}{h^2}\right) \quad (1.1)$$

Where:

$v_{(x,y)}$: velocity at a point in the cross-section

v_{\max} : maximum velocity (at the centre, $x = 0, y = 0$)

w : channel width

h : channel height.

Derivation of the average velocity

The average velocity is obtained by integrating the velocity profile over the cross-sectional area and dividing by the total area:

$$v_{\text{avg}} = \frac{1}{A} \int_A v(x,y) dA \quad (1.2)$$

Since the cross-section is rectangular, we write:

$$v_{\text{avg}} = \frac{1}{wh} \int_{-w/2}^{w/2} \int_{-h/2}^{h/2} v_{\max} \left(1 - \frac{x^2}{w^2}\right) \left(1 - \frac{y^2}{h^2}\right) dx dy$$

Expanding the expression:

$$v_{\text{avg}} = \frac{v_{\max}}{wh} \int_{-w/2}^{w/2} \left(1 - \frac{x^2}{w^2}\right) dx \int_{-h/2}^{h/2} \left(1 - \frac{y^2}{h^2}\right) dy$$

We solve each integral separately.

First Integral (over x):

$$I_x = \int_{-w/2}^{w/2} \left(1 - \frac{x^2}{w^2}\right) dx$$

Using the standard integral formulas:

$$\int x^2 dx = \frac{x^3}{3}$$

Evaluating from $-w/2$ to $w/2$:

$$I_x = \left[x - \frac{x^3}{3w^2} \right]_{-w/2}^{w/2}$$

Since the cubic terms cancel:

$$I_x = w - \frac{w}{12} = \frac{10w}{12} = \frac{5w}{6}$$

Second Integral (over y):

Similarly,

$$I_y = \int_{-h/2}^{h/2} \left(1 - \frac{y^2}{h^2}\right) dy$$

$$I_y = h - \frac{h}{12} = \frac{10h}{12} = \frac{5h}{6}$$

Final Computation of Average Velocity

Substituting these results:

$$v_{\text{avg}} = \frac{v_{\text{max}}}{wh} \times \left(\frac{5w}{6}\right) \times \left(\frac{5h}{6}\right)$$

$$v_{\text{avg}} = v_{\text{max}} \times \frac{25}{36}$$

$$v_{\text{avg}} \approx \frac{2}{3} v_{\text{max}}$$

Final Relationship

For a rectangular microchannel:

$$v_{\text{avg}} \approx \frac{2}{3} v_{\text{max}} \tag{1.3}$$

Thus, the average velocity is approximately 67% of the maximum velocity in a rectangular channel.

1.5 Aims and Objectives of the project

With the increasing need for high-throughput assessment of cellular mechanosensitivity, this project aims to develop and apply innovative tools for real-time functional analysis of stem cells.

The primary objectives of this thesis are as follows:

1. **Device Development:**

To design and fabricate a microfluidic device capable of monitoring intracellular calcium (Ca^{2+}) signalling in real time with high throughput. This allows dynamic tracking of cellular responses to external stimuli at single-cell resolution.

2. **Mechanical Stimulation and Response Analysis:**

To integrate a mechanical stimulation feature into the device, enabling the mechanical stimulation of cells (compression) while simultaneously recording their Ca^{2+} signalling responses.

3. **Ageing effects on Stem Cell Mechanosensitivity:**

To investigate how stem cell mechanosensitivity is modulated by ageing (see subsection 5.1.2). This includes comparing the expression of mechanosensitive markers of aged and non-aged stem cells. The long-term vision would be to characterise and sort stem cells based on their mechanosensitivity. Such a tool would enable the selection of cells best suited for specific therapeutic or engineering applications, improving treatment outcomes and product consistency.

Chapter 2

Methodology

This chapter provides a comprehensive overview of the materials, general techniques, and experimental protocols employed throughout this study. In addition, the statistical analysis approach applied to process and interpret the experimental data is described. Materials and methods specific to each experimental chapter are detailed within the corresponding chapters.

2.1 Materials

The materials used in this project are listed in the following tables:

Product	ID	Provider
BD Plastipak Luer Lock Concentric Tip Syringes 3mL x 200	309658	Medisave Ltd
Miraject Endo Luer 0.3 x 40 mm, G30	138484	Praxisdienst
Polyethylene (PE) Tubing	BTPE-20, PE-20	Linton
Standard Infuse/Withdraw PHD ULTRA™ Syringe Pumps	70-3007	Harvard Apparatus
Inverted microscope	IX73	Olympus
Confocal microscope	LSM980	Zeiss
Inverted microscope	EVOS M7000	Thermo Fisher

Table 2.1: Microfluidics materials.

Reagent	ID	Provider
DMEM	11995065	Gibco
DPBS	14040-083	Gibco
FBS	A5256801	Gibco
Penicillin-Streptomycin	15140122	Gibco
DMSO	276855	Sigma
Trypsin - EDTA	0000249968	Sigma
Cal-520, AM	ab171868	Abcam
ATP	R0441	Thermo Fisher Scientific
Yoda1	5586/10	Bio-Techne
Trypan Blue	15250061	Gibco
Accumax	00466656	Thermo Fisher Scientific
Optiprep	07820	STEMCELL Technologies
Alamar Blue	DAL1100	Thermo Fisher Scientific
NEAA	11140-035	Gibco
Amphotericin B	15290-026	Gibco
FxCycle™PI/RNase	P5770417	Thermo Fisher
IRDye® 800CW Goat Anti-Mouse IgG	926-32210	Licor
IRDye® 800CW Goat Anti-Rabbit IgG	926-32211	Licor
IRDye® 680CRD Goat Anti-Rabbit IgG	926-68071	Licor

Table 2.2: Reagents used in cell culturing and testing.

2.2 Cells

Human embryonic kidney cells (HEK293T) were used for the experiments in Chapters 3 and 4, and human mesenchymal stem cells (hMSCs) were used for the experiments in Chapter 5.

HEK293T cells were used as the model cell line for the development and validation of the HT microfluidic device, and it was selected for multiple reasons. First, they possess a well-characterised mechanosensitive channel expression and gating mechanism [50]. HEK293T cells are widely used to study the expression of mechanosensitive ion channels, and in par-

ticular, Piezo1, the activation of which has been shown to depend solely on membrane tension rather than integrin–ECM interactions [52, 174]. This means that direct mechanical deformation, whether applied via substrate stretch or by squeezing a suspended cell through a microchannel, can reliably open Piezo1 in HEK293, independent of cell adhesion [116]. Second, as an immortalised line, HEK293T cells proliferate rapidly, remain phenotypically stable across passages, and tolerate repeated detachment–seeding cycles without loss of viability or mechanosensitive function [3]. Together, these features (robust, adhesion-independent channel activation, continuous availability, and consistent behaviour) make HEK293T cells an ideal platform for developing a high-throughput, real-time mechanosensitivity assay.

Human mesenchymal stem cells (hMSCs) are highly relevant in clinical and regenerative medicine applications. As multipotent stem cells that can differentiate into bone, cartilage, and fat tissues—key targets in tissue engineering—they offer valuable insights with direct translational potential [61, 66]. Importantly, studies have shown that hMSCs from older donors display reduced responsiveness to substrate stiffness and altered calcium signalling compared to younger donors, leading to impaired osteogenic and chondrogenic differentiation [166, 184]. Given these age-related functional changes, the ability to characterise hMSCs based on their mechanosensitivity is critically important. For this reason, hMSCs were selected for a preliminary study exploring how ageing influences their mechanosensitive response.

2.2.1 HEK293T cells

The cell line HEK293T was obtained from the ATCC company (CRL-3216TM).

Cell culturing

The cells were cultured in pyruvate-free Dulbecco’s Modified Eagle Medium (DMEM) supplemented with 1% Penicillin-Streptomycin (P/S) and 10% Fetal Bovine Serum (FBS) (Table 2.2). Cultures were maintained at 37°C in a humidified incubator with 5% CO₂. The medium was replaced every 2 or 3 days until the cells reached 70% confluency. At this point, the cells were passaged by treating them with 0.25% Trypsin-EDTA for 3 minutes in the incubator. After incubation, trypsin activity was neutralised by adding DMEM to the flask in a volume twice that of the trypsin used. The solution containing trypsin, DMEM, and detached cells was transferred to a falcon tube and centrifuged for 5 minutes at 1300 rpm. After centrifugation, the supernatant was discarded, and the cell pellet was resuspended in DMEM. A 10 µL aliquot of the resuspended pellet is mixed with trypan blue at a 1:1 ratio to assess cell viability. The stained sample was then transferred to a hemocytometer, and the cell count and viability (percentage of live and dead cells) were determined using a cell counter (Invitrogen Countess 3). Following the appropriate calculations, the resuspended cell pellet could be used for subcultures or further

processing, such as staining.

2.2.2 Human mesenchymal stem cells (hMSCs)

The hMSCs were purchased from PromoCell (C-12974, lot number: 488Z011).

Cell culturing

The cells were cultured in Dulbecco's Modified Eagle Medium (DMEM) supplemented with 1% Penicillin-Streptomycin (P/S) and antifungal, 10% Fetal Bovine Serum (FBS), 1% Pyruvate, 1% Non-Essential Amino Acids (NEAA), (Table 2.2). Cultures were maintained at 37°C in a humidified incubator with 5% CO₂. The medium was replaced every 2 or 3 days until the cells reached 70% confluency. At this point, the cells were passaged the same way as described in subsection 2.2.1. After counting, the hMSCs were either subcultured or used for intended experiments.

2.2.3 Cell staining with calcium-sensitive dye

The cells were seeded on a cell culture-treated surface (petri dish or well plate) at a density of approximately $35 \times 10^3 \text{ cm}^{-2}$ and incubated overnight to promote cell adhesion. The next day, the culture medium was replaced with fresh medium containing 5 μM Cal520AM. The petri dish was covered with aluminium foil to protect the light-sensitive stain from photobleaching. The cells were then incubated for 1.5 hours to allow the stain to diffuse into the cytoplasm. After the incubation period, the medium is discarded, and the cells were washed three times with 1 mL physiological solution (preparation protocol to follow) to remove any remnants. Thereafter, the cells were ready to be used for any desired application.

2.3 Cell-based analytical techniques

2.3.1 Alamar blue

Alamar Blue is a cell viability assay reagent used to measure cell proliferation, cytotoxicity, and metabolic activity in various biological experiments. It is a non-toxic, water-soluble compound containing resazurin, a blue dye redox indicator that changes colour in response to metabolic reduction within cells. Its reduced form, resorufin, appears pink and exhibits strong fluorescence. The fluorescence intensity, or else the reduction of the Alamar Blue, is directly proportional to the number of metabolically active cells [121].

Staining

The medium in the flasks containing the cultures under investigation was replaced with fresh medium supplemented with 10% Alamar Blue.

The flasks were then incubated for 8 hours at 37°C in a humidified incubator with 5% CO₂. As a negative control, plain medium with 10% Alamar Blue was incubated under the same conditions. After incubation, aliquots of the medium from each flask were transferred to a 96-well plate, with three technical replicates prepared for each sample. Similarly, the plain medium containing Alamar Blue was aliquoted into three replicates. Finally, the 96-well plate was analysed using a plate reader to measure the absorbance at 570 nm and 600 nm wavelengths.

The following equation was used to calculate the percentage reduction of Alamar Blue:

$$\text{Percentage Reduction of Alamar Blue} = \frac{(O_2 \times A_1) - (O_1 \times A_2)}{(R_1 \times N_2) - (R_2 \times N_1)} \times 100 \quad (2.1)$$

Where,

O₁= Molar extinction coefficient (E) oxidised Alamar Blue at 570 nm

O₂= Molar extinction coefficient (E) oxidised Alamar Blue at 600 nm

R₁= Molar extinction coefficient (E) of reduced Alamar Blue at 570 nm

R₂= Molar extinction coefficient (E) of reduced Alamar Blue at 600 nm

A₁= Absorbance of test wells at 570 nm

A₂= Absorbance of test wells at 600 nm

N₁= Absorbance of negative control well (media plus Alama Blue but no cells) at 570 nm

P₂= Absorbance of negative control well (media plus Alama Blue but no cells) at 600 nm

A higher percentage value indicates more significant metabolic activity in the cells being studied.

2.3.2 Flow cytometry - cell cycle

The cell cycle refers to the process of cell division. Flow cytometry is a powerful technique used to analyse the cell cycle by quantifying the DNA content of individual cells. This method provides insights into the distribution of cells across different cell cycle phases (G₀/G₁ where the cell increases in size, S where it copies its DNA, G₂ where it prepares to divide and M where it divides). It is widely employed in research areas such as cancer biology, drug development, and cell biology [7, 12, 102].

Cell fixation

Before the staining, the cells must be fixed to preserve their structure.

Cells were harvested as described in "Cell Culture" in subsection 2.2.1. Three technical replicates were prepared for each cell sample, with each replicate consisting of 100,000 cells. The cells were pelleted by centrifugation, and the supernatant was discarded. The cell pellet is gently loosened by tapping the tube to resuspend it in the residual liquid.

Subsequently, 1 mL of room-temperature PBS was added to the tube. The entire resuspended cell solution was then slowly transferred into 4 mL of absolute ethanol stored at -20°C. During this step, the cell suspension was added dropwise to the ethanol while vortexing the tube at maximum speed. The sample was incubated at -20°C for 5 to 15 minutes.

Cell staining

Following incubation, the cells were pelleted again by centrifugation, and the supernatant was carefully removed. Tapping the tube gently loosened the pellet, and 500 μ L of FxCycle™ PI/RNase staining solution was added. The solution was mixed by gently pipetting up and down, followed by vortexing. The tube is then left in the dark for 15 minutes before analysis.

FlowJo analysis

FlowJo software was used to analyse this project's Cell Cycle tests. FlowJo is a powerful software tool used to analyse flow cytometry data.

The analysis started by plotting the data as FSC vs SSC. The data gating followed, which allows the user to select the cell population of interest. The bottom left population (red circle) (Figure 3.3A) represents events with low side scatter, which typically corresponds to cell debris, dead cells, or small non-cellular particles. These are not of interest because they lack the granularity and size expected from intact, viable cells like mesenchymal stem cells (MSCs). The population enclosed in the yellow circle (Figure 2.1A) includes the larger and more granular events consistent with viable MSCs. These cells show moderate to high SSC-A, indicating healthy, intact cells with expected internal complexity. Since this is the population of interest, it is gated as shown in Figure 2.1B and isolated for further analysis (Figure 2.1C).

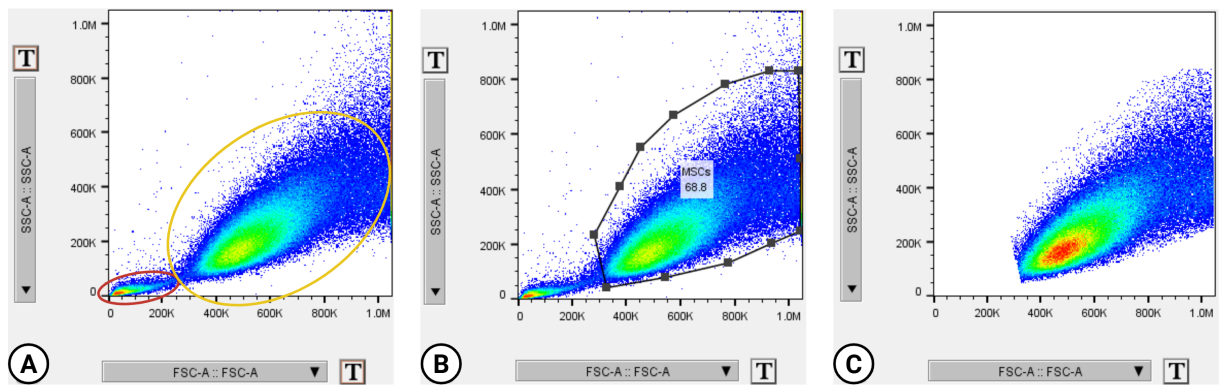


Figure 2.1: Gating of the desired cell population with the FlowJo software. (A) The lower left corner (red circle) is excluded because it mostly contains non-viable cells or debris, which do not meet the size and granularity criteria for MSCs. (B) The gate selects for the main population of viable, intact MSCs, ensuring that (C) downstream analyses focus on relevant biological events. (Created in BioRender.com).

Once the gating was completed and the population of interest had been defined, the plotting changed to a histogram of the PI-A channel. This graph revealed the distribution of the cell population in the 3 phases of the cell cycle (Figure 2.2).

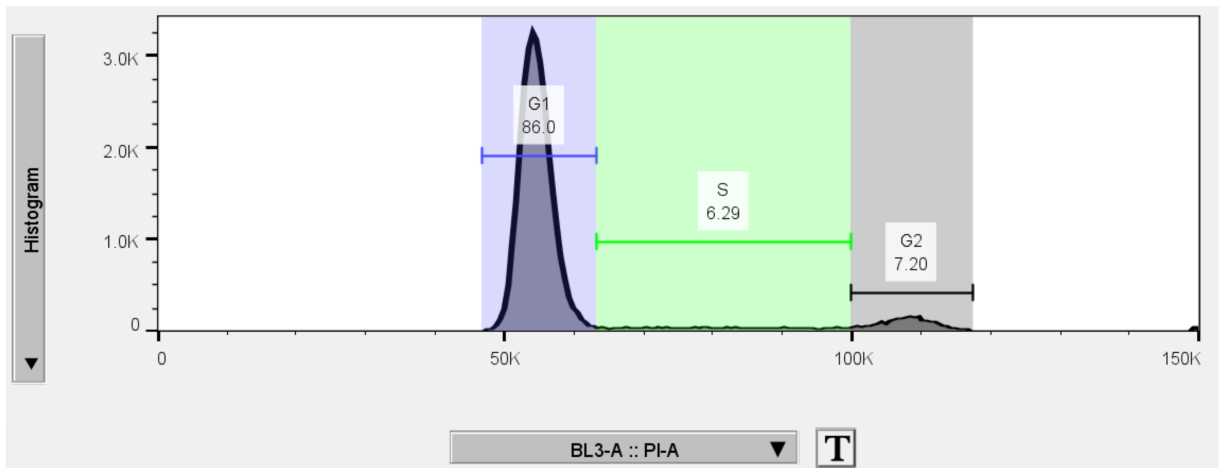


Figure 2.2: Histogram showing the distribution of DNA content in a cell population stained with Propidium Iodide (PI). The x-axis (BL3-A :: PI-A) represents the PI fluorescence intensity (area under the curve), which correlates with the amount of DNA per cell and allows discrimination between cell cycle phases. The y-axis indicates the number of events (cells) counted at each fluorescence intensity. Based on DNA content, cells are classified into G1, S and G2 phases (Created in BioRender.com).

2.3.3 Quantitative Polymerase Chain Reaction

Quantitative PCR (qPCR), or real-time PCR, is a technique used to amplify and quantify a specific DNA sequence. It is widely employed in molecular biology for applications such as gene expression analysis, genetic variation detection, and pathogen identification [4, 63, 192].

For experiments designated for qPCR analysis, cells were seeded in a 12-well plate at a density of 4,000 cells per cm^2 for further treatment. Following the intended treatment, the cells are washed with PBS and are ready for cell lysis.

RNA extraction

RNA samples were extracted using the Qiagen RNeasy microkit per the manufacturer's protocol. 175 μL of RLT buffer was added to each well. To create one experimental replicate, the lysates from two wells were pooled (350 μL cell lysate) and transferred to a 1.5 mL Eppendorf tube. If RNA extraction was not performed immediately, the cell lysates were stored at -80°C until the extraction process was conducted.

To each experimental replicate, an equal volume (350 μL) of 70% ethanol was added and thoroughly mixed by pipetting. The resulting mixture, including any precipitate, was transferred to an RNeasy MinElute spin column placed in a 2 mL collection tube and centrifuged at $8,000 \times g$ for 14 seconds. The flow-through was discarded, and 350 μL of RW1 buffer was added to the column. The column was centrifuged again at $8,000 \times g$ for 15 seconds, and the flow-through was discarded.

At this stage, the DNase I incubation mix was prepared by combining 10 μL of DNase I stock solution with 70 μL of RDD buffer. The solution was mixed by gentle inversion. Next, 60 μL of the DNase I incubation mix was applied directly to the column membrane, and the column was incubated at room temperature for 15 minutes.

Following the incubation, 350 μL of RW1 wash buffer was added to the column, which was then centrifuged at $8,000 \times g$ for 15 seconds. The collection tube was discarded, and the spin column was placed into a new 2 mL collection tube. Subsequently, 500 μL of RPE wash buffer was added to the column and centrifuged at $8,000 \times g$ for 15 seconds. After discarding the flow-through, 500 μL of 80% ethanol was added to the column, and the column was centrifuged at $8,000 \times g$ for 2 minutes. The flow-through was discarded, and the column was further dried by centrifugation at full speed for 5 minutes with the lid open.

The dried column was then transferred to a clean 1.5 mL Eppendorf tube. To elute the RNA, 14 μL of RNase-free water was applied directly to the centre of the column's membrane, and the column was centrifuged at full speed for 1 minute. If cDNA synthesis was not performed immediately following RNA extraction, the RNA should be stored at -80°C .

RNA concentration quantification

RNA quantification is the process of determining the concentration of RNA in a sample before downstream experiments [10].

There are different methods to conduct the quantification. UV-Vis spectroscopy was used for this project. This technique is the most commonly used method for RNA quantification, and it entails measuring the absorbance of a diluted RNA sample at 260 nm and 280 nm. Then, Beer-Labert's Law is used to calculate the concentration of RNA from the absorbance measurements.

Beer-Lambert's Law is an empirical relationship that establishes a correlation between the absorbance of a sample and its concentration. Specifically, the Law states that when a beam of visible light passes through a chemical solution in a container of known path length, the amount of light absorbed is directly proportional to the concentration of the solute. The following equation describes this relationship:

$$A = \epsilon \times c \times l \quad (2.2)$$

Where,

A= Absorbance

ϵ = Molar absorption coefficient [$M^{-1}cm^{-1}$]

c= Molar concentration [M]

l= Optical path length [cm]

For this purpose, the NANODROP 2000c, from Thermo Scientific was used (2.3) . The NanoDrop spectrophotometer was initialised and blanked using 1-2 μ L of RNase-free water or the elution buffer from RNA extraction to ensure accurate baseline readings. A 1 μ L aliquot of each RNA sample was carefully pipetted onto the NanoDrop pedestal (2.3 A), ensuring no bubbles or contaminants were introduced. The spectrophotometer's arm was lowered (2.3 B) to create a liquid column between the pedestal and the arm. The RNA concentration (μ g/ μ L) was automatically calculated through Beers-Labert's Law, based on the absorbance at 260 nm (A_{260}). The ratio of A_{260}/A_{280} was used to evaluate the protein contamination, with values between 1.8 and 2.2 indicating pure DNA.

After each measurement, the pedestal was cleaned with RNase-free water and a lint-free tissue before proceeding to the following sample.

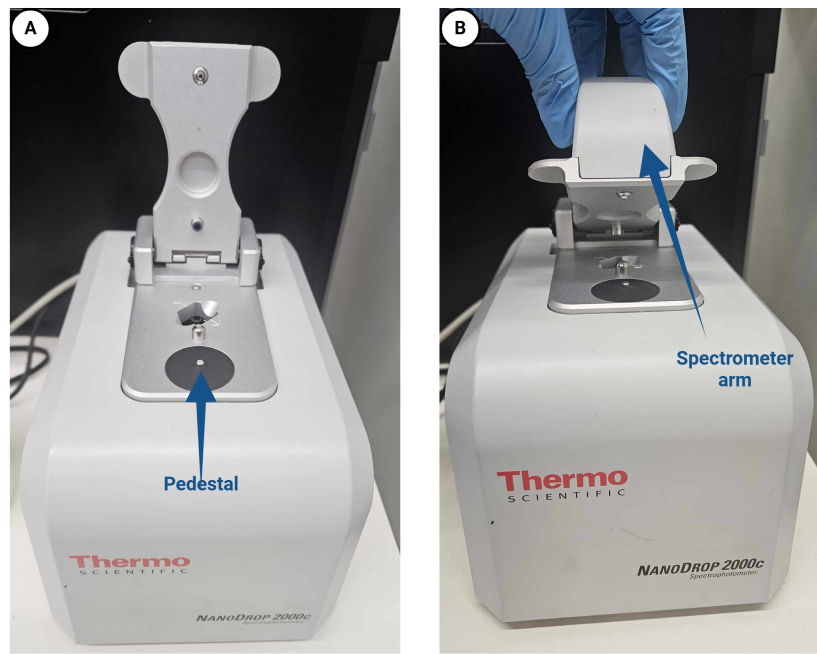


Figure 2.3: The device used to quantify the RNA concentration is illustrated in this figure (Created in BioRender.com).

Reverse transcription cDNA

The template RNA, which serves as the starting material for reverse transcription into complementary DNA (cDNA), was prepared by determining the volume needed from the 14 μL of extracted RNA to obtain 200–400 ng of RNA. The required volume of RNase-free H_2O was added to adjust the final volume to 12 μL , forming the template RNA.

The quantitect cDNA kit from Qiagen was used for the cDNA synthesis. The process started with preparing the master mix solution (Table 2.3). All the samples and buffers were kept on the ice for the entire duration of the reverse transcription.

Component	Volume
Quantiscript Reverse Transcriptase	1 μL
Quantiscript RT buffer	4 μL
RT primer mix	1 μL

Table 2.3: Master Mix recipe.

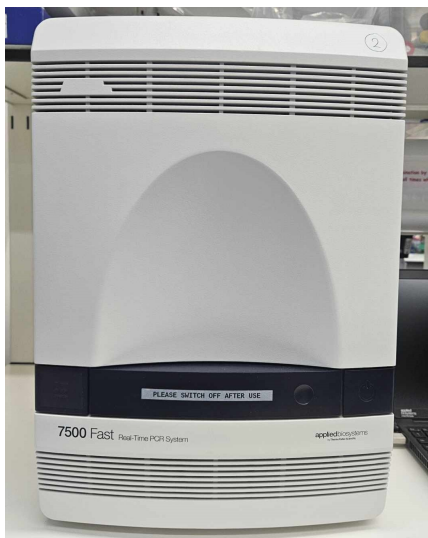
In a 200 μL thin-walled tube, 2 μL of gDNAse enzyme was combined with the template RNA (12 μL). The mixture was incubated at 42°C for 2 minutes, after which 6 μL of the master mix was added, resulting in a final volume of 20 μL . The solution was then incubated at 42°C for

15 minutes, followed by incubation at 95°C for 3 minutes to inactivate the Quantiscript reverse transcriptase.

The cDNA concentration was adjusted to 8ng/rxn by adding nuclease-free water to standardise all samples at the same concentration. If the real-time PCR was not conducted immediately following reverse transcription, the cDNA should be stored at -80°C.

Real-time PCR

For the PCR tests of this project, the Quantifast SYBR Green qPCR Kit (Qiagen) was used to perform amplification with specific primers (Eurofins Genomics, Ebersberg, Germany) related to ageing and mechanosensitivity, as well as GAPDH and RPL3, which were used as a genetic internal control. PCR was quantified using the $2^{-\Delta\Delta C\tau}$ method, and amplification was carried out using an Applied Biosystems 7500 Real-Time PCR system (2.4a). The reaction mix is prepared as shown in 2.4b.



(a) Device used for the qPCR analysis (Created in BioRender.com).

Component	Volume
2 × SYBR Green PCR Master Mix	10 μ L
Primer 1 (100pmol stock)	0.1 μ L
Primer 2 (100pmol stock)	0.1 μ L
RNase-free-water 2	7.8 μ L
cDNA (8ng/rxn)	2 μ L
Total reaction volume	20 μL

(b) Reaction mix recipe.

Figure 2.4: qPCR device and reaction mix.

Primer 1 and Primer 2 refer to the forward and reverse primers, respectively. These are short sequences of nucleotides designed for precise binding to the target DNA sequence surrounding the region of interest. The forward primer binds to the complementary strand at the 5' end of the target region and initiates DNA synthesis in the forward direction. The reverse primer binds to the opposite strand at the 3' end of the target region and promotes DNA synthesis in the reverse direction. Together, these primers contribute to the amplification of the specific DNA segment during the PCR cycles.

18 μL of the reaction mix are added to 2 μL of cDNA. All the samples are prepared in 96-well plates, and the plate is transferred into the qPCR machine for the actual test. The process begins with the denaturation step, where the double-stranded DNA template is heated to a high temperature, usually around 95°C , causing the DNA to separate into two single strands. Next, during the annealing phase, the temperature is lowered to allow the primers, which are short single-stranded sequences complementary to the regions immediately adjacent to the gene of interest, to bind to their corresponding sequences on the single-stranded DNA templates. This binding occurs at a specific temperature, typically between 50°C and 60°C , depending on the primer sequence.

Following primer binding, the extension phase takes place. During this phase, the temperature is raised to the optimal working temperature for the polymerase, typically around 72°C . The DNA polymerase enzyme then synthesises a complementary DNA strand by adding nucleotides to the primer, thus extending the DNA strand and amplifying the targeted region. The gene amplifies exponentially with each cycle, where the amount of DNA doubles.

As the DNA is amplified, a fluorescent signal accumulates, which the qPCR system measures in real time. The fluorescence intensity correlates with the amount of the amplified DNA, allowing for the quantification of the gene of interest. This process is repeated for many cycles, typically between 30 to 40, each cycle further amplifying the targeted gene, and the fluorescence signal continues to increase, providing real-time data on the amount of amplified product. The quantity of the target gene is then determined by comparing the fluorescence data to a standard curve or a reference gene, allowing for the accurate quantification of gene expression levels.

In the 2.4 that follows, the thermal cycling of the qPCR test is summarised.

Step	Temperature (°C)	Time	Cycles	Purpose
Initial Denaturation	95	2 minutes	1	Breaks the hydrogen bonds in the double-stranded DNA to produce single strands.
Denaturation	95	15-30 seconds	35-40	Separates DNA strands to enable primer binding in subsequent steps.
Annealing	55-65 (variable)	15-30 seconds	35-40	Allows primers to bind to their complementary sequences on the DNA template.
Extension	72	1 minute per kb	35-40	DNA polymerase synthesises new DNA strands by extending from the primers.
Final Extension	72	5-10 minutes	1	Ensures complete synthesis of all DNA fragments.
Hold	4	Indefinite	-	Preserves the amplified DNA for later use.

Table 2.4: PCR cycle conditions and their purposes.

There are two fluorescent detection types: dye-based and probe-based. In this project, the dye-based detection was utilised. The SYBR Green binds to double-stranded DNA and fluoresces.

2.3.4 In Cell Western

In-cell Western (ICW) is a quantitative immunofluorescence assay performed directly on cultured fixed cells. This method uses fluorescently labelled antibodies to measure protein expression, post-translational modifications, or other molecular targets within intact cells. Unlike traditional Western blotting, ICW does not require cell lysis, electrophoresis, or membrane transfer, making it a more straightforward and higher-throughput alternative [9, 123].

For the experiments of this project, cells intended for the ICW test were seeded on 12- or 48-well

plates before any treatment.

Cell fixation

Cells were washed with PBS and fixed with formaldehyde. Recipes of both are presented in Table 2.5a and Table 2.5b, respectively.

Component	Volume
PBS	1 tablet
MilliQ water	200 mL

(a) PBS recipe.

Component	Volume
Formaldehyde	10 mL
PBS	90 mL
Sucrose	2 gr

(b) Formaldehyde fixative recipe.

Figure 2.5: PBS and Formaldehyde recipes

The cells were incubated with the fixative for 30 minutes in a 37°C incubator. The fixative was removed after the incubation, and the cells were washed with PBS.

Antibody staining

The cells were permeabilised by incubating them in 150 μ L of permeable buffer (refer to Table 2.6a) at 4°C for 4 minutes. After removing the permeable buffer, 150 μ L of blocking buffer (Table 2.6b) was added to the cells to prevent non-specific antibody binding, and the plate was placed on a shaker at room temperature for 1.5 hours.

Before the staining process, primary antibodies targeting the protein of interest were diluted in a blocking buffer at 1:100. Primary antibodies were added to the cells and incubated for at least 2 hours at room temperature. Subsequently, the primary antibodies were removed, and the cells were washed with wash buffer (Table 2.6c) 3 times, 5 minutes per time, on a shaker at room temperature.

Component	Volume
Sucrose	10.3 gr
NaCl	0.292 gr
MgCl ₂	0.06 gr
Hepes	0.476 gr
PBS	100 mL
Triton X	0.5 mL

(a) Permeable Buffer recipe.

Component	Volume
Milk powder	0.5 gr
PBS	50 mL

(b) Blocking Buffer recipe.

Component	Volume
Tween 20	0.1 mL
PBS	100 mL

(c) Wash Buffer recipe.

Figure 2.6: Permeable, Blocking and Washing Buffer Recipes

Fluorescently labelled secondary antibodies (IRDye[®]), diluted in blocking buffer at a 1:1000 ratio, were added to the cells for detection. CellTag[™] 700 stain (for detecting one antibody per well) and CellTag[™] 520 stain (for detecting two antibodies per well) was also added as an internal control for normalisation. The secondary antibodies were selected to target the host species in which the primary antibodies were raised. The well plate, wrapped in aluminium foil to protect the fluorescently labelled antibodies, is incubated at room temperature on a shaker for one hour. After incubation, the secondary antibodies were removed, and the cells were washed four times with wash buffer while gently agitated on a shaker at room temperature.



Figure 2.7: The figure shows the device used for the ICW cell analysis (Created in BioRender.com).

The washing buffer is removed, and the plates are left at 4°C, wrapped in aluminium foil, to dry. The samples are imaged using the LI-COR Odyssey M device (Figure 2.7).

2.4 Microfluidics

For this project, various microfluidic device designs were utilised. Some of these devices were designed and fabricated by the author, while others were created by a fellow PhD student collaborating on the research. The subsequent sections will outline the design and fabrication processes, detailing the specific contributions of each individual involved.

2.4.1 Design

The microfluidic devices were designed using AutoCAD. The channel diameter was selected based on the approximate diameter of HEK cells in suspension ($\sim 15 \mu\text{m}$). Initially, channels with a diameter of $45 \mu\text{m}$ were used. This was later increased to $60 \mu\text{m}$ in order to reduce the velocity of the cells and keep them within the field of view for a longer duration. Subsequently, the diameter was further increased to $100 \mu\text{m}$ to allow for higher flow rates while maintaining low cell velocity. The presence of the meander in all the microfluidic devices of this project serves two purposes: (a) to facilitate the mixing of the two compounds and (b) to elongate the field of view (keep the cell in the field of view for a more extended period to observe its response).

Microfluidic devices developed at the University of Glasgow

These devices were designed and fabricated by a fellow PhD student, Matthew Woods, in collaboration with the experiments conducted in Chapter 3. Details of the materials used to manufacture these devices can be found in the table 2.5.

Product	ID	Provider
Photoresist	SU-8 3025 and 3045 series	Microchem
Photomask	-	Micro Lithography Services Ltd
SYLGARD 184 Silicone Elastomer Kit	000201000032	Ellsworth Adhesives

Table 2.5: Microfluidics materials UoG.

In the following figure, the design of the two microfluidic devices fabricated by Matthew Woods is depicted.

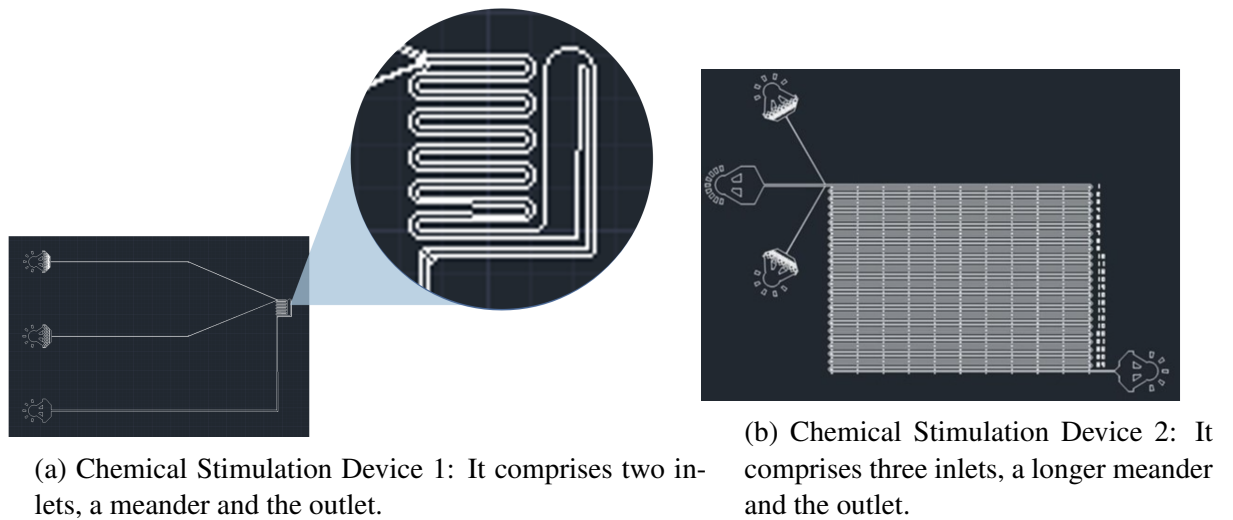


Figure 2.8: Microfluidic devices developed in UoG.

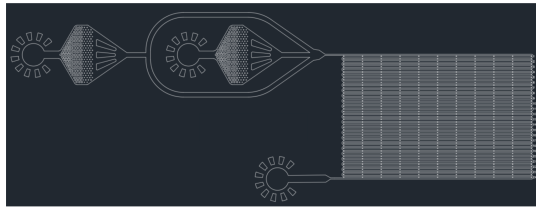
Microfluidic devices developed at the Harvard Centre for Nanoscale Systems (CNS)

These devices were designed by me and fabricated in collaboration with Pascal Spink, the microfluidic specialist at Cytonome, where I completed a three-month placement during my studies. Details of the materials used to fabricate these devices are found in Table 2.6.

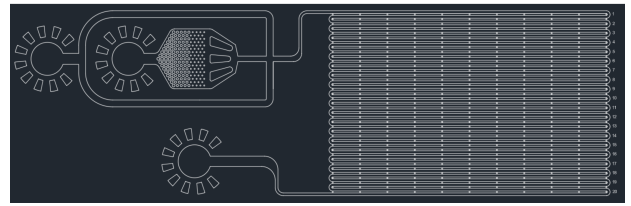
Product	ID	Provider
Silicon wafers	447	UniversityWafer
Photoresist	SU-8 3000 series	Kayaku
Photomask	-	Artnet Pro Inc
SYLGARD 184 Silicone Elastomer Kit	000201000032	Ellsworth Adhesives

Table 2.6: Microfluidics materials Cytonome.

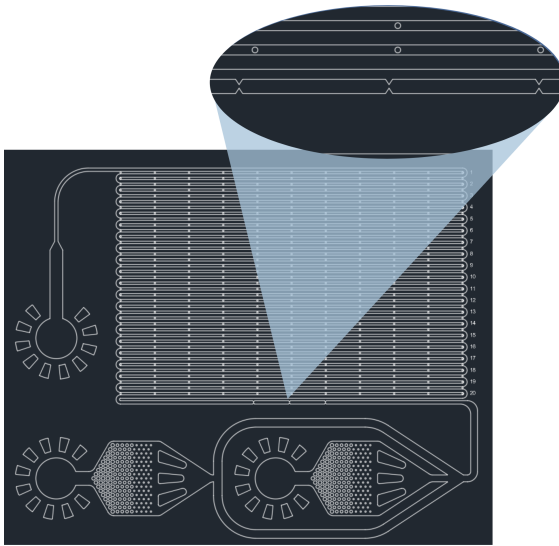
In the following figure, the design of the microfluidic devices fabricated by me is depicted.



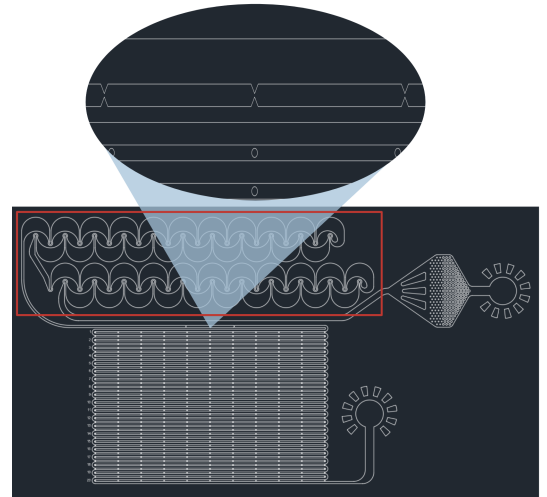
(a) Chemical Stimulation Device 3: The chemical stimulant is introduced through the left inlet (sheath flow), while the cell sample enters the device through the right inlet.



(b) Mechanical Stimulation Device 1: The sheath flow intersects perpendicularly with the cell sample flow. By adjusting the sheath flow rate, varying force magnitudes can be applied to the cells.



(c) Mechanical Stimulation Device 2: Sheath flow is used to maintain the cells in the central plane of the channel. Cells pass through three successive constrictions of the same width. The width of this constriction was $10\ \mu\text{m}$, while the channel's width was $100\ \mu\text{m}$.



(d) Mechanical device 2: This design eliminates the need for sheath flow by utilising repeated curvatures and narrow channels (highlighted in the red rectangle) immediately following the inlet. These features create a controlled environment that naturally focuses cells into a central streamline. As the cells flow through the device, they pass through three successive constrictions; the channel width is significantly reduced compared to the surrounding regions. The width of this constriction was $15\ \mu\text{m}$, while the channel's width was $100\ \mu\text{m}$.

Figure 2.9: Microfluidic devices developed by me.

2.4.2 Fabrication

Master mold fabrication

The microchannel designs created in AutoCAD are transferred onto a film photomask (Table 2.5 and Table 2.6). This photomask, created using high-resolution printing, is the template for defining the microfluidic patterns.

A silicon wafer is then prepared as the substrate for the mould. The wafer is thoroughly cleaned with 100% acetone and isopropyl alcohol (IPA) to remove any contaminants and ensure optimal adhesion of the photoresist. To ensure the elimination of any moisture, the wafer is left on a heat plate at 150°C for 5 minutes.

Next, a layer of the SU-8 photoresist (3050) is spin-coated (at 3000 rpm for 45 seconds) onto the wafer to get 50 μm thickness. The wafer was then soft-baked on a heat plate at 95°C for 15 minutes to solidify the photoresist. After that, the photomask is placed on top of the coated wafer and exposed for 38 seconds at 250 mJ/cm^2 . Finally, the photomask is removed, and the wafer is post-baked on a heat plate at 65°C for 1 minute, followed by 5 minutes at 95°C.

The wafer was immersed in a developer (PGMEA) for 8 minutes to remove the unexposed photoresist. After rinsing the wafer with IPA and drying it using nitrogen, the raised microchannel patterns could be clearly seen on the wafer. To improve the mechanical stability and adhesion of the structures, the wafer is hard-baked on a heat plate at 150°C for 5 minutes.

PDMS device fabrication

The master mould, consisting of the wafer with the developed microchannel structures, is placed inside a plastic petri dish. A PDMS mixture, prepared at a 10:1 base-to-curing agent ratio, was then poured over the master mould to form the device. The PDMS is allowed to cure for 2 hours at 65°C, resulting in a solidified replica of the microfluidic design. After curing, holes are punched at the designated inlet and outlet locations, and the device is ready for bonding onto a glass slide.

PDMS bonding to glass slide

Bonding a PDMS device to a glass slide is a crucial step in fabricating microfluidic devices, ensuring the formation of sealed channels for fluid flow. The procedure involves surface activation and covalent bonding between the PDMS and glass.

The glass slide is thoroughly cleaned using a sequential wash of ethanol and deionised (DI) water to remove any contaminants that could interfere with surface activation and bonding. After cleaning, the slide is dried using nitrogen gas. Similarly, the PDMS device is rinsed with ethanol to remove debris, dust, or uncured residues, followed by drying with nitrogen gas. This ensures uniform activation during the bonding process.

The PDMS device and the glass slide are placed in a plasma oven, exposing their bonding surfaces. Oxygen plasma was applied for 5 minutes. The PDMS and glass slide surfaces are bombarded with oxygen ions, breaking the existing bonds. This process introduces hydroxyl

groups (-OH) on the glass surface and silanol groups (Si-OH) on the PDMS surface.

Immediately after plasma treatment, the PDMS device is aligned and gently placed onto the glass slide, ensuring the bonding surfaces come into contact. The silanol groups (Si-OH) on both surfaces undergo a condensation reaction:



This reaction forms strong covalent siloxane (Si-O-Si) bonds, creating a permanent seal between the PDMS and glass.

Finally, the bonded device is placed in the oven at 70°C for 10–30 minutes to accelerate the condensation reaction and ensure the removal of residual water, resulting in a robust and durable bond.

2.5 Statistical analysis

The statistical analysis of this project's results was performed using the MiniTab 21_21.4.1.0 software. All graphs represent mean \pm standard deviation (SD) unless otherwise noted. Initially, the normality of data was assessed with the Ryan-Joiner (RJ) normality test for small sample sizes ($N \leq 50$) and the Anderson-Darling (AD) test for larger sample sizes ($N > 50$). For very small sample sizes ($N < 10$), normality tests may not be very reliable, and therefore, visual methods were implemented (e.g. probability plots or histograms). The Pearson correlation test was used to measure the strength and direction of the relationship of two continuous variables for normally distributed data, and the Spearman correlation test for non-normally distributed data (perfect positive correlation when $r=1$, perfect negative correlation when $r=-1$, and no correlation when $r=0$). To compare a single parameter in three or more groups of normally distributed data, a one-way ANOVA test was used with Tukey's post hoc test (for multiple comparisons) or Dunnett's (for comparing all groups to a single control). The Kruskal-Wallis test was performed for non-normally distributed data, followed by the Mann-Whitney test for multiple comparisons. Significant differences among groups are stated as follows: for p-values < 0.05 (*), when p-values < 0.005 (**), for p-values < 0.001 (***)

Chapter 3

Calcium Signalling Tracking with High-Throughput

In this chapter, all preparatory steps required for the optimisation of cell sample conditions are described. The optimal cell concentration, buffer composition, and conditions for cell culture, staining, and preparation are determined. The impact of flow rate and laser power on cellular responses is also examined. Finally, a concentration-dependent response of cells to chemical stimulation is presented, accompanied by appropriate controls.

3.1 Introduction

As discussed earlier in the Literature review chapter, a tracking tool is needed to observe the cells' response to a stimulant, whether this is chemical or mechanical. Calcium signalling is the cells' most common mechanism to regulate various physiological processes, such as muscle contraction, neurotransmitter release, gene expression, and cell division [31, 136].

3.1.1 Ca^{2+} signalling as a tracking tool

Calcium, one of the most abundant elements in the earth's crust, ranking fifth in occurrence after oxygen, silicon, aluminium, and iron, has been available since the inception of life [181]. It is a fundamental constituent of almost every biochemical process in prokaryotic and eukaryotic cells [78]. The homeostasis of cellular ions, especially the regulation of calcium concentration, is essential for life evolution as the ion composition of the cell interior must be compatible with the biochemical reactions needed for cell survival and proper functioning. One of the critical aspects of this homeostasis is the regulation of Ca^{2+} concentration, which is achieved by the movement of Ca ions between the extracellular milieu and the cytosol through Ca^{2+} pumps and exchangers. Ca^{2+} pumps, such as PMCAs and SERCAs, use ATP hydrolysis to transport Ca^{2+} ions against their concentration gradient, while Ca^{2+} exchangers, such as NCX and CAX, ex-

change Ca^{2+} ions for Na^+ or H^+ ions across the plasma membrane or organellar membranes, respectively [31, 185]. Additionally, Ca^{2+} binding proteins, such as calmodulin, sense changes in Ca^{2+} concentration and initiate various signalling pathways [26, 47]. This process is considered the primary survival system preventing Ca^{2+} -mediated cell damage [77].

Calcium signalling is a critical process that involves the influx of calcium ions triggered by an increase in calcium pressure in the extracellular matrix and small changes in calcium permeability of the plasma membrane [181]. The Ca^{2+} influx activates various downstream signalling pathways, and downstream effectors trigger the specific cellular responses required for cell survival and function. These events include but are not limited to gene transcription, muscle contraction, neural transmission, and secretion of saliva [136]. Dysregulation of Ca^{2+} signalling can lead to various pathological conditions, highlighting the importance of understanding this process for biomedical research. The mechanisms involved in calcium signalling are highly regulated and maintain the calcium concentration within a narrow range. The interplay between calcium influx and homeostasis, calcium-binding proteins, and downstream effectors are intricate and crucial in the calcium signalling process [39].

3.1.2 Ca^{2+} signalling in disease

Elevated intracellular Ca^{2+} levels in the micromolar range can adversely affect Ca^{2+} signalling. Under harmful conditions that increase plasma membrane permeability, allowing for abnormal Ca^{2+} influx, mitochondria attempt to manage the resulting cytosolic Ca^{2+} overload. If the harmful agent is rapidly removed, the cell may be salvaged. However, if the agent persists and cytosolic Ca^{2+} overload is prolonged, various intracellular systems are affected, and many key calcium transport mechanisms, such as plasma membrane Ca^{2+} -ATPase (PMCAs), endoplasmic reticulum Ca^{2+} -ATPase (SERCA), $\text{Na}^+/\text{Ca}^{2+}$ exchanger, and mitochondrial Ca^{2+} uniporter, get impaired. This leads to the activation of Ca^{2+} -dependent hydrolytic enzymes, including proteases, which may trigger cell death beyond a point of no return [39].

Calcium signalling is also essential for neuronal function. The precise balance of calcium within neurons is crucial as they are incredibly responsive to changes in their concentration. Even minor irregularities in maintaining this balance can have severe and damaging effects on neuronal activity, leading to a disruption in normal functioning and eventually causing neurological disorders such as Alzheimer's disease, Huntington's disease, and Parkinson's disease [29, 49, 147]. For instance, in Alzheimer's disease, calcium dysregulation leads to the accumulation of amyloid-beta protein, which forms senile plaques and contributes to neuronal cell death. Additionally, mutations in the genes encoding voltage-gated calcium channels are associated with various neurological disorders, including epilepsy and migraine [37, 150].

The proper functioning of the human heart relies on the precise regulation of calcium (Ca^{2+}) signalling, which is responsible for controlling muscle contractions and electrical signals that determine heart rhythm and regulate cell growth. Any disturbance in the regulation of Ca^{2+} handling proteins can lead to a malfunction of the signalling pathway, resulting in various cardiovascular diseases, including heart failure, arrhythmias, and other cardiac disorders. For instance, gene mutations encoding ryanodine receptors and sarcoplasmic reticulum calcium ATPase have been linked to arrhythmogenic disorders such as catecholaminergic polymorphic ventricular tachycardia. Additionally, calcium overload in cardiac cells can lead to calcium-dependent cell death and is implicated in the development of heart failure [83, 110, 145].

Ca^{2+} signalling was considered the ideal tracking tool for our device as it has been used in the past to track cells' response in similar applications [76, 87, 127, 198]. The main distinction between previous approaches and the one presented in this chapter lies in the HT nature of the method. In earlier studies, calcium signalling was tracked in adherent cells, typically using low-throughput imaging techniques that assess relatively small cell populations [33, 76, 87, 115, 124, 189]. In contrast, the method proposed here enables stimulation and real-time screening of cells as they flow through a microfluidic channel. This dynamic, suspension-based approach offers the potential to analyse hundreds of thousands of cells within minutes, significantly increasing throughput and enabling large-scale mechanosensitivity assessment.

3.2 Materials and methods

HEK293T cells were used for this chapter's experiments. They were cultured and stained as described in Chapter 2, section 2.2.1, and subsection 2.2.3.

3.2.1 Stimulation of adherent and suspended cells

Before conducting experiments on cells flowing in a microfluidic device, a proof of concept experiment should confirm whether a) the stain and stimulation concept work and b) the cells respond to chemical stimulation while in suspension.

For the first question, adherent HEK293T cells were stimulated with Yoda1, an agonist molecule of the mechanosensitive channel Piezo1. Yoda1 will be further discussed in Chapter 4, subsection 4.1.2. Following cell passaging and counting (Subsection 2.2.1 F), approximately 35×10^3 cells per cm^2 were seeded onto a 35 mm glass-bottom petri dish (Ibidi) and incubated overnight to promote cell adhesion. The next day, the culture medium was replaced with fresh medium containing $5 \mu\text{M}$ Cal520AM. The petri dish was covered with aluminium foil to protect the light-sensitive stain from photobleaching. The cells were then incubated for 1.5 hours to allow the stain to diffuse into the cytoplasm.

After incubation, the medium was discarded, and the cells were washed three times with 1 mL of physiological solution (Figure 3.1). Finally, fresh medium was added to the petri dish and placed under a fluorescent microscope for observation. Yoda1 was used for the chemical stimulation of the cells. Yoda1 is a synthetic small molecule that selectively activates the mechanosensitive ion channel Piezo1 without requiring mechanical stimulation. It will be extensively discussed in the next chapter (Subsection 4.1.2). 1 μM of Yoda1 was added, dropwise, and Ca^{2+} influx was determined as the fluorescent intensity.

10x Solution		1x Solution	
Component	Concentration mM	Component	Quantity
NaCl	1400	10x Pphysiological Solution	100
KCL	54	milliQ water	900 mL
HEPES	100	Glucose	10 mL
		Glucose	10 mM
		MgCl ₂	1 mM
		CaCl ₂	1.8 mM
		NAOH	To reach PH 7.4

(a) 10x Physiological solution.

(b) 1x Physiological solution.

Figure 3.1: Physiological Solution recipe

For the second question, HEK293T cells in suspension were chemically stimulated with Yoda1 as described below.

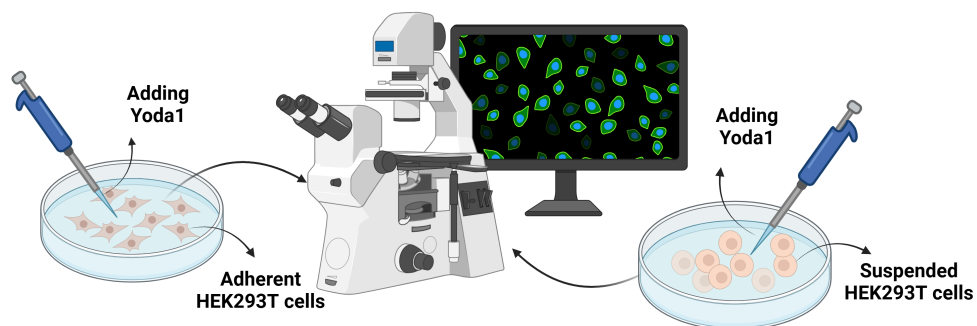


Figure 3.2: Experimental setup for stimulating HEK293T cells in adherent and suspended states (Created in BioRender.com).

Following the staining procedure, the cells were trypsinised to detach them from the culture surface. Subsequently, they were transferred to a petri dish and chemically stimulated with

Yoda1, using the same protocol as for the adherent cells (Figure 3.2).

3.2.2 Sedimentation test

Sedimentation is the process of solid particles settling or sinking to the bottom of a fluid container.

Cell sedimentation emerged as a significant challenge in maintaining consistent cell flow within the microchannels in the preliminary experiments. To address this issue, a density gradient medium (Optiprep) was utilised to match the density of the cells, ensuring they remained suspended in the medium and preventing sedimentation.

A sedimentation test was conducted to determine the appropriate ratio of OptiPrep to media. Four different concentrations of OptiPrep in media were tested (5%, 10%, 20%, and 30%), along with a negative control (media without OptiPrep). The total volume of each solution was 2 ml. After adding OptiPrep, the remaining percentage consisted of equal parts DMEM and Accumax, a dissociation medium used to prevent cell aggregation. Three million cells were carefully added to each solution, and the Eppendorf tubes were undisturbed for 4 hours. After this period, samples were collected from three different heights (top, middle, and bottom) of each Eppendorf tube, and the number of cells in each sample was counted using the Countess 3 automated cell counter from Thermo Fisher Scientific [5]. 10 μ L of each sample was placed on the Countess reusable slide, which was then inserted into the Countess device for automated counting.

3.2.3 Investigation of laser power and flow rate effect on the signal

Before conducting the main experiments, optimal operating parameters had to be determined by examining how flow rate and laser power affect the fluorescence signal. HEK293T cells were stained with Cal520AM according to the protocol (subsection 2.2.3) and suspended in a 1:1 mixture of DMEM and Accumax containing the optimal concentration of OptiPrep. This suspension was introduced into the microfluidic device shown in Figure 2.8a, and 10 μ M ATP was added to activate the stain. These preliminary tests were performed to define the settings that maximise signal quality without damaging the cells or compromising throughput.

To identify the optimal laser power, the flow rate was fixed at 50 μ L/hr while the laser power was varied. The chosen laser power needed to be sufficiently high to excite the Cal520AM fluorophore and enable clear observation of the calcium response, yet low enough to avoid photodamage or “burning” of the cells. For the flow rate assessment, the laser power was held steady at 10 mW, and the flow rate was adjusted. Here, the goal was to find a flow rate that would allow

high throughput—processing many cells per unit time—while still keeping each cell within the field of view long enough for a measurable calcium response to occur.

3.2.4 Stimulation of suspended HEK293T cells with ATP in a microfluidic device

HEK293T cells were stained with cal520AM according to the protocol described in subsection 2.2.3. They were then trypsinised and spun down, and the cell pellet was resuspended in a 1:1 DMEM: Accumax solution containing the optimal concentration of Optiprep.

ATP served as the chemical stimulant, with the devices shown in Figure 2.8a and 2.8b used as the experimental platform. The cellular response was assessed at different positions within the microfluidic device to establish the most suitable probing point. After determining the optimal probing position, a dose-dependent ATP response was evaluated, accompanied by negative controls.

3.3 Results

3.3.1 Stimulation of adherent and suspended cells

For each experiment, a time-lapse sequence of images was captured at 1-second intervals for 2 minutes using a fluorescent microscope. The chemical was introduced 10 seconds after the start of image acquisition. The image stack was then processed into a video using ImageJ software. A region of interest (ROI) was defined, and the Corrected Total Cell Fluorescence (CTCF) was calculated throughout the video using the following equation:

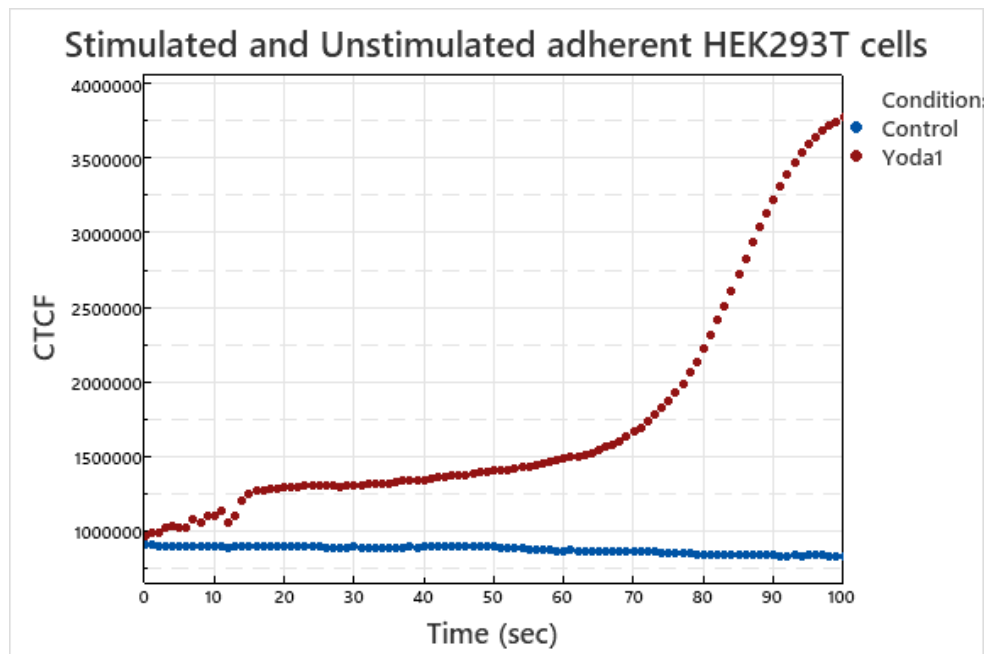
$$\text{CTCF} = \text{Integrated Density} - (\text{Area of the cell} \times \text{Mean Background Intensity}) \quad (3.1)$$

Where,

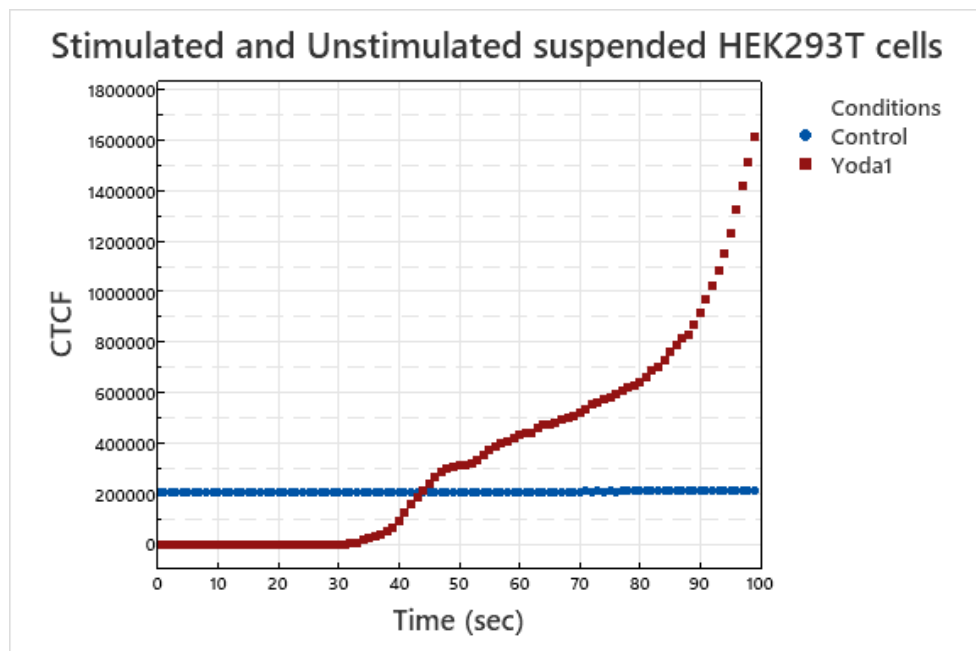
Integrated Density: The total fluorescence intensity within the region of interest (ROI).

Area of the cell: The number of pixels in the ROI.

Mean Background Intensity: The average fluorescence intensity of a background area (to correct for background fluorescence).



(a) Response of adherent cells. The control condition corresponds to introducing plain DMEM into the petri dish containing adherent cells. The Yoda1 condition refers to introducing $1\ \mu\text{M}$ Yoda1 into the petri dish with adherent cells.



(b) Response of suspended cells. The control condition corresponds to introducing plain DMEM into the petri dish containing suspended cells. The Yoda1 condition refers to introducing $1\ \mu\text{M}$ Yoda1 into the petri dish with adherent cells.

Figure 3.3: Preliminary Experiments. (a) Stimulation of adherent HEK293T cells with $1\ \mu\text{M}$ Yoda1 to confirm that the cell line responds to chemical stimulation. (b) Stimulation of suspended HEK293T cells with $1\ \mu\text{M}$ Yoda1 to confirm that the cell line responds to chemical stimulation even when in suspension.

Graph (Figure 3.3a) shows that adherent cells responded to chemical stimulation with 1 μM Yoda1, as indicated by increased fluorescence intensity over time. In contrast, the negative control (plain DMEM) exhibited a stable fluorescence intensity throughout the experimental duration.

Suspended cells similarly exhibited a strong response to chemical stimulation (1 μM Yoda1) as evidenced by the increase in fluorescence intensity compared to the negative control (Figure 3.3b). This result confirms that HEK293T cells can be used within a microfluidic device and remain responsive to chemical stimulation while in flow.

3.3.2 Sedimentation test

As depicted in the following graph, at lower OptiPrep concentrations, most cells sediment to the bottom, whereas at higher concentrations (20% and 30%), a greater proportion remains in the middle and top layers, indicating altered sedimentation dynamics. The Countess device, which was used for cell quantification, also provided cell viability measurements by reporting the percentages of live and dead cells. In all cell sample assessments, the viability consistently exceeded 90%.

The most uniform distribution of cells within the Eppendorf tube is observed when the medium is supplemented with 20% OptiPrep (Figure 3.4). Due to this balanced distribution, 20% OptiPrep is selected as the optimal concentration for sample preparation in all subsequent microfluidic experiments.

The counted cell number was converted to a percentage through the relationship below:

$$\frac{\text{measured cell number of an area}}{\text{total cell count of all three areas}} \times 100\%$$

For instance, in the case of the 20% OptiPrep, the cell count was:

top= 118 cells
middle= 123 cells
bottom= 105 cells
total cell count= 346 cells

Converting them to percentages:

$$\text{top} : \frac{118}{346} \times 100\% = 34.10$$

$$\text{middle} : \frac{23}{346} \times 100\% = 35.5$$

$$\text{bottom} : \frac{105}{346} \times 100\% = 30.3$$

According to the manufacturer (Stem Cell Technologies [8]), OptiPrep has a density of $1.320 \pm 0,001$ gr/mL. In our microfluidic experiments, cell sample volumes were 3 mL. Therefore, a 3 mL suspension containing 20 % OptiPrep (v/v) corresponds to a final density of 0.792 gr/mL.

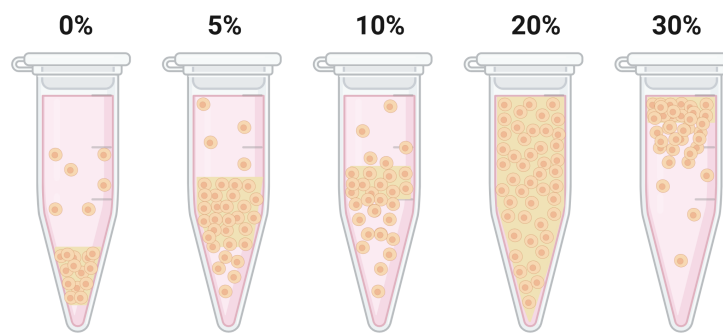


Figure 3.4: Illustration of cell sedimentation at varying concentrations (0%, 5%, 10%, 20%, and 30%) of OptiPrep (Created in BioRender.com).

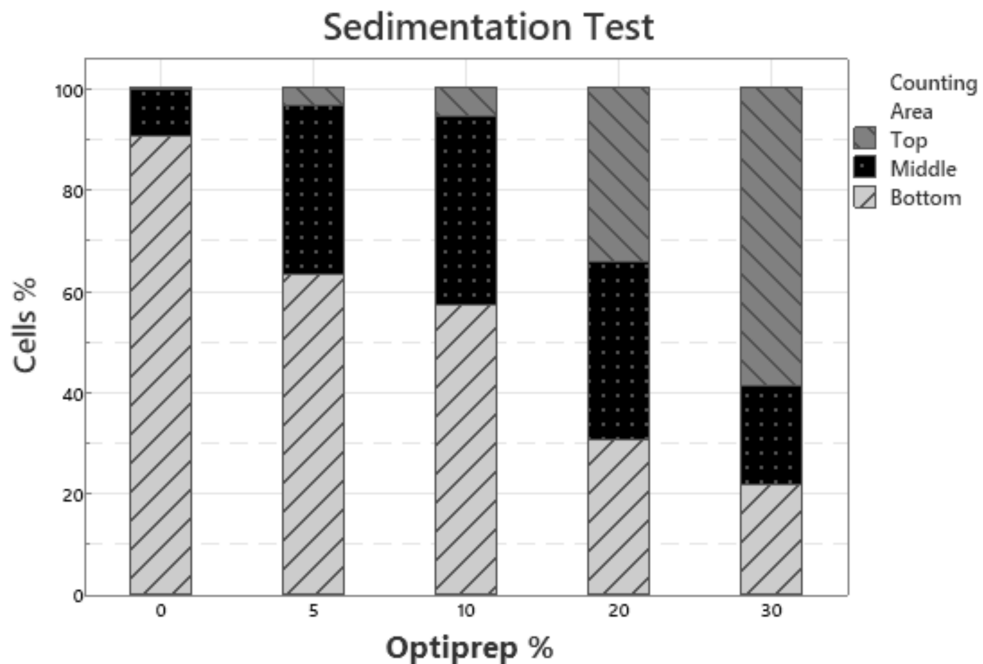


Figure 3.5: Stack column bar graph: Illustrates the distribution of cells within the Eppendorf tube at varying OptiPrep concentrations (0% to 30%). Cells were categorised based on their position within the tube: Bottom, Middle, and Top.

3.3.3 Characterisation of experimental parameters

The first device (Figure 2.8a) was used to investigate the individual parameters involved in the microfluidic experiments (signal profile, mixing profile, laser power, flow rate) and how they affect cells' response.

Experimental setup

The calcium signalling response was evaluated using fluorescence by staining the cells with Cal-520AM, a calcium-sensitive intracellular dye. As the cells passed through the laser spot, key features of the resulting fluorescence signal (peak intensity and peak duration) were recorded. The signal, detected by a photomultiplier tube (PMT), was processed in real time using custom LabView software. The background signal remained stable, while transient fluorescence peaks were observed as labelled cells moved through the laser-illuminated region.

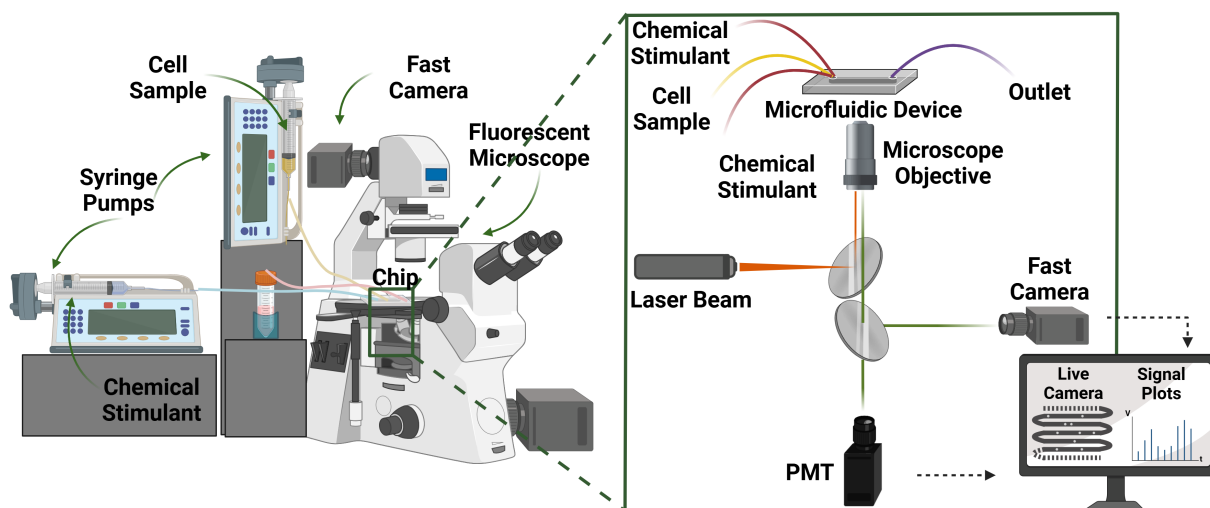


Figure 3.6: The system comprises syringe pumps that introduce the cell suspension and chemical stimulant into the microfluidic device, which is mounted on a fluorescent microscope. A fast camera captures real-time imaging while a laser beam excites fluorescently labelled cells. The emitted fluorescence is collected by a microscope objective and detected by a photomultiplier tube (PMT). The inset provides a detailed schematic of the microfluidic device, showing the fluidic inputs, optical detection system, and data acquisition setup, where live imaging and signal plots are displayed for analysis. (Created in BioRender.com).

Signal profile

In the preliminary experiments, no external stimulus was applied. The cells were stained with a fluorescent dye excited at 492 nm and emitting at 514 nm. A laser with an emission wavelength of 488 nm was used, focusing on a specific spot to observe the cells' response (Figure 3.7A and Figure 3.7B). The diameter of the laser beam was comparable to the cell diameter, approximately 15 μm (Figure 3.7C). The actual response is depicted as a Gaussian-like profile with a width

(peak duration) and amplitude (Voltage) exceeding a predefined threshold (Figure 3.7D). The threshold was set to the lowest voltage that still exceeded the background signal produced by cell debris.

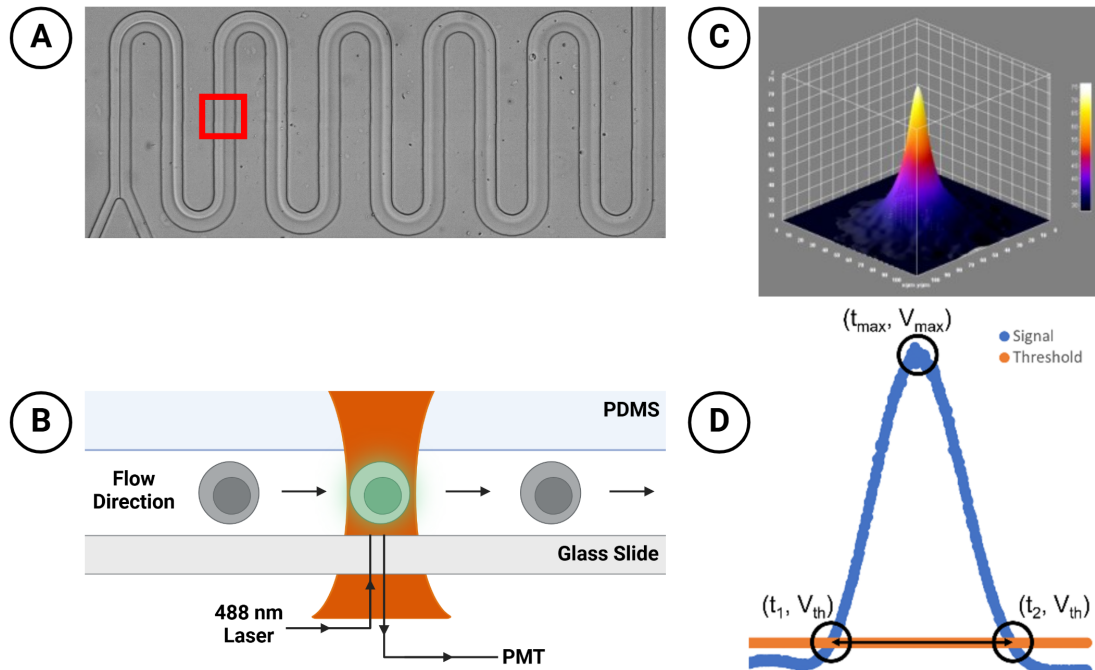


Figure 3.7: (A) Bright-field image of the microfluidic channel with a serpentine geometry. The red square highlights the interrogation region. (B) Schematic representation of the laser-based fluorescence detection setup. A 488 nm laser is focused on the channel, and the emitted fluorescence is collected using a photomultiplier tube (PMT). (C) The 3D intensity profile of the laser spot shows the excitation beam's spatial distribution. The diameter of the laser spot is $15 \mu\text{m}$. (D) Example of a fluorescence signal profile. The blue curve represents the detected signal, while the orange line indicates the threshold. The peak value V_{\max} is recorded at t_{\max} , while the signal duration is determined by the crossing points (t_1, V_1) and (t_2, V_2) . (Created in BioRender.com)

To determine whether the signal originated from a single cell or a cell cluster, the signal plots were correlated with the corresponding images, which were acquired simultaneously. It was observed that when a single cell passed through the laser beam, a single peak appeared in the signal response (Figure 3.8B and Figure 3.8C). In contrast, cell clusters produced multiple peaks (Figure 3.8D and Figure 3.8E).

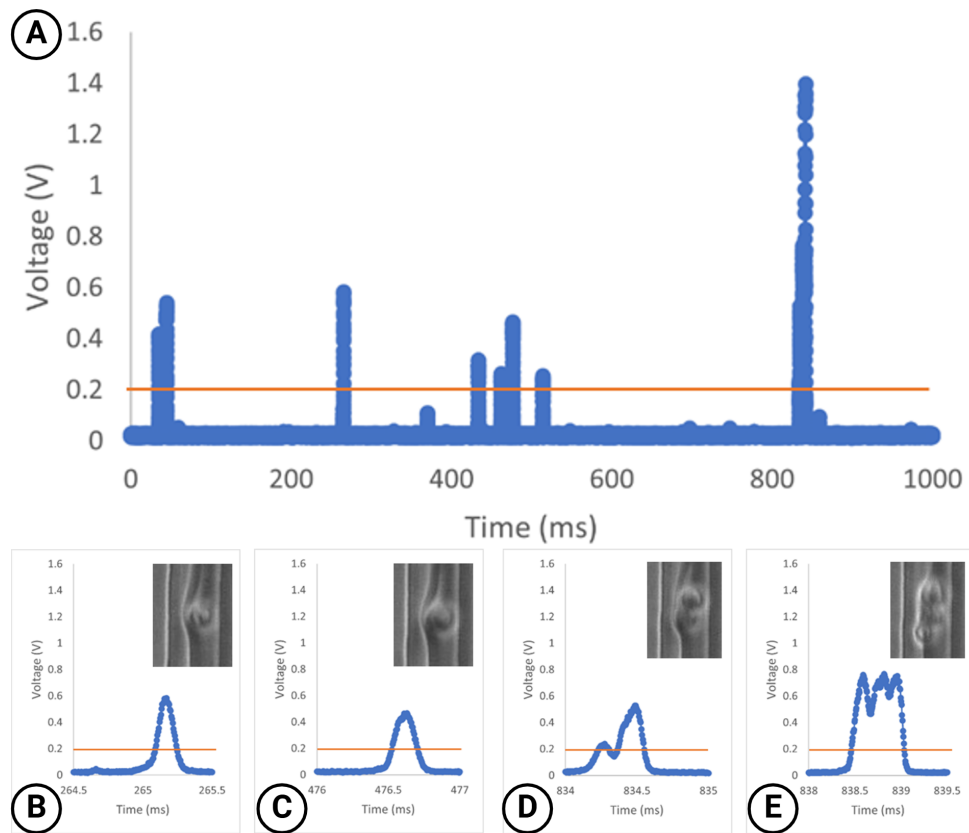


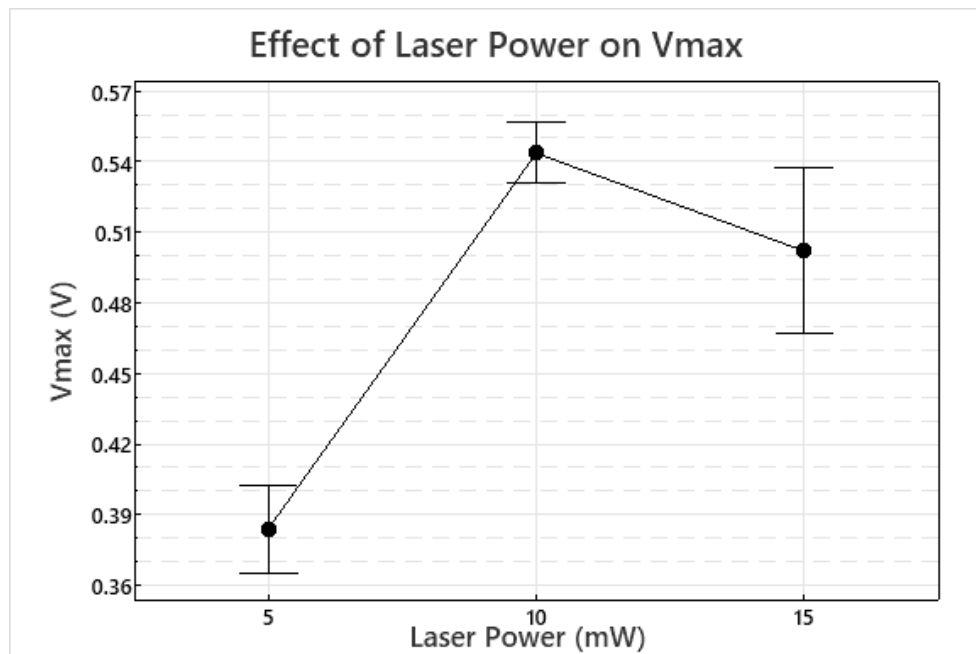
Figure 3.8: (A) voltage measurements over time, with the orange line representing the threshold level. Peaks above the threshold indicate detected fluorescence signals. The bottom panel presents four representative signal peaks with corresponding microscopic images of cells. (B, C) Single peaks correspond to individual cells. The microscopic images on the top right of these two graphs show a cell flowing in the microfluidic channel. (D, E) Broader or multiple peaks suggest cell clusters passing through the detection region. The microscopic images on the top right of these two graphs show a cluster of 2 (C) or 3 (D) cells passing through the laser spot, producing a multiple peak signal. The curved line visible in the channel flow is an artefact of the phase-contrast imaging and results from the refractive-index contrast introduced by the OptiPrep in the cell suspension.

Investigation of laser power and flow rate effect on the signal

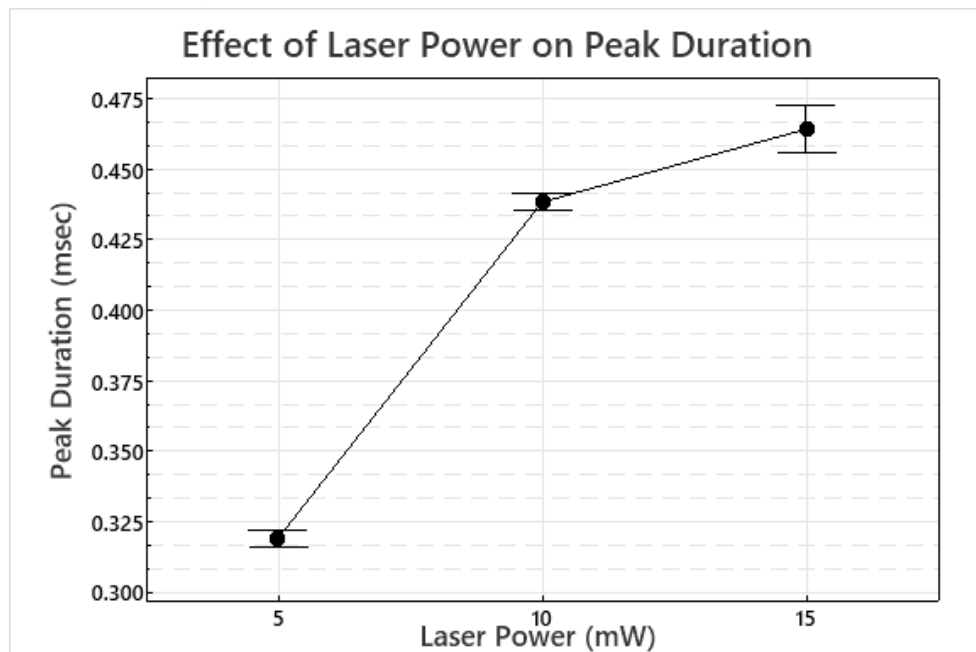
- **Laser Power**

As illustrated in Figure 3.9a V_{\max} exhibits an increasing trend with Laser Power. However, beyond 10 mW, a decline in V_{\max} was observed, likely due to sample degradation and burning caused by excessive laser exposure.

As shown in Figure 3.9b, peak duration increases with the laser power. This effect arises because the detection threshold was held constant throughout the experiment rather than being adjusted to compensate for the higher laser intensity.



(a) The Vmax increases with the Laser Power ($r=1$).



(b) The Peak Duration shows no specific linear correlation with the Laser Power.

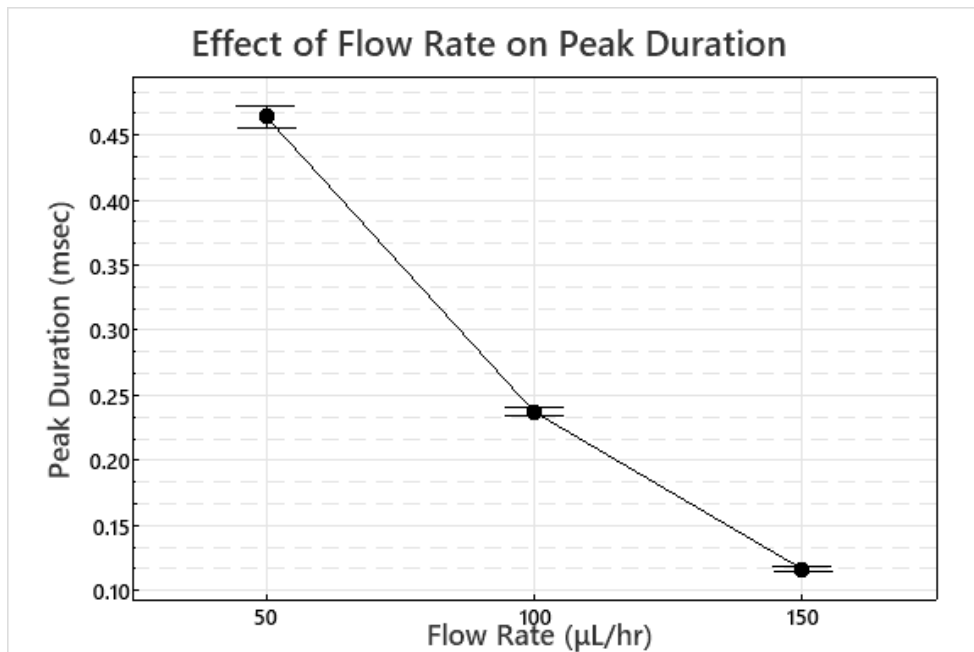
Figure 3.9: Effect of Laser Power on Vmax and Peak Duration.

These factors suggest that 15 mW might exceed the optimal laser power threshold, leading to signal distortion and reduced measurement accuracy. Consequently, a Laser Power of 10 mW was selected for the experiments conducted in this chapter.

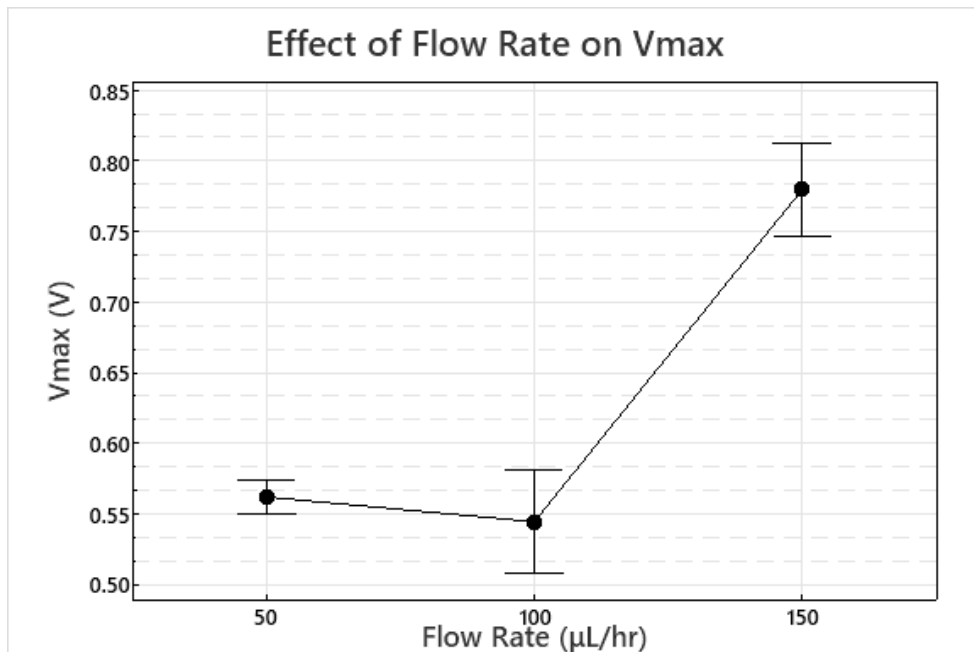
- **Flow Rate**

As the flow rate increases, the time a cell spends within the laser beam decreases, leading to a shorter peak duration (Figure 3.10a). Simultaneously, the increased flow rate reduces diffusion

effects and minimises photobleaching, allowing a higher concentration of fluorophores to contribute to the fluorescence signal. This results in an increase in V_{\max} (Figure 3.10b), as the peak intensity is enhanced by the shorter exposure time and reduced signal decay.



(a) The Peak Duration decreases with the Flow Rate ($r=-1$).



(b) The V_{\max} shows no specific correlation with the Flow Rate.

Figure 3.10: Effect of Flow Rate on Peak Duration and V_{\max} .

3.3.4 Stimulation of suspended HEK293T cells in microfluidic devices

After conducting preliminary experiments on cell behaviour and evaluating the conditions influencing their response in microfluidic devices, the next step was to initiate the chemical stimulation of HEK293T cells and assess their response in a high-throughput manner.

Mixing profile

An experiment was conducted to characterise the mixing of two compounds to determine the trigger point within the meander. Fluorescein was used in place of the chemical stimulant, and the mixing profile of the two flows was captured at both the beginning and the end of the meander.

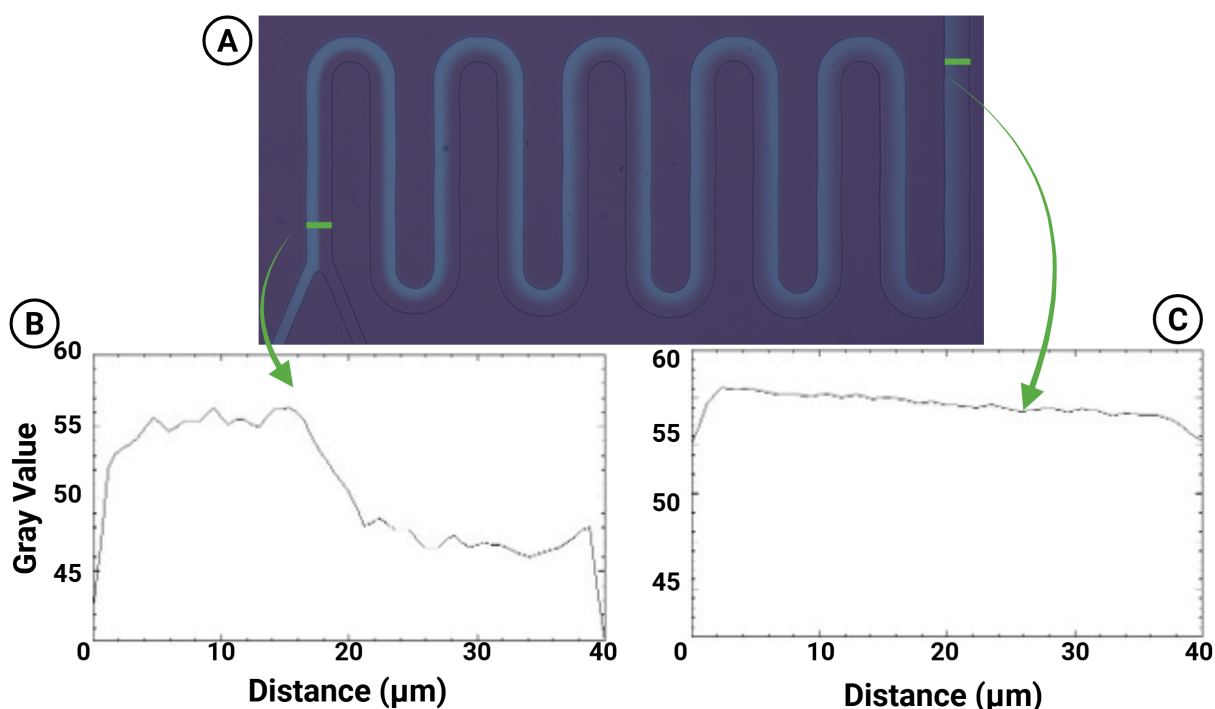


Figure 3.11: (A) Fluorescein was used to visualise the mixing of two fluid streams, with measurements taken at the beginning and end of the meander. (B) The grey value profile at the beginning of the meander shows a clear separation between the two streams. (C) The grey value profile at the end of the meander indicates increased mixing and a more uniform distribution.

As observed in both the images and the corresponding plot, the interfaces of the two flows remained clearly separated at the beginning of the meander (Figure 3.11B). However, as the fluids progressed, the interface gradually became smoother, and by the end of the meander, the mixing was more evenly distributed (Figure 3.11C).

Chemical stimulation

The device presented in Figure 2.8a was initially used. Multiple positions within the device were selected as probing points (Figure 3.12). The laser was focused on each of these points, and the response of each cell passing through the laser beam was recorded—each measurement corresponds to a different cell rather than tracking the same cell across positions. The flow rate for both inlets was maintained at $50 \mu\text{L/hr}$, with the laser power set to 10 mW. The cell sample used consisted of 3×10^6 cells in 3 mL of DMEM-Accumax solution, supplemented with 20% OptiPrep. For the test experiments, cells were stimulated with $10 \mu\text{M}$ ATP, while for the control experiments, plain DMEM was used in the second inlet instead of the chemical stimulant. ATP is an extracellular signalling molecule that binds to purinergic receptors on the cell surface [191] and triggers calcium-permeable channels, resulting in Ca^{2+} influx from the extracellular space. In HEK293T cells, ATP activates the P2Y receptors, which are G-protein-coupled receptors [162]. The resulting rise in intracellular Ca^{2+} produces a measurable fluorescence signal, which we record as each cell passes through the laser beam.

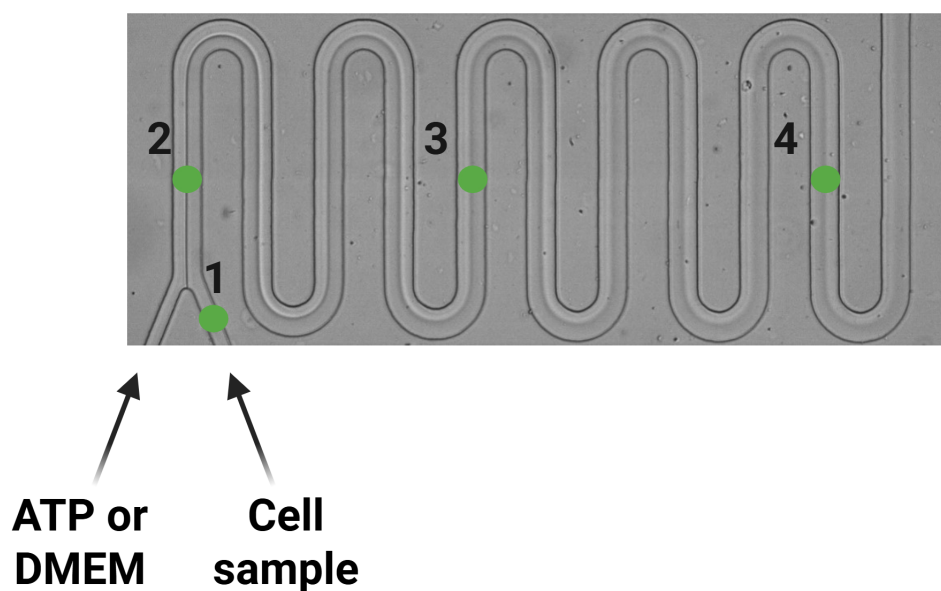


Figure 3.12: Schematic of the meander of the microfluidic device no1. The positions highlighted in green are the positions where the laser spot was focused for the data acquisition.

Data filtering

The peak duration values were correlated with the corresponding simultaneously acquired images to filter the data. This approach differentiated signals from single cells, cell clusters, or debris. Signals with a peak duration of less than 0.1 ms were observed to be associated with debris, while signals from single cells ranged between 0.1 and 0.32 ms. In contrast, signals from cell clusters exhibited peak durations exceeding 0.32 ms (Figure 3.13). Therefore, the data selected for analysis correspond to the green-highlighted area.

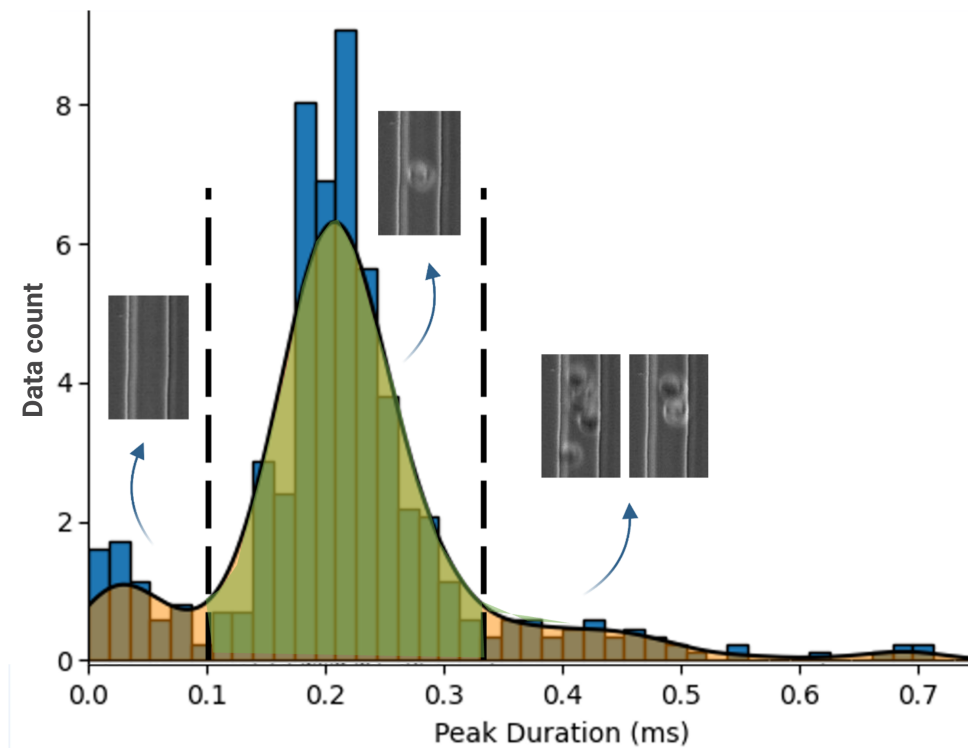


Figure 3.13: The black dashed lines mark the filtering thresholds. Insets show representative microscopy images illustrating these different cases. The scatter plot at the bottom displays individual data points.

Following the data filtering process described above, the results for both the test and control experiments were plotted for all selected positions.

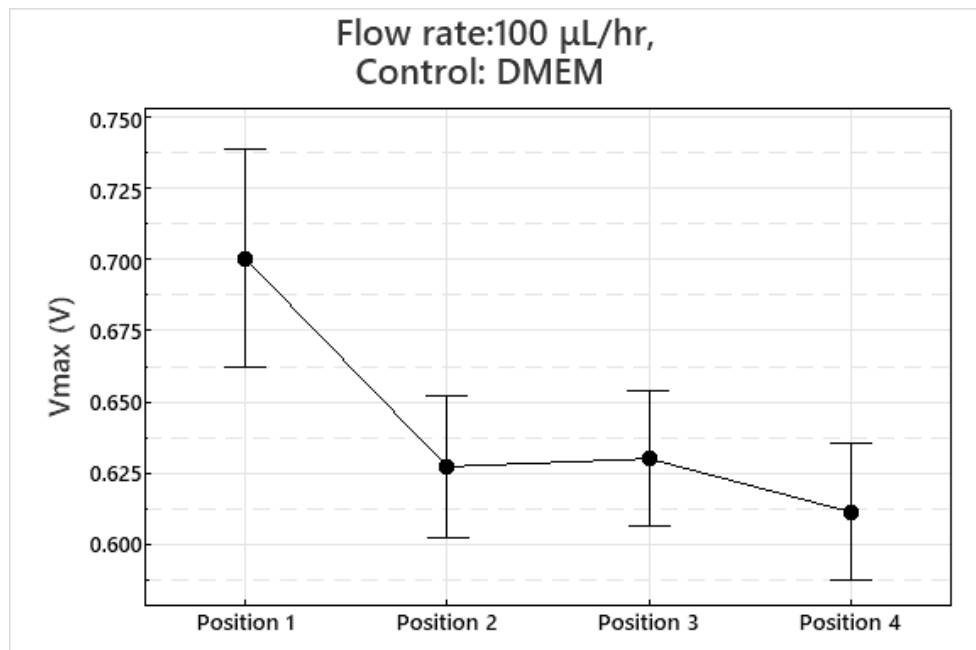


Figure 3.14: Maximum Voltage of unstimulated cells' response in different positions. The total flow rate in the device is $100 \mu\text{L/hr}$, since it is the sum of the flow rate of the two inlets ($50 \mu\text{L/hr}$ each)

The data were found to be non-normally distributed, and non-parametric tests were used to compare all the positions. The Kruskal-Wallis test showed a P-value equal to 0. However, the huge error bars indicate that the test could be less meaningful. Therefore, the eta squared (Effect size for Kruskal-Wallis) was calculated ([111]):

$$\eta^2 = \frac{H - k + 1}{N - k} \tag{3.2}$$

Where,

N= Total number of observations

k= Number of groups

H= Kruskal-Wallis statistic

When:

$\eta^2 < 0.01 \rightarrow$ Very weak effect

$0.01 \leq \eta^2 < 0.06 \rightarrow$ Weak effect

$0.06 \leq \eta^2 < 0.14 \rightarrow$ Moderate effect

$\eta^2 \geq 0.14 \rightarrow$ Strong effect

The 3.2 for the control experiment is:

$$\eta^2 = \frac{249.4 - 4 + 1}{2000 - 4} = 0.12$$

Based on the above findings, the effect size of the Kruskal-Wallis comparison was moderate.

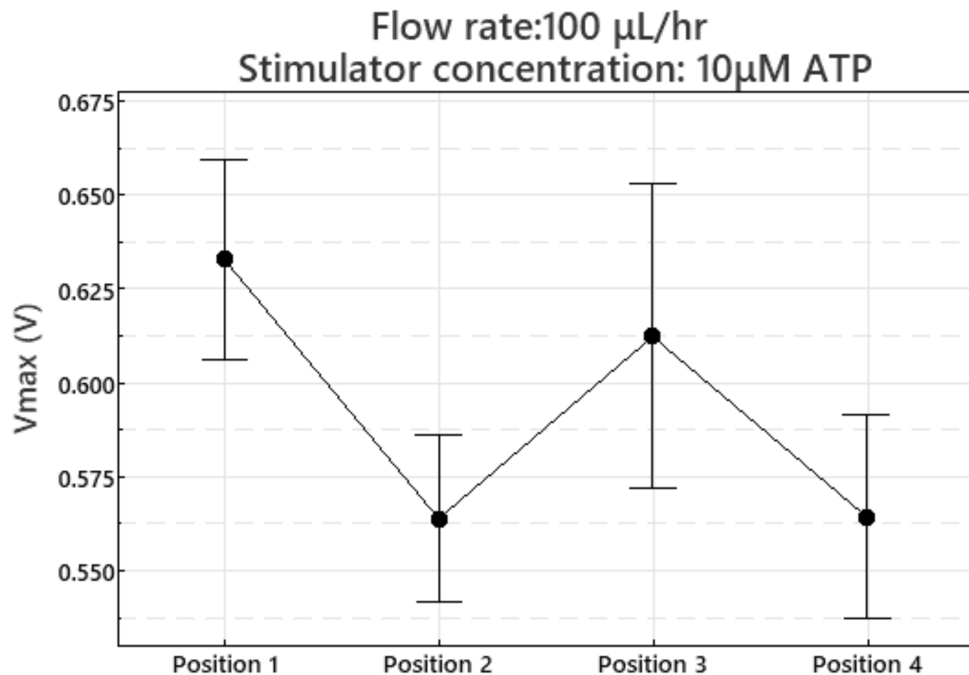


Figure 3.15: Maximum Voltage of stimulated cells' response in different positions.

Similarly, since the data were not normally distributed, a Kruskal-Wallis test was performed to compare the responses in each position for the test experiment. Although the P-value was equal to 0, the effect size was calculated according to Equation 3.2.

$$\eta^2 = \frac{38.1 - 4 + 1}{3500 - 4} = 0.01$$

Based on the above findings, the Kruskal-Wallis comparison test result was rejected.

The same trend was observed in additional test experiments conducted with varying concentrations of the chemical stimulant. This observation prompted an experimental investigation to determine the time required for suspended cells to respond to chemical stimulation following exposure to the chemical.

Estimation of cell response time

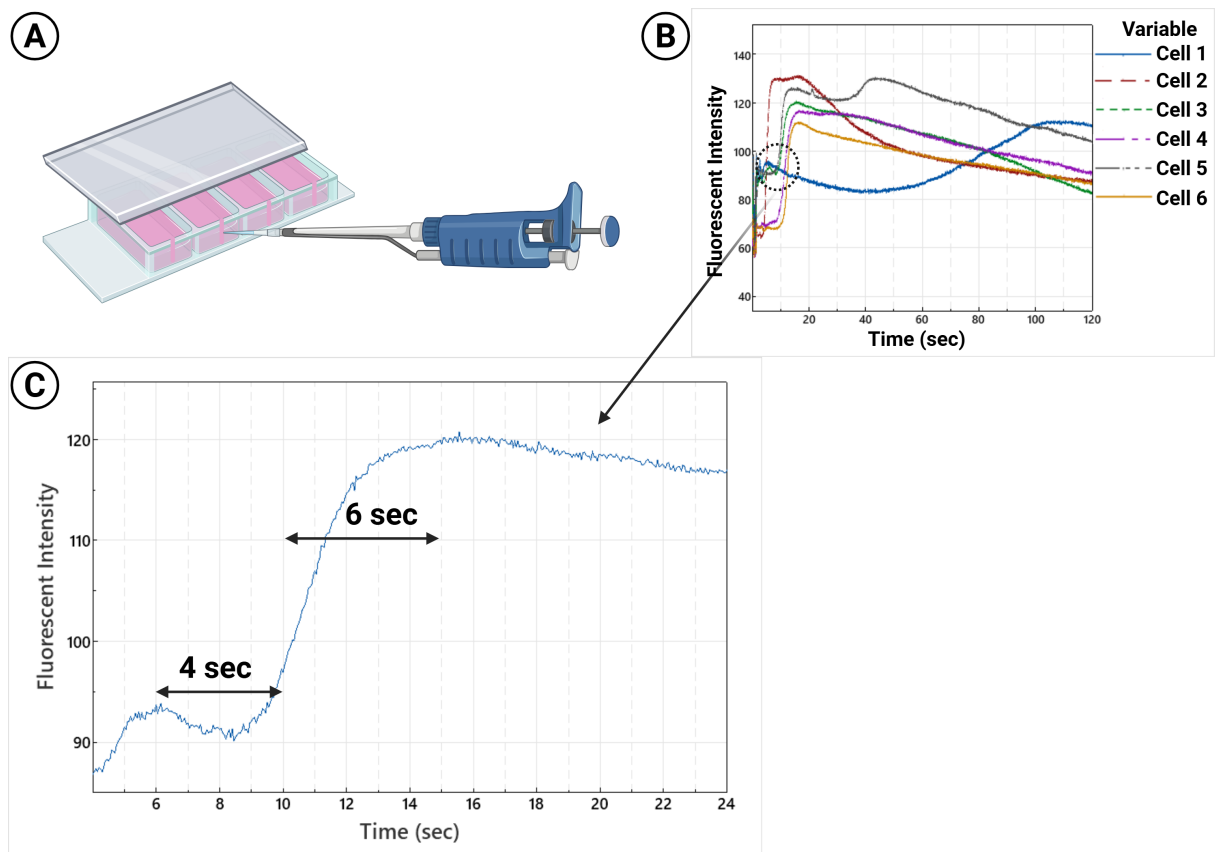


Figure 3.16: (A) Experimental setup, where the chemical stimulant is inserted into the cell sample in microfluidic chambers. (B) Fluorescence intensity traces over time for different cells, showing their response to stimulation. (C) Zoomed-in view of a representative fluorescence intensity trace. The zoomed-in area highlights the cell's initial response to the stimulant, marked by the first rise in fluorescence intensity.

Cells were stained following standard procedures, detached from the culture dish, and introduced into multiple PDMS chambers to obtain technical replicates (Figure 3.16A). Each chamber was treated with 10 μM ATP, and a 120-second video was recorded for each replicate.

The data were then plotted as Fluorescent Intensity over Time (Figure 3.16B). Upon closer examination of the inflection point of the graph, it was determined that the cellular response began approximately four seconds after stimulation, reaching a peak signal about six seconds later (Figure 3.16C), yielding a total response time of 10 seconds from stimulation to maximum fluorescence.

Its velocity needed to be calculated to investigate whether the cell remained in the field of view 10 seconds after stimulation. The following equation was used:

$$Q = v_{\text{avg}} \times A \quad (3.3)$$

Where,

Q= Flow Rate

$v_{(\text{avg})}$ = Average velocity

A= Cross-sectional area

The meander dimensions of device no1 (Figure 2.8a) are shown below:

Length= 0.57 mm

Width= 40 μm

Depth= 25 μm

The flow rate of each inlet is 50 $\mu\text{L/hr}$. Since there are two inlets, the total flow rate in the device is 100 $\mu\text{L/hr}$. Based on Equation 3.3, the following calculation was performed:

$$v_{\text{avg}} = \frac{100 \times 10^{-6} \times 10^{-3} \text{ m}^3}{10 \times 10^{-10} \times 3600 \text{ m}^2 \text{sec}} = \frac{50 \times 10^{-1} \text{ m}}{10 \times 36 \text{ s}} = 27.78 \frac{\text{mm}}{\text{sec}}$$

The cells were expected to flow in the middle plain with the maximum velocity of the laminar flow. As has been proven in Chapter 2, the relationship between v_{avg} and v_{max} is described by Equation 1.3.

Therefore,

$$v_{\text{max}} = 1.5 \times v_{\text{avg}} = 1.5 \times 27.78 = 41.67 \frac{\text{mm}}{\text{sec}}$$

Based on the device's dimensions, the calculated velocity of the cells indicated that the cell exits

the meander of the device in 0.1 sec (Figure 3.12). More precisely, the time needed for a cell to reach each position highlighted in the meander is 6.8 msec for position 2, 6.5 msec for position 3 and 129.9 msec for position 4. Position 1 is the point where the cell suspension meets the chemical stimulant, and therefore it is considered as the starting position of the cell (i.e. $t=0$ msec). Consequently, it was inferred that the cell's response could not be observed due to the device's size.

The first solution explored was to decrease the flow rate of the cell sample. However, this approach was unsuccessful and compromised the high throughput, which was a key objective of the project. As a result, the focus shifted towards developing a new device with a longer meander and broader channels.

Therefore, a second microfluidic device with three inlets and a longer meander was designed and fabricated (Figure 2.8b). The meander dimensions of this new device are shown below:

Length= 1 cm
 Width= 60 μm
 Depth= 45 μm

The flow rate of each inlet is 50 $\mu\text{L/hr}$, which results in a total flow rate of 150 $\mu\text{L/hr}$ in the device. Based on Equation 3.3, the following calculation was performed:

$$v_{\text{avg}} = \frac{150 \times 10^{-6} \times 10^{-3} \text{ m}^3}{27 \times 10^{-10} \times 3600 \text{ m}^2 \text{ sec}} = \frac{150 \times 10^{-1} \text{ m}}{27 \times 36 \text{ s}} = 15.43 \frac{\text{mm}}{\text{sec}}$$

Similarly, to calculate the $v_{(\text{max})}$:

$$v_{\text{max}} = 1.5 \times v_{\text{avg}} = 1.5 \times 15.43 = 23.15 \frac{\text{mm}}{\text{sec}}$$

The time required for the cells to reach each corner position of the meander was calculated. Based on these calculations, combined with the results from Figure 3.16, the cellular response was anticipated to occur between position 5 (4 seconds) and position 12 (10 seconds).

Multiple experiments were conducted with this device. The control experiments involved the insertion of either plain DMEM or PBS Ca^{2+} and Mg^{2+} free in the sheath flows, whereas for the test experiments different concentrations of ATP were tested (5 μM and 30 μM).

The tested positions are presented in Figure 3.17. In the initial experiment, no chemical stimulant was introduced. Instead, plain DMEM was supplied through the two sheath flow channels, while the central stream contained HEK293T cells stained with Cal520 (Figure 3.18).

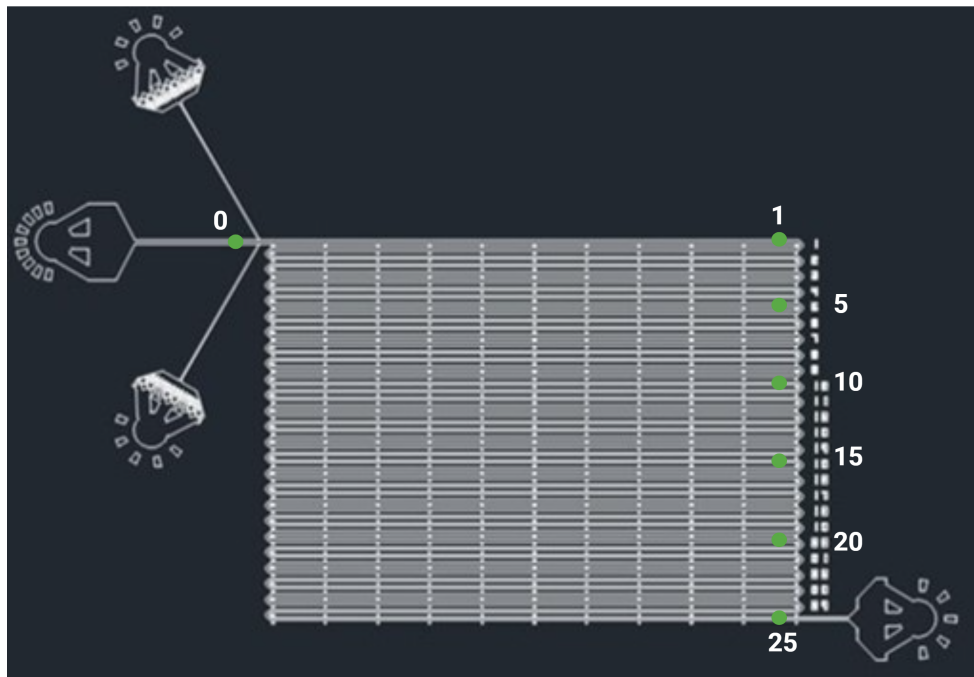


Figure 3.17: Schematic of the meander of the microfluidic device no2. The positions highlighted in green are the positions where the laser spot was focused for the data acquisition.

The flow rate for all three inlets was maintained at $50 \mu\text{L/hr}$. These experiments, conducted in the absence of chemical stimulation, served not only as a negative control but also to assess whether the sheath flows exerted any mechanical stimulation on the cells in the central stream due to compression.

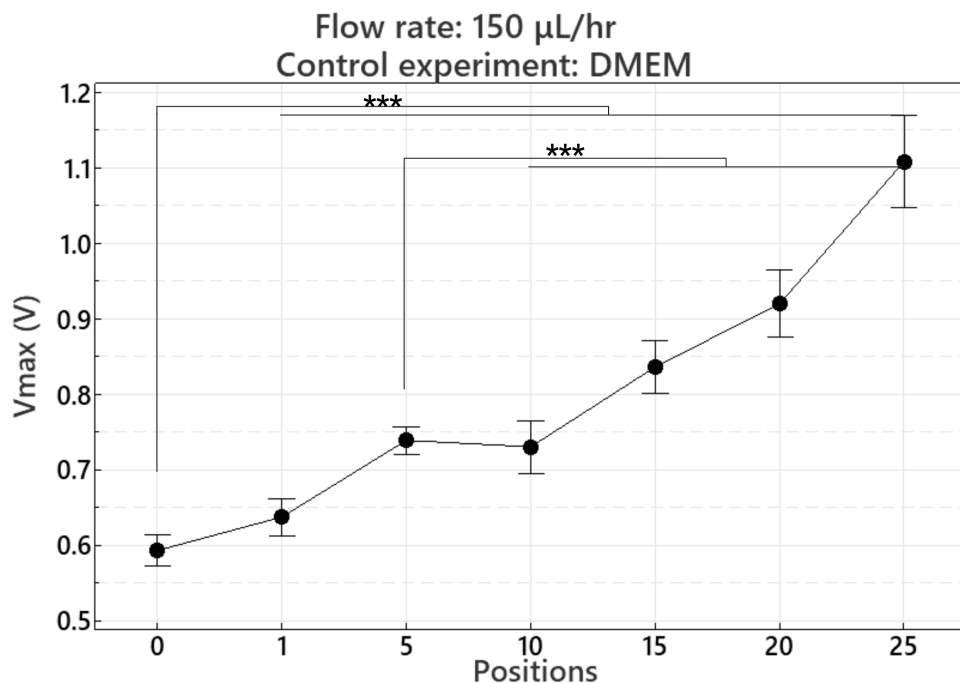


Figure 3.18: The total flow rate of the device is the sum of the three inlets ($50 \mu\text{L/hr}$ each). Maximum Voltage of unstimulated cells' response in different positions (**p-values < 0.001).

Anderson-Darling tests were performed to check the normality of all the positions' data. Since they were found to be non-normally distributed, non-parametric tests (Kruskal-Wallis and Mann-Whitney) were used to check for statistical significance among the groups (positions). The effect size n^2 was calculated in both cases (control and test experiments). It was found to be 0.24 and 0.17, respectively, indicating a strong effect of the Kruskal-Wallis tests (Equation 3.2).

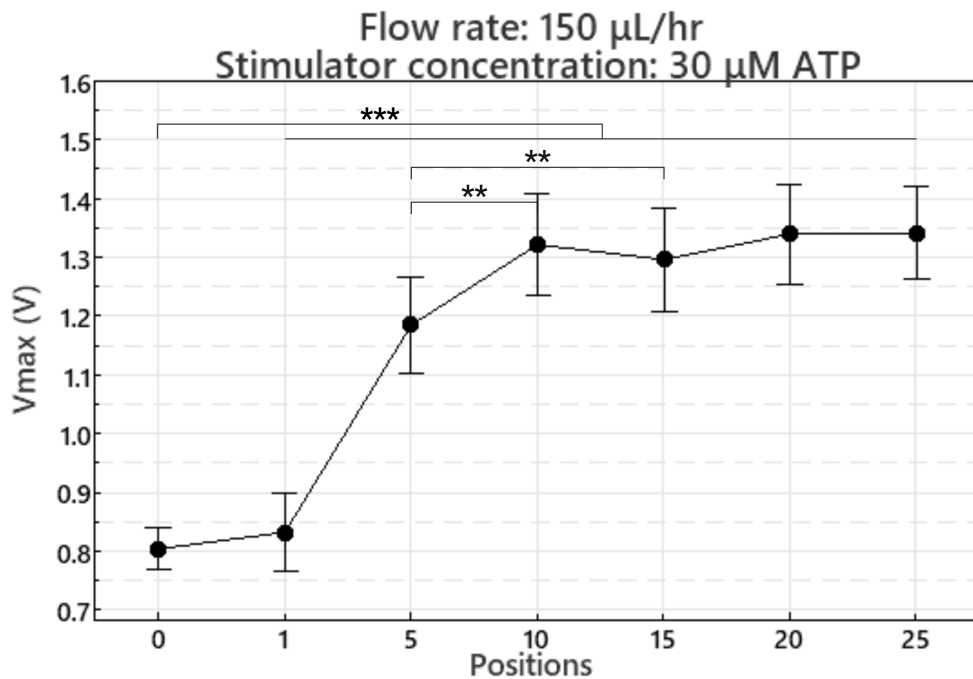


Figure 3.19: Maximum Voltage of stimulated cells' response in different positions (**p-values < 0.005, ***p-values < 0.001).

As shown in Figure 3.18, a slight increase in response (V_{max}) is observed after position five, potentially indicating mechanical stimulation in the form of shear stress applied by the sheath flow. To further investigate, data acquisition was performed at various positions within the meander during the chemical stimulation experiments (Figure 3.19). The highest response was recorded at position 20, which, based on the calculated cell velocity, corresponds to 17 seconds. This result deviates from expectations, as prior measurements of cell response to stimulation (Figure 3.16) indicated a response time of approximately 10 seconds post-stimulation.

When comparing these results with those from the control experiments, it can be inferred that cells respond faster to the chemical stimulation (i.e. ATP) compared to the shear stress applied by the sheath flow in the control experiment. It seems that after position 10 (corresponding to $t=8.2$ sec), the cellular response plateaus. The fluorescence intensity due to Ca^{2+} release has reached the maximum, and therefore, additional shear stress cannot further increase this response. Instead, the ongoing shear stress appears to sustain this plateau, preventing the fluorescence signal from declining as the cells begin to recover.

A lower concentration of ATP was also used to stimulate the cells, and a calcium-free medium was used as a control.

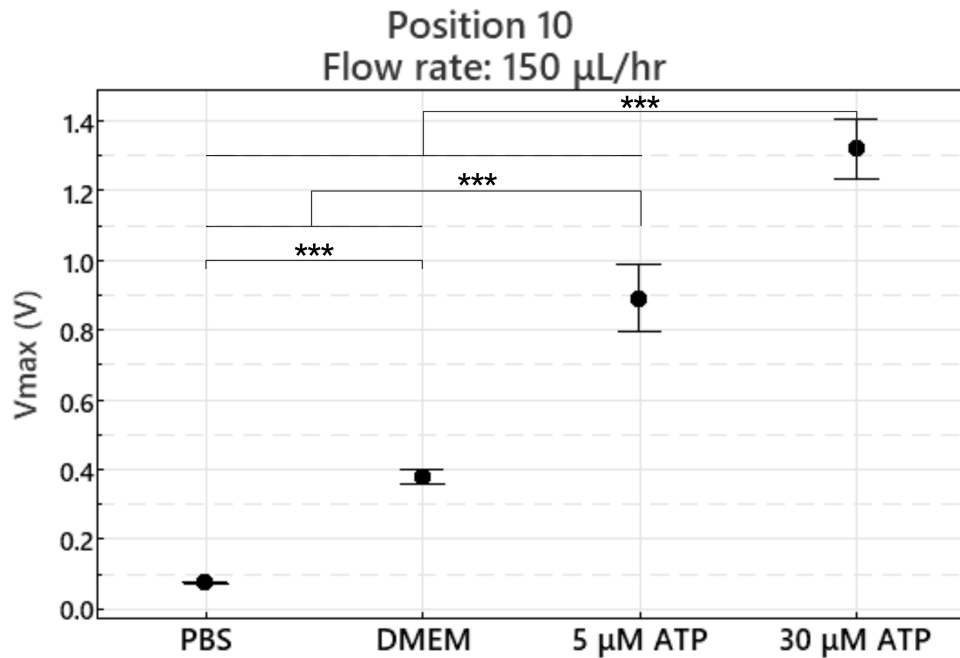


Figure 3.20: Maximum Voltage of the cells at position 10 under different conditions (***) p-values < 0.001).

A Kruskal-Wallis test was conducted to compare the median values among the groups, indicating a statistically significant result ($p = 0.000$). Subsequent pairwise Mann-Whitney tests, performed for all possible group combinations, revealed statistically significant differences between all groups ($p = 0.000$).

As Figure 3.20 shows, the higher ATP concentration resulted in a stronger response, while the calcium-free medium control produced an almost negligible signal.

3.4 Discussion

The work carried out in this chapter contributed towards the optimisation of the cell sample, the device design and the experimental conditions.

3.4.1 Proof of concept: Stimulation of adherent and suspended cells

Initially, it was confirmed that HEK293T cells are responsive to chemical stimulation, whether adherent on a tissue culture plate or in suspension. The importance of this validation lies in the proof that cellular responses can be reliable under both experimental conditions, establishing the foundation for the following experiments.

3.4.2 Sedimentation test: optimising cell sample solution

Afterwards, the constitution of the cell sample solution was optimised to prevent aggregation and sedimentation, common challenges in microfluidic experiments that can compromise data quality. Maintaining a uniform cell distribution is essential for consistent analysis and signal acquisition. To address this, OptiPrepTM, a density-matching medium, was incorporated into the suspension to achieve near-neutral buoyancy of the cells during flow. This approach is consistent with prior studies where OptiPrep has been effectively used to prevent cell sedimentation in microfluidic single-cell encapsulation assays [118], facilitate extracellular vesicle separation based on buoyant density [74], and improve purification of primary cell types such as platelets and pancreatic islets without compromising viability or function [20, 133]. These precedents support the use of OptiPrep as a reliable agent for density adjustment in cell-based microfluidic applications.

3.4.3 Signal profile: effect of laser power and flow rate

The effect of laser power and flow rate on the acquired signal was investigated after optimising the cell sample composition. It was shown that the signal gets stronger as the laser power increases. However, the cell can be damaged at extreme laser power, which should be kept in mind when setting the power.

On the other hand, the peak duration decreases as the flow rate increases, as the time that cells spend in the laser beam reduces. This finding highlights the importance of choosing a flow rate that promotes an effective stimulation with adequate time for cellular response.

3.4.4 Chemical stimulation experiments

Many studies have shown that extracellular ATP elicits a rapid, dose-dependent rise in intracellular Ca^{2+} in HEK293T cells via activation of purinergic receptors (subsection 3.3.4). For instance, Ralevic and Burnstock (2012) document that ATP binds surface P2Y receptors and triggers downstream G-protein-mediated Ca^{2+} release and influx [35]. Atwood et al. (2011) confirmed that HEK293T cells endogenously express multiple P2Y subtypes, making them responsive to ATP stimulation [19].

In the experiments where device 2 was used (longer meander), the peak response to 10 μM ATP occurred around 8.2 s after stimulation, comparable to the few-second latencies reported in adherent systems [175]. The dose-dependence we observed (stronger fluorescence at higher ATP concentrations, minimal response in Ca^{2+} free control) aligns well with these prior findings. In adherent cultures, time-lapse microscopy often reports ATP-induced Ca^{2+} peaks within 2–6 s of application; the ~ 8 s response in the experiments of this chapter may be slightly delayed due to

the time needed for ATP to mix and reach cells in the microchannel. Still, the overall kinetics remain in the same order of magnitude.

3.4.5 Suspension Format vs. Adherent Assays

Almost all published ATP-triggered Ca^{2+} studies in HEK cells use adherent monolayers on glass or plastic. In contrast, my work screens suspended cells flowing through a microfluidic channel, which has several important implications.

Piezo1 gating and P2Y signalling in HEK cells do not require adhesion to the ECM [50, 174]. However, specific modulatory effects, such as focal-adhesion-linked kinases, are lost in suspension. By working in flow, it is ensured that any observed Ca^{2+} influx arises purely from receptor activation and mechanical deformation, rather than from substrate-associated signalling pathways.

In traditional adherent cell assays, the diffusion of ATP and the formation of local concentration gradients can lead to heterogeneous stimulation across the culture dish. This spatial variability results in inconsistent cellular responses, complicating the interpretation of experimental outcomes. For instance, studies have shown that in static cultures, the accumulation of secreted factors and uneven distribution of stimuli can significantly influence cell behaviour [90].

In contrast, microfluidic systems offer a controlled environment where cells are exposed to uniform ATP concentrations and consistent shear stress profiles as they flow through microchannels. This setup ensures that each cell experiences the same stimulation conditions, leading to more reproducible, population-level data. The precise control over the microenvironment in microfluidic devices minimises variability and enhances the reliability of experimental results.

3.4.6 Influence of Mechanical Stimulus (Shear Stress)

Even when the primary goal is to track ATP-induced Ca^{2+} influx, mechanical forces, especially shear stress from fluid flow, can modulate or independently trigger Ca^{2+} signals. Several studies highlight this effect. Gossett et al. (2012) used inertial microfluidic constrictions to deform suspended cells. They observed mechanosensitive signalling (e.g., Rho kinase activation), implying that shear or deformation in a channel is sufficient to induce Ca^{2+} -linked responses in some cell types [79]. Sackmann et al. (2014) review how shear stress alone can trigger Ca^{2+} transients via mechanosensitive channels even in the absence of chemical ligands [159].

In the data collected, particularly at position 20 of Device 2, where both the ATP and the shear stress stimulations were experienced by the cells, a higher fluorescence signal was observed

compared to upstream positions exposed only to shear stress (control experiment Figure 3.18). This indicates that shear stress contributes to the chemical stimulation by sustaining or enhancing Ca^{2+} influx. Although a robust response can be obtained by ATP alone, the combined mechano-chemical stimulation at position 20 is likely responsible for prolonging or amplifying the plateau phase, rather than allowing it to decline during the recovery period. This limitation in distinguishing between chemical and mechanical stimulation (shear stress applied by the sheath flow) could be overcome by designing a microfluidic device that operates without the use of sheath flow.

3.4.7 Relevance of Suspension-Based Assays and Limitations

Suspension-based assays utilising HEK cells in microfluidic channels offer distinct advantages for specific applications. These systems are particularly beneficial when high-throughput analysis is essential, such as in drug screening or rare-cell detection, due to their ability to process large numbers of cells efficiently [45]. Moreover, they facilitate label-free sorting of mechanosensitive subpopulations, a task challenging for traditional FACS systems, which typically cannot separate cells based on deformation or real-time calcium flux without exogenous tags [144]. Additionally, the microfluidic environment ensures rapid and uniform mixing of stimulants and removes the influence of the ECM, thereby isolating the effects of soluble stimuli [71].

However, these advantages come with certain compromises. One notable limitation is baseline mechanical activation. Even at low flow rates, shear stress can induce a background calcium influx independent of ATP stimulation. While selecting moderate flow rates (e.g., $50 \mu\text{L/hr}$) can minimise this effect, it cannot be eliminated [117]. Another limitation is the loss of adherent signalling modules. In suspension, key signalling molecules such as focal adhesion kinases (FAKs) often remain inactive, restricting the study of long-term or integrin-mediated responses [154]. Furthermore, the brief duration that suspended cells remain within the observation window limits the assay to capturing only the early kinetics of calcium signalling, typically within the first 10 seconds, making it challenging to monitor slower downstream effects, such as transcriptional responses to ATP or mechanical cues [199].

3.5 Conclusion

In conclusion, this study demonstrates the importance of optimising experimental conditions, including cell sample preparation, flow rate, and laser power, when using microfluidic devices to study cellular responses. The proof-of-concept experiments successfully validated the ability of HEK293T cells to respond to chemical stimuli in both adherent and suspended states, establishing a solid foundation for the subsequent experiments. Optimisation of the cell suspension

process ensured that the cells remained evenly distributed throughout the experiment.

The first device was found to be unsuitable for capturing cellular responses due to its short meander design, which limited the observation window. In contrast, the second device was more effective, providing sufficient time for cells to respond to stimuli and producing robust and reliable results. The statistical analysis of Device 2 confirmed the validity of the data obtained, suggesting that it is a suitable platform for investigating cellular responses to chemical stimuli.

Overall in this chapter, it was demonstrated for the first time that suspended HEK cells can respond to chemical stimulation while flowing through a microfluidic channel, with their calcium signalling captured in real time, enabling high-throughput analysis. A primary limitation encountered was the difficulty in distinguishing the effects of chemical stimulation from those induced by shear stress generated by the sheath flow. This challenge could be addressed in future designs by employing sheathless microfluidic configurations to reduce mechanical interference. Nevertheless, the approach presented here offers a scalable and label-free method for probing mechanosensitive cellular responses in suspension, with promising applications in drug screening, stem cell classification, and mechanobiology research.

Chapter 4

Mechanical Stimulation of HEK293T Cells with Microfluidics

This chapter focuses on the chemical activation of the mechanosensitive ion channel Piezo1 using the small molecule Yoda1. This investigation is a foundation for the subsequent experiments involving the mechanical stimulation of HEK293T cells. The following sections will briefly overview Piezo1's structure and function, followed by an analysis of cellular response to Yoda1 and mechanical stimulation.

4.1 Introduction

4.1.1 Piezo1 structure and function

Piezo1 is a large, trimeric ion channel that plays a critical role in mechanosensation, first identified in Neuro2A (glial tumour cell line) by the Patapoutian group as a potential ion channel [50]. Its distinctive structure resembles a propeller with three identical subunits arranged symmetrically around a central pore [92]. Each subunit contains approximately 38 transmembrane helices, forming extended blade-like arms that radiate outward [201, 207]. These arms interact with the lipid bilayer, sensing mechanical forces such as membrane tension or shear stress. The central pore, located at the core of the trimer, serves as the pathway for ion flow and is lined with specific amino acids that control ion selectivity. Additionally, Piezo1 features a cap domain that stabilises the channel and an intracellular anchor domain that links it to the cytoskeleton, potentially modulating its mechanosensitivity [160].

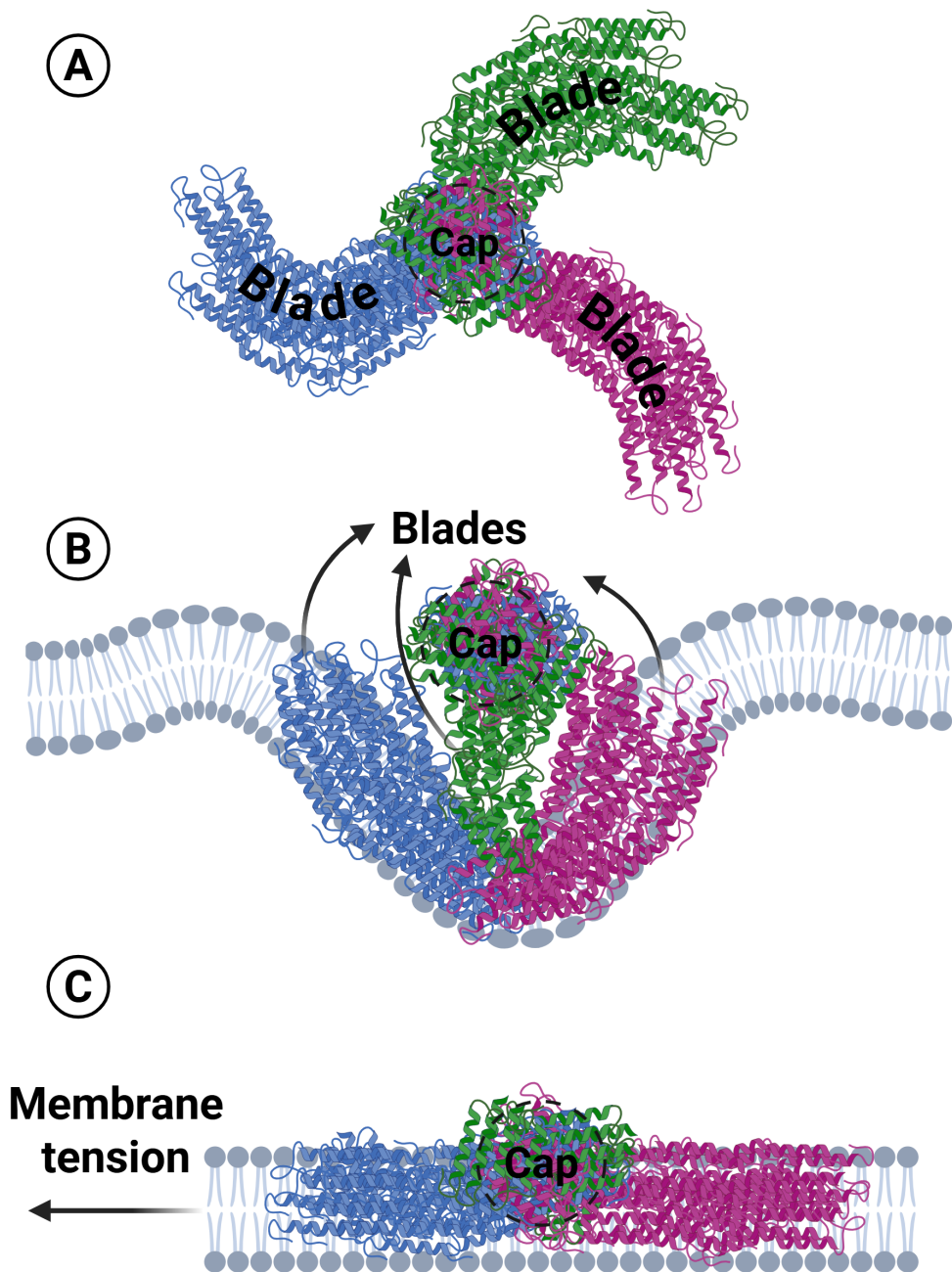


Figure 4.1: (A) Top view of the mechanosensitive ion channel Piezo1. The schematic (top) shows three curved, blade-like structures symmetrically arranged around a central pore, which is covered by a cap domain. (B) In the closed state, the blades remain curved, the cap is in the "up" position, and the ion channel is shut. (C) When membrane tension is applied, Piezo1 undergoes a conformational change into a flattened, open state. The cap shifts to the "down" position, allowing the central pore to open and ions to pass through. (Created in BioRender.com).

The channel opens in response to mechanical stimuli, such as membrane stretching or compression. These forces are detected by the blade regions, causing a conformational change that flattens the dome-like curvature of the Piezo1 complex. This structural rearrangement widens the central pore, allowing ions—primarily calcium (Ca^{2+})—to pass through the membrane. This ion influx depolarises the cell membrane and initiates downstream signalling pathways. The re-

sponse is highly sensitive, with Piezo1 opening rapidly upon detecting sufficient mechanical force, enabling the channel to mediate acute responses to mechanical stress. Once the mechanical stimulus is removed, Piezo1 transitions back to its closed state, restoring its curved, dome-like shape. [196].

4.1.2 Yoda1 as Piezo1 activator

Yoda1 is a synthetic small molecule that selectively activates the mechanosensitive ion channel Piezo1 without requiring mechanical stimulation. It has been widely used in research to study Piezo1 function, particularly in calcium signalling, mechanotransduction, and physiological processes such as blood flow regulation and cell migration [108, 175].

Yoda1 binds to Piezo1 and stabilises its open conformation, increasing ion permeability. In contrast to mechanical stimuli that induce transient channel activation, Yoda1 can prolong Piezo1 activity, leading to a sustained influx of calcium (Ca^{2+}). Although the precise binding site of Yoda1 remains unclear, evidence suggests that it interacts with both the extracellular and transmembrane domains of Piezo1 [32].

However, careful consideration must be given to the concentration of Yoda1 used in experiments, as prolonged exposure has been reported to cause desensitisation or cytotoxicity. This underscores the importance of dosage optimisation to ensure reliable experimental outcomes while minimising potential adverse effects [54].

4.1.3 Piezo1 response

The response of Piezo1 to mechanical or chemical stimulation typically exhibits two distinct phases: a rapid initial response with low amplitude and a delayed sustained response of higher amplitude [50, 155].

In particular, the rapid activation occurs within milliseconds (1-10 msec) following the stimulation, and it represents a quick but relatively low influx of ions, primarily Ca^{2+} . This phase allows cells to detect immediate mechanical changes, and it is followed by a rapid inactivation phase. This process is crucial for regulating Piezo1's role in mechanotransduction and preventing excessive ion influx. A fast inactivation rate ensures Piezo1 responds dynamically to short-lived mechanical stimuli, and the cell is well protected against non-specific responses [80]. Mutations that slow down inactivation lead to prolonged ion influx, disrupting cell homeostasis.

Following the rapid response of Piezo1 and its inactivation, a delayed but stronger response is observed within tens to hundreds of milliseconds. This prolonged phase is primarily driven

by an increase in intracellular Ca^{2+} levels, facilitated by both continued ion influx and the release of Ca^{2+} from cytosolic stores. This sustained signalling plays a critical role in downstream cellular processes, including gene expression regulation, cytoskeletal remodelling, and long-term adaptive responses to mechanical stimuli [92, 176].

This dual response enables Piezo1 to mediate both immediate and prolonged cellular reactions to mechanical stimuli, making it a versatile sensor in various physiological contexts.

4.2 Materials and methods

For the experiments conducted in this chapter, the microfluidic device employed was Chemical Stimulation Device 3, which was developed by me and described in Chapter 2 (Figure 2.9a). In addition, all the experiments were conducted under the Zeiss LSM980 confocal microscope.

4.2.1 Microfluidic device

The meander dimensions of the device used for the experiments of this chapter (Devices 2.9a, 2.9b 2.9c 2.9d) are:

Length= 1 cm

Width= 100 μm

Depth= 50 μm

Mixing profile

The mixing profile of this device was obtained at a flow rate of 100 $\mu\text{L/hr}$ for both the sheath and sample inlets. Imaging was performed using the EVOS M7000 microscope. Fluorescein was administered through the cell sample inlet, and plain DMEM was inserted in the sheath flow inlet. The mixing behaviour was analysed by capturing images at multiple points along the meandering channel.

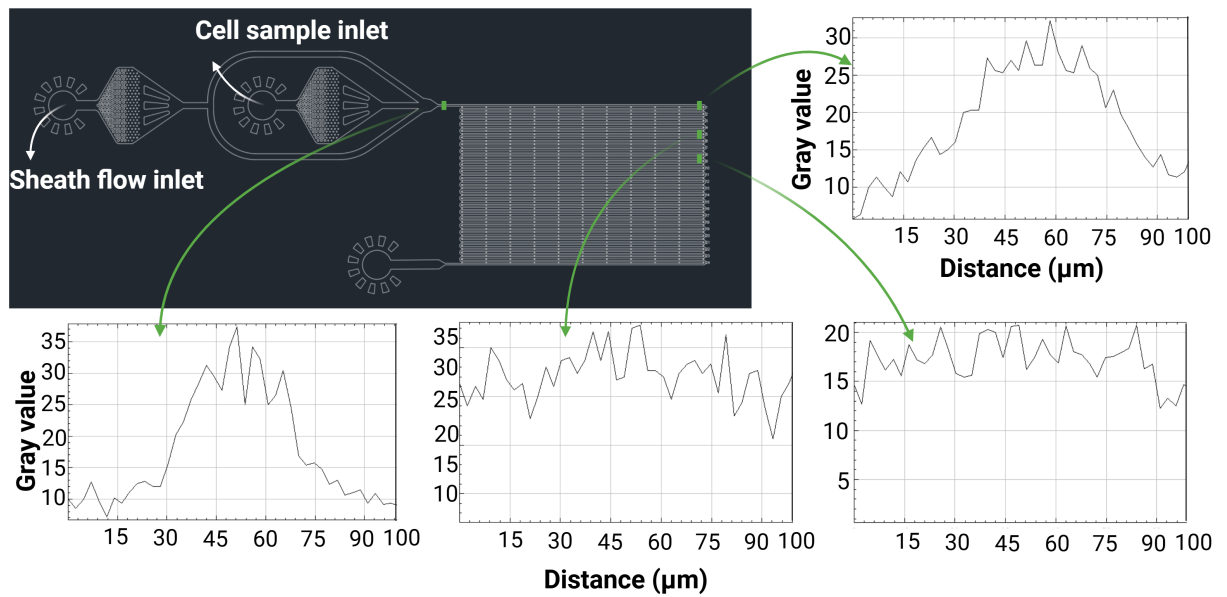


Figure 4.2: The mixing profile of the microfluidic device, corresponding to the image, is shown in the accompanying graphs. The meander channel has a diameter of $100\ \mu\text{m}$, meaning the channel walls correspond to positions 0 and 100 on the graph's x-axis.

4.2.2 Confocal microscope

The Zeiss LSM 980 is a high-resolution confocal laser scanning microscope designed for advanced imaging applications, including live-cell imaging, spectral imaging, and fluorescence correlation spectroscopy. The key difference between a confocal and a conventional microscope lies in the presence of a pinhole in the light path of the former. By adjusting the opening of this pinhole, the collection of out-of-focus fluorescence can be reduced. However, for the experiments of this chapter, this pinhole is kept fully open to ensure that the fluorescent signal of the cells will be collected regardless of their position within the channel's height.

Another key feature of LSM 980 is its versatile acquisition modes, which include:

- **Frame scanning** - where the laser scans a predefined area, generating a complete image.
- **Line scanning** - where the laser scans along a predefined line, capturing intensity variations along that path.
- **Spot scanning** - where the laser remains fixed on a predefined spot, allowing for high-temporal-resolution signal detection.

For the experiments described in this chapter, the spot scanning acquisition mode was used.

Spot scanning in the Zeiss LSM 980

In confocal microscopy, point scanning involves tightly focusing a laser beam onto a diffraction-limited spot, where it remains fixed rather than scanning across a larger area. As fluorescence-emitting samples pass through the laser-illuminated spot, the emitted signal is detected by a photomultiplier tube (PMT). This signal is recorded as a voltage (representing the fluorescence intensity) over time, producing a time-resolved trace (Figure 4.3).

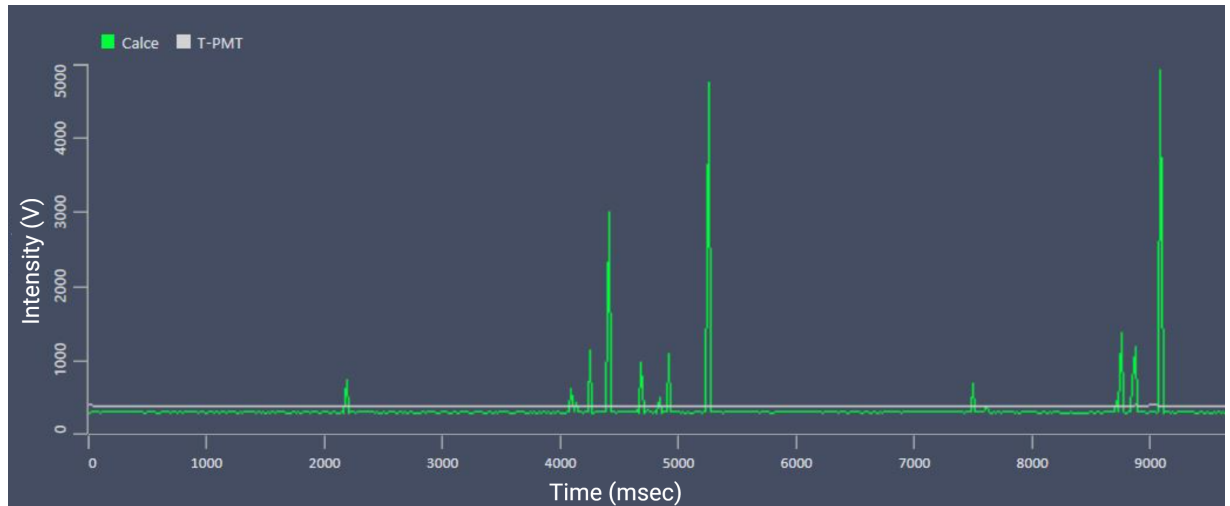


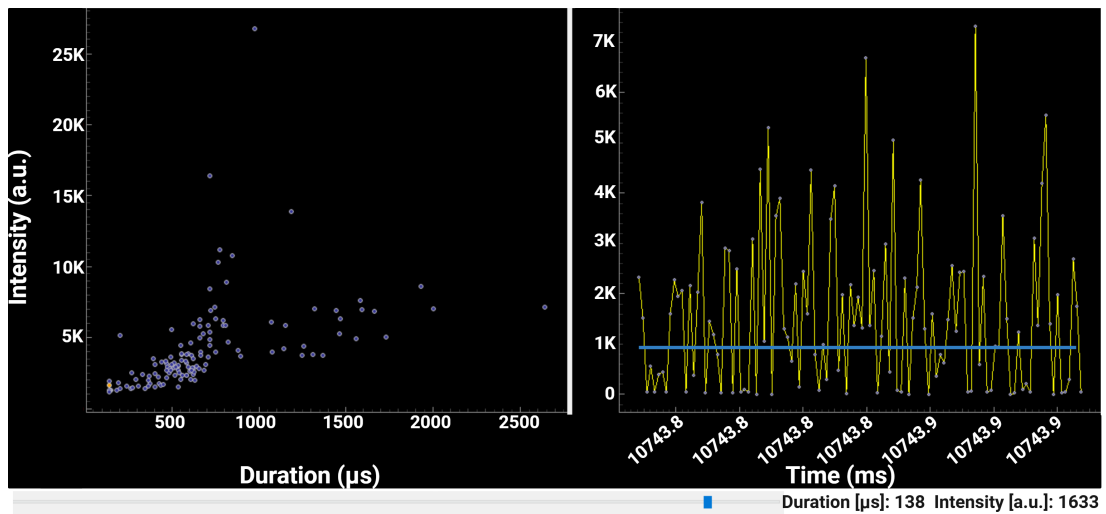
Figure 4.3: Confocal Signal Output.

This method is particularly useful for capturing rapid changes in fluorescence intensity, making it ideal for studying dynamic events in microfluidic systems, single-molecule detection, or fluorescence correlation spectroscopy (FCS).

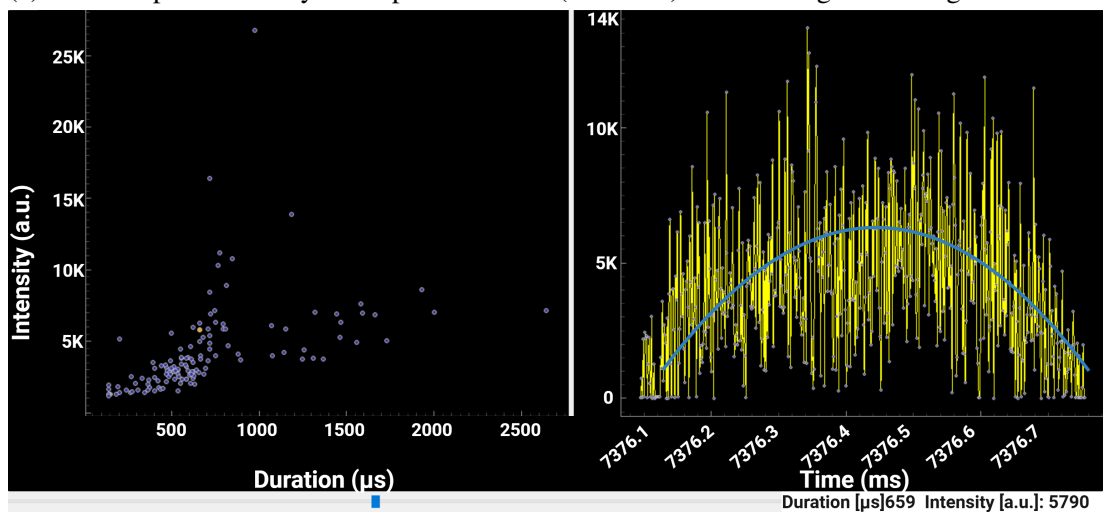
4.2.3 Data filtering

The acquired data were processed through a Python program written by Prof Massimo Vassalli (primary investigator for this PhD project). This data processing provides the duration and amplitude of each peak.

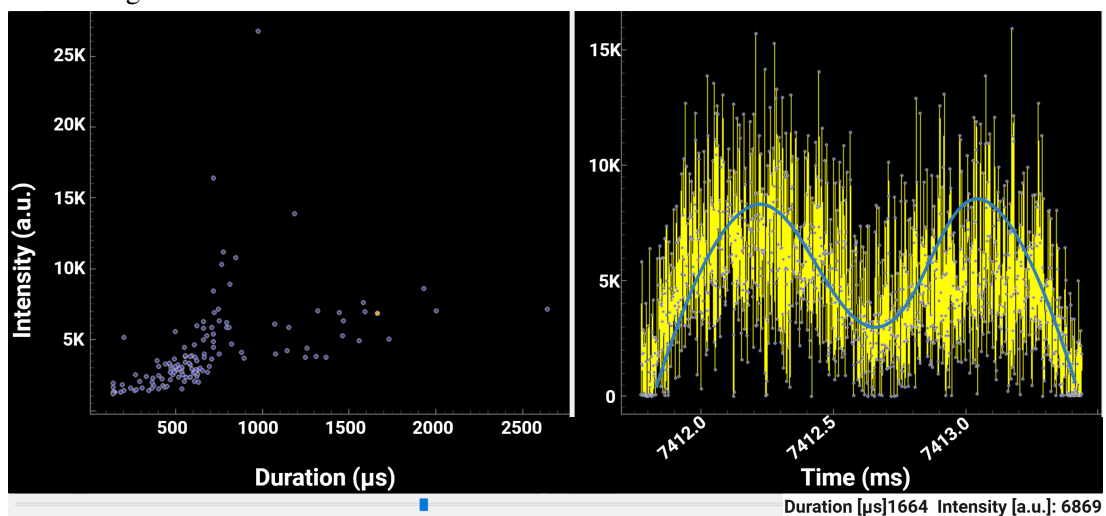
Based on the signal profile in Chapter 3, Figure 3.8, the data in this chapter were sorted by observing the signal shape and peak duration.



(a) No clear peak and very small peak duration (0.1 msec) indicates signal coming from debris



(b) Clear single peak and medium peak duration (0.7 msec) indicating that the signal comes from a single cell.



(c) Two peaks connected, giving a broader signal with a peak duration of 1.6 msec, indicating signal coming from a cell cluster.

Figure 4.4: The data processing provides a scatter plot of the signal intensity over the peak duration of each particle that responds to a stimulation. (a) Signal from debris, (b) Signal from single cell, (c) Signal from cell cluster.

4.2.4 Chemical stimulation

Since the microscope used in this chapter differs from that in Chapter 3, an ATP-based chemical stimulation experiment was performed to verify that the system was functioning as expected using Device 2.9a. As in Chapter 3, HEK293T cells were stained with cal520 following the protocol outlined in Chapter 2 and stimulated with 10 μM ATP. The flow rates at both inlets were set to 100 $\mu\text{L/hr}$, yielding a total flow rate of 200 $\mu\text{L/hr}$. The average and maximum velocities of the cells were then calculated as described below:

$$v_{\text{avg}} = \frac{200 \times 10^{-6} \times 10^{-3} \text{ m}^3}{50 \times 10^{-10} \times 3600 \text{ m}^2 \text{sec}} = \frac{200 \times 10^{-1} \text{ m}}{50 \times 36 \text{ s}} = 11.11 \frac{\text{mm}}{\text{sec}}$$

To calculate the $v_{(\text{max})}$:

$$v_{\text{max}} = 1.5 \times v_{\text{avg}} = 1.5 \times 11.11 = 16.67 \frac{\text{mm}}{\text{sec}}$$

Following this experiment, Yoda1 was administered in the sheath flow, as the chemical stimulant in subsequent experiments to investigate the Piezo1 response.

The positions plotted in both experiments are shown in the following figure (Figure 4.5)

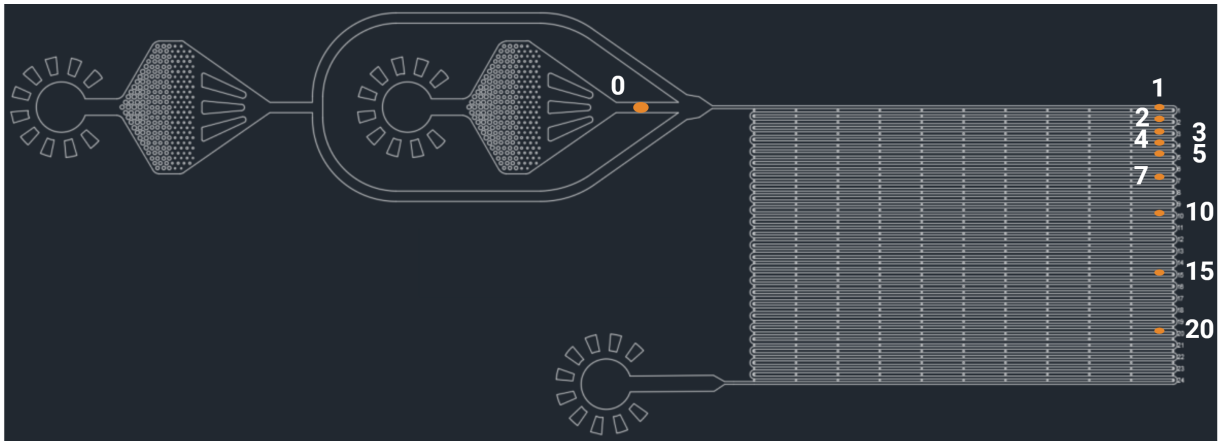


Figure 4.5: The data acquired from the positions highlighted in orange were used at the plots of the chemical stimulation (ATP and Yoda1) experiments.

4.2.5 Mechanical stimulation

Cells from the same cell line (HEK293T) were stained with cal520 (following the protocol in section ??) and subjected to mechanical stress via compression using various microfluidic devices with defined geometries.

Initially, Device 2.9c was employed, featuring three constrictions arranged in a row, each with a width of 10 μm . The flow rates at both inlets were set to 100 $\mu\text{L/hr}$, resulting in a total flow rate

of 200 $\mu\text{L/hr}$. The average and maximum velocities of the cells were calculated as described below:

$$v_{\text{avg}} = \frac{200 \times 10^{-6} \times 10^{-3} \text{ m}^3}{50 \times 10^{-10} \times 3600 \text{ m}^2 \text{ sec}} = \frac{200 \times 10^{-1} \text{ m}}{50 \times 36 \text{ s}} = 11.11 \frac{\text{mm}}{\text{sec}}$$

To calculate the $v_{(\text{max})}$:

$$v_{\text{max}} = 1.5 \times v_{\text{avg}} = 1.5 \times 11.11 = 16.67 \frac{\text{mm}}{\text{sec}}$$

The positions plotted are illustrated in Figure 4.6.

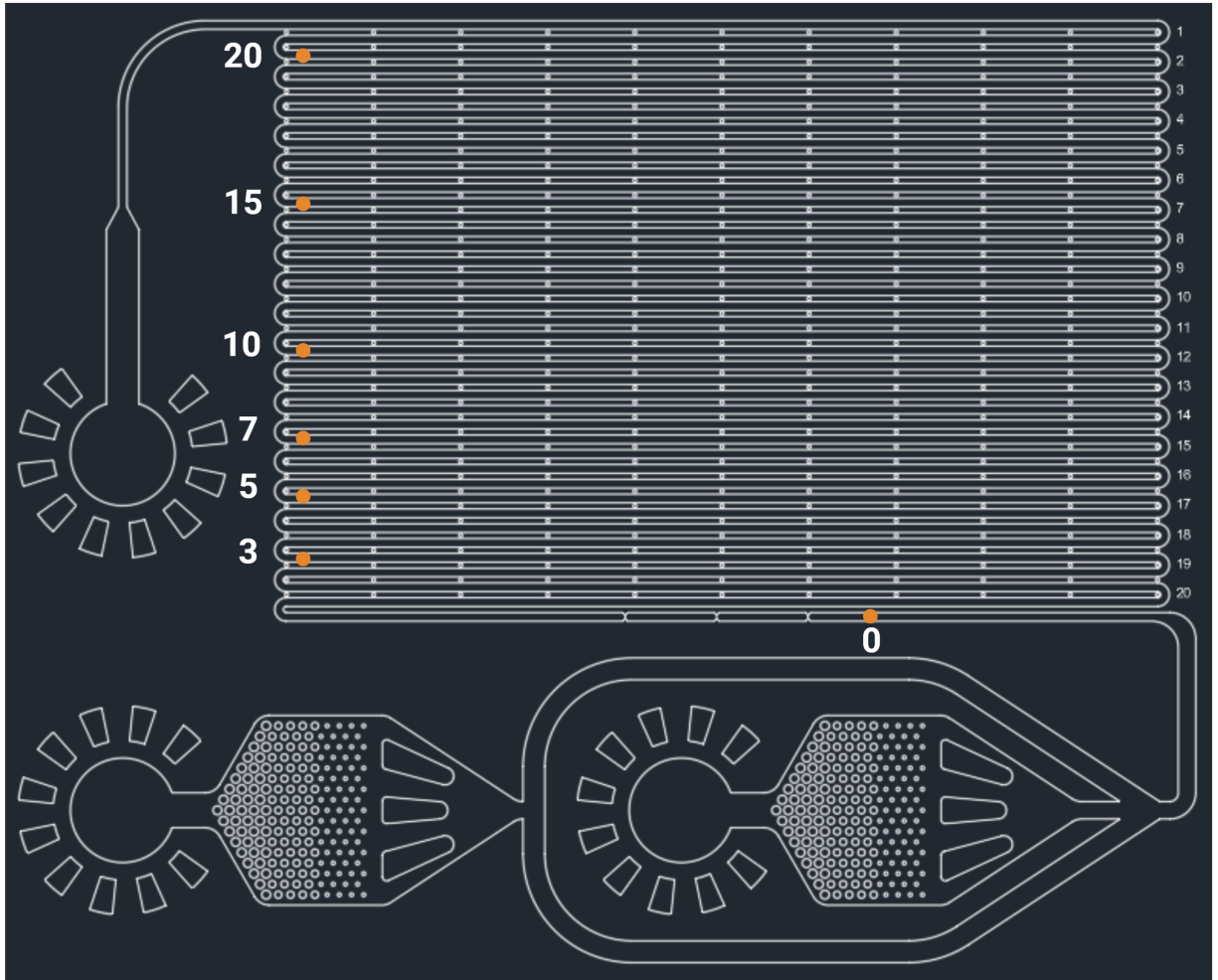


Figure 4.6: The data acquired from the positions highlighted in orange were used in the plot of the mechanical stimulation experiment with this device.

Next, Device 2.9d, featuring three constrictions arranged in a row with a width of 15 μm each, was used. The single inlet flow rate was set to 200 $\mu\text{L/hr}$, resulting in a cell velocity identical to that calculated for the previous device (i.e., 16.67 mm/sec). The plotted positions are presented in Figure 4.7.

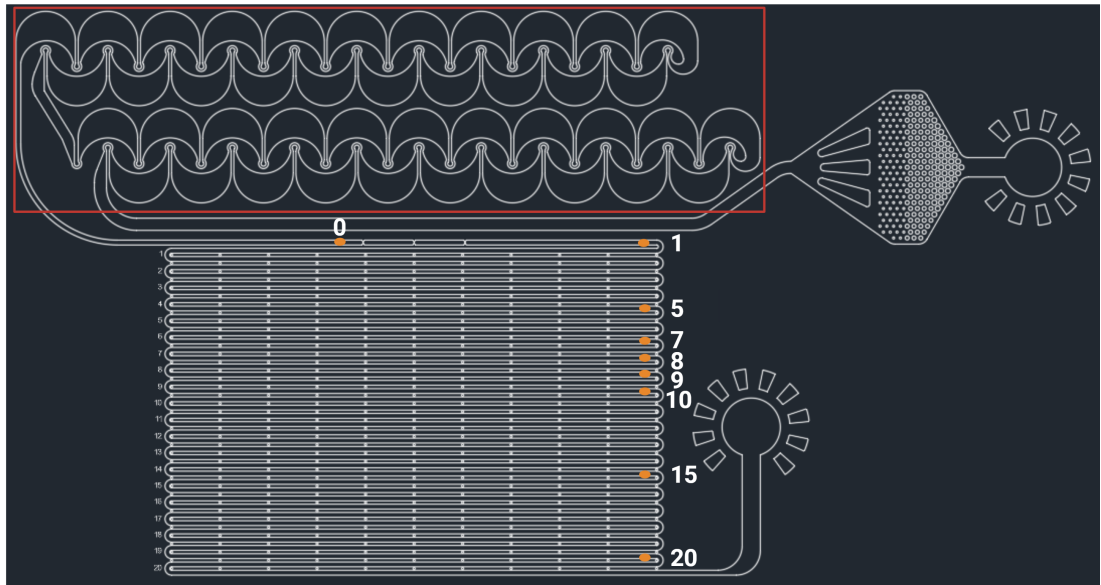


Figure 4.7: The data acquired from the positions highlighted in orange were used in the plot of the mechanical stimulation experiment with this device. The area with the repeated curvatures and narrow channels (highlighted in the red rectangle) is used to align the cells in a single plane without the need of the sheath flow.

Finally, Device 2.9b was employed to compress the cells using the sheath flow alone, without any constrictions along the channel. To achieve cell compression, the sheath flow was set to 200 $\mu\text{L/hr}$ while the sample inlet was maintained at 50 $\mu\text{L/hr}$. In this configuration, the total flow rate increased to 250 $\mu\text{L/hr}$, and the average cell velocity was calculated as follows:

$$v_{\text{avg}} = \frac{250 \times 10^{-6} \times 10^{-3} \text{ m}^3}{50 \times 10^{-10} \times 3600 \text{ m}^2 \text{ sec}} = \frac{250 \times 10^{-1} \text{ m}}{50 \times 36 \text{ s}} = 13.89 \frac{\text{mm}}{\text{sec}}$$

To calculate the $v_{(\text{max})}$:

$$v_{\text{max}} = 1.5 \times v_{\text{avg}} = 1.5 \times 13.89 = 20.84 \frac{\text{mm}}{\text{sec}}$$

The positions used for plotting are shown in Figure 4.8

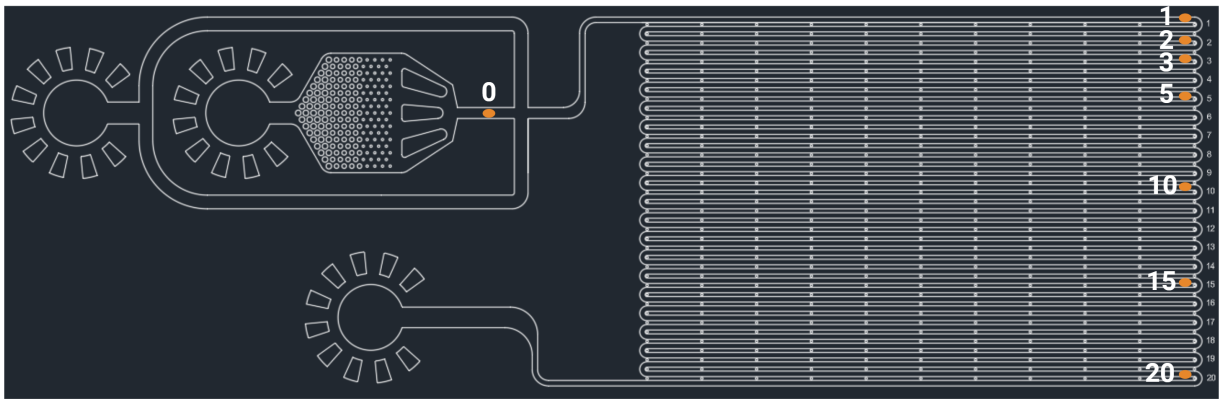


Figure 4.8: The data acquired from the positions highlighted in orange were used in the plot of the mechanical stimulation experiment with this device.

4.3 Results

4.3.1 Chemical stimulation

The chemical stimulation of HEK cells with ATP (Figure 4.9) produced a response trend similar to that observed in Chapter 3 (Figure 3.19).

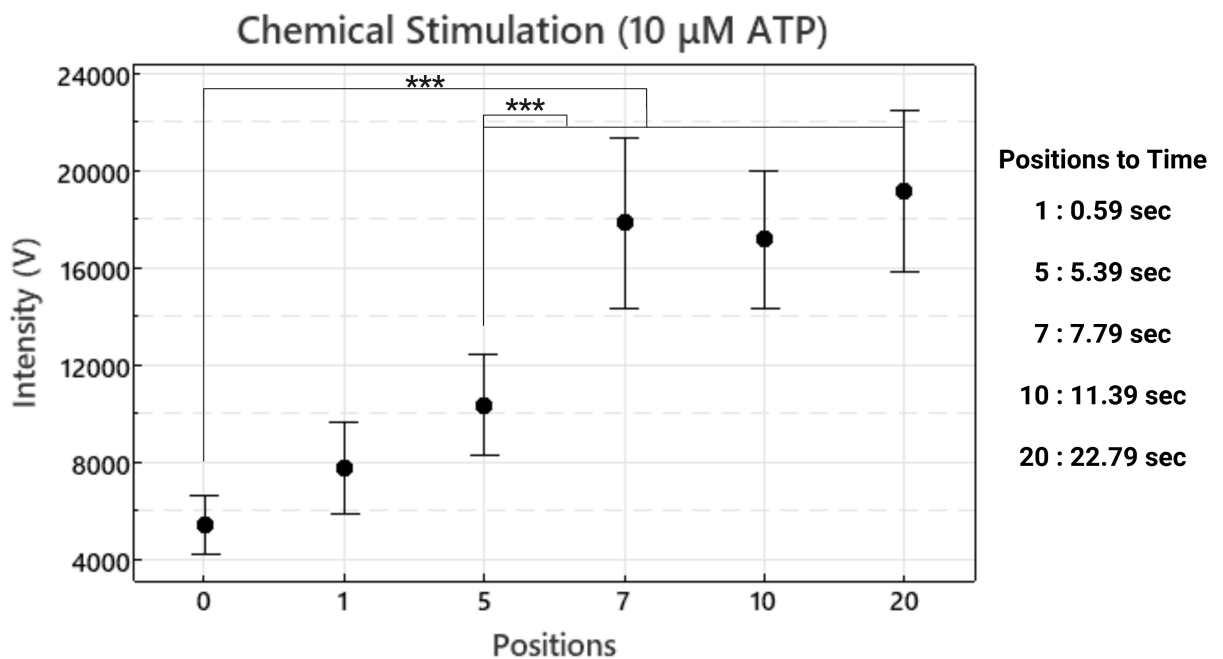


Figure 4.9: Response of HEK293T cells to ATP stimulation as recorded by the lsm980 (***p*-values < 0.001).

Normality of the data from each position was evaluated using Anderson-Darling tests, which indicated a non-normal distribution. Consequently, non-parametric tests (Kruskal-Wallis and Mann-Whitney) assessed statistical significance across different positions. The analysis revealed

that, beyond position five, the cell response was significantly elevated compared to position zero (p-value < 0.001), where the cells were not exposed to the chemical stimulant. Furthermore, after position five, the response increased significantly and then remained relatively constant, with only minor fluctuations (Figure 4.9).

The subsequent stimulation with Yoda1 did not display a consistent trend across the positions. However, a statistically significant increase in cell response was observed at position five, while a significant decrease was detected at position ten. Beyond these points, the cell response remained nearly constant, with only minor fluctuations that were not statistically significant (Figure 4.10).

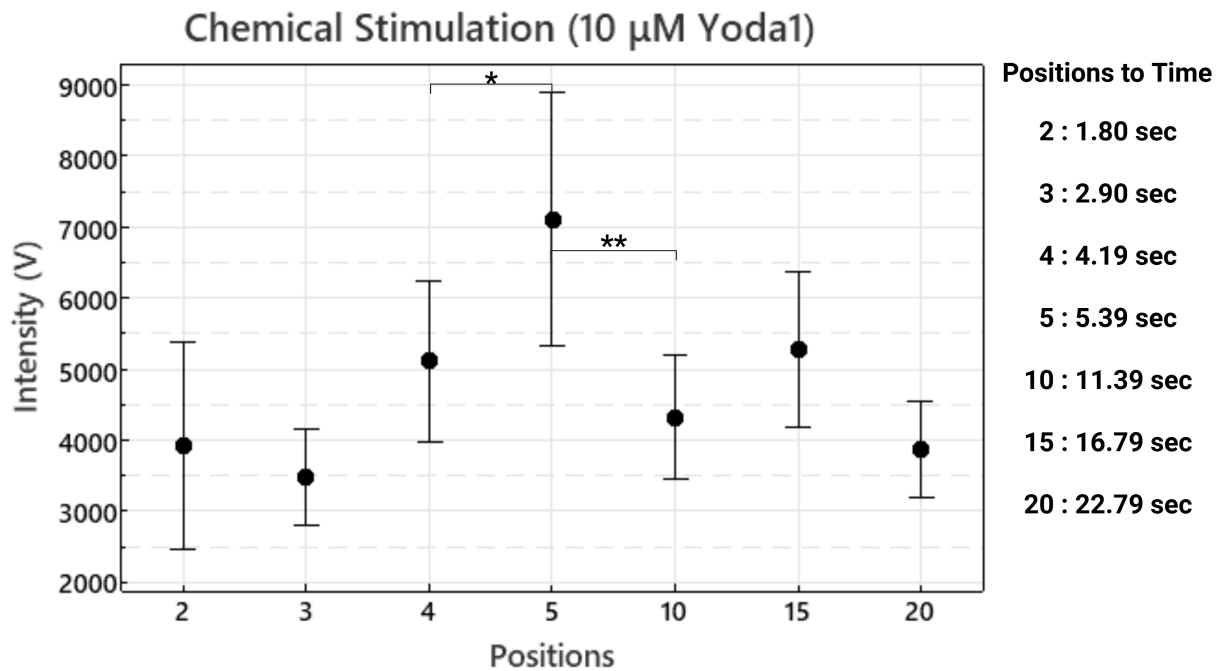


Figure 4.10: Response of HEK293T cells to Yoda1 stimulation as recorded by the lsm980 (*p-values < 0.05, **p-values < 0.005).

Nevertheless, when various concentrations of Yoda1 were administered using the same device, a clear concentration-dependent effect on the cell response was observed. Since the data were found to be non-normally distributed, non-parametric tests (Kruskal-Wallis and Mann-Whitney) assessed statistical significance across different concentrations. Notably, at a concentration of 100 μ M, the cell response declined significantly, which may be attributed to the cytotoxic effects of high levels of Yoda1 (Figure 4.11).

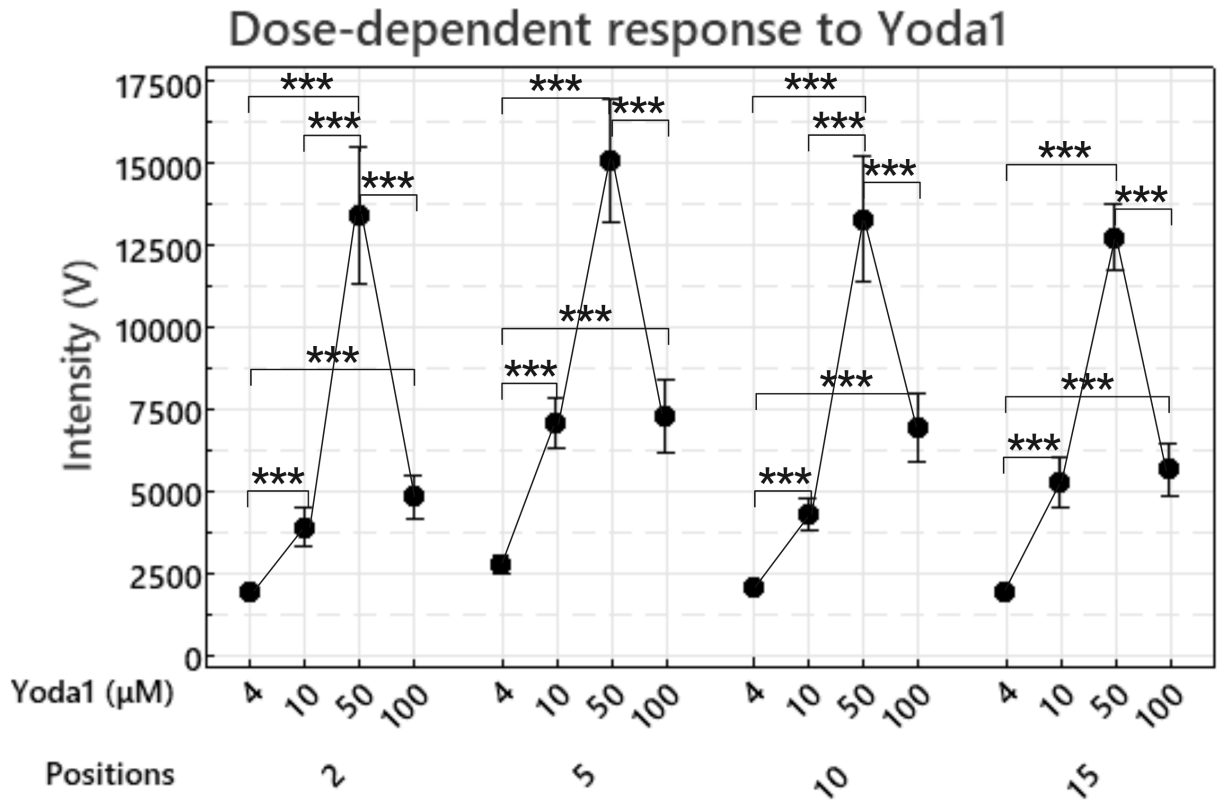


Figure 4.11: Dose-dependent of HEK293T cells to Yoda1 stimulation as recorded by the lsm980 (**p-values < 0.001)

4.3.2 Mechanical stimulation

The data of all the mechanical stimulation experiments were evaluated using Anderson-Darling tests, which indicated a non-normal distribution. Therefore, in the following graphs, the presented statistics are derived from non-parametric statistical tests (Kruskal-Wallis and Mann-Whitney).

The initial mechanical stimulation experiment demonstrated that the cell response exhibited a rapid and pronounced increase approximately 4 seconds after the cells passed through the 10 μm constrictions (Figure)4.12. This elevated response was sustained for roughly 7 seconds, after which a marked decline was observed at position 15 (Figure 4.6). These findings indicate that the mechanical compression imposed by the constrictions induces a transient response, with a notable peak that subsequently diminishes over time.

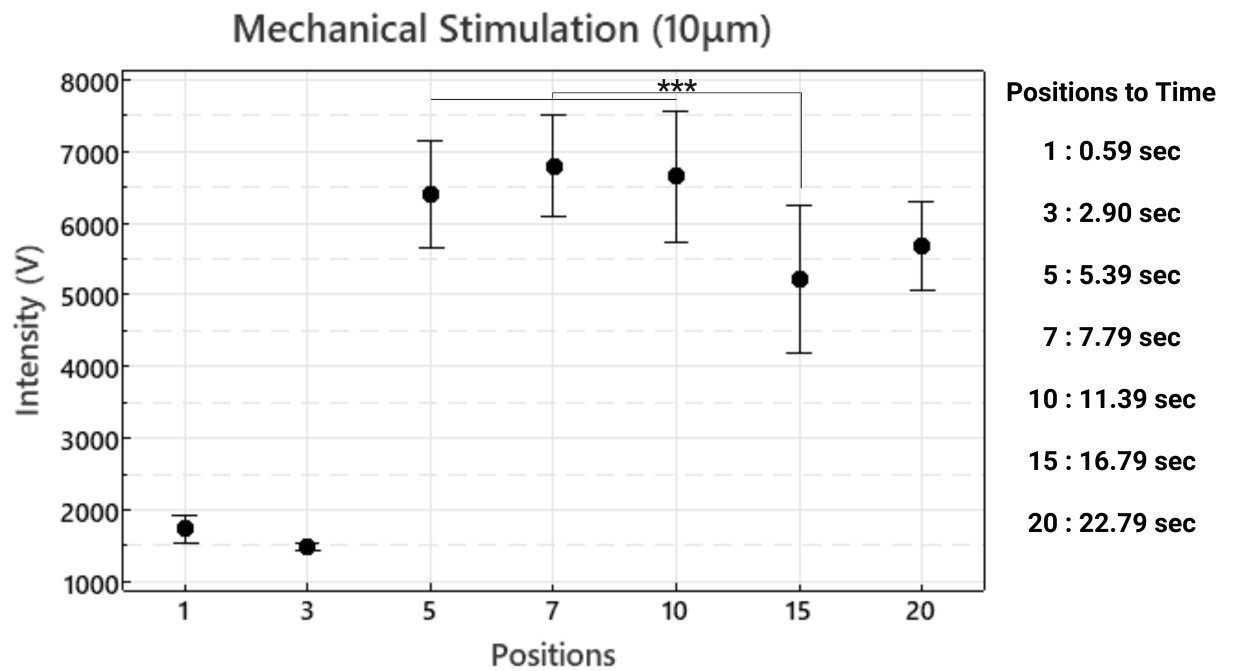


Figure 4.12: Response of HEK293T cells to mechanical stimulation as recorded by the lsm980 (**p-values < 0.001). The three constrictions are located 5mm (0.3 sec) before position 1.

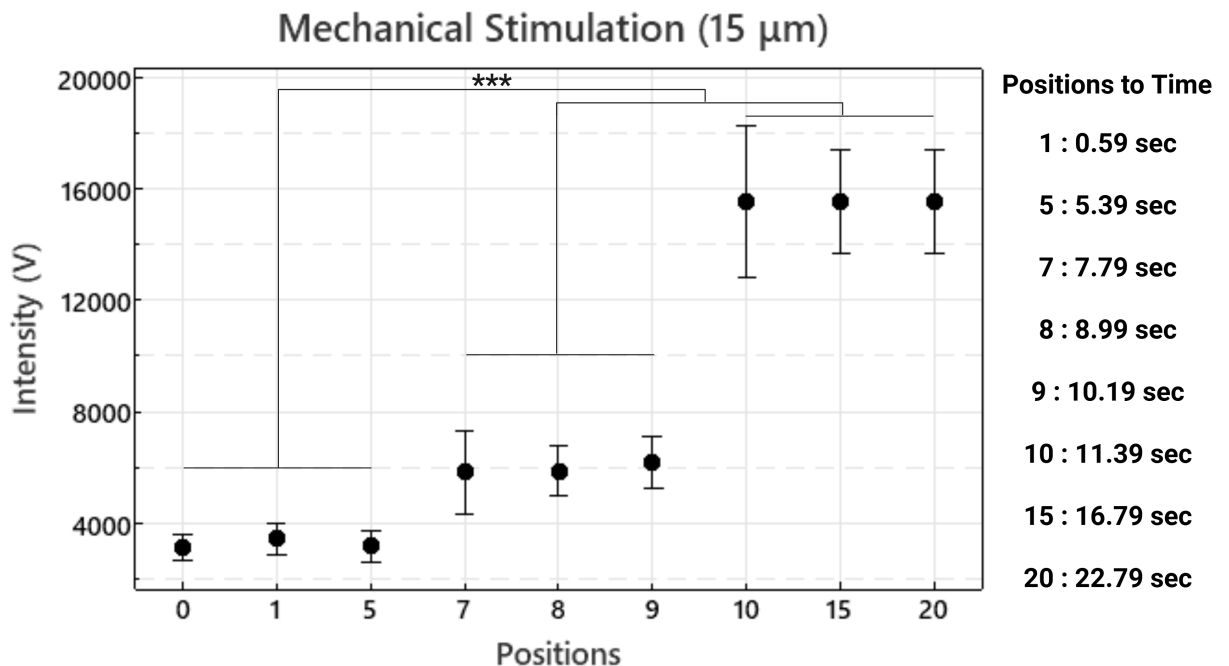


Figure 4.13: Response of HEK293T cells to mechanical stimulation as recorded by the lsm980 (**p-values < 0.001).

The second device (Figure 2.9d) used for mechanical stimulation differed not only in having wider constrictions (15 μ m) but also in its focusing method, as it entirely lacked sheath flows for cell sample alignment.

Initially, at positions 0, 1, and 5, (Figure 4.7) the response remains low and relatively constant (Figure 4.13). However, a significant increase in intensity is observed at position 7, which continues to rise until position 9. Statistical analysis confirms a highly significant difference in response between the early and later positions (p -value < 0.001). Beyond position 10, the intensity stabilises, maintaining a consistent level with minor fluctuations up to position 20. These results suggest that mechanical stimulation through the constrictions elicits a delayed but sustained response in the cells, which reaches a plateau after an initial steep increase.

The results indicate that the cellular response is significantly higher ($\approx 16,000$ V) when passing through the wider $15 \mu\text{m}$ constrictions (Figure 4.13) compared to the response observed with the $10 \mu\text{m}$ constrictions ($\approx 7,000$ V) (Figure 4.12). This discrepancy may be due to excessive compression within the narrower constrictions, which could have caused cellular damage and thereby reduced the observed response despite stimulation. However, this explanation remains hypothetical since cell viability was not assessed after passage through the constrictions. Additionally, the presence of sheath flow in the first device could have introduced an additional mechanical stimulus, further influencing the observed cellular response.

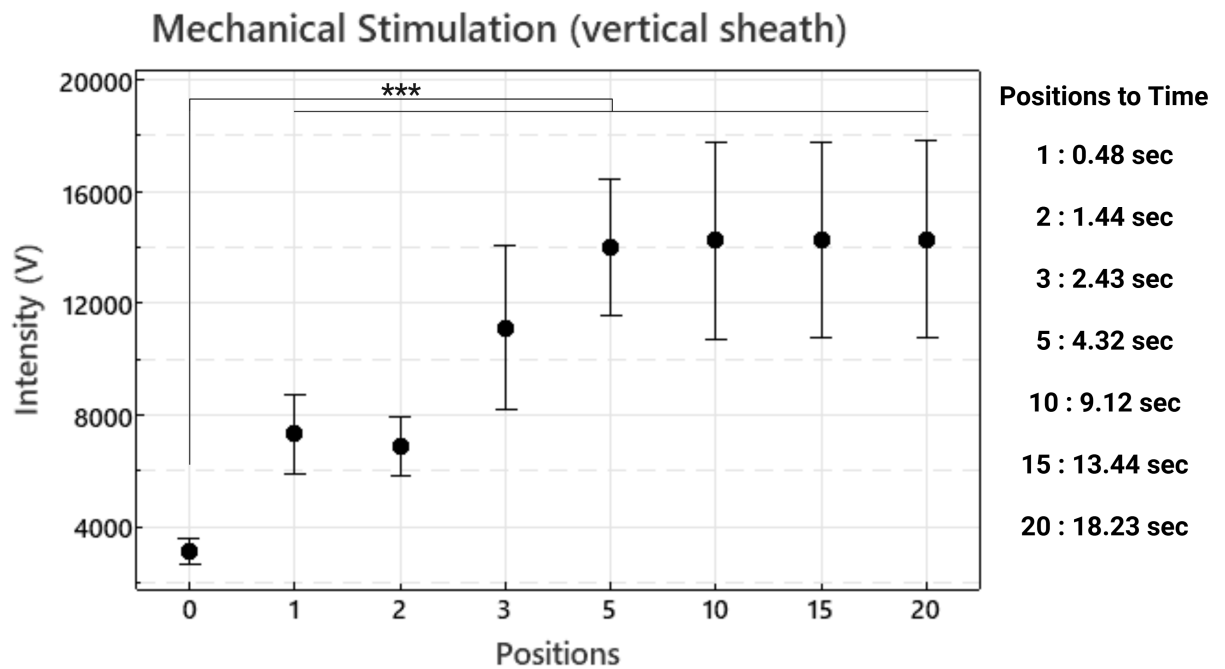


Figure 4.14: Response of HEK293T cells to mechanical stimulation as recorded by the lsm980 (** p -values < 0.001). The term "vertical sheath" refers to the sheath flow intersecting the central cell stream perpendicularly, effectively compressing the cells at the point of intersection.

Finally, the device with a perpendicular sheath flow relative to the cell sample flow was employed. The results closely align with those obtained from the device featuring $15 \mu\text{m}$ constrictions, further reinforcing the notion that gentler mechanical stimulation elicits a stronger cellular response.

Statistical analysis revealed that beyond the junction point, where cells undergo compression due to the sheath flows, the increase in response is statistically significant across all observed positions. Moreover, following the initial rise at position five, the cell response reaches a plateau, indicating a sustained level of activation.

4.4 Discussion

This chapter investigated the mechanosensitive behaviour of suspended HEK293T cells subjected to controlled chemical and mechanical stimuli in microfluidic devices, using real-time fluorescence detection via a photomultiplier tube (PMT). The results confirm that mechanosensitive calcium signalling can be resolved in a high-throughput (HT), flow-based assay and provide insights into how cells respond to different types and magnitudes of stimulation under non-adherent conditions.

4.4.1 Biological Interpretation and Comparison with Literature

ATP stimulation evoked robust and reproducible calcium influx in flowing HEK293T cells, in agreement with established mechanisms where ATP activates P2Y receptors, initiating IP₃-mediated calcium release from internal stores [72]. In contrast to adherent assays where ATP diffusion leads to spatially heterogeneous stimulation [165], the use of microfluidic flow ensures rapid and uniform exposure of each suspended cell to the same ATP concentration. This enhances the reproducibility of population-level data and avoids local gradient effects, which are common in static cultures.

Yoda1, an agonist of the Piezo1 channel, elicited a dose-dependent response only when its concentration was varied. A marked reduction in signalling was observed at 100 μM , likely due to cytotoxic effects or receptor desensitisation. This observation aligns with findings by Davies et al. (2019), who reported significant cytotoxicity at higher Yoda1 concentrations [54].

Mechanical stimulation via constriction channels showed that cells subjected to 15 μm constrictions generated higher voltage signals ($\approx 16,000$ V) compared to the 10 μm device ($\approx 7,000$ V). This suggests that gentler compression is more effective in triggering Ca²⁺ influx. In contrast, excessive compression (in narrower channels), combined with shear stress (from the sheath flow), may damage cellular membranes or disrupt calcium homeostasis, thus diminishing the response. This interpretation aligns with studies showing reduced viability or altered signalling following excessive deformation [98, 195, 200]. Moreover, in the device utilising perpendicular sheath flow, voltage signals were comparable to the 15 μm constriction response, supporting the idea that more moderate mechanical stimuli are optimal.

4.4.2 Technical Limitations and Drawbacks

Despite the promising results in assessing cellular mechanosensitivity in HT, several technical limitations were identified. One critical issue is the lack of quantification of the mechanical forces experienced by the cells as they pass through the microfluidic constrictions. The magnitude and spatial distribution of the compressive stress are not explicitly measured, making it difficult to directly compare the mechanical stimulation used here with those reported in other studies. To accurately benchmark these results, computational simulations such as finite element analysis (FEA) or computational fluid dynamics (CFD) modelling would be necessary to estimate the local stress and strain experienced by the cells. Without this, the mechanistic interpretation remains qualitative.

Additionally, the viability of cells post-stimulation was not assessed. This is particularly important in the 10 μm constriction device, where the observed reduction in calcium signalling could be due not only to excessive mechanical stress but also to compromised cell integrity. Without post-assay viability evaluation, such as using Trypan Blue exclusion or live/dead staining assays like calcein-AM and propidium iodide, it is not possible to distinguish whether the reduced signal arises from a biologically relevant attenuation of the calcium response or simply from cellular damage or death.

4.4.3 Suggested Improvements and Future Directions

To improve the system's reliability and interpretability, several refinements can be considered. First, the development of sheath-free device designs could help eliminate the vertical sheath flow, which currently introduces shear stress that may confound the interpretation of results. By adopting alternatives such as inertial focusing or tailored microchannel geometries to align cells within the flow, it would be possible to reduce or eliminate the contribution of shear, thereby allowing a clearer separation of the nature of the mechanical stimulation effects on calcium signalling. Inertial focusing techniques, for instance, utilise the balance of inertial lift forces and Dean drag forces within microfluidic channels to focus particles or cells without the need for sheath flow [205]. A study by Al-Halhouli et al. (2019) demonstrated enhanced inertial focusing by integrating trapezoidal microchambers in spiral microfluidic channels, achieving a cell focusing efficiency of 99.1 % for *Saccharomyces cerevisiae* yeast cells [15]. Similarly, Kim et al. (2016) explored inertial focusing in non-rectangular cross-section microchannels, finding that the broken symmetry of non-equilateral triangular channels led to the shifting of focusing positions with varying Reynolds numbers [101].

Second, incorporating computational modelling approaches, such as computational fluid dynamics (CFD) or finite element analysis, would allow for the quantitative estimation of the

mechanical forces cells experience as they pass through the constrictions. These force estimates would enable more direct comparisons with the mechanobiology literature and help define the thresholds of mechanical loading that activate signalling without causing cellular damage.

Finally, integrating a downstream module for viability assessment would allow for real-time or post-assay validation of cell health, using methods such as Trypan Blue exclusion or fluorescence-based live/dead staining. This would ensure that observed variations in signal are due to functional cellular responses rather than artefacts arising from mechanical injury or compromised membrane integrity.

This method addresses a significant gap in mechanobiology by enabling high-throughput assessment of dynamic Ca^{2+} responses in suspended cells, a capability not achievable with conventional adherent assays or FACS-based platforms. The system shows strong potential in several areas. One application is drug screening aimed at targeting mechanotransduction pathways, including the evaluation of pharmacological agents that influence Piezo1, TRPV4, or downstream Ca^{2+} signalling. Another promising use is in mechanophenotyping heterogeneous cell populations; by correlating mechanical response profiles with the PMT readouts, it becomes possible to identify and analyse subpopulations with distinct mechano-responsiveness, similar to approaches demonstrated in deformability cytometry systems [144]. This capability is especially useful in studying complex mixtures such as stem cells, cancer cells, or immune cells, where different subsets may exhibit unique mechano-signalling profiles. Ultimately, it opens up the possibility of sorting or isolating mechanosensitive cell types for further study or therapeutic targeting.

4.5 Conclusion

These findings highlight the importance of both the magnitude and mode of mechanical stimulation in modulating cellular responses. Excessive compression may lead to cellular damage, dampening the response, while controlled mechanical forces effectively activate mechanosensitive pathways. It was demonstrated that both chemical and mechanical stimulation trigger responses in HEK293T cells, with the nature and intensity of the stimulus playing a crucial role in determining cellular behaviour. ATP stimulation produced a consistent increasing response trend, whereas Yoda1-induced responses varied across positions but followed a dose-dependent pattern. Mechanical compression through microfluidic constrictions effectively triggered mechanosensitive responses, with wider constrictions and gentler stimulation yielding stronger responses.

Overall, this study demonstrates that calcium signalling in suspended HEK293T cells can be

reliably stimulated and measured in flow using a PMT-based microfluidic platform. The results are technically promising, but additional simulation, viability validation, and design refinement are required to make the platform suitable for predictive, high-throughput mechanobiology screening.

Chapter 5

Stem Cell Ageing and Mechanosensitivity

This chapter explores various methods for ageing hMSCs and investigates how their mechanosensitivity is affected. Chemical and mechanical stimulation are applied to the aged populations to explore the potential reversal of age-related effects. The following sections provide a brief overview of ageing with a particular interest in stem cell ageing. The bioreactor used to stimulate the hMSCs mechanically is also described.

5.1 Introduction

5.1.1 Ageing

Ageing is a chronic and multifactorial process that leads to cumulative degenerative changes in biological systems. It is characterised by irreversible and progressive deterioration at the cellular and tissue levels, particularly affecting the structural and functional properties of cells. Among the most impacted domains is cellular mechanobiology, which includes alterations in cytoskeletal organisation, mechanosensitive signalling pathways, intracellular force generation, and the overall ability of cells to detect and respond to mechanical cues via mechanotransduction. These impairments contribute to dysfunctions across various systems, including the cardiovascular, musculoskeletal, immune, and integumentary systems [21].

Significantly, these mechanobiological alterations also extend to intracellular calcium dynamics. Mechanosensitive calcium channels, such as Piezo1 and TRP channels, exhibit age-related changes in expression and gating behaviour, leading to dysregulated Ca^{2+} influx in response to mechanical stimuli [137]. In parallel, age-associated remodelling of mitochondria and the endoplasmic reticulum—two critical organelles responsible for calcium storage, buffering, and release—further impairs intracellular Ca^{2+} homeostasis [132, 142]. Together, these changes exacerbate the cellular vulnerability to mechanical stress and may underlie several age-associated pathologies.

5.1.2 Stem cell ageing and consequences

A critical component of the ageing process is the ageing of stem cells, which significantly affects their regenerative capabilities. Stem cells are essential for maintaining tissue homeostasis and repairing damaged tissues. However, as organisms age, there is increasing evidence to suggest that stem cell mechanosensitivity decreases and their functionality declines, leading to a diminished ability to repair and regenerate tissues [119]. This decline contributes to various age-related disorders [14], further exacerbating the physiological decline associated with ageing [132, 142].

Hematopoietic stem cells (HSCs), for example, become less mechanosensitive with age, decreasing their ability to regenerate new blood cells [171]. This loss of mechanosensitivity has been attributed to changes in the stiffness of the bone marrow microenvironment, where HSCs reside [194]. The bone marrow microenvironment is a complex network of cells, proteins, and other molecules that provides the necessary support and signals for the proper function of HSCs [202]. Age-related changes in the microenvironment, such as alterations in the extracellular matrix and cellular composition, can negatively impact the ability of HSCs to sense and respond to mechanical cues [105, 114]. Muscle stem cells (MuSCs) also show a decline in mechanosensitivity with age, contributing to impaired muscle regeneration. Research has shown that changes in the extracellular matrix surrounding the MuSCs are responsible for this loss of mechanosensitivity. The extracellular matrix is a complex network of proteins and other molecules that provides cells with structural support and signalling cues. Age-related changes in the extracellular matrix can lead to alterations in its composition and stiffness, which can negatively impact the ability of MuSCs to sense mechanical signals in their environment [30, 84].

The question that arises is: What is the mechanism behind cellular ageing? Several factors influence the molecular basis of ageing. Among the most significant factors is DNA damage due to the accumulation of mutations, which results in genomic instability [179]. This DNA damage can be induced by reactive oxygen species (ROS), ultraviolet radiation, environmental mutagens, and various chemicals [107], and it is associated with numerous diseases, including cancers, cardiovascular diseases, autoimmune disorders, and other age-related conditions [203]. Another important regulator of the ageing mechanism is telomeres, which generally protect the DNA integrity, and it has been observed that their length decreases with age [36, 170]. Additionally, changes in epigenetic modifications, including methylation and DNA demethylation or histones and histone deacetylation, have been shown to impact stem cell ageing and alter their functions, particularly through interactions with metabolic mechanisms [73, 161]. However, the reversibility of epigenetic alterations has attracted interest for its potential therapeutic applications in improving life quality in old age and treating ageing-related diseases, especially cancer and cardiovascular diseases [14].

5.1.3 Ageing indicators

Stem cell ageing is associated with alterations in cell cycle dynamics and metabolic activity, which together impact both proliferation and regenerative capacity. As stem cells age, they often show an increased tendency to arrest in the G0/G1 phase due to factors such as accumulated DNA damage, telomere shortening, and the upregulation of cell cycle inhibitors like P16 and P21 [6]. This results in a lower proportion of actively cycling cells and a diminished proliferative capacity. Enhanced activation of cell cycle checkpoints in response to stress or DNA damage further slows cell division, compounding the decline in regenerative potential [106].

In parallel, metabolic activity, as measured by the Alamar Blue assay, declines with age. This assay reflects the reducing power of cellular enzymes and, by extension, mitochondrial function. In aged stem cells, mitochondrial efficiency decreases, reducing ATP production and overall metabolic output. Additionally, increased oxidative stress associated with ageing damages mitochondrial components, further impairing metabolism. A shift in metabolic pathways—such as a transition from oxidative phosphorylation to glycolysis—can also occur, contributing to the lower fluorescence signals observed in the Alamar Blue assay [122]. These changes in cell cycle regulation and metabolic function collectively underscore the reduced regenerative capacity of aged stem cells.

5.1.4 Nanokicking

Nanokicking is a technique that applies high-frequency, nanoscale mechanical vibrations to cells, typically using piezoelectric actuators. It was initially developed to induce osteogenesis in mesenchymal stem cells (MSCs) by mimicking the mechanical cues that occur in bone remodelling. The method is based on delivering low-amplitude (typically in the nanometer range) and high-frequency (often in the kilohertz range) vibrations to adherent cells, influencing their mechanotransduction pathways [139].

Nanokicking plays a significant role in cellular mechanotransduction by stimulating mechanosensitive ion channels such as Piezo1 and Piezo2, thereby influencing intracellular signalling pathways and gene expression. This nanoscale vibrational stimulation has been shown to promote mesenchymal stem cell (MSC) differentiation, particularly into osteoblasts, without the need for chemical inducers, as demonstrated in studies by Tsimbouri et al. [140, 178]. Moreover, emerging evidence suggests that nanokicking may influence cellular ageing by modulating cytoskeletal organisation and affecting cell cycle progression [143]. Beyond its well-documented role in osteogenesis, nanokicking is increasingly being explored for its broader applications in regenerative medicine, highlighting its potential to impact diverse areas of cell biology and therapeutic development [93].

Nanokicking, as a mechanotransductive stimulus, is particularly relevant to this study as it offers a non-chemical approach to modulating both cellular ageing and mechanosensitivity in mesenchymal stem cells (MSCs). Investigating the potential of nanokicking to reverse or modulate ageing-related changes in MSCs could provide valuable insights into its application for maintaining stem cell function and enhancing their responsiveness to mechanical cues. This study explores whether nanokicking can mitigate senescence-induced alterations in mechanosensitivity, particularly through regulating Piezo1 expression and activity.

5.2 Materials and methods

Both physical and chemical methods were employed to induce cellular senescence in mesenchymal stem cells (MSCs).

5.2.1 Physical methods for ageing induction

The physical methods involved repeated cell passaging and prolonged culturing. These approaches are known to contribute to cellular ageing and senescence [107]. Repeated cell passaging can lead to the accumulation of cellular stress and genetic alterations, resulting in a decline in cell proliferation and hence the regenerative potential of MSCs [14, 103].

Cells were seeded in 12 and 48-well plates at a density of 2,000 cells per cm^2 and maintained in culture for five weeks, with media changes performed twice a week. The Alamar Blue assay was conducted weekly to assess cell growth and metabolic activity over time. After five weeks, cells were harvested and analysed by flow cytometry to evaluate cell cycle distribution. Additionally, an In-Cell Western (ICW) analysis was performed to quantify Piezo1 expression.

Similarly, ten flasks were subjected to weekly passaging to assess the effects of serial passaging on cellular ageing. The Alamar Blue assay was performed weekly to monitor cell growth and metabolic activity throughout the experiment. At the end of each week, cells from two flasks were harvested for analysis, including flow cytometry to evaluate cell cycle distribution and ICW to quantify Piezo1 expression, as described before.

These experiments aimed to determine which of the two physical approaches—prolonged culturing or regular passaging—more effectively induces senescence through cell cycle arrest. Additionally, the study sought to examine the impact of cellular ageing on mechanosensitivity, with a specific focus on Piezo1 expression.

5.2.2 Chemical methods for ageing induction

In addition to physical methods, chemical agents were employed to induce senescence in MSCs. These included MS275, a histone deacetylase (HDAC) inhibitor, as well as tumour necrosis factor-alpha (TNF- α) and actinomycin D. MS275 has been shown to promote cellular ageing by altering gene expression patterns through epigenetic modifications [149]. TNF- α , a pro-inflammatory cytokine, has been implicated in the induction of senescence by triggering inflammatory signalling pathways and oxidative stress. Actinomycin D, an inhibitor of RNA synthesis, has been used to induce senescence by disrupting transcriptional activity and promoting DNA damage responses. Collectively, these chemical agents were utilised to explore different pathways of senescence induction in MSCs [58, 149].

Similarly to the physical methods, cells were seeded in 12- and 48-well plates at a density of 2,000 cells per cm^2 , with four plates allocated to each condition. The chemical treatments were administered under specific conditions: MS-275 was applied at a concentration of 1.5 μM and maintained in culture for three days, while TNF- α was added at 10 ng/mL and incubated for the same duration. In contrast, Actinomycin D was introduced at 0.5 $\mu\text{g/mL}$ but remained in the culture for only three hours. Following the chemical treatments, two plates from each condition were subjected to nanokicking for seven days. Yoda1 was added at a concentration of 2 μM to one non-nanokicked plate and one nanokicked plate for 24 hours.

Flow cytometry was conducted for all experimental conditions to evaluate the cell cycle status. Additionally, the expression of various mechanosensitive and senescence-associated proteins was assessed using ICW, while gene expression levels were quantified through real-time qPCR.

The protocols followed for all the tests conducted in this chapter are described in Chapter ref Ch3.

5.2.3 Nanokicking bioreactor

For the mechanical stimulation of the cells in this chapter, a nanokicking bioreactor was used (Figure 5.1). The bioreactor's surface with dimensions 130 \times 178 was designed to facilitate two well plates (Corning, NY). It incorporated low-profile piezo actuators (PL088.30, Physik Instrumente, Karlsruhe, Germany) with a large attachment area to ensure effective mechanical stimulation. To secure the well plates, the upper platform featured magnetic attachments, while 3 mm thick magnetic sheets were affixed to the underside of the well plates before their placement on the nanokicker [178].

The magnetic flux at the surface of these magnets is measured at 700 gauss (0.07 T), which

is considered too low as a static field to impact cellular function significantly. However, since these magnets are configured as Halbach arrays, their magnetism is concentrated on the side facing the bioreactor, leaving the opposite side—where the cell culture is located—mostly unaffected. As a result, any residual magnetic fields reaching the cells are expected to be minimal [178].

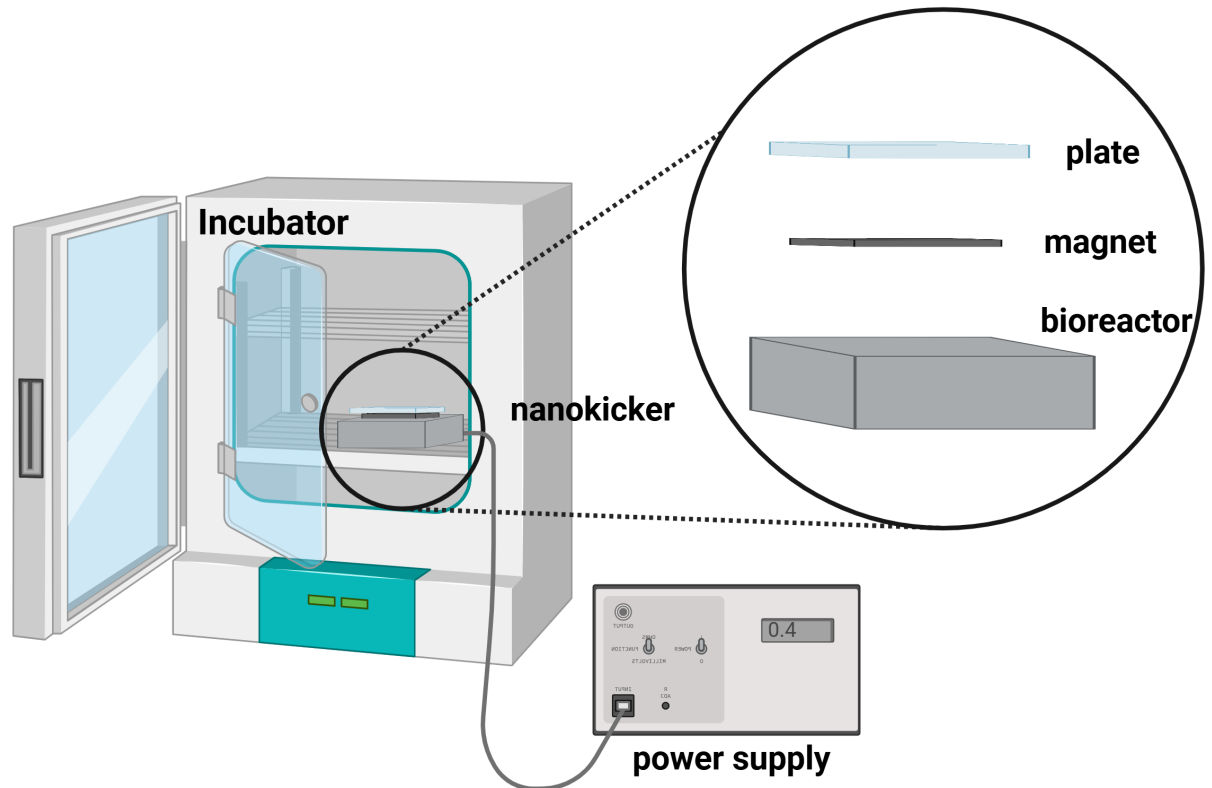


Figure 5.1: Schematic illustration of the nanokicker bioreactor and experimental setup. The nanokicker bioreactor is placed on a shelf inside the incubator and is connected to an external power supply. A magnet attached beneath the well plate secures it to the bioreactor, ensuring stable mechanical stimulation during the experiment. (Created in BioRender.com).

Interferometric measurements

Laser interferometry is a precise optical technique used to measure small displacements, surface irregularities, refractive index changes, and vibrations by exploiting the principle of interference between coherent laser beams.

To quantify the vibrational amplitude of the nanokicker platform, a laser interferometry system was employed, following previously established methodologies [46, 89, 178]. The experimental setup consisted of a USB laser interferometer (Model SP-S, SIOS Messtechnik GmbH, Ilmenau, Germany), which was mounted on a stable optical frame, ensuring precise alignment and minimal external interference.

A 3 mm-thick magnetic sheet (NeoFlex Flexible Neodymium Magnetic Sheet, 3M, MN, USA) was affixed to the underside of each well plate to ensure secure attachment to the nanokicker bioreactor and to transfer the vibrations inside the plate. This magnetic attachment helped maintain stability during vibration, preventing unwanted movement that could introduce measurement artefacts. The well plates (one 12-well plate and one 48-well plate) were thoroughly cleaned with 70% ethanol and allowed to dry before placement on the nanokicker to eliminate dust or debris that could interfere with laser reflection. The prepared well plates were placed on the top surface of the nanokicker, ensuring that the magnetic attachments were aligned correctly for secure fixation.

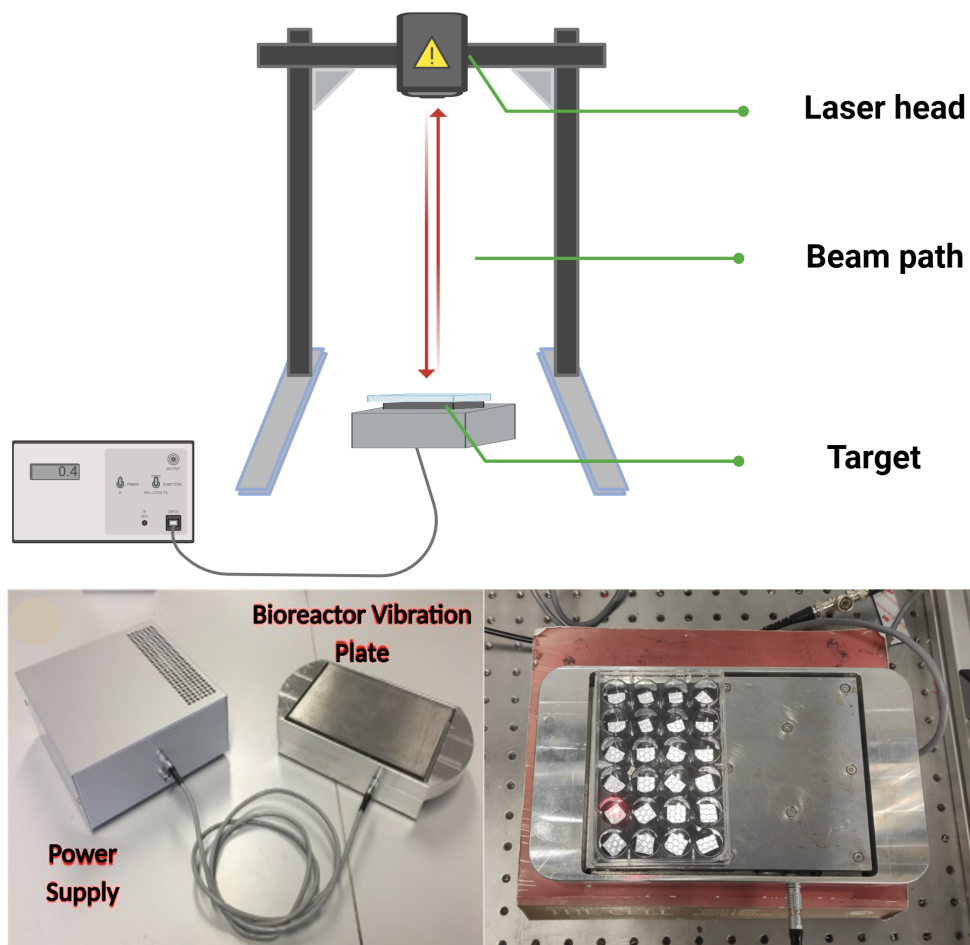


Figure 5.2: Schematic illustration of the laser interferometry setup for precision measurement of nanoscale displacements. (Created in BioRender.com).

Reflective tape was added in each well, and the laser beam was directed perpendicularly onto the surface of the nanokicker bioreactor, which was vibrating at a predefined frequency (1kHz), the same that has been in previous studies to differentiate MSCs towards osteogenic phenotype [178]. As the surface oscillated, it induced variations in the optical path length of the reflected laser beam (Figure 5.2). These variations resulted in changes in the interference pattern when

the reflected beam was combined with a reference beam within the interferometer. The interferometer detected these phase shifts, allowing for the precise quantification of nanoscale displacements. Five measurements were taken for each well of the well plates

The PhD student Eva Bohti conducted the measurements, and the raw data obtained from the interferometry measurements were processed using INFAS software, which provided real-time displacement curves and frequency domain analyses. The interferometer was calibrated before each measurement session to ensure accuracy and reproducibility. All measurements were performed in a controlled environment to minimise external vibrations and thermal fluctuations that could affect the readings.

The data analysis was conducted by me, and the results for the well-plates tested in this system are presented in the following table (Table 5.1):

Well plate	average displacement (nm)	STD (nm)
12-well plate	32.2	3.5
48-well plate	30.8	1.9

Table 5.1: Measurements produced in a range of culture well-plates used in the experiments at 1 kHz. Data were acquired for each well of the 12- and 48-well plates. The results are illustrated in the form of mean \pm SD.

This methodology ensured that the vibrational amplitudes applied to the mesenchymal stem cells (MSCs) were accurately characterised, allowing for precise control over the mechanical stimulation parameters in subsequent biological experiments.

5.3 Results

5.3.1 Physical methods for ageing induction

Flow cytometry analysis was performed to assess cell cycle status in each experimental condition, following the protocol detailed in subsection 2.3.2.

The graph in Figure 5.3 depicts cells' distribution across the cell cycle phases (G1, S, and G2) in different culturing periods. The x-axis represents different time points (day 7, day 14, etc.), whereas the y-axis indicates the percentage of cells in each phase. It was observed that most cells remained in the G1 phase throughout the experiment, which is typical for a proliferating population. The S phase, representing DNA synthesis, appears more prominent at earlier time points, particularly on day 7 and day 14, but declines at later time points. Meanwhile, the G2 phase remained relatively small across all conditions, with only slight variations.

When comparing all conditions, a clear trend emerges in which prolonged culturing appears more effective in inducing senescence than regular passaging. Across the time points, a gradual and dramatic decline in the S phase is observed, indicating a reduction in DNA replication as the cells age. While both passage-based ageing and prolonged culturing lead to an accumulation of cells in G1 and a decrease in proliferation, the most pronounced effect is seen in the "day 35 long" condition. This condition exhibits a statistically significant reduction in S phase activity compared to day 35 (Figure 5.4) and the highest proportion of cells arrested in G1, strongly suggesting a more advanced state of senescence.

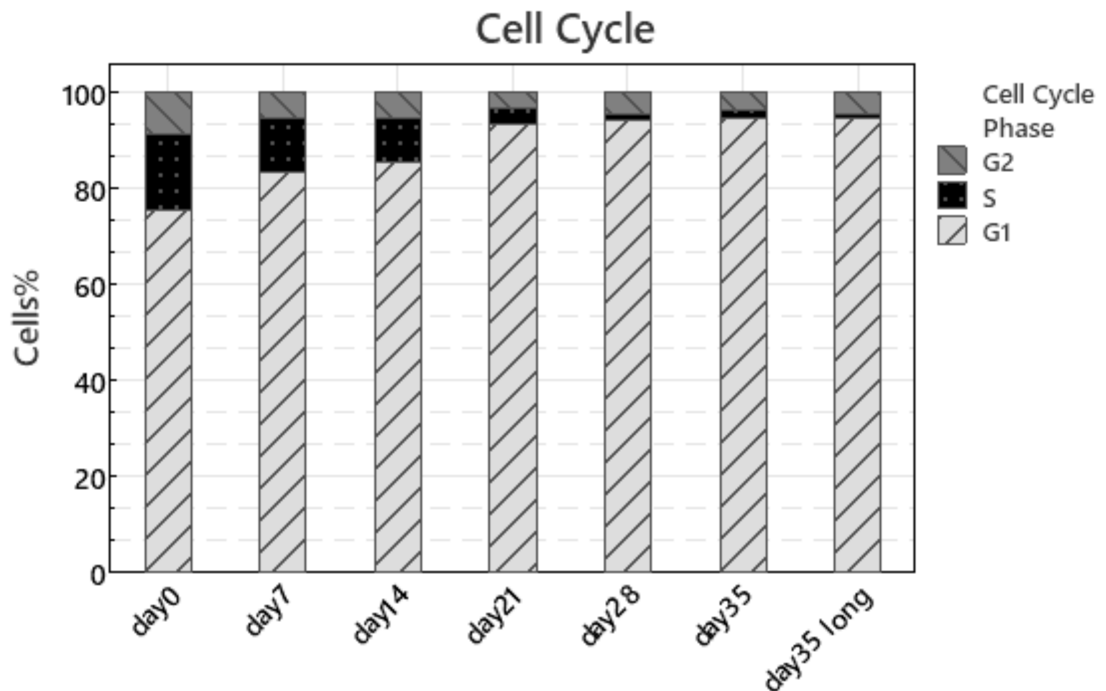


Figure 5.3: Flow Cytometry to assess the cell cycle arrest of the different cell sample conditions.

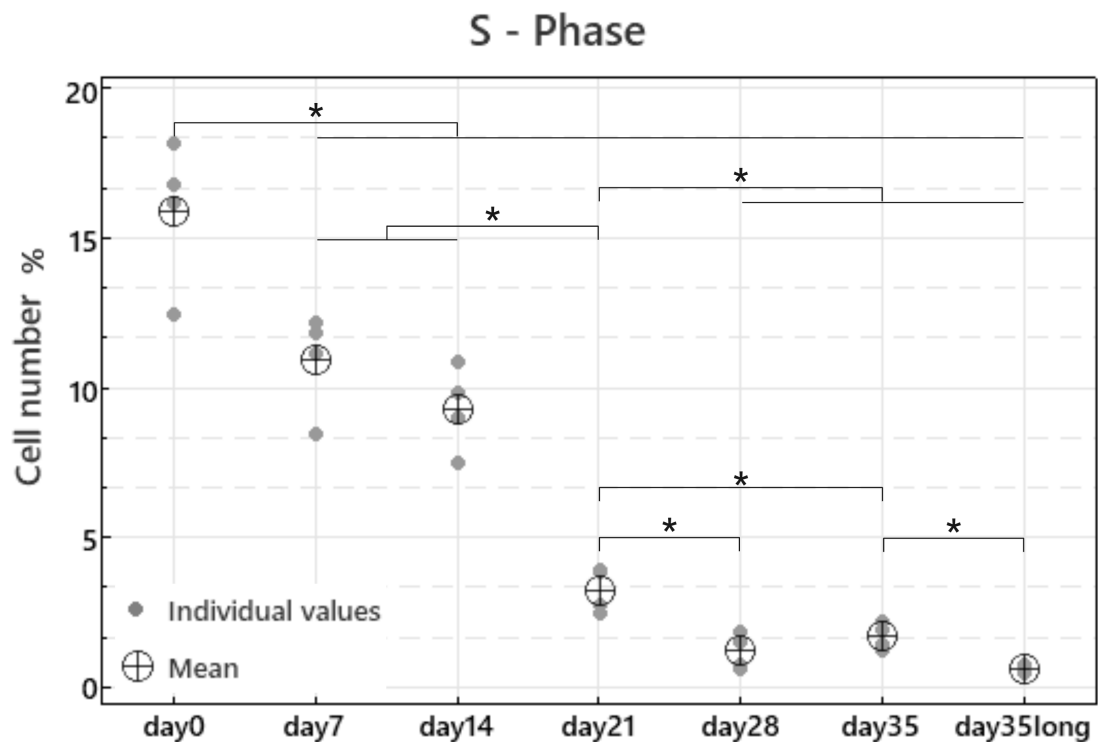


Figure 5.4: Comparison of the S-phase of cell cycle, among the different culturing time points (*p-values < 0.05).

In contrast, the regularly passaged cells at day 35 show only a modest increase in G2 arrest and maintain a slightly higher proportion of cells in S phase, indicating that some level of proliferation persists. This suggests that while repeated passaging contributes to cellular ageing, it is less efficient in driving full senescence than prolonged culturing. Thus, the data support the conclusion that extended culture duration, rather than serial passaging, is the most effective method for inducing cellular senescence and arresting the cell cycle.

Since prolonged culturing was identified as the most effective physical method for inducing senescence in MSCs, an Alamar Blue test was conducted at all stages of the prolonged culture, up to five weeks, to evaluate metabolic activity. The protocol followed for this test is described in the subsection 2.3.1.

This graph (Figure 5.5) represents the percentage of Alamar Blue reduction over time in MSCs subjected to prolonged culturing. Alamar Blue reduction indicates cellular metabolic activity, with higher reduction percentages reflecting greater metabolic function.

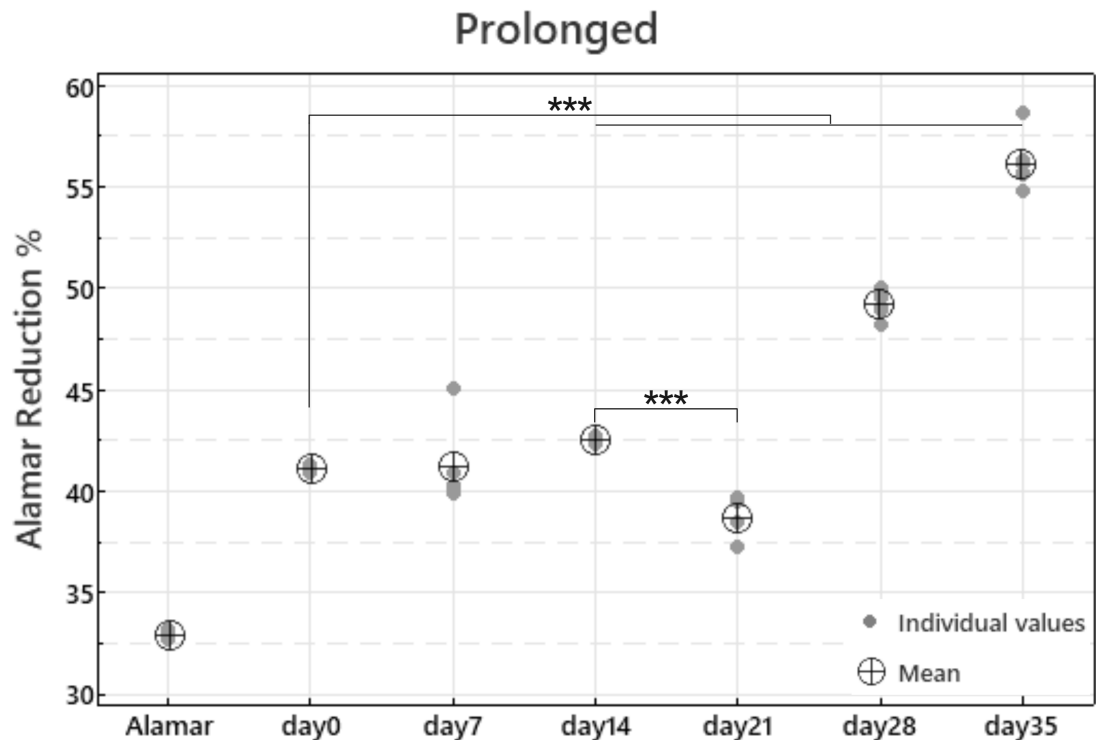


Figure 5.5: Alamar Blue assay shows the effect of prolonged culturing on MSCs metabolic activity (***) p-values < 0.005).

Initially, the metabolic activity appears relatively stable, with minor fluctuations observed between day 0 and day 21. However, a notable increase in Alamar reduction occurs after day 21, peaking at day 35. Since the Alamar Blue reduction percentage has not been normalised to cell number, this increase at days 28 and 35 can likely be attributed to the higher number of cells present due to the extended culture duration. As the culture progresses, cell density naturally increases, leading to a greater cumulative metabolic activity, which may not accurately reflect the metabolic state of individual cells. This makes it challenging to correlate the rise in Alamar reduction with cellular senescence directly.

On the other hand, the decrease in metabolic activity observed at day 21 is more indicative of cells undergoing senescence. A decline in Alamar Blue reduction at this stage suggests that a portion of the cell population has entered a state of growth arrest, characteristic of senescence, where cellular metabolism slows down. This reduction is more reflective of a true shift in cell function rather than simply a difference in cell number. However, to draw more definitive conclusions from the Alamar Blue assay, it would have been important to normalise the fluorescence signal to actual cell number to distinguish between metabolic decline per cell versus reduced cell proliferation.

5.3.2 Chemical methods for ageing induction

Cells treated with Actinomycin D did not survive, leading to the disposal of those samples. Since MS-275 and TNF- α treatments were administered for three days, a separate control sample was incubated under the same conditions for three days without any treatment to serve as a baseline for comparison.

The following graph (Figure 5.6) illustrates the distribution of cells across different phases of the cell cycle (G1, S, and G2) under the various treatments.

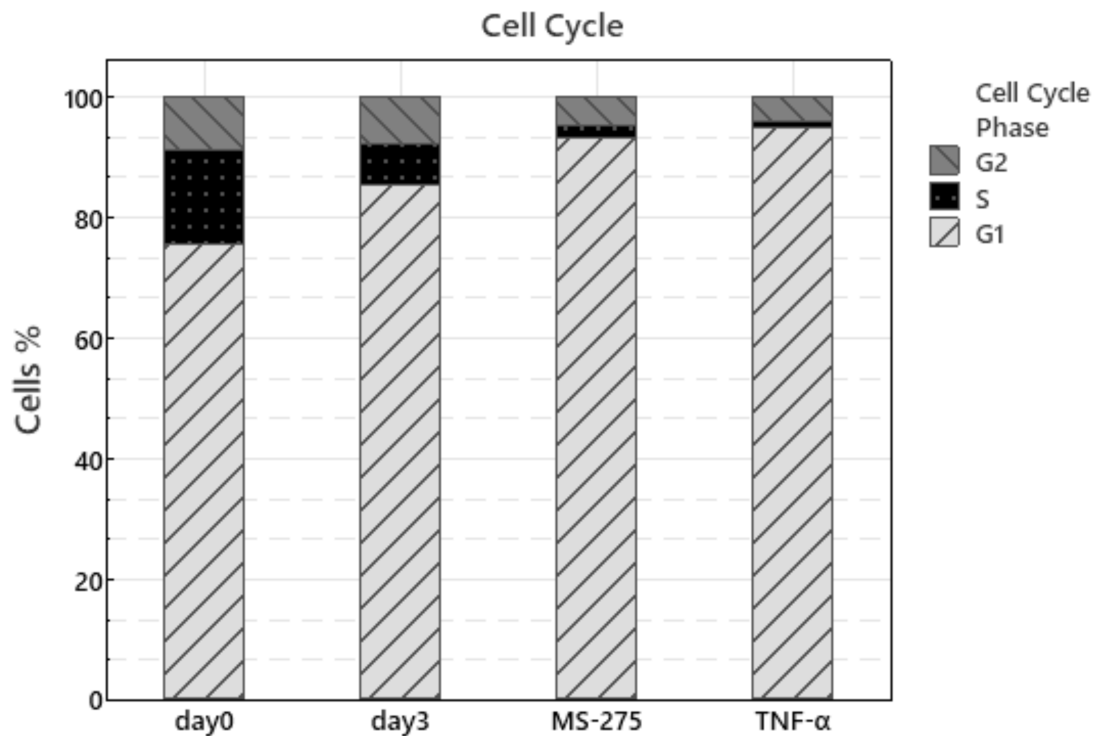


Figure 5.6: Flow Cytometry to assess the cell cycle arrest of the different cell sample conditions. The chemical treatments (MS-275 and TNF- α) are applied to cell cultures on day 0.

On day three, compared to day zero, there is an increase in the G1 phase and a significant decrease in the S phase, indicating a decline in the cells' proliferative capacity (Figure 5.6). This trend becomes more pronounced in the MS-275 and TNF- α conditions. Both treatments result in a statistically significant reduction of the S phase (Figure 5.7) and a greater accumulation of cells in the G1 phase, showing a decrease in proliferation, potentially indicating the initiation of senescence. TNF- α exhibits a slightly higher G1 percentage than MS-275, indicating a stronger senescence-inducing effect. However, since TNF- α may also trigger inflammatory responses alongside senescence, MS-275 could be considered a more targeted approach for inducing cellular ageing.

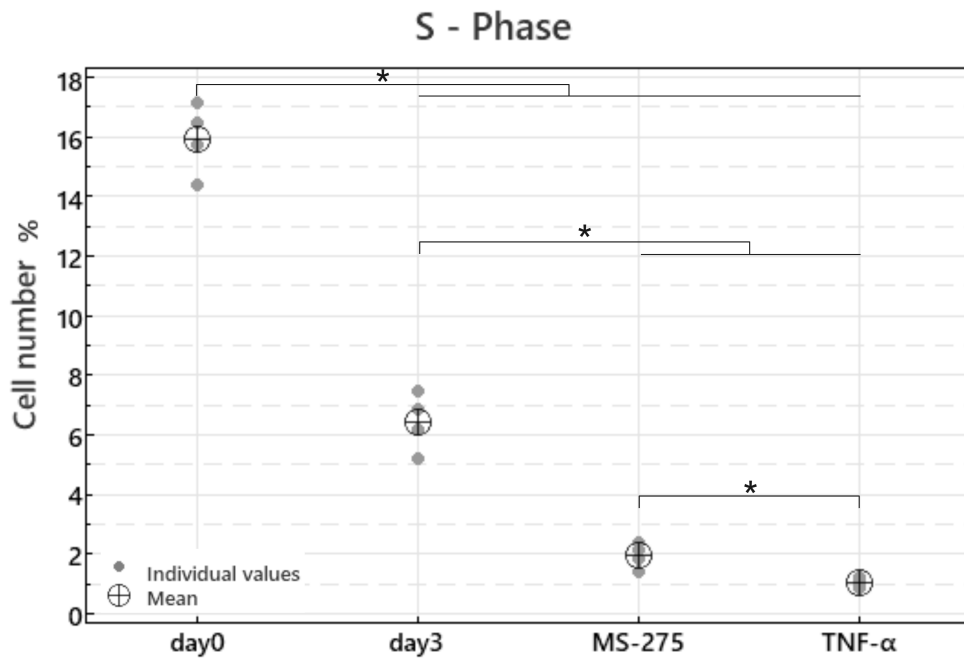


Figure 5.7: Comparison of the S-phase of cell cycle, among the different culturing time points (*p-values < 0.05).

The first graph (5.8) presents the qPCR analysis of P16 and P53, markers of cellular senescence, along with Piezo1, a mechanosensitivity marker, across different conditions. P16 expression remains relatively stable after 28 days of culturing. However, in the TNF- α condition, P16 levels decrease significantly, following the same trend as P53.

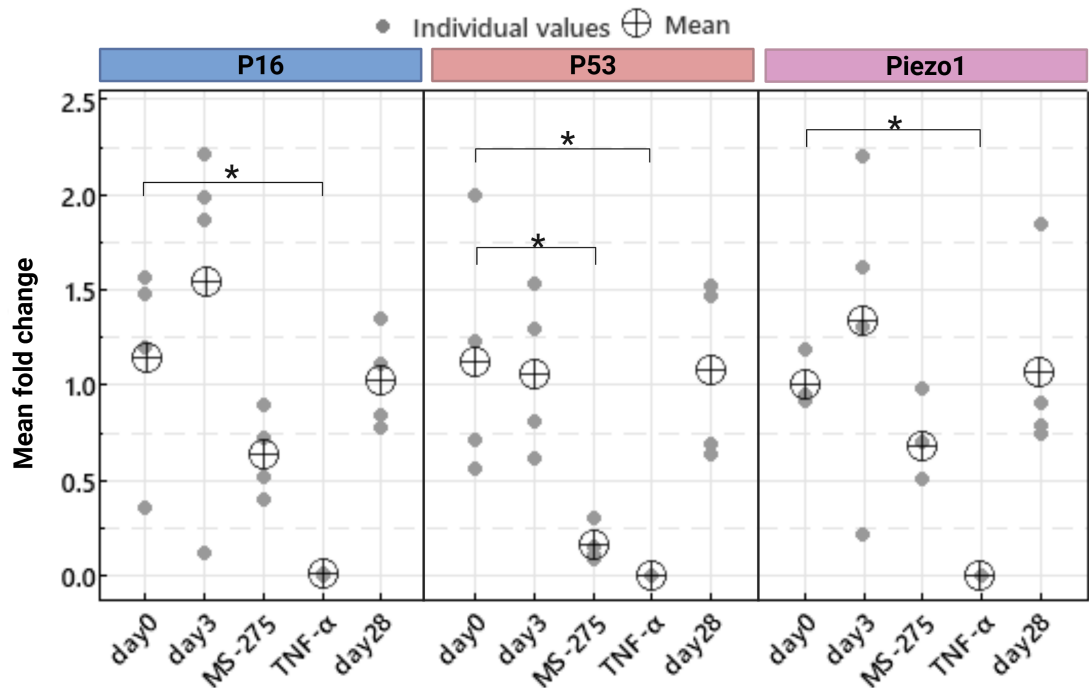


Figure 5.8: qPCR results show the effect of physical and chemical treatments on the expression of senescence markers (P16, P53) and mechanosensitivity genes (Piezo1) (*p-values < 0.05).

This decrease in senescence markers in the aged groups could be attributed to transcriptional repression due to specific signalling pathways activated by the ageing inducer, particularly $\text{TNF-}\alpha$. While $\text{TNF-}\alpha$ is pro-inflammatory and can induce senescence, its signalling pathways (e.g., $\text{NF-}\kappa\text{B}$, MAPK) are incredibly complex and context-dependent. It's likely that certain downstream transcriptional factors or co-repressors activated by $\text{TNF-}\alpha$ could directly bind to or recruit epigenetic machinery to the promoter regions of the *CDKN2A* (P16) and *TP53* (P53) genes, leading to their transcriptional silencing or downregulation [24, 96]. This might not be a general senescence-inducing mechanism but rather a specific transcriptional response to intense $\text{TNF-}\alpha$ signalling, leading to epigenetic modifications that suppress gene expression.

Additionally, Piezo1 expression declines in the chemically treated samples, particularly in the $\text{TNF-}\alpha$ condition, suggesting a potential reduction in mechanosensitivity in aged cells.

The second graph (5.9) displays ICW assay data measuring P16, P21 (a downstream effector often transcriptionally regulated by P53) [65], Piezo1, and TRPV1 protein levels.

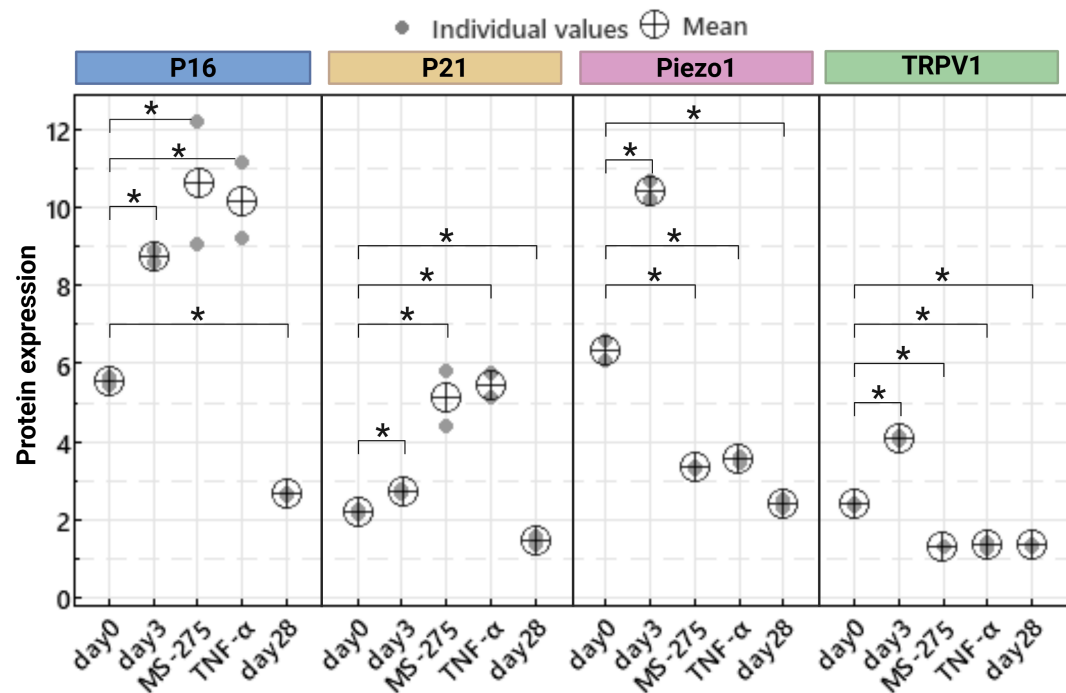


Figure 5.9: In Cell Western test results show the effect of physical and chemical treatments on the expression of senescence markers (P16, P21) and mechanosensitivity proteins (Piezo1, TRPV1) (*p-values < 0.05).

Unlike the qPCR results, P16 levels increase significantly under MS-275 and $\text{TNF-}\alpha$ treatment compared to day 0, indicating that these treatments may enhance senescence through P16 upregulation at the protein level. This discrepancy suggests potential post-transcriptional regulation affecting P16 expression. For instance, Wang et al. (2001) demonstrated that loss of HuR during

senescence reduces P16 mRNA stability, leading to lower P16 transcript levels despite ongoing or increased translation of existing mRNA pools [188]. P21 expression increases significantly under MS-275 and TNF- α treatment, although P53 mRNA levels decrease in the same group. El-Deiry et al. (1993) showed that stress signals (including TNF- α) can activate the P21 promoter via NF- κ B or ATF sites, boosting translation efficiency and protein levels independent of mRNA [65]. This suggests these treatments strongly activate P21, reinforcing their role in cell cycle arrest and senescence induction.

Piezo1 expression declines by day 28 compared to earlier time points, confirming that aged cells progressively lose mechanosensitivity. Interestingly, MS-275 and TNF- α exhibit intermediate Piezo1 levels, lower than day 0 but not as drastically reduced as in long-term aged cells, indicating a partial suppression of mechanotransduction. TRPV1 decreases significantly in almost all conditions compared to day 0. The upregulation of both Piezo1 and TRPV1 proteins in the day 3 group may reflect an assay-related artefact or a short-lived, temporary change in cellular behaviour, rather than a sustained biological adaptation. Without parallel measurements of channel activity (e.g., patch-clamp recordings) or mRNA stability, it is impossible to distinguish a true upregulation from rapid post-translational redistribution or slowed degradation.

A key discrepancy is observed between the qPCR and ICW results for P16: while qPCR shows a decrease in P16 expression under MS-275 and TNF- α , ICW reveals an increase at the protein level. This suggests differences in transcriptional and post-transcriptional regulation, potentially due to mechanisms such as protein stabilisation or post-translational modifications [97]. Overall, these findings indicate that MS-275 and TNF- α effectively promote senescence, as evidenced by increased P16 and P21 levels. Meanwhile, the decline in Piezo1 highlights the association between cellular ageing and reduced mechanosensitivity.

The following graphs illustrate the effects of Yoda1, nanokicking (NK), and their combination on the day 0 group, which represents healthy, untreated cells (Figures 5.10 and 5.11).

P16 expression remains relatively stable across conditions, with minor variations. Nanokicking alone does not significantly alter P16 levels compared to the control (day 0). However, Yoda1 treatment leads to a significant increase in P16 expression. P53 does not exhibit any statistically significant difference among the different conditions. Piezo1 expression remains unchanged mainly across conditions, except for a statistically significant decrease in response to nanokicking treatment (Figure 5.10).

Consistent with the qPCR results, the ICW analysis reveals a significant increase in P16 expression under Yoda1 treatment. This stronger increase at the protein level may be due to post-

transcriptional regulation, where P16 mRNA levels remain stable or decrease while the protein is stabilised and accumulates. P21 protein levels also significantly increase with Yoda1 treatment, whereas nanokicking alone leads to a decrease.

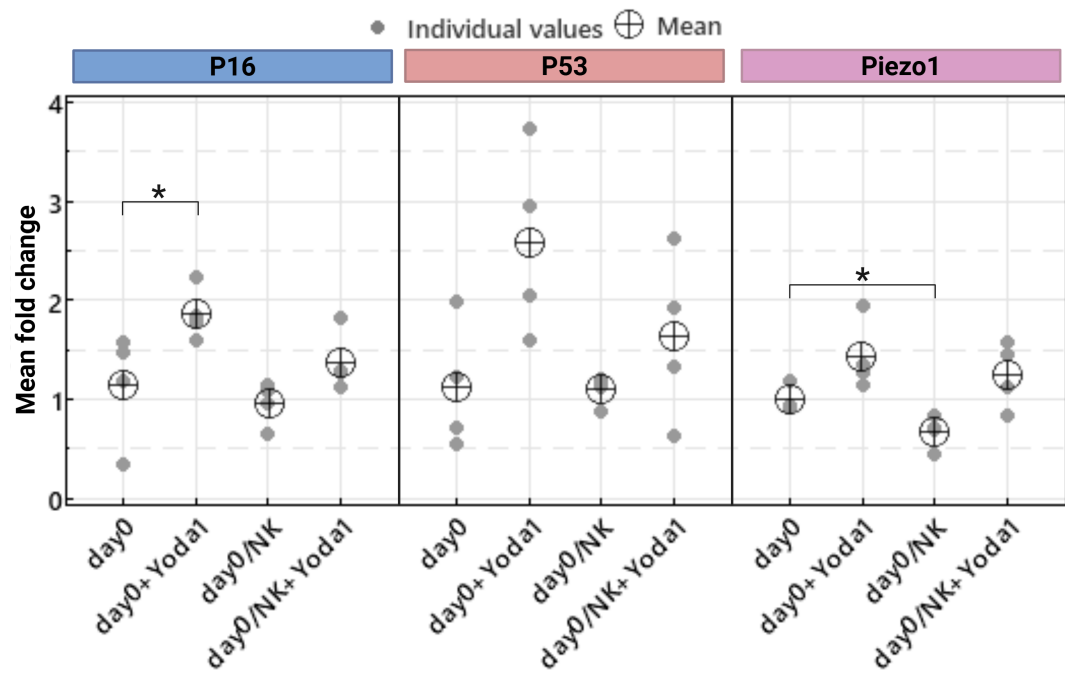


Figure 5.10: qPCR results show the effect of Yoda1 and nanokicking on the expression of senescence markers (P16, P53) and mechanosensitivity genes (Piezo1) (*p-values < 0.05).

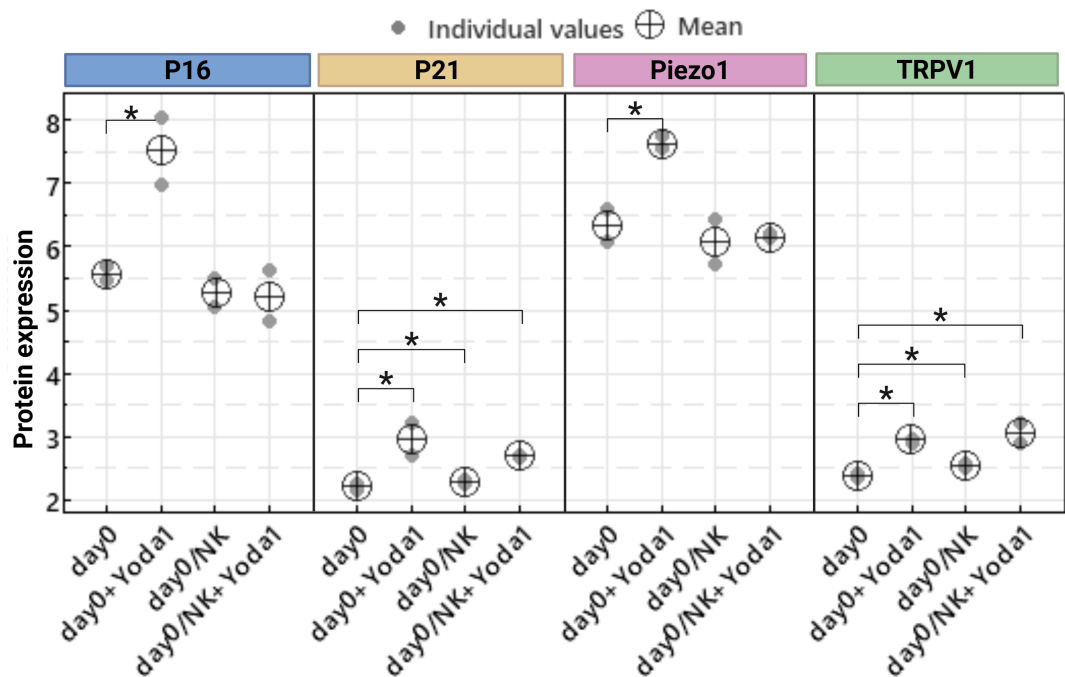


Figure 5.11: In Cell Western result show the effect of Yoda1 and nanokicking on the expression of senescence markers (P16, P21) and mechanosensitivity proteins (Piezo1, TRPV1) (*p-values < 0.05).

As expected, Piezo1 expression increases following Yoda1 treatment, reinforcing its role as a Piezo1 agonist. Additionally, TRPV1, another mechanosensitive protein, significantly increases across all conditions, with the highest expression observed in the Yoda1-treated samples (Figure 5.11).

Day 3 represents the cell group that remained in culture for three days, allowing for a certain degree of ageing to occur. The following graphs (Figures 5.12 and 5.13) illustrate the effects of Yoda1, nanokicking, and their combination on the different conditions within this group.

The expression of P16 significantly decreases following nanokicking treatment, as well as with the combined application of nanokicking and Yoda1. Similarly, P53 levels decline after treatment with Yoda1 and nanokicking. Notably, Piezo1 expression is reduced across all treatment conditions, with the most significant decrease observed in the combination of nanokicking and Yoda1 (Figure 5.12).

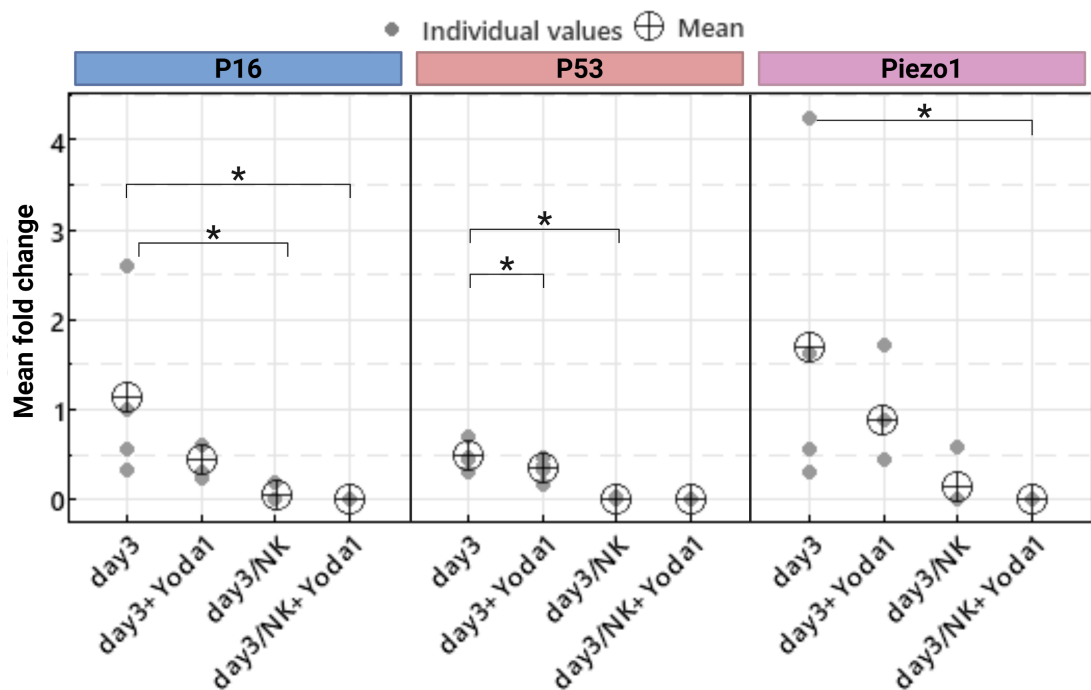


Figure 5.12: qPCR results show the effect of on the expression of senescence markers (P16, P53) and mechanosensitivity genes (Piezo1) (*p-values < 0.05).

At the protein level (Figure 5.13), both P16 and P21 levels rise significantly following nanokicking treatment, as well as in the combined nanokicking + Yoda1 condition. This suggests that mechanical stimulation alone (nanokicking) is sufficient to induce early senescence-associated markers, and that Yoda1 (a Piezo1 agonist) does not prevent, but may even reinforce, this up-regulation. Such rapid induction of P16 and P21 has been observed in other studies of acute mechanical stress: for example, cyclic stretch applied to human mesenchymal stem cells (hM-

SCs) for 24 h led to a significant increase in P21 protein before transcriptional changes became evident, indicating that post-translational stabilization plays a role in the early response to mechanical load [113].

Piezo1 protein levels also increase across all treatments, with the highest increase after nanokicking alone. This is consistent with the notion that acute mechanical perturbation upregulates Piezo1 membrane localisation or stability, even before mRNA levels change. In osteoblast-lineage cells, mechanical loading has been shown to induce Piezo1 accumulation at the plasma membrane within hours, enhancing mechanosensitive calcium currents [172]. We therefore hypothesise that nanokicking similarly drives Piezo1 stabilisation or trafficking to the membrane in aged hMSCs, boosting their mechanosensitive capacity.

By contrast, TRPV1 expression remains low and unchanged, in line with its established role as a thermo- and chemosensor rather than a primary mechanotransducer in mesenchymal cells. In HEK293 and MSC models, TRPV1 upregulation has only been reported under sustained inflammatory or thermal stress, not under purely mechanical stimuli [183]. The lack of TRPV1 induction here implies that nanokicking \pm Yoda1 acts predominantly via Piezo1-mediated pathways, and that TRPV1 does not significantly contribute to the acute mechanosensitive response in this context.

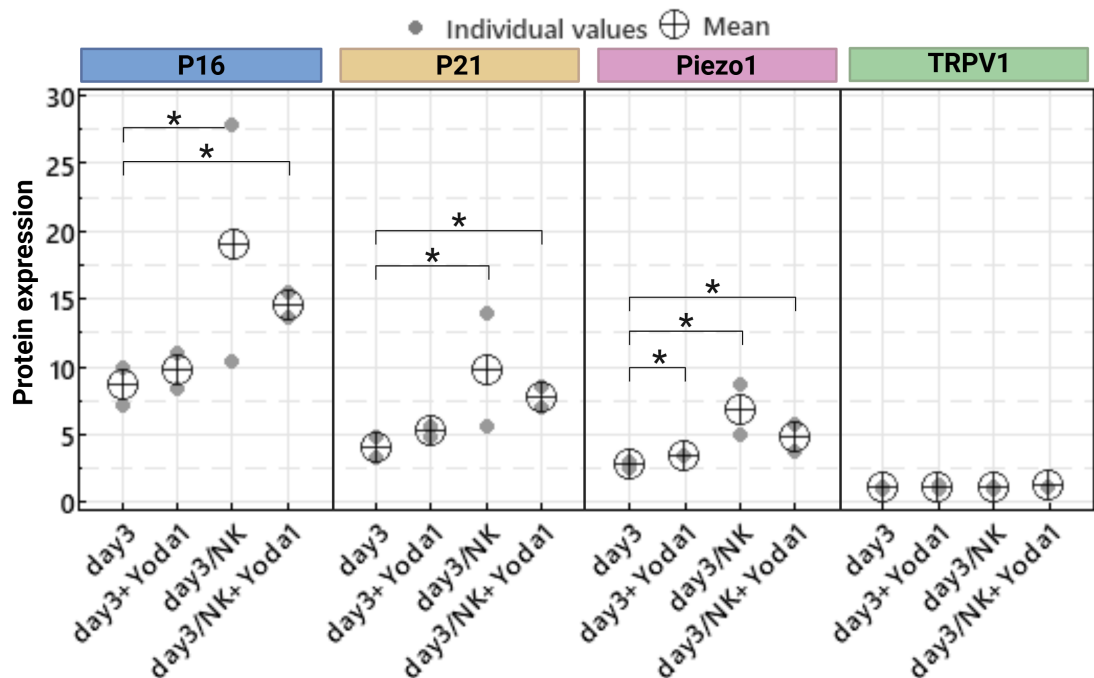


Figure 5.13: In Cell Western results show the effect of Yoda1 and nanokicking on the expression of senescence markers (P16, P21) and mechanosensitivity proteins (Piezo1, TRPV1) (*p-values < 0.05).

The following graphs represent the cells treated with MS-275 for three days (Figures 5.14 and

5.15), a condition previously shown to induce cellular senescence (Figure 5.6). These results illustrate the effects of Yoda1, nanokicking, and their combination on this senescent cell group.

P16 mRNA levels decrease significantly in the nanokicking (NK) and NK + Yoda1 groups, mirroring the trend in P53 transcripts. Despite lower P16 mRNA with nanokicking, P16 protein remains unchanged across all conditions. Likewise, P21 protein levels do not shift, even though P16 transcripts fall. This discordance likely reflects post-transcriptional and post-translational regulation in senescent cells. In ageing or HDAC-inhibited MSCs, mRNA destabilisation (e.g., via reduced HuR activity or increased senescence-associated microRNAs) can lower P16 transcript counts without immediately impacting the existing protein pool, which is often stabilised by decreased proteasome activity [38]. Indeed, Wang et al. (2001) showed that loss of HuR in senescent cells leads to rapid P16 mRNA decay, whereas P16 protein persists due to slower degradation [188]. Similarly, P21 protein is known to be protected from proteasomal turnover when cells enter cell-cycle arrest [13], which could explain its stable abundance despite upstream transcript fluctuations.

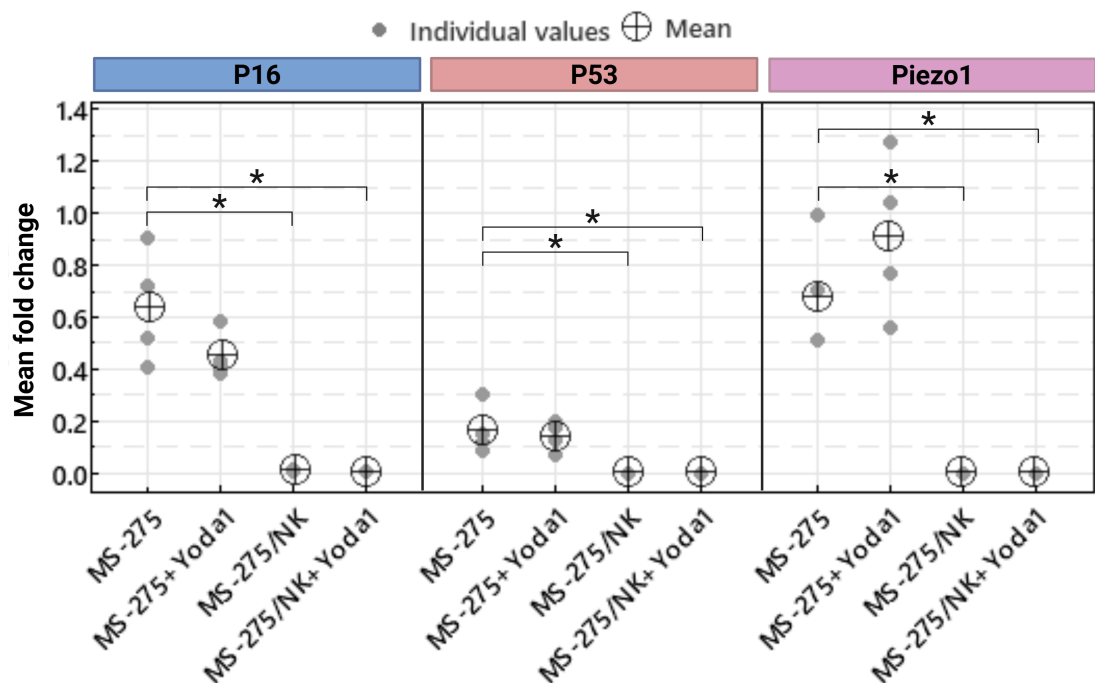


Figure 5.14: qPCR results show the effect of Yoda1 and nanokicking on the expression of senescence markers (P16, P53) and mechanosensitivity genes (Piezo1) (*p-values < 0.05).

Piezo1 mRNA does not change significantly with Yoda1 alone, but decreases significantly in both NK and NK + Yoda1 samples. By contrast, Piezo1 protein shows a small but statistically significant increase in the NK and NK + Yoda1 groups, despite the reduced mRNA, suggesting enhanced channel stabilisation or trafficking to the membrane.

Acute mechanical perturbation (nanokicking) may trigger rapid translocation of existing Piezo1 to the plasma membrane without requiring new transcription, leading to a transient protein increase even as mRNA is downregulated. Sun et al. (2019) demonstrated that mechanical loading in osteoblast-lineage cells induces rapid Piezo1 membrane accumulation prior to any mRNA up-regulation [172, 187].

ICW analysis revealed a significant decrease in TRPV1 protein levels after Yoda1 treatment alone, after nanokicking (NK) alone, and after the combined NK + Yoda1 treatment ($p < 0.05$ for all comparisons). This pattern suggests that, unlike Piezo1, TRPV1 is not upregulated in response to acute mechanical or Piezo1-specific chemical stimulation in these aged hMSCs. Instead, TRPV1 appears to be suppressed when cells experience either direct Piezo1 activation (Yoda1) or mechanical perturbation (NK).

One possible explanation is that TRPV1 serves primarily as a thermo- or inflammatory sensor rather than a mechanosensor in mesenchymal stem cells. For example, sustained TRPV1 activation by capsaicin or inflammatory mediators can induce channel desensitisation and enhanced ubiquitin-mediated degradation in non-neuronal cells [183].

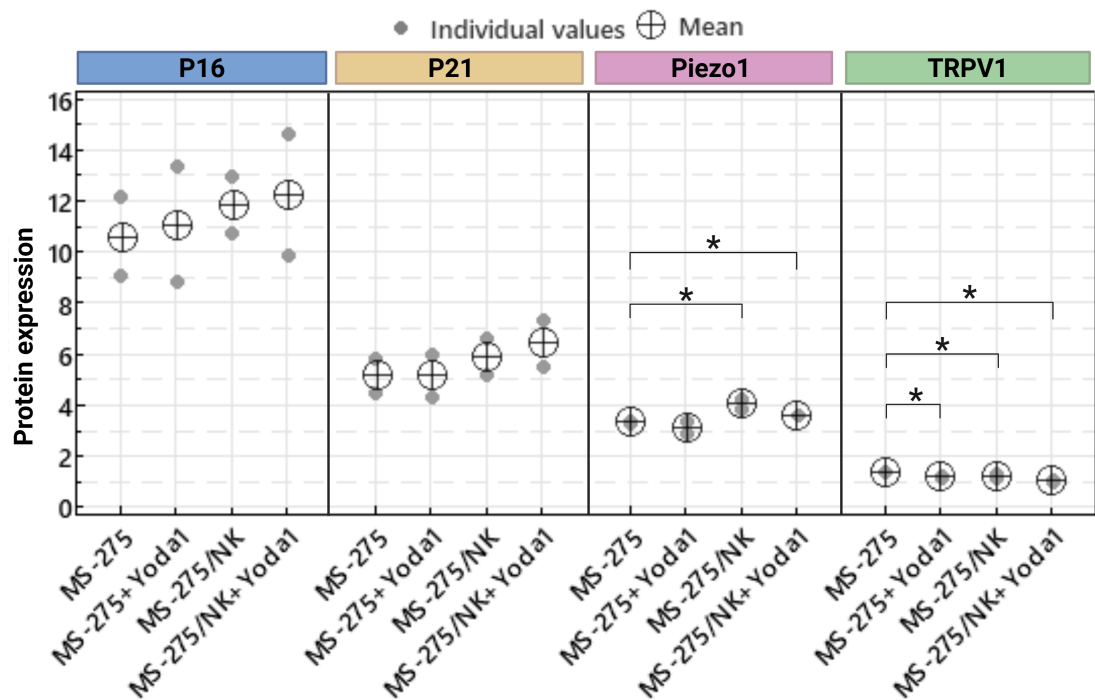


Figure 5.15: In Cell Western test results show the effect of Yoda1 and nanokicking on the expression of senescence markers (P16, P21) and mechanosensitivity proteins (Piezo1, TRPV1) (* p -values < 0.05).

The following graphs represent the cells treated with $TNF-\alpha$ for three days (Figures 5.16 and 5.17), a condition previously shown to induce cellular senescence (Figure 5.6). These results

illustrate the effects of Yoda1, nanokicking, and their combination on this senescent cell group.

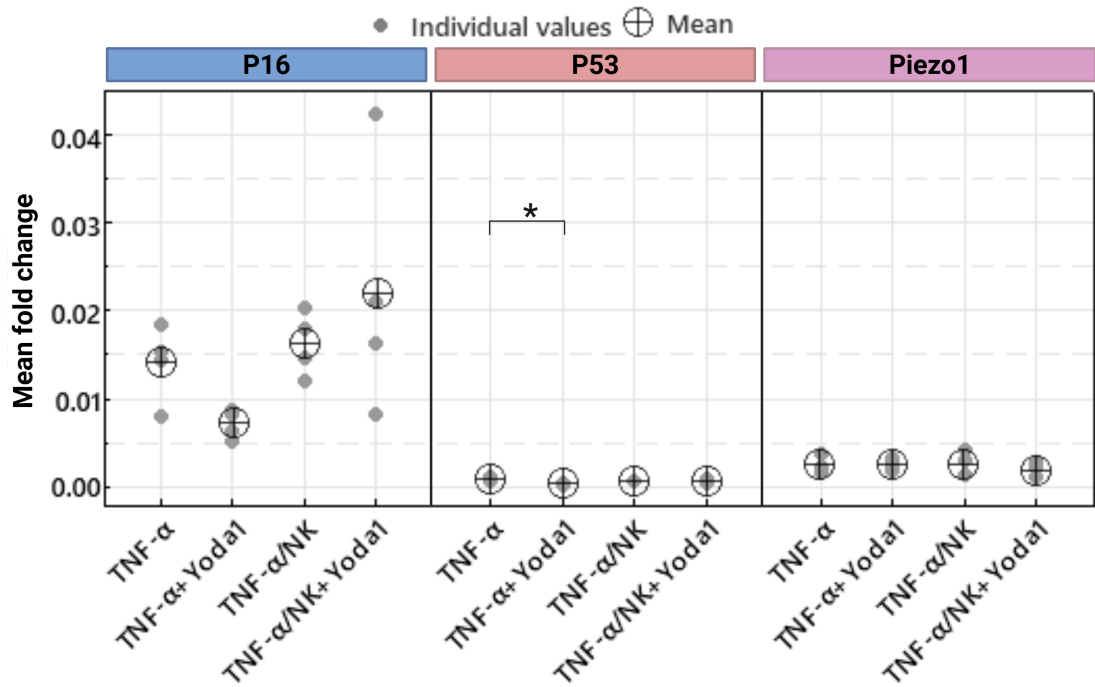


Figure 5.16: qPCR shows the effect of Yoda1 and nanokicking on the expression of senescence markers (P16, P53) and mechanosensitivity genes (Piezo1) (*p-values < 0.05).

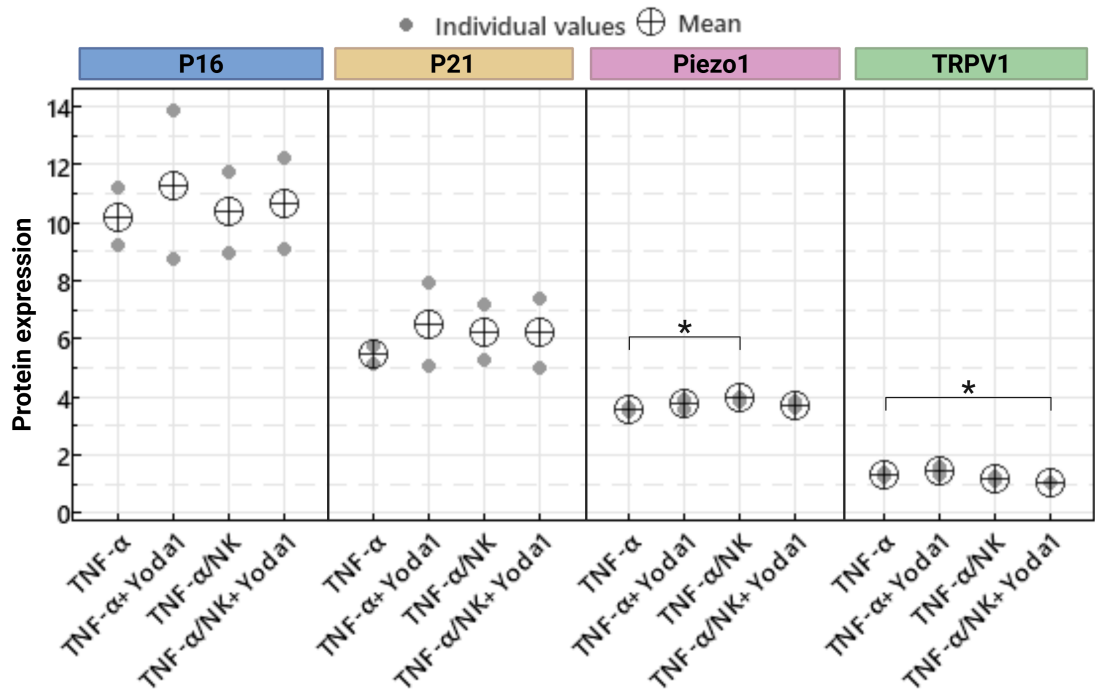


Figure 5.17: In Cell Western test shows the effect of Yoda1 and nanokicking on the expression of senescence markers (P16, P21) and mechanosensitivity proteins (Piezo1, TRPV1) (*p-values < 0.05).

In the TNF- α group, qPCR analysis (Figure 5.16) revealed that P53 mRNA levels were significantly reduced upon Yoda1 addition ($p < 0.05$). In contrast, Piezo1 and P16 mRNA showed no significant changes across TNF- $\alpha \pm$ Yoda1, indicating that acute Piezo1 activation does not immediately alter their transcript abundance in TNF- α treated MSCs.

At the protein level (Figure 5.17), Piezo1 expression increased significantly after nanokicking (NK) alone ($p < 0.01$). This finding is consistent with reports that mechanical perturbation can rapidly stabilise or recruit existing Piezo1 to the plasma membrane independently of transcription; for instance, Sun et al. (2019) showed that mechanical loading induces Piezo1 membrane accumulation within hours in osteoblastic cells [172, 187]. Furthermore, the combined NK \pm Yoda1 treatment caused a significant increase in TRPV1 protein ($p < 0.05$). By contrast, P16 and P21 protein levels remained unchanged across all TNF- α conditions, despite earlier mRNA changes. This likely reflects post-transcriptional buffering in senescent cells, where P16 and P21 proteins are stabilised by reduced proteasomal degradation [188].

The following graphs demonstrate the cell groups that were kept in culture for 28 days, resulting in a certain degree of cellular ageing (Figures 5.18 and 5.19). These results illustrate the effects of Yoda1, nanokicking, and their combination on this senescent cell group.

The combined nanokicking (NK) and Yoda1 treatment induced a statistically significant increase in P53 transcript levels ($p < 0.05$). This suggests activation of DNA damage or stress pathways, as elevated intracellular Ca^{2+} , via Piezo1 activation by Yoda1 or mechanical perturbation, can trigger P53 transcription. For example, cyclic mechanical tension in nucleus pulposus cells has been shown to induce DNA damage and activate the P53-P21 pathway, leading to premature senescence [69]. Similarly, in aged hMSCs, NK + Yoda1 likely exacerbates mechanical and ionic stress, driving P53 upregulation.

Piezo1 transcript levels declined significantly after NK alone ($p < 0.05$). This may reflect a homeostatic feedback: short-term mechanical stimulation can cause Piezo1 channels already at the membrane to remain active while their gene transcription is transiently repressed. As previously discussed, in osteoblastic cells, mechanical load rapidly redistributes existing Piezo1 to the membrane before mRNA changes occur [172, 187]. In day 28, group hMSCs, NK may similarly mobilise Piezo1 protein, prompting a compensatory drop in Piezo1 transcription.

P16 mRNA did not exhibit any statistically significant changes among the different treatments. However, at the protein level, P16 rose significantly ($p < 0.05$) following the Yoda1 treatment. Piezo1 activation by Yoda1 can induce P16 stabilisation via Ca^{2+} -dependent kinases (e.g., p38 MAPK) that protect P16 from degradation [38]. In addition, P16 protein fell significantly (p

< 0.05) after being subjected to nanokicking. This suggests mechanical stimulation may transiently downregulate P16 protein—perhaps via enhanced proteasomal turnover following mechanical remodelling, as mechanical stretch can activate Rho-p38 signalling leading to selective degradation of senescence proteins [129].

Together, these data imply that pure Yoda1 engagement fosters senescence marker accumulation, whereas NK alone triggers pathways that selectively reduce P16 protein in day 28 cells.

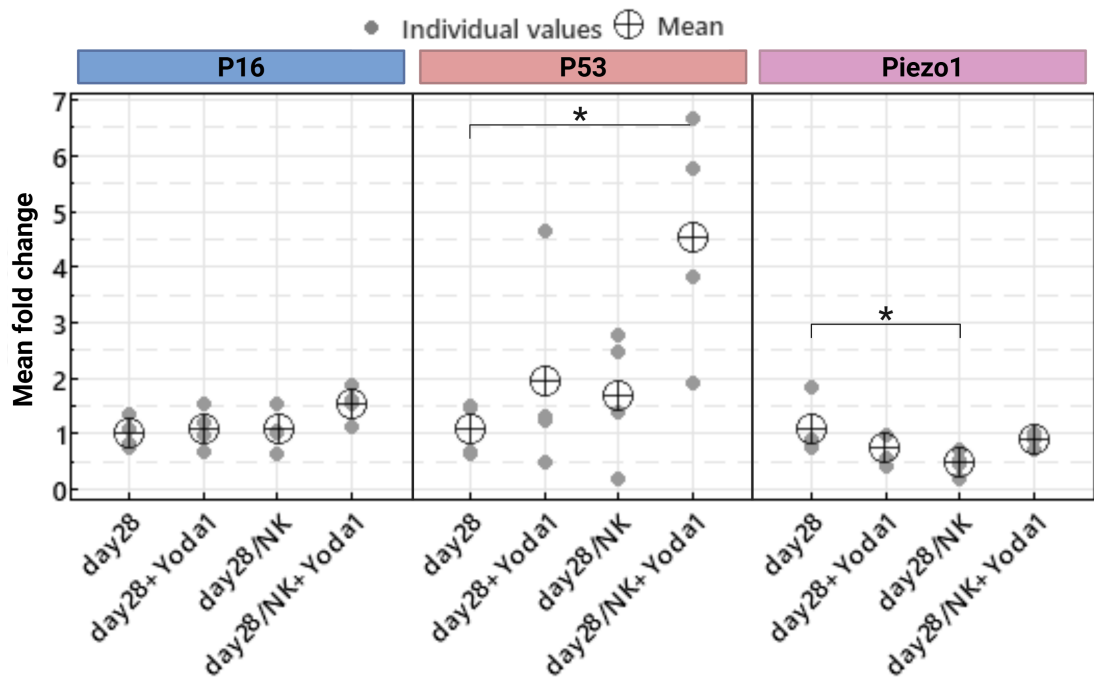


Figure 5.18: qPCR test shows the effect of Yoda1 and nanokicking on the expression of senescence markers (P16, P53) and mechanosensitivity genes (Piezo1) (*p-values < 0.05).

Similarly to P16, P21 protein was significantly reduced following NK ($p < 0.05$). Mechanical tension, especially in aged or long-term-cultured cells, has been shown to activate proteasome-dependent P21 degradation, even when P21 mRNA remains unchanged [188]. Thus, mechanical forces from NK likely accelerate P21 turnover, overriding any transcriptional signals.

Although Piezo1 mRNA fell with NK, Piezo1 protein increased significantly after NK alone and increased even more under NK + Yoda1. This indicates that mechanical stimulation rapidly stabilises or traffics existing Piezo1 channels to the membrane. Yoda1 binding can prevent Piezo1 internalisation, further boosting protein levels [152]. Together, NK + Yoda1 produce a synergistic effect: NK mobilises Piezo1, while Yoda1 locks it in an active state, leading to maximal protein retention. Finally, the TRPV1 protein decreased significantly under NK alone and under the combination of Yoda1 + NK treatment. As discussed previously, TRPV1 acts primarily as a thermo- and inflammatory sensor; mechanical stimulation or Piezo1-driven Ca^{2+}

influx can activate downstream kinases (e.g., PKC) that target TRPV1 for phosphorylation and rapid endocytic degradation [183].

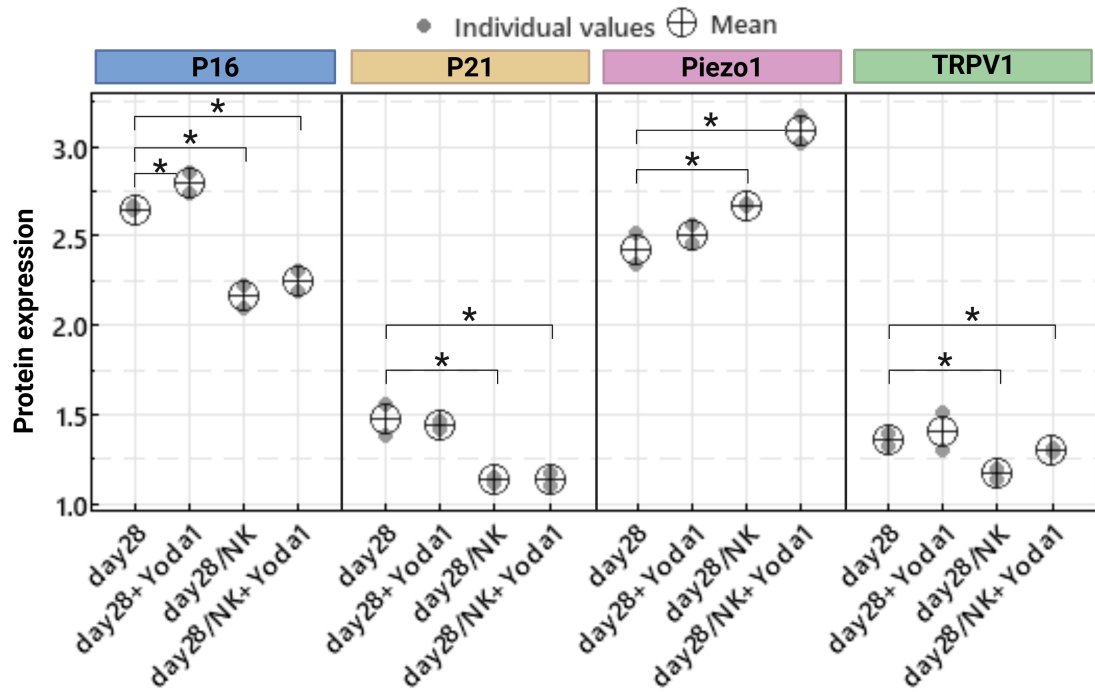


Figure 5.19: In Cell Western test shows the effect of Yoda1 and nanokicking on the expression of senescence markers (P16, P21) and mechanosensitivity proteins (Piezo1, TRPV1) (*p-values < 0.05).

In summary, P53 upregulation under NK + Yoda1 indicates combined mechanical and Piezo1-mediated Ca^{2+} stress activating DNA damage pathways. Piezo1 mRNA falls with NK, while protein rises due to rapid membrane recruitment and stabilisation; Yoda1 further amplifies this effect. P16/P21 proteins respond differently: Yoda1 boosts P16, whereas NK reduces both P16 and P21, reflecting stress-dependent degradation. And finally, TRPV1 declines under NK \pm Yoda1, consistent with mechanically induced channel internalisation and proteasomal turnover. These patterns illustrate how aged hMSCs integrate mechanical and chemical inputs—via Piezo1 and p53 pathways—to modulate senescence and mechanosensitivity at multiple regulatory levels.

These interpretations are based on existing literature but remain speculative. To draw firmer conclusions, the underlying signalling pathways must be investigated in detail. Future studies should include targeted experiments—such as kinase assays, ubiquitination analyses, and transcription factor profiling—to confirm how mechanical and chemical cues interact. Such work goes beyond the scope of the current project but will be essential to validate these hypotheses.

5.4 Discussion

This chapter represents an exploratory investigation into how induced ageing affects human mesenchymal stem cell (hMSC) mechanobiology, serving as a proof-of-concept rather than a comprehensive study. The ultimate aim was to establish and optimise protocols for inducing senescence, by either prolonged culturing or chemical treatments (MS-275 treatment, or TNF- α exposure), so that these aged cells could subsequently be studied in my microfluidic platform for real-time, high-throughput (HT) mechanosensitivity assessment. Below, I place the key findings in context, discuss methodological strengths and limitations, and suggest refinements for future work.

5.4.1 Summary of Findings and Context

Senescence Induction and Cell-Cycle Arrest

Extended culture (21+ days) and three-day chemical treatments (MS-275, TNF- α) all produced increased G1-phase accumulation and reduced S-phase entry by flow cytometry, indicating growth arrest [88]. These results align with established protocols for replicative and induced senescence in hMSCs [184]. G1 arrest by day 21 confirms that prolonged culturing is sufficient to trigger age-related cell-cycle changes [59].

qPCR versus Protein Discrepancies

In MS-275 and TNF- α groups, mRNA levels of P16 and P53 decreased, whereas ICW showed increased P16/P21 proteins [188]. Day 28 cells exhibited elevated P53 mRNA with nanokicking + Yoda1, but P16/P21 proteins responded variably to treatments. These mismatches illustrate common post-transcriptional and post-translational regulation in senescent cells [97, 100]. Without kinetics (mRNA half-life or protein-turnover assays), it is difficult to conclude whether transcriptional suppression or protein stabilisation predominates [186].

Mechanosensitive Channel Expression

Piezo1 protein often rose acutely under mechanical stimuli (nanokicking), even when its mRNA fell. TRPV1 remained low or decreased under most conditions. This suggests that short-term mechanical perturbation mobilises existing Piezo1 channels before transcriptional feedback suppresses Piezo1 mRNA. Such rapid trafficking has precedent in osteoblast models [152]. In contrast, TRPV1 appears less relevant to hMSC mechanosensitivity under these regimens [183].

Metabolic Activity (Alamar Blue) and Senescence

Alamar Blue reduction was stable until day 21, then spiked (reflecting higher cell counts) and declined at day 21 (indicating senescence). Without normalising to cell number, interpreting intrinsic metabolic changes per cell is impossible. A true metabolic decline per cell likely began around day 21, coinciding with cell-cycle arrest [38].

5.4.2 Methodological Reflections and Limitations

Exploratory Scope

This chapter aimed to identify effective senescence induction conditions rather than fully map mechanistic pathways. As such, protocols were not exhaustively optimised, and sample sizes were limited to technical triplicates. Future studies should incorporate additional biological replicates and sample cells at multiple time points, such as day 21 and day 35, to better characterise the progression of induced senescence. It would also be valuable to include hMSCs from several elderly donors, allowing direct comparison between *in vitro*-induced ageing and naturally aged, *in vivo* cells.

qPCR and ICW Normalisation

qPCR relied on housekeeping genes (GAPDH, RPL13A). However, ageing and stress can alter their expression, skewing results [180]. Including multiple reference genes or using global mean normalisation could improve accuracy. ICW was normalised to total protein per well. Yet ageing can change overall protein synthesis and cell size, affecting total protein measurements [18]. Incorporating cell counts or DNA staining (e.g., Hoechst) in parallel wells could refine normalisation.

Senescence Heterogeneity and Single-Cell Analysis

Bulk qPCR and ICW average responses across heterogeneous cultures. Yet senescence often occurs in subpopulations. Single-cell RNA-seq or flow-cytometric detection of P16 and SA- β -gal could reveal whether only a fraction of cells drive overall marker shifts [197]

Alamar Blue Assay Caveats

Without normalising to cell number or performing parallel viability assays (e.g., Trypan Blue), Alamar Blue data can be misleading. Future studies should normalise fluorescence to cell count via automated counters (as used with Countess) or calibrate Alamar Blue readings with known cell densities [27].

5.4.3 Suggestions for Future Optimisation

Further Senescence Characterization

Incorporate multiple senescence markers—SA- β -gal staining, γ -H2AX immunofluorescence, SASP profiling (e.g., IL-6, IL-8 ELISAs)—to confirm functional senescence rather than relying solely on cell-cycle and P16/P21 readouts [88].

Enhanced Normalisation and Controls

Utilisation of multiple housekeeping genes for qPCR and normalising ICW to DNA content or cell count. Vehicle controls (e.g., DMSO-only) should also be included for chemical treatments to rule out solvent effects [149].

5.4.4 Applicability and Potential Impact

Although preliminary, these data demonstrate that hMSC senescence can be induced within a month (or even three days chemically) and that key mechanosensitive channels (Piezo1, TRPV1) and senescence markers (P16, P21, P53) respond in complex, dynamic ways. Establishing reliable ageing protocols is a crucial first step. Once standardised, aged hMSCs can be introduced into my previously developed microfluidic devices to measure their mechanosensitivity in real time and at HT.

This approach could support disease modelling, for example, by examining how aged MSCs from patients with osteoporosis or osteoarthritis respond to mechanical stimuli. It could also be applied to drug screening, using the flow-based platform to evaluate compounds that restore mechanosensitivity or delay senescence rapidly. In regenerative medicine, this system could help isolate MSC subpopulations that retain mechanosensitivity despite cellular ageing, potentially improving therapeutic outcomes.

However, caution is needed. Altered mechanosensitivity in aged hMSCs is not proven by these findings; only marker expression under static or acute nanokicking/Yoda1 conditions is shown to shift. More robust functional assays and improved normalisation strategies will be required before definitive conclusions about aged cell mechanobiology can be drawn.

5.5 Conclusion

Overall, this chapter provided an initial look at how prolonged culturing and chemical treatments induce senescence in hMSCs and how these aged cells respond at the molecular level to mechanical cues. Although changes in senescence and mechanosensor markers were observed,

the results remain preliminary and must be interpreted cautiously. Future work should focus on validating these findings with more functional assays, improved normalisation, and comparisons to naturally aged MSCs. With these refinements, we can better understand aged cell mechanobiology and integrate aged hMSCs into our microfluidic platform for high-throughput mechanosensitivity screening.

Chapter 6

Conclusions and Future Work

This work was designed to develop a high-throughput method for characterising calcium dynamics for single cells. The project was driven by the need to monitor cellular responses to mechanical stimulation using prototype microfluidic devices. In parallel, the study investigated the mechanosensitivity of hMSCs, with a focus on how this is affected by ageing (as indicated by senescence markers). Together, the experimental chapters on calcium signalling, mechanical stimulation, and stem cell ageing were designed to complement each other and provide a comprehensive understanding of how cells respond to physical and biochemical cues.

6.1 Experimental Findings

The first phase of the research confirmed the feasibility of using calcium signalling as a reliable readout of cellular response in HEK293T cells. This initial work validated that both adherent and suspended cells respond to chemical stimulants such as ATP and Yoda1. The effect of experimental conditions- including cell sample preparation, flow rate, and laser power was investigated. The careful adjustment of these parameters ensured that the following assays could reliably measure dynamic changes in calcium signalling. Moreover, identifying optimal conditions for cell suspension and microfluidic design sets the basis for experiments that require prolonged cell observation, an important factor for high-throughput analysis.

Building on these findings, the second experimental phase focused on mechanical stimulation. Here, microfluidic devices with different geometrical features were used to apply compression forces. The experiments showed that the magnitude and mechanical stimulation type are key parameters determining the cellular response. For example, cells compressed through gentler, wider constrictions exhibited significantly higher responses than those subjected to more extreme compression. These results indicated the importance of balancing effective mechanostimulation and cell protection. The observation that even a tiny mechanical variation (such as this derived from the sheath flow) can influence the response further emphasises the attention

that should be paid to device design. This phase of the study not only confirmed the role of mechanical stimulations in modulating cell behaviour but also highlighted that a combined approach—using both chemical and mechanical stimuli—can offer more detailed insights into cellular mechanotransduction.

The third experimental chapter extended the investigation to stem cell ageing and its impact on mechanosensitivity. Here, hMSCs were purposely aged using both physical and chemical methods, and their responses to mechanical stimulation were compared with those of untreated fresh hMSCs. The experiments revealed that ageing alters cell cycle dynamics, metabolic activity, and the expression of key mechanosensitive proteins such as Piezo1. Interestingly, while ageing was associated with reduced overall responsiveness to stimuli, some compensatory mechanisms were observed at the post-transcriptional level. The divergence between mRNA and protein levels of senescence markers suggests that cells may adopt adaptive strategies to maintain a degree of mechanosensitivity despite the adverse effects of ageing. This finding is critical for regenerative medicine as it indicates that even aged stem cells might be sorted or rejuvenated based on their mechanosensitive profiles, thus potentially enhancing their therapeutic efficiency.

6.1.1 Combining findings towards a common goal

Taken together, the three experimental chapters form a consistent narrative that addresses both fundamental and practical aspects of cellular mechanosensitivity. The calcium signalling studies provided the methodological basis for real-time, high-throughput analysis of cell activation. At the same time, the mechanical stimulation experiments demonstrated that the cellular response is highly dependent on the physical parameters of the applied force. Finally, our preliminary investigation into MSC ageing offered initial clues about how mechanosensitivity changes in the ageing state and suggested ways it could be maintained—or even improved—under optimised conditions. However, these observations remain tentative and will require further validation.

This overall strategy is promising for regenerative medicine. If stem cells can be sorted by their mechanosensitive response, it would be possible to select those with the highest regenerative potential, such as younger or more responsive cells, for therapy. Aged cells, whose mechanosensitivity is reduced, could become targets for rejuvenation protocols. Ultimately, refining these approaches into a high-throughput assay could streamline drug or treatment screening aimed at modulating mechanotransduction pathways, paving the way for improved clinical outcomes.

A possible microfluidic strategy for mechanosensitivity-based sorting relies on the fact that aged (with impaired mechanosensitivity) and non-aged hMSCs differ in their immediate calcium response when mechanically stimulated. In such a device, a mixed suspension of cells would flow sequentially through a short constriction region that applies a standardised mechanical pulse

to each cell, forcing a brief membrane deformation. An immediate detection region where a focused laser excites Cal520AM-loaded cells, and a photomultiplier records the resulting Ca^{2+} -dependent fluorescence. Because non-aged hMSCs typically exhibit a larger, faster Ca^{2+} spike under mechanical stress than aged counterparts, a real-time threshold can be defined. If a cell's fluorescence peak exceeds that threshold, indicating a "non-aged" phenotype, it is allowed to continue into outlet A. Cells showing a smaller or delayed Ca^{2+} response (indicative of "aged" hMSCs) would fall below the threshold and be passively directed into outlet B. The optimal method for switching outlets has yet to be determined. This proposal remains a future prospect that will require substantial optimisation of the microfluidic platform and validation of the stem cell findings before implementation.

6.1.2 Limitations

Several limitations were encountered during this study that should be considered when interpreting the results.

Microfluidic Assay Variability

First, the microfluidic devices, although optimised for high-throughput analysis, exhibited variability in flow dynamics and cell positioning. Minor inconsistencies in channel geometry and flow rate control may have contributed to fluctuations in cellular responses, making it challenging to completely decouple the effects of mechanical stimulation from inherent device-induced variations.

Fluorescence Readout Constraint

Relying on Cal520AM fluorescence as a proxy for Ca^{2+} influx introduces potential artefacts. Heterogeneous dye loading and cell-to-cell staining differences could affect signal amplitude and timing. Moreover, the presence of fluorescent labels is incompatible with many translational scenarios. Therapeutic applications demand unaltered cells, and regulatory requirements discourage exogenous dyes. Alternatively, label-free readouts (e.g., impedance or mechanical deformability [144]) should be explored to improve clinical relevance.

Mechanical Stimulation Uncertainties

In Chapter 4, applying constriction-based stimuli highlighted the sensitivity of cell responses to exact force magnitudes. Without direct quantification of the mechanical loads (e.g., such as computational fluid dynamics (CFD) simulations), it remains difficult to compare our constriction-induced pressures to literature-reported thresholds.

Ageing Model Relevance

The senescence protocols in Chapter 5 (prolonged culturing, MS-275, and TNF- α treatments) successfully induced cell-cycle arrest and marker shifts, but they do not fully replicate the multifaceted, lifelong ageing process *in vivo*. Differences between mRNA and protein levels (P16, P21, Piezo1) indicate complex post-transcriptional regulation that we could not fully investigate. To better bridge *in vitro* and *in vivo* ageing, future work should incorporate hMSCs from elderly donors and include longer time-course studies of SASP factors, ROS levels, and mitochondrial function.

In summary, these challenges (device variability, reliance on fluorescent labels, mechanical force quantification, and ageing model limitations) highlight areas for refinement. It is critical that they be addressed before the high-throughput mechanosensitivity platform can be translated into broader research and clinical contexts.

6.2 Future work

The implications of this research extend beyond mechanosensitivity assays alone. By showing that chemical and mechanical stimuli can be used to modulate cellular responses, and that these responses change with cellular ageing, a foundation is laid for future work in tissue engineering and regenerative medicine. The microfluidic systems created here demonstrate how cell activation can be monitored in real time based on dynamic calcium signalling, providing a highly controlled environment for studying and potentially selecting specific cell phenotypes.

Future efforts should focus on optimising these microfluidic designs to improve both sensitivity and throughput. Equally important will be testing the platform with primary stem cells from donors of different ages to ensure the assay's relevance in clinical settings. Ultimately, this approach could underpin next-generation cell-sorting technologies that feed directly into personalised regenerative therapies, enabling more effective and tailored treatments.

6.3 Conclusion

In summary, this project demonstrates that high-throughput mechanosensitivity assays based on microfluidic platforms are both feasible and informative. The comprehensive investigation—including calcium signalling, mechanical stimulation, and stem cell ageing—has revealed critical insights into how cells respond to various stimuli and how these responses are altered by ageing. These findings not only validate the proposed approach but also highlight its potential applications in regenerative medicine, particularly in the context of stem cell sorting and

rejuvenation. Through the careful optimisation of experimental conditions and device design, this research initiates progress towards future innovations in mechanobiology and cell-based therapies.

Appendix A

Microfluidic devices

The following devices were fabricated during my industrial placement in Cytonome, Boston, but not used in the project's experiments.

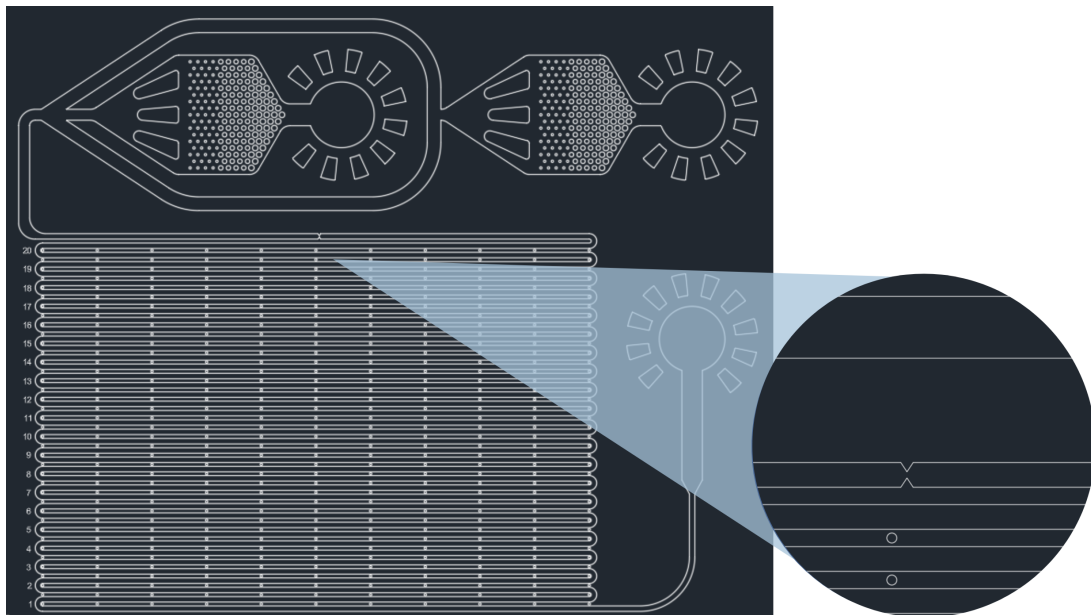


Figure A.1: Mechanical Stimulation Device 2: Sheath flow is used to maintain the cells in the central plane of the channel. Cells pass through a constriction, where the channel width is reduced compared to the surrounding areas. The width of this constriction ranges from $10\ \mu\text{m}$ to $25\ \mu\text{m}$.

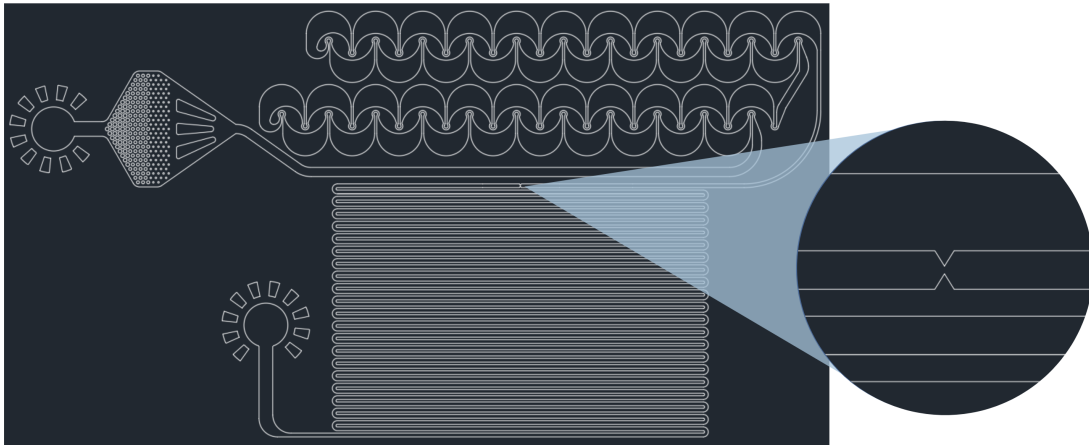


Figure A.2: Mechanical stimulation device 4: This design eliminates the need for sheath flow by utilizing repeated curvatures and narrow channels immediately following the inlet. These features create a controlled environment that naturally focuses cells into a central streamline. As the cells flow through the device, they pass through a single constriction where the channel width is significantly reduced compared to the surrounding regions. The width of these constrictions varies between $10\ \mu\text{m}$ and $25\ \mu\text{m}$.

Appendix B

Python code for confocal data processing

The following code was developed by Prof. Massimo Vassalli, for processing the data acquired from the Zeiss LSM980 microscope.

```
1 import sys
2 import numpy as np
3 from PySide6.QtWidgets import (
4     QApplication, QWidget, QPushButton, QVBoxLayout, QHBoxLayout,
5     QFileDialog,
6     QLabel, QSpinBox, QSlider, QMessageBox, QDialog, QSizePolicy
7 )
8 from PySide6.QtCore import Qt
9 from scipy.signal import savgol_filter as savgol
10 import pyqtgraph as pg
11 import csv
12 class RandomScatterPlotDialog(QDialog):
13     def __init__(self):
14         super().__init__()
15         self.setWindowTitle('Random Scatter Plot')
16         self.setGeometry(200, 200, 600, 400)
17
18         layout = QVBoxLayout()
19
20         innerlayout = QHBoxLayout()
21         self.plotWidget = pg.PlotWidget()
22         self.plotWidget.getViewBox().setMouseMode(pg.ViewBox.RectMode)
23         self.plotWidget.setLabel('left', 'Intensity [a.u.]')
```

```
24     self.plotWidget.setLabel('bottom', 'Duration [us]')
25     self.graphWidget = pg.PlotWidget()
26     self.graphWidget.setLabel('left', 'Intensity [a.u.]')
27     self.graphWidget.setLabel('bottom', 'Time [us]')
28     innerlayout.addWidget(self.plotWidget)
29     innerlayout.addWidget(self.graphWidget)
30
31     lowelayout = QHBoxLayout()
32     self.selectedpeak = QSlider(Qt.Orientation.Horizontal)
33     self.selectedpeak.setMinimum(0)
34     self.selectedpeak.setMaximum(100)
35     self.selectedpeak.setSizePolicy(QSizePolicy.Policy.Expanding,
36                                     QSizePolicy.Policy.Preferred)
37     lowelayout.addWidget(self.selectedpeak)
38     lowelayout.addWidget(QLabel('Duration [us]:'))
39     self.Lduration = QLabel('n/a')
40     lowelayout.addWidget(self.Lduration)
41     lowelayout.addWidget(QLabel('Intensity [a.u.]:'))
42     self.Lpeak = QLabel('n/a')
43     lowelayout.addWidget(self.Lpeak)
44
45     layout.addLayout(innerlayout)
46     layout.addLayout(lowelayout)
47
48     self.setLayout(layout)
49     self.peaks=[]
50     self.generateRandomData()
51
52     def generateRandomData(self, x=None, y=None, data=None):
53         self.plotWidget.clear()
54         self.graphWidget.clear()
55         if x is None:
56             x = np.random.rand(1000)
57             y = np.random.rand(1000)
58         self.selectedpeak.setMaximum(len(x)-1)
59         self.x, self.y=x, y
60         self.peaks=data
61         self.plotWidget.plot(x, y, pen=None, symbol='o', symbolSize
62                               =5)
63         self.point = self.plotWidget.plot([x[0]], [y[0]], pen=None,
64                                             symbol='o', symbolSize=5, symbolBrush='orange')
```

```
62     self.selectedpeak.setValue(0)
63     self.selectedpeak.valueChanged.connect(self.updatePoint)
64     self.updatePoint()
65
66     def updatePoint(self, value=0):
67         # Update the point based on the selected peak value
68         if self.peaks is not None:
69             peak = self.peaks[value]
70             self.graphWidget.clear()
71             self.graphWidget.plot(peak[:,0], peak[:,1], pen='y', symbol
              = 'o', symbolSize=3)
72             self.point.setData([self.x[value]], [self.y[value]]) #
              Assuming peaks is a list of (x, y) tuples
73             self.Lpeak.setText(f' {int(self.y[value])} ')
74             self.Lduration.setText(f' {int(self.x[value])} ')
75
76     class MyApp(QWidget):
77         def __init__(self):
78             super().__init__()
79             self.initUI()
80             self.loaded = False
81             self.finished=False
82             self.inmemory = False
83             self.duration,self.intensity = [],[]
84             self.safepeaks = []
85
86         def initUI(self):
87             self.setWindowTitle('AMK data analyser')
88             self.setGeometry(100, 100, 800, 600)
89
90             layout = QVBoxLayout()
91
92             controlLayout = QHBoxLayout()
93             self.selectButton = QPushButton('Select CSV', self)
94             self.selectButton.clicked.connect(self.openFileDialog)
95             controlLayout.addWidget(self.selectButton)
96
97             # Button to show plot
98             self.showButton = QPushButton('Show', self)
99             self.showButton.clicked.connect(self.showRandomScatterPlot)
100            controlLayout.addWidget(self.showButton)
```

```
101
102     self.messageLabel = QLabel('', self)
103     controlLayout.addWidget(self.messageLabel)
104
105     self.pointsLabel = QLabel('Points to Plot:', self)
106     controlLayout.addWidget(self.pointsLabel)
107     self.pointsSpinBox = QSpinBox(self)
108     self.pointsSpinBox.setRange(1, 999999)
109     self.pointsSpinBox.setValue(1000)
110     self.pointsSpinBox.valueChanged.connect(self.sizeChanged)
111     controlLayout.addWidget(self.pointsSpinBox)
112
113     self.winLabel = QLabel('Window:', self)
114     controlLayout.addWidget(self.winLabel)
115     self.winSpinBox = QSpinBox(self)
116     self.winSpinBox.setRange(1, 999)
117     self.winSpinBox.setValue(31)
118     self.winSpinBox.valueChanged.connect(self.updatePlot)
119     self.winSpinBox.setSingleStep(10)
120     controlLayout.addWidget(self.winSpinBox)
121
122     # Label and SpinBox for threshold
123     self.thresholdLabel = QLabel('Threshold:', self)
124     controlLayout.addWidget(self.thresholdLabel)
125     self.thresholdSpinBox = QSpinBox(self)
126     self.thresholdSpinBox.setRange(0, 65535)
127     self.thresholdSpinBox.setValue(0)
128     self.thresholdSpinBox.setSingleStep(1000)
129     controlLayout.addWidget(self.thresholdSpinBox)
130     self.thresholdSpinBox.valueChanged.connect(self.moveThreshold
131         )
132
133     self.prevButton = QPushButton('Reset', self)
134     self.prevButton.clicked.connect(self.prevWindow)
135     controlLayout.addWidget(self.prevButton)
136
137     self.isolateButton = QPushButton('Isolate', self)
138     self.isolateButton.clicked.connect(self.isolatePeaks)
139     controlLayout.addWidget(self.isolateButton)
140
141     self.saveButton = QPushButton('Save CSV', self)
```

```
141     self.saveButton.clicked.connect(self.saveData)
142     controlLayout.addWidget(self.saveButton)
143
144
145     layout.addLayout(controlLayout)
146
147     self.sliding = QSlider(Qt.Orientation.Horizontal,self)
148     self.sliding.setMinimum(0)
149     self.sliding.setMaximum(100000)
150     self.sliding.setPageStep(1000)
151     self.sliding.valueChanged.connect(self.updatePlot)
152     layout.addWidget(self.sliding)
153
154     self.plotWidget1 = pg.PlotWidget(title="Intensity vs Time")
155     self.plotWidget2 = pg.PlotWidget(title="PMT vs Time")
156     self.plotWidget1.getViewBox().setMouseMode(pg.ViewBox.
157         RectMode)
158     self.plotWidget2.getViewBox().setMouseMode(pg.ViewBox.
159         RectMode)
160
161     self.plotWidget1.getViewBox().sigXRangeChanged.connect(lambda
162         vb, range: self.on_xrange_changed(self.plotWidget1.
163         getAxis('bottom'), range))
164     self.plotWidget2.getViewBox().sigXRangeChanged.connect(lambda
165         vb, range: self.on_xrange_changed(self.plotWidget2.
166         getAxis('bottom'), range))
167
168     layout.addWidget(self.plotWidget1)
169     layout.addWidget(self.plotWidget2)
170
171     self.setLayout(layout)
172
173     def openFileDialog(self):
174         filePath, _ = QFileDialog.getOpenFileName(self, 'Open CSV', '
175             ', 'CSV Files (*.csv);;All Files (*)')
176         if filePath:
177             self.filename= filePath
178             self.loaded = False
179             self.finished=False
180             self.inmemory = False
181             self.loadAndPlotData()
```

```
175
176     def saveData(self):
177         defaultName = self.filename.rsplit('.', 1)[0] + '_processed.
178             csv'
179         filePath, _ = QFileDialog.getSaveFileName(self, 'Save CSV',
180             defaultName, 'CSV Files (*.csv);;All Files (*)')
181         QApplication.setOverrideCursor(Qt.WaitCursor)
182         if not filePath:
183             return
184         if self.finished is False:
185             QMessageBox.warning(self, 'Warning', 'Please do isolate
186                 the peaks first.')
187             return
188         #if len(self.duration) == 0:
189         self.calculateFeatures()
190         with open(filePath, 'w', newline='') as csvfile:
191             csvwriter = csv.writer(csvfile)
192             for duration, intensity in zip(self.duration, self.
193                 intensity):
194                 csvwriter.writerow([duration, intensity])
195         QApplication.restoreOverrideCursor()
196         QMessageBox.information(self, 'Data Saved', f'Data
197             successfully saved to {filePath}.')
198
199     def loadAndPlotData(self):
200         QApplication.setOverrideCursor(Qt.WaitCursor)
201         self.line_offset = []
202         f = open(self.filename)
203         offset = 0
204         for line in f:
205             self.line_offset.append(offset)
206             offset += len(line)+1
207         endtime,tmpfluo=[float(number) for number in line.strip().
208             split(', ')[:2]]
209         f.close()
210         self.number = len(self.line_offset)-1
211         self.acqtime = (endtime)/(self.number-1)
212         self.range=[1,self.number]
213         N = self.pointsSpinBox.value()
214         self.pointsSpinBox.setMaximum(self.number)
215         self.pointsSpinBox.setMinimum(100)
```

```
210     self.sliding.setMaximum(self.number-N-1)
211     QApplication.restoreOverrideCursor()
212     QMessageBox.information(self, 'File loaded', f'File {self.
        filename} opened.\nA total of {self.number} lines has been
        read.\nTotal acquisition time of the track: {int(endtime
        /10)/100}s\nAcquisition time {int(self.acqtime*1e5)/100}us
        ')
213
214     self.messageLabel.setText(f'Loaded file: {self.filename}')
215
216
217     self.plotWidget1.clear()
218     self.line1 = self.plotWidget1.plot([], [], pen='y', symbol='o'
        , symbolSize=3)
219     self.fit1 = self.plotWidget1.plot([], [], pen='r')
220     self.threshline = self.plotWidget1.plot([], [], pen='b')
221     self.plotWidget2.clear()
222     self.line2 = self.plotWidget2.plot([], [], pen='y', symbol='o'
        , symbolSize=3)
223     self.fit2 = self.plotWidget2.plot([], [], pen='r')
224
225     self.loaded = True
226     self.updatePlot()
227
228
229     def sizeChanged(self):
230         if self.loaded is False:
231             return
232         self.sliding.setMaximum(self.number-self.pointsSpinBox.value
            ()-1)
233         self.sliding.setPageStep(self.pointsSpinBox.value())
234         self.updatePlot()
235
236     def on_xrange_changed(self, axis, range):
237         if self.loaded is False:
238             if self.finished is True:
239                 self.plotWidget1.setXRange(*range, padding=0)
240                 self.plotWidget2.setXRange(*range, padding=0)
241                 self.range=[int(range[0]/self.acqtime), min(int(range
                    [1]/self.acqtime), len(self.line_offset)-1)]
242                 return
```

```

243     self.loaded = False
244     self.plotWidget1.setXRange(*range, padding=0)
245     self.plotWidget2.setXRange(*range, padding=0)
246     self.range=[int(range[0]/self.acqtime),min(int(range[1]/self.
        acqtime),len(self.line_offset)-1)]
247     self.loaded = True
248     self.updatePlot()
249
250     def moveThreshold(self):
251         th=self.thresholdSpinBox.value()
252         view_range = self.plotWidget1.viewRange()
253         x_range = view_range[0]
254         self.threshline.setData(x_range , [th,th])
255
256     def updatePlot(self):
257         if self.loaded is False:
258             return
259         win = self.winSpinBox.value()
260         if win%2 == 0:
261             win+=1
262         N = self.pointsSpinBox.value()
263         #position = self.sliding.value() #change here for the
            starting position of the slice in ms
264         f = open(self.filename)
265         time=[]
266         fluo=[]
267         pmt=[]
268         for position in np.linspace(self.range[0],self.range[1],N):
269             f.seek(self.line_offset[int(position)])
270             riga = f.readline()
271             tmptime,tmpfluo,tmppmt=[float(number) for number in riga.
                strip().split(',')[:3]]
272             time.append(tmptime)
273             fluo.append(tmpfluo)
274             pmt.append(tmppmt)
275         f.close()
276
277         self.loaded = False
278         self.line1.setData(time, fluo)
279         self.fit1.setData(time,savgol(fluo,win,1))
280         th=self.thresholdSpinBox.value()

```

```
281         self.threshline.setData([min(time),max(time)], [th,th])
282         #self.plotWidget1.autoRange()
283         self.line2.setData(time, pmt)
284         self.fit2.setData(time, savgol(pmt,win,1), pen='y')
285         #self.plotWidget2.autoRange()
286         self.loaded=True
287
288     def calculateFeatures(self):
289         win = self.winSpinBox.value()
290         if win%2 == 0:
291             win+=1
292         peaks=[]
293         prevtime=0
294         tmp=[]
295         for i in range(1,len(self.xtime)):
296             time = self.xtime[i]
297             fluo = self.xfluo[i]
298             if int((time-prevtime)*1000) > int(self.acqtime*1000):
299                 if len(tmp)>win:
300                     peaks.append(np.array(tmp))
301                     tmp=[]
302                 else:
303                     tmp.append([time, fluo])
304                 prevtime = time
305         intensity= []
306         duration = []
307         for p in peaks:
308             intensity.append(np.max(savgol(p[:,1],win,1)))
309             duration.append((p[-1,0]-p[0,0])*1000)
310         self.duration,self.intensity = duration,intensity
311         self.safepeaks = peaks
312
313     def showRandomScatterPlot(self):
314         dialog = RandomScatterPlotDialog()
315
316         if self.finished is True:
317             self.calculateFeatures()
318             dialog.generateRandomData(self.duration,self.intensity,
319                                     self.safepeaks)
320
321         dialog.exec_()
```

```
321
322     def prevWindow(self):
323         self.range=[1,self.number]
324         self.updatePlot()
325         self.plotWidget1.autoRange()
326         self.plotWidget2.autoRange()
327
328     def isolatePeaks(self):
329         win = self.winSpinBox.value()
330         if win%2 == 0:
331             win+=1
332         QApplication.setOverrideCursor(Qt.WaitCursor)
333         self.loaded=False
334         self.finished=True
335         if self.inmemory is False:
336             f = open(self.filename)
337             self.memfluo=[]
338             self.mempmt=[]
339             self.memtime=[]
340             f.readline()
341             for riga in f:
342                 tmptime,tmpfluo,tmppmt=[float(number) for number in
343                     riga.strip().split(',')[:3]]
344                 self.memtime.append(tmptime)
345                 self.memfluo.append(tmpfluo)
346                 self.mempmt.append(tmppmt)
347             f.close()
348             self.inmemory = True
349
350         filtered = savgol(self.memfluo,win,1)
351         threshold = self.thresholdSpinBox.value()
352
353         block = np.where(filtered>threshold)
354
355         self.xtime = np.array(self.memtime)[block]
356         self.xfluo = np.array(self.memfluo)[block]
357         self.xpmt = np.array(self.mempmt)[block]
358
359         self.line1.setData(self.xtime, self.xfluo)
360         self.fit1.setData(self.xtime,savgol(self.xfluo,win,1))
361         th=self.thresholdSpinBox.value()
```

```
361     self.threshline.setData([min(self.xtime),max(self.xtime)], [th
        ,th])
362     self.plotWidget1.autoRange()
363     self.line2.setData(self.xtime, self.xpmt)
364     self.fit2.setData(self.xtime, savgol(self.xpmt,win,1), pen='y
        ')
365     self.plotWidget2.autoRange()
366
367     QApplication.restoreOverrideCursor()
368     QMessageBox.information(self, 'File analysed', f'A total of {
        len(self.xtime)} points lay above the smoothed threshold,
        corresponding to {np.sum( (self.xtime[1:]-self.xtime[:-1])
        >self.acqtime )} events.')
369
370
371 if __name__ == '__main__':
372     app = QApplication(sys.argv)
373     ex = MyApp()
374     ex.show()
375     sys.exit(app.exec())
```

Bibliography

- [1] <https://geoniti.com/articles/exploring-microfluidics-principles-applicat>
Accessed: 2025-2-27.
- [2] https://en.wikipedia.org/wiki/Hagen--Poiseuille_equation?utm_source=chatgpt.com. Accessed: 2025-3-1.
- [3] <https://physionyx.com/articles/hek293t-suspension-cells-overview/#:~:text=These>. Accessed: 2025-5-15.
- [4] <https://www.bio-rad.com/en-uk/applications-technologies/what-real-time-pcr-qpcr?ID=LUS04W8UU>. Accessed: 2025-1-13.
- [5] Automated cell counters - US.
- [6] Cellular senescence. <https://www.cellsignal.com/science-resources/overview-of-cellular-senescence?srsltid=AfmBOopcPyMWzBBalTqRWv0Hqm0-4giY2qCw1DnoaIPkWTBgSWu0E2oX>. Accessed: 2025-3-21.
- [7] Miltenyi biotec. <https://www.miltenyibiotec.com/GB-en/applications/flow-cytometry-applications/cell-cycle-analysis.html>. Accessed: 2025-1-13.
- [8] OptiPrep™ (iodixanol) density gradient medium. <https://www.stemcell.com/products/optipreptm.html>. Accessed: 2025-6-2.
- [9] Quantitative immunofluorescent assays using fluorescent imaging. <https://www.licorbio.com/applications/in-cell-western-assay>. Accessed: 2025-1-15.
- [10] RNA/DNA quantification - US.
- [11] Biomechanical characterization at the cell scale: Present and prospects, 2018.
- [12] How to complete cell cycle analysis via flow cytometry. <https://nanocollect.com/blog/how-to-complete-cell-cycle-analysis-via-flow-cytometry/>, February 2020. Accessed: 2025-1-13.

- [13] Tarek Abbas and Anindya Dutta. P21 in cancer: Intricate networks and multiple activities. *Nat. Rev. Cancer*, 9(6):400–414, June 2009.
- [14] Mahmoud Al-Azab, Mohammed Safi, Elina Idiiatullina, Fadhl Al-Shaebi, and Mohamed Y Zaky. Aging of mesenchymal stem cell: machinery, markers, and strategies of fighting. *Cell. Mol. Biol. Lett.*, 27(1):69, August 2022.
- [15] Ala’aldeen Al-Halhouli, Ahmed Albagdady, Wisam Al-Faqheri, Jonathan Kottmeier, Sven Meinen, Lasse Jannis Frey, Rainer Krull, and Andreas Dietzel. Enhanced inertial focusing of microparticles and cells by integrating trapezoidal microchambers in spiral microfluidic channels. *RSC Adv.*, 9(33):19197–19204, June 2019.
- [16] B. F. Alfonso and M. Al-Rubeai. *Flow Cytometry*, volume 1. Elsevier B.V., second edition edition, 2011.
- [17] Joji Ando and Kimiko Yamamoto. Vascular mechanobiology endothelial cell responses to fluid shear stress. *Circ. J.*, 73(11):1983–1992, 2009.
- [18] Aleksandra S Anisimova, Alexander I Alexandrov, Nadezhda E Makarova, Vadim N Gladyshev, and Sergey E Dmitriev. Protein synthesis and quality control in aging. *Aging (Albany NY)*, 10(12):4269–4288, December 2018.
- [19] Brady K Atwood, Jacqueline Lopez, James Wager-Miller, Ken Mackie, and Alex Straiker. Expression of G protein-coupled receptors and related proteins in HEK293, AtT20, BV2, and N18 cell lines as revealed by microarray analysis. *BMC Genomics*, 12(1):14, January 2011.
- [20] Krisztina Bagamery, Krisztian Kvell, Ruth Landau, and John Graham. Flow cytometric analysis of CD41-labeled platelets isolated by the rapid, one-step OptiPrep method from human blood. *Cytometry A*, 65(1):84–87, May 2005.
- [21] Apratim Bajpai, Rui Li, and Weiqiang Chen. The cellular mechanobiology of aging: from biology to mechanics. *Ann. N. Y. Acad. Sci.*, 1491(1):3–24, May 2021.
- [22] Bela Balint, Mirjana Pavlović, Olivera Marković, Saša Borović, and Milena Todorović. A stem cell overview: From evolving hemobiological concepts to (auto)grafting in clinical practice. *Srpski medicinski časopis Lekarske komore*, 3(2):135–148, 2022.
- [23] G. K. Batchelor. *Kinematics of the Flow Field*, page 71–130. Cambridge Mathematical Library. Cambridge University Press, 2000.
- [24] S B Baylin and J G Herman. DNA hypermethylation in tumorigenesis: epigenetics joins genetics. *Trends Genet.*, 16(4):168–174, April 2000.
- [25] Martin Bergert, Sergio Lembo, Sumana Sharma, Luigi Russo, Danica Milovanović, Kristjan H Gretarsson, Mandy Börmel, Pierre A Neveu, Jamie A Hackett, Evangelia Petsalaki, and Alba Diz-Muñoz. Cell surface mechanics gate embryonic stem cell differentiation. *Cell Stem Cell*, 28(2):209–216.e4, February 2021.

- [26] Michael J Berridge, Martin D Bootman, and H Llewelyn Roderick. Calcium signalling: dynamics, homeostasis and remodelling. *Nat. Rev. Mol. Cell Biol.*, 4(7):517–529, July 2003.
- [27] Michael V Berridge, Patries M Herst, and An S Tan. Tetrazolium dyes as tools in cell biology: New insights into their cellular reduction. In *Biotechnology Annual Review*, Biotechnology annual review, pages 127–152. Elsevier, 2005.
- [28] Alexander D Bershadsky, Nathalie Q Balaban, and Benjamin Geiger. Adhesion-dependent cell mechanosensitivity. *Annu. Rev. Cell Dev. Biol.*, 19(1):677–695, 2003.
- [29] Ilya Bezprozvanny. Calcium signaling and neurodegenerative diseases. *Trends Mol. Med.*, 15(3):89–100, March 2009.
- [30] Heleen E Boers, Mohammad Haroon, Fabien Le Grand, Astrid D Bakker, Jenneke Klein-Nulend, and Richard T Jaspers. Mechanosensitivity of aged muscle stem cells. *J. Orthop. Res.*, 36(2):632–641, February 2018.
- [31] M D Bootman, T J Collins, C M Peppiatt, L S Prothero, L MacKenzie, P De Smet, M Travers, S C Tovey, J T Seo, M J Berridge, F Ciccolini, and P Lipp. Calcium signalling—an overview. *Semin. Cell Dev. Biol.*, 12(1):3–10, February 2001.
- [32] Wesley M Botello-Smith, Wenjuan Jiang, Han Zhang, Alper D Ozkan, Yi-Chun Lin, Christine N Pham, Jérôme J Lacroix, and Yun Luo. A mechanism for the activation of the mechanosensitive piezo1 channel by the small molecule yoda1. *Nat. Commun.*, 10(1):4503, October 2019.
- [33] Nicoletta Braidotti, Giorgia Demontis, Martina Conti, Laura Andolfi, Catalin Dacian Ciubotaru, Orfeo Sbaizero, and Dan Cojoc. The local mechanosensitive response of primary cardiac fibroblasts is influenced by the microenvironment mechanics. *Sci. Rep.*, 14(1):10365, May 2024.
- [34] B F Brehm-Stecher. Flow cytometry. In *Encyclopedia of Food Microbiology*, pages 943–953. Elsevier, 2014.
- [35] Geoffrey Burnstock and Alexei Verkhratsky. Receptors for purines and pyrimidines. In *Purinergic Signalling and the Nervous System*, pages 119–244. Springer Berlin Heidelberg, Berlin, Heidelberg, 2012.
- [36] Christopher R Burtner and Brian K Kennedy. Progeria syndromes and ageing: what is the connection? *Nat. Rev. Mol. Cell Biol.*, 11(8):567–578, August 2010.
- [37] Stuart M Cain and Terrance P Snutch. Voltage-gated calcium channels in epilepsy. *Epilepsia*, 51:11–11, December 2010.
- [38] Judith Campisi and Fabrizio d’Adda di Fagagna. Cellular senescence: when bad things happen to good cells. *Nat. Rev. Mol. Cell Biol.*, 8(9):729–740, September 2007.
- [39] Ernesto Carafoli. Calcium signaling: a tale for all seasons. *Proc. Natl. Acad. Sci. U. S. A.*, 99(3):1115–1122, February 2002.

- [40] Antonio Casado-Díaz. Stem cells in regenerative medicine. *J. Clin. Med.*, 11(18):5460, September 2022.
- [41] Pedro C Chagastelles and Nance B Nardi. Biology of stem cells: an overview. *Kidney Int. Suppl.* (2011), 1(3):63–67, September 2011.
- [42] Eleni Chantzoura and Keisuke Kaji. *Flow Cytometry*. Elsevier Inc., 2017.
- [43] Ioannis Alexandros Charitos, Andrea Ballini, Stefania Cantore, Mariarosaria Boccellino, Marina Di Domenico, Elisa Borsani, Riccardo Nocini, Michele Di Cosola, Luigi Santacroce, and Lucrezia Bottalico. Stem cells: A historical review about biological, religious, and ethical issues. *Stem Cells Int.*, 2021:9978837, April 2021.
- [44] Chak Kwong Cheng, Nanping Wang, Li Wang, and Yu Huang. Biophysical and biochemical roles of shear stress on endothelium: A revisit and new insights. *Circ. Res.*, 136(7):752–772, March 2025.
- [45] Chun-Wei Chi, Ah Rezwanuddin Ahmed, Zeynep Dereli-Korkut, and Sihong Wang. Microfluidic cell chips for high-throughput drug screening. *Bioanalysis*, 8(9):921–937, May 2016.
- [46] Peter G Childs, Christina A Boyle, Gabriel D Pemberton, Habib Nikukar, Adam S G Curtis, Fiona L Henriquez, Matthew J Dalby, and Stuart Reid. Use of nanoscale mechanical stimulation for control and manipulation of cell behaviour. *Acta Biomater.*, 34:159–168, April 2016.
- [47] David E Clapham. Calcium signaling. *Cell*, 131(6):1047–1058, December 2007.
- [48] Jean-Philippe Coppé, Christopher K Patil, Francis Rodier, Yu Sun, Denise P Muñoz, Joshua Goldstein, Peter S Nelson, Pierre-Yves Desprez, and Judith Campisi. Senescence-associated secretory phenotypes reveal cell-nonautonomous functions of oncogenic RAS and the p53 tumor suppressor. *PLoS Biol.*, 6(12):2853–2868, December 2008.
- [49] Luísa Cortes, João Malva, Ana Cristina Rego, and Cláudia Fragão Pereira. Calcium signaling in aging and neurodegenerative diseases 2019. *Int. J. Mol. Sci.*, 21(3):1125, February 2020.
- [50] Bertrand Coste, Jayanti Mathur, Manuela Schmidt, Taryn J Earley, Sanjeev Ranade, Matt J Petrus, Adrienne E Dubin, and Ardem Patapoutian. Piezo1 and piezo2 are essential components of distinct mechanically activated cation channels. *Science*, 330(6000):55–60, October 2010.
- [51] Bertrand Coste, Bailong Xiao, Jose S Santos, Ruhma Syeda, Jörg Grandl, Kathryn S Spencer, Sung Eun Kim, Manuela Schmidt, Jayanti Mathur, Adrienne E Dubin, Mauricio Montal, and Ardem Patapoutian. Piezo proteins are pore-forming subunits of mechanically activated channels. *Nature*, 483(7388):176–181, February 2012.
- [52] Charles D Cox, Chilman Bae, Lynn Ziegler, Silas Hartley, Vesna Nikolova-Krstevski, Paul R Rohde, Chai-Ann Ng, Frederick Sachs, Philip A Gottlieb, and Boris Martinac. Removal of the mechanoprotective influence of the cytoskeleton reveals PIEZO1 is gated by bilayer tension. *Nat. Commun.*, 7(1):10366, January 2016.

- [53] L Scott Cram. Flow cytometry, an overview. In *Advanced Flow Cytometry: Applications in Biological Research*, pages 1–9. Springer Netherlands, Dordrecht, 2003.
- [54] Jessica E Davies, Dora Lopresto, Bonita H R Apta, Zhiyuan Lin, Wenxin Ma, and Matthew T Harper. Using yoda-1 to mimic laminar flow in vitro: A tool to simplify drug testing. *Biochem. Pharmacol.*, 168:473–480, October 2019.
- [55] Rumi De. Cell mechanosensing. *Reson.*, 24(3):289–296, March 2019.
- [56] Etienne de Coulon, Christian Dellenbach, and Stephan Rohr. Advancing mechanobiology by performing whole-cell patch clamp recording on mechanosensitive cells subjected simultaneously to dynamic stretch events. *iScience*, 24(2):102041, February 2021.
- [57] Xingpeng Di, Xiaoshuai Gao, Liao Peng, Jianzhong Ai, Xi Jin, Shiqian Qi, Hong Li, Kunjie Wang, and Deyi Luo. Cellular mechanotransduction in health and diseases: from molecular mechanism to therapeutic targets. *Signal Transduct. Target. Ther.*, 8(1):282, July 2023.
- [58] Giovanni Di Bernardo, Tiziana Squillaro, Carmela Dell’Aversana, Marco Miceli, Marilena Cipollaro, Antonino Cascino, Lucia Altucci, and Umberto Galderisi. Histone deacetylase inhibitors promote apoptosis and senescence in human mesenchymal stem cells. *Stem Cells Dev.*, 18(4):573–581, May 2009.
- [59] G P Dimri, X Lee, G Basile, M Acosta, G Scott, C Roskelley, E E Medrano, M Linskens, I Rubelj, and O Pereira-Smith. A biomarker that identifies senescent human cells in culture and in aging skin in vivo. *Proc. Natl. Acad. Sci. U. S. A.*, 92(20):9363–9367, September 1995.
- [60] Dennis E Discher, Paul Janmey, and Yu-Li Wang. Tissue cells feel and respond to the stiffness of their substrate. *Science*, 310(5751):1139–1143, November 2005.
- [61] Dennis E Discher, David J Mooney, and Peter W Zandstra. Growth factors, matrices, and forces combine and control stem cells. *Science*, 324(5935):1673–1677, June 2009.
- [62] Hannah Drescher, Sabine Weiskirchen, and Ralf Weiskirchen. Flow cytometry: A blessing and a curse. *Biomedicines*, 9(11):1613, November 2021.
- [63] Jessica S. Dymond. Explanatory chapter: Quantitative pcr. *Methods in Enzymology*, 529:279–289, 1 2013.
- [64] Beate Eckes, Thomas Krieg, and Sara A Wickström. Role of integrin signalling through integrin-linked kinase in skin physiology and pathology. *Exp. Dermatol.*, 23(7):453–456, July 2014.
- [65] W S el Deiry, T Tokino, V E Velculescu, D B Levy, R Parsons, J M Trent, D Lin, W E Mercer, K W Kinzler, and B Vogelstein. WAF1, a potential mediator of p53 tumor suppression. *Cell*, 75(4):817–825, November 1993.
- [66] Adam J Engler, Shamik Sen, H Lee Sweeney, and Dennis E Discher. Matrix elasticity directs stem cell lineage specification. *Cell*, 126(4):677–689, August 2006.

- [67] Yun Fang, David Wu, and Konstantin G Birukov. Mechanosensing and mechanoregulation of endothelial cell functions, March 2019.
- [68] Chenjie Fei, Li Nie, Jianhua Zhang, and Jiong Chen. Potential applications of fluorescence-activated cell sorting (FACS) and droplet-based microfluidics in promoting the discovery of specific antibodies for characterizations of fish immune cells. *Front. Immunol.*, 12:771231, November 2021.
- [69] Chencheng Feng, Minghui Yang, Yang Zhang, Minghong Lan, Bo Huang, Huan Liu, and Yue Zhou. Cyclic mechanical tension reinforces DNA damage and activates the p53-p21-rb pathway to induce premature senescence of nucleus pulposus cells. *Int. J. Mol. Med.*, February 2018.
- [70] Pedro Fernandes. Basic principles of microfluidics. In *AAPS Introductions in the Pharmaceutical Sciences*, pages 1–26. Springer Nature Switzerland, Cham, 2024.
- [71] Miriam Filippi, Thomas Buchner, Oncay Yasa, Stefan Weirich, and Robert K Katzschmann. Microfluidic tissue engineering and bio-actuation. *Adv. Mater.*, 34(23):e2108427, June 2022.
- [72] Wolfgang Fischer, Heike Franke, Helke Gröger-Arndt, and Peter Illes. Evidence for the existence of P2Y_{1,2,4} receptor subtypes in HEK-293 cells: reactivation of P2Y₁ receptors after repetitive agonist application. *Naunyn. Schmiedeberg's. Arch. Pharmacol.*, 371(6):466–472, June 2005.
- [73] Julia Franzen, Anne Zirkel, Jonathon Blake, Björn Rath, Vladimir Benes, Argyris Papantonis, and Wolfgang Wagner. Senescence-associated DNA methylation is stochastically acquired in subpopulations of mesenchymal stem cells. *Aging Cell*, 16(1):183–191, February 2017.
- [74] Daniela Freitas, Meritxell Balmaña, Juliana Poças, Diana Campos, Hugo Osório, Andriana Konstantinidi, Sergey Y Vakhrushev, Ana Magalhães, and Celso A Reis. Different isolation approaches lead to diverse glycosylated extracellular vesicle populations. *J. Extracell. Vesicles*, 8(1):1621131, June 2019.
- [75] Gurisha Garg, Preeti Patel, Ghanshyam Das Gupta, and Balak Das Kurmi. A review on working principle and advanced applications of fluorescence activated cell sorting machine (FACS). *Curr. Pharm. Anal.*, 20(2):85–97, February 2024.
- [76] Benjamin M Gaub and Daniel J Müller. Mechanical stimulation of piezo1 receptors depends on extracellular matrix proteins and directionality of force. *Nano Lett.*, 17(3):2064–2072, March 2017.
- [77] Bastien D Gomperts, Ijsbrand M Kramer, and Peter E R Tatham. Calcium effectors. In *Signal Transduction*, pages 221–242. Elsevier, 2009.
- [78] Bastien D Gomperts, Ijsbrand M Kramer, and Peter E R Tatham. Intracellular calcium. In *Signal Transduction*, pages 185–220. Elsevier, 2009.

- [79] Daniel R Gossett, Henry T K Tse, Serena A Lee, Yong Ying, Anne G Lindgren, Otto O Yang, Jianyu Rao, Amander T Clark, and Dino Di Carlo. Hydrodynamic stretching of single cells for large population mechanical phenotyping. *Proc. Natl. Acad. Sci. U. S. A.*, 109(20):7630–7635, May 2012.
- [80] Philip A Gottlieb and Frederick Sachs. Piezo1: properties of a cation selective mechanical channel. *Channels (Austin)*, 6(4):214–219, July 2012.
- [81] S A Gudipaty, J Lindblom, P D Loftus, M J Redd, K Edes, C F Davey, V Krishnegowda, and J Rosenblatt. Mechanical stretch triggers rapid epithelial cell division through piezo1. *Nature*, 543(7643):118–121, March 2017.
- [82] Annie Handler and David D Ginty. The mechanosensory neurons of touch and their mechanisms of activation. *Nat. Rev. Neurosci.*, 22(9):521–537, September 2021.
- [83] Masahide Harada, Xiaobin Luo, Toyooki Murohara, Baofeng Yang, Dobromir Dobrev, and Stanley Nattel. MicroRNA regulation and cardiac calcium signaling: role in cardiac disease and therapeutic potential. *Circ. Res.*, 114(4):689–705, February 2014.
- [84] Mohammad Haroon, Heleen E Boers, Astrid D Bakker, Niek G C Bloks, Willem M H Hoogaars, Lorenzo Giordani, René J P Musters, Louise Deldicque, Katrien Koppo, Fabien Le Grand, Jenneke Klein-Nulend, and Richard T Jaspers. Reduced growth rate of aged muscle stem cells is associated with impaired mechanosensitivity. *Aging (Albany NY)*, 14(1):28–53, January 2022.
- [85] Christoph A Haselwandter and Roderick MacKinnon. Piezo’s membrane footprint and its contribution to mechanosensitivity. *Elife*, 7, November 2018.
- [86] Li He, Muhammad Ahmad, and Norbert Perrimon. Mechanosensitive channels and their functions in stem cell differentiation. *Exp. Cell Res.*, 374(2):259–265, January 2019.
- [87] Lijuan He, Jiaxiang Tao, Debonil Maity, Fangwei Si, Yi Wu, Tiffany Wu, Vishnu Prasath, Denis Wirtz, and Sean X Sun. Role of membrane-tension gated ca^{2+} flux in cell mechanosensation. *J. Cell Sci.*, 131(4):jcs208470, February 2018.
- [88] Alejandra Hernandez-Segura, Jamil Nehme, and Marco Demaria. Hallmarks of cellular senescence. *Trends Cell Biol.*, 28(6):436–453, June 2018.
- [89] Thomas Hodgkinson, P Monica Tsimbouri, Virginia Llopis-Hernandez, Paul Campsie, David Scurr, Peter G Childs, David Phillips, Sam Donnelly, Julia A Wells, Manuel Salmeron-Sanchez, Karl Burgess, Morgan Alexander, Massimo Vassalli, Richard O C Oreffo, Stuart Reid, David J France, and Matthew J Dalby. The use of nanovibration to discover specific and potent bioactive metabolites that stimulate osteogenic differentiation in mesenchymal stem cells. February 2020.
- [90] Deborah Huber, Ali Oskooei, Xavier Casadevall i Solvas, Andrew deMello, and Govind V Kaigala. Hydrodynamics in cell studies. *Chem. Rev.*, 118(4):2042–2079, February 2018.

- [91] Maziyar Jalaal, Nico Schramma, Antoine Dode, H el ene de Maleprade, Christophe Raufaste, and Raymond E Goldstein. Stress-induced dinoflagellate bioluminescence at the single cell level. *Phys. Rev. Lett.*, 125(2):028102, July 2020.
- [92] Yan Jiang, Xuzhong Yang, Jinghui Jiang, and Bailong Xiao. Structural designs and mechanogating mechanisms of the mechanosensitive piezo channels. *Trends Biochem. Sci.*, 46(6):472–488, June 2021.
- [93] Olivia Johnson-Love, Manuel Salmeron-Sanchez, Stuart Reid, Peter G Childs, and Matthew J Dalby. Vibration-based cell engineering. *Nat Rev Bioeng*, February 2025.
- [94] K. Kalra and Pushpa C Tomar. 33. stem cell: Basics, classification and applications. *American Journal of Phytomedicine and Clinical Therapeutics*, 2014.
- [95] I. Kiseleva A. Kamkin. *Mechanosensitivity and Mechanotransduction*. 2011.
- [96] Renuka Kandhaya-Pillai, Francesc Miro-Mur, Jaume Alijotas-Reig, Tamara Tchkonina, James L Kirkland, and Simo Schwartz, Jr. TNF α -senescence initiates a STAT-dependent positive feedback loop, leading to a sustained interferon signature, DNA damage, and cytokine secretion. *Aging (Albany NY)*, 9(11):2411–2435, November 2017.
- [97] Donghee Kang, Yurim Baek, and Jae-Seon Lee. Mechanisms of RNA and protein quality control and their roles in cellular senescence and age-related diseases. *Cells*, 11(24):4062, December 2022.
- [98] Wonmo Kang, Michael C Robitaille, Marriner Merrill, Kirubel Teferra, Chunghwan Kim, and Marc P Raphael. Mechanisms of cell damage due to mechanical impact: an in vitro investigation. *Sci. Rep.*, 10(1):12009, July 2020.
- [99] Navid Kashaninejad. A new form of velocity distribution in rectangular microchannels with finite aspect ratios. May 2019.
- [100] In es Khatir, Marie A Brunet, Anna Meller, Florent Amiot, Tushar Patel, Xavier Lapointe, Jessica Avila Lopez, No e Guillo, Anne Castonguay, Mohammed Amir Husain, Joannie St Germain, Fran ois-Michel Boisvert, M elanie Plourde, Xavier Roucou, and Benoit Laurent. Decoupling of mRNA and protein expression in aging brains reveals the age-dependent adaptation of specific gene subsets. *Cells*, 12(4):615, February 2023.
- [101] J Kim, J Lee, C Wu, S Nam, D Di Carlo, and W Lee. Inertial focusing in non-rectangular cross-section microchannels and manipulation of accessible focusing positions. *Lab Chip*, 16(6):992–1001, March 2016.
- [102] Kang Ho Kim and Joel M Sederstrom. *Assaying cell cycle status using flow cytometry*, pages 28.6.1–28.6.11. John Wiley & Sons, Inc., Hoboken, NJ, USA, July 2015.

- [103] Si-Na Kim, Byeol Choi, Chan-Ju Lee, Jeong Hyun Moon, Min Kyoung Kim, Eunkyung Chung, and Sun Uk Song. Culturing at low cell density delays cellular senescence of human bone marrow-derived mesenchymal stem cells in long-term cultures. *Int. J. Stem Cells*, 14(1):103–111, February 2021.
- [104] George Kolios and Yuben Moodley. Introduction to stem cells and regenerative medicine. *Respiration*, 85(1):3–10, 2013.
- [105] Larisa V Kovtonyuk, Kristin Fritsch, Xiaomin Feng, Markus G Manz, and Hitoshi Takizawa. Inflamm-aging of hematopoiesis, hematopoietic stem cells, and the bone marrow microenvironment. *Front. Immunol.*, 7:502, November 2016.
- [106] Ruchi Kumari and Parmjit Jat. Mechanisms of cellular senescence: Cell cycle arrest and senescence associated secretory phenotype. *Front. Cell Dev. Biol.*, 9:645593, March 2021.
- [107] Gabrielis Kundrotas, Evelina Gasperskaja, Grazina Slapsyte, Zivile Gudleviciene, Jan Krasko, Ausra Stumbryte, and Regina Liudkeviciene. Identity, proliferation capacity, genomic stability and novel senescence markers of mesenchymal stem cells isolated from low volume of human bone marrow. *Oncotarget*, 7(10):10788–10802, March 2016.
- [108] Jerome J Lacroix, Wesley M Botello-Smith, and Yun Luo. Probing the gating mechanism of the mechanosensitive channel piezo1 with the small molecule yoda1. *Nat. Commun.*, 9(1), May 2018.
- [109] Austin Lai, Peter Thurgood, Charles D Cox, Chanly Chheang, Karlheinz Peter, Anthony Jaworowski, Khashayar Khoshmanesh, and Sara Baratchi. Piezo1 response to shear stress is controlled by the components of the extracellular matrix. *ACS Appl. Mater. Interfaces*, 14(36):40559–40568, September 2022.
- [110] Andrew P Landstrom, Dobromir Dobrev, and Xander H T Wehrens. Calcium signaling and cardiac arrhythmias. *Circ. Res.*, 120(12):1969–1993, June 2017.
- [111] Learn Statistics Easily. Kruskal-Wallis test: Mastering non-parametric analysis for multiple groups. <https://statisticseasily.com/kruskal-wallis-test/>, February 2024. Accessed: 2025-1-31.
- [112] Hong-Pyo Lee, Farid Alisafaei, Kolade Adebawale, Julie Chang, Vivek B Shenoy, and Ovijit Chaudhuri. The nuclear piston activates mechanosensitive ion channels to generate cell migration paths in confining microenvironments. *Sci. Adv.*, 7(2):eabd4058, January 2021.
- [113] Sunny Shinchen Lee, Thu Thuy Vū, Anthony S Weiss, and Giselle C Yeo. Stress-induced senescence in mesenchymal stem cells: Triggers, hallmarks, and current rejuvenation approaches. *Eur. J. Cell Biol.*, 102(2):151331, June 2023.
- [114] Nils B Leimkühler and Rebekka K Schneider. Inflammatory bone marrow microenvironment. *Hematology Am. Soc. Hematol. Educ. Program*, 2019(1):294–302, December 2019.

- [115] Elizabeth S Li and Margaret S Saha. Optimizing calcium detection methods in animal systems: A sandbox for synthetic biology. *Biomolecules*, 11(3):343, February 2021.
- [116] Defei Liao, Fenfang Li, David Lu, and Pei Zhong. Activation of piezo1 mechanosensitive ion channel in HEK293T cells by 30 MHz vertically deployed surface acoustic waves. *Biochem. Biophys. Res. Commun.*, 518(3):541–547, October 2019.
- [117] Bo Liu, Shaoying Lu, Shuai Zheng, Zonglai Jiang, and Yingxiao Wang. Two distinct phases of calcium signalling under flow. *Cardiovasc. Res.*, 91(1):124–133, July 2011.
- [118] Hangrui Liu, Ming Li, Yan Wang, Jim Piper, and Lianmei Jiang. Improving single-cell encapsulation efficiency and reliability through neutral buoyancy of suspension. *Micromachines (Basel)*, 11(1):94, January 2020.
- [119] Huijuan Liu, Xuechun Xia, and Baojie Li. Mesenchymal stem cell aging: Mechanisms and influences on skeletal and non-skeletal tissues. *Exp. Biol. Med. (Maywood)*, 240(8):1099–1106, August 2015.
- [120] C M Lo, H B Wang, M Dembo, and Y L Wang. Cell movement is guided by the rigidity of the substrate. *Biophys. J.*, 79(1):144–152, July 2000.
- [121] Eleonora Marta Longhin, Naouale El Yamani, Elise Rundén-Pran, and Maria Dusinska. The alamar blue assay in the context of safety testing of nanomaterials. *Front. Toxicol.*, 4:981701, September 2022.
- [122] Carlos López-Otín, Maria A Blasco, Linda Partridge, Manuel Serrano, and Guido Kroemer. The hallmarks of aging. *Cell*, 153(6):1194–1217, June 2013.
- [123] Lily D Lu and Joseph M Salvino. The In-Cell western immunofluorescence assay to monitor PROTAC mediated protein degradation. In *Targeted Protein Degradation*, Methods in enzymology, pages 115–153. Elsevier, 2023.
- [124] Ines Lüchtefeld, Igor V Pivkin, Lucia Gardini, Elaheh Zare-Eelanjegh, Christoph Gäbelein, Stephan J Ihle, Andreas M Reichmuth, Marco Capitano, Boris Martinac, Tomaso Zambelli, and Massimo Vassalli. Dissecting cell membrane tension dynamics and its effect on piezo1-mediated cellular mechanosensitivity using force-controlled nanopipettes. *Nat. Methods*, 21(6):1063–1073, June 2024.
- [125] Tadanori Mammoto and Donald E Ingber. Mechanical control of tissue and organ development. *Development*, 137(9):1407–1420, May 2010.
- [126] M M Maneshi, P A Gottlieb, and S Z Hua. A microfluidic approach for studying piezo channels. In *Current Topics in Membranes*, Current topics in membranes, pages 309–334. Elsevier, 2017.
- [127] Mohammad M Maneshi, Lynn Ziegler, Frederick Sachs, Susan Z Hua, and Philip A Gottlieb. Enantiomeric A β peptides inhibit the fluid shear stress response of PIEZO1. *Sci. Rep.*, 8(1):14267, September 2018.

- [128] Robert L Mauck, Michael A Soltz, Christopher C B Wang, Dennis D Wong, Pen-Hsiu Grace Chao, Wilmot B Valhmu, Clark T Hung, and Gerard A Ateshian. Functional tissue engineering of articular cartilage through dynamic loading of chondrocyte-seeded agarose gels. *J. Biomech. Eng.*, 122(3):252–260, June 2000.
- [129] Manuel Mayr, Yanhua Hu, Hainaut Hainaut, and Qingbo Xu. Mechanical stress-induced DNA damage and rac-p38MAPK signal pathways mediate p53-dependent apoptosis in vascular smooth muscle cells. *FASEB J.*, 16(11):1423–1425, September 2002.
- [130] Rowena McBeath, Dana M Pirone, Celeste M Nelson, Kiran Bhadriraju, and Christopher S Chen. Cell shape, cytoskeletal tension, and RhoA regulate stem cell lineage commitment. *Dev. Cell*, 6(4):483–495, April 2004.
- [131] Katherine M McKinnon. Flow cytometry: An overview. *Curr. Protoc. Immunol.*, 120(1):5.1.1–5.1.11, February 2018.
- [132] Liangyu Mi, Junping Hu, Na Li, Jinfang Gao, Rongxiu Huo, Xinyue Peng, Na Zhang, Ying Liu, Hanxi Zhao, Ruiling Liu, Liyun Zhang, and Ke Xu. The mechanism of stem cell aging. *Stem Cell Rev Rep*, 18(4):1281–1293, April 2022.
- [133] A Mita, C Ricordi, S Messinger, A Miki, R Misawa, S Barker, R D Molano, R Haertter, A Khan, S Miyagawa, A Pileggi, L Inverardi, R Alejandro, B J Hering, and H Ichii. Antiproinflammatory effects of iodixanol (OptiPrep)-based density gradient purification on human islet preparations. *Cell Transplant.*, 19(12):1537–1546, August 2010.
- [134] Aya Miyazaki, Asuna Sugimoto, Keigo Yoshizaki, Keita Kawarabayashi, Kokoro Iwata, Rika Kurogoushi, Takamasa Kitamura, Kunihiro Otsuka, Tomokazu Hasegawa, Yuki Akazawa, Satoshi Fukumoto, Naozumi Ishimaru, and Tsutomu Iwamoto. Coordination of WNT signaling and ciliogenesis during odontogenesis by piezo type mechanosensitive ion channel component 1. *Sci. Rep.*, 9(1):14762, October 2019.
- [135] Jeffery D Molkenin, Darrian Bugg, Natasha Ghearing, Lisa E Dorn, Peter Kim, Michelle A Sargent, Jagadambika Gunaje, Kinya Otsu, and Jennifer Davis. Fibroblast-specific genetic manipulation of p38 mitogen-activated protein kinase in vivo reveals its central regulatory role in fibrosis. *Circulation*, 136(6):549–561, August 2017.
- [136] Sarah Moore. What is calcium signaling? <https://www.news-medical.net/life-sciences/What-is-Calcium-Signaling.aspx>, February 2020. Accessed: 2025-1-6.
- [137] Andrea E Morrell, Samuel T Robinson, Matthew J Silva, and X Edward Guo. Mechanosensitive ca^{2+} signaling and coordination is diminished in osteocytes of aged mice during ex vivo tibial loading. *Connect. Tissue Res.*, 61(3-4):389–398, May 2020.

- [138] S M Naqvi and L M McNamara. Stem cell mechanobiology and the role of biomaterials in governing mechanotransduction and matrix production for tissue regeneration. *Front. Bioeng. Biotechnol.*, 8:597661, December 2020.
- [139] Habib Nikukar, Peter G Childs, Adam S G Curtis, Ian W Martin, Mathis O Riehle, Matthew J Dalby, and Stuart Reid. Production of nanoscale vibration for stimulation of human mesenchymal stem cells. *J. Biomed. Nanotechnol.*, 12(7):1478–1488, July 2016.
- [140] Habib Nikukar, Stuart Reid, P Monica Tsimbouri, Mathis O Riehle, Adam S G Curtis, and Matthew J Dalby. Osteogenesis of mesenchymal stem cells by nanoscale mechanotransduction. *ACS Nano*, 7(3):2758–2767, March 2013.
- [141] I V Ogneva. Cell mechanosensitivity: mechanical properties and interaction with gravitational field. *Biomed Res. Int.*, 2013:598461, 2013.
- [142] Juhyun Oh, Yang David Lee, and Amy J Wagers. Stem cell aging: mechanisms, regulators and therapeutic opportunities. *Nat. Med.*, 20(8):870–880, August 2014.
- [143] Wich Orapiriyakul, Monica P Tsimbouri, Peter Childs, Paul Campsie, Julia Wells, Marc A Fernandez-Yague, Karl Burgess, K Elizabeth Tanner, Manlio Tassieri, Dominic Meek, Massimo Vassalli, Manus J P Biggs, Manuel Salmeron-Sanchez, Richard O C Oreffo, Stuart Reid, and Matthew J Dalby. Nanovibrational stimulation of mesenchymal stem cells induces therapeutic reactive oxygen species and inflammation for three-dimensional bone tissue engineering. *ACS Nano*, 14(8):10027–10044, August 2020.
- [144] Oliver Otto, Philipp Rosendahl, Alexander Mietke, Stefan Golfier, Christoph Herold, Daniel Klaue, Salvatore Girardo, Stefano Pagliara, Andrew Ekpenyong, Angela Jacobi, Manja Wobus, Nicole Töpfner, Ulrich F Keyser, Jörg Mansfeld, Elisabeth Fischer-Friedrich, and Jochen Guck. Real-time deformability cytometry: on-the-fly cell mechanical phenotyping. *Nat. Methods*, 12(3):199–202, 4 p following 202, March 2015.
- [145] Jae-Ho Park and Changwon Kho. MicroRNAs and calcium signaling in heart disease. *Int. J. Mol. Sci.*, 22(19):10582, September 2021.
- [146] Matthew J Paszek, Nastaran Zahir, Kandice R Johnson, Johnathon N Lakins, Gabriela I Rozenberg, Amit Gefen, Cynthia A Reinhart-King, Susan S Margulies, Micah Dembo, David Boettiger, Daniel A Hammer, and Valerie M Weaver. Tensional homeostasis and the malignant phenotype. *Cancer Cell*, 8(3):241–254, September 2005.
- [147] Ekaterina Pchitskaya, Elena Popugaeva, and Ilya Bezprozvanny. Calcium signaling and molecular mechanisms underlying neurodegenerative diseases. *Cell Calcium*, 70:87–94, March 2018.
- [148] Stephen P Perfetto, Pratip K Chattopadhyay, and Mario Roederer. Seventeen-colour flow cytometry: unravelling the immune system. *Nat. Rev. Immunol.*, 4(8):648–655, August 2004.

- [149] Nadezhda V Petrova, Artem K Velichko, Sergey V Razin, and Omar L Kantidze. Small molecule compounds that induce cellular senescence. *Aging Cell*, 15(6):999–1017, December 2016.
- [150] Daniela Pietrobon. Calcium channels and migraine. *Biochim. Biophys. Acta*, 1828(7):1655–1665, July 2013.
- [151] Salomon Poliwoda, Nazir Noor, Evan Downs, Amanda Schaaf, Abigail Cantwell, Latha Ganti, Alan D Kaye, Luke I Mosel, Caroline B Carroll, Omar Viswanath, and Ivan Urits. Stem cells: a comprehensive review of origins and emerging clinical roles in medical practice. *Orthop. Rev. (Pavia)*, 14(3):37498, August 2022.
- [152] Kate Poole, Regina Herget, Liudmila Lapatsina, Ha-Duong Ngo, and Gary R Lewin. Tuning piezo ion channels to detect molecular-scale movements relevant for fine touch. *Nat. Commun.*, 5(1):3520, March 2014.
- [153] E M Purcell. Life at low reynolds number. *Am. J. Phys.*, 45(1):3–11, January 1977.
- [154] M W Renshaw, L S Price, and M A Schwartz. Focal adhesion kinase mediates the integrin signaling requirement for growth factor activation of MAP kinase. *J. Cell Biol.*, 147(3):611–618, November 1999.
- [155] Pietro Ridone, Massimo Vassalli, and Boris Martinac. Piezo1 mechanosensitive channels: what are they and why are they important. *Biophys. Rev.*, 11(5):795–805, October 2019.
- [156] Ryan Robinson and Stefan Pellenz. What is flow cytometry (FACS analysis)? <https://www.antibodies-online.com/resources/17/1247/what-is-flow-cytometry-facs-analysis>, December 2013. Accessed: 2024-11-13.
- [157] Etienne Roux, Pauline Bougaran, Pascale Dufourcq, and Thierry Couffinhal. Fluid shear stress sensing by the endothelial layer. *Front. Physiol.*, 11:861, July 2020.
- [158] I J Russell, G P Richardson, and A R Cody. Mechanosensitivity of mammalian auditory hair cells in vitro. *Nature*, 321(6069):517–519, 1986.
- [159] Eric K Sackmann, Anna L Fulton, and David J Beebe. The present and future role of microfluidics in biomedical research. *Nature*, 507(7491):181–189, March 2014.
- [160] Kei Saotome, Swetha E Murthy, Jennifer M Kefauver, Tess Whitwam, Ardem Patapoutian, and Andrew B Ward. Structure of the mechanically activated ion channel piezo1. *Nature*, 554(7693):481–486, February 2018.
- [161] Jūratė Savickienė, Sandra Baronaitė, Aistė Zentelytė, Gražina Treigyte, and Rūta Navakauskienė. Senescence-associated molecular and epigenetic alterations in mesenchymal stem cell cultures from amniotic fluid of normal and fetus-affected pregnancy. *Stem Cells Int.*, 2016(1):2019498, October 2016.

- [162] J B Schachter, S M Sromek, R A Nicholas, and T K Harden. HEK293 human embryonic kidney cells endogenously express the P2Y1 and P2Y2 receptors. *Neuropharmacology*, 36(9):1181–1187, September 1997.
- [163] Céline Schmitter, Mickaël Di-Luoffo, and Julie Guillermet-Guibert. Transducing compressive forces into cellular outputs in cancer and beyond. *Life Sci. Alliance*, 6(9), September 2023.
- [164] Yue Shao, Jianming Sang, and Jianping Fu. On human pluripotent stem cell control: The rise of 3D bioengineering and mechanobiology. *Biomaterials*, 52:26–43, June 2015.
- [165] Kenta Shinha, Wataru Nihei, and Hiroshi Kimura. A microfluidic probe integrated device for spatiotemporal 3D chemical stimulation in cells. *Micromachines (Basel)*, 11(7):691, July 2020.
- [166] Georg Siegel, Torsten Kluba, Ursula Hermanutz-Klein, Karen Bieback, Hinnak Northoff, and Richard Schäfer. Phenotype, donor age and gender affect function of human bone marrow-derived mesenchymal stromal cells. *BMC Med.*, 11(1):146, June 2013.
- [167] Ranbir Chander Sobti, Awtar Krishan, and Devendra K Agrawal, editors. *Flow cytometry*. Springer, Singapore, Singapore, 2024 edition, December 2024.
- [168] Todd M Squires and Stephen R Quake. Microfluidics: Fluid physics at the nanoliter scale. *Rev. Mod. Phys.*, 77(3):977–1026, October 2005.
- [169] Asuna Sugimoto, Aya Miyazaki, Keita Kawarabayashi, Masayuki Shono, Yuki Akazawa, Tomokazu Hasegawa, Kimiko Ueda-Yamaguchi, Takamasa Kitamura, Keigo Yoshizaki, Satoshi Fukumoto, and Tsutomu Iwamoto. Piezo type mechanosensitive ion channel component 1 functions as a regulator of the cell fate determination of mesenchymal stem cells. *Sci. Rep.*, 7(1), December 2017.
- [170] Bingdong Sui, Chenghu Hu, and Yan Jin. Mitochondrial metabolic failure in telomere attrition-provoked aging of bone marrow mesenchymal stem cells. *Biogerontology*, 17(2):267–279, April 2016.
- [171] Deqiang Sun, Min Luo, Mira Jeong, Benjamin Rodriguez, Zheng Xia, Rebecca Hannah, Hui Wang, Thuc Le, Kym F Faull, Rui Chen, Hongcang Gu, Christoph Bock, Alexander Meissner, Berthold Göttgens, Gretchen J Darlington, Wei Li, and Margaret A Goodell. Epigenomic profiling of young and aged HSCs reveals concerted changes during aging that reinforce self-renewal. *Cell Stem Cell*, 14(5):673–688, May 2014.
- [172] Weijia Sun, Shaopeng Chi, Yuheng Li, Shukuan Ling, Yingjun Tan, Youjia Xu, Fan Jiang, Jianwei Li, Caizhi Liu, Guohui Zhong, Dengchao Cao, Xiaoyan Jin, Dingsheng Zhao, Xingcheng Gao, Zizhong Liu, Bailong Xiao, and Yingxian Li. The mechanosensitive piezo1 channel is required for bone formation. *Elife*, 8, July 2019.
- [173] Wenxu Sun, Xiang Gao, Hai Lei, Wei Wang, and Yi Cao. Biophysical approaches for applying and measuring biological forces. *Adv. Sci. (Weinh.)*, 9(5):e2105254, February 2022.

- [174] Ruhma Syeda, Maria N Florendo, Charles D Cox, Jennifer M Kefauver, Jose S Santos, Boris Martinac, and Ardem Patapoutian. Piezo1 channels are inherently mechanosensitive. *Cell Rep.*, 17(7):1739–1746, November 2016.
- [175] Ruhma Syeda, Jie Xu, Adrienne E Dubin, Bertrand Coste, Jayanti Mathur, Truc Huynh, Jason Matzen, Jianmin Lao, David C Tully, Ingo H Engels, H Michael Petrassi, Andrew M Schumacher, Mauricio Montal, Michael Bandell, and Ardem Patapoutian. Chemical activation of the mechanotransduction channel piezo1. *Elife*, 4, May 2015.
- [176] William K Taverner, Egon J Jacobus, John Christianson, Brian Champion, Adrienne W Paton, James C Paton, Weiheng Su, Ryan Cawood, Len W Seymour, and Janet Lei-Rossmann. Calcium influx caused by ER stress inducers enhances oncolytic adenovirus enadenotucirev replication and killing through PKC α activation. *Mol. Ther. Oncolytics*, 15:117–130, December 2019.
- [177] Benoit Tesson and Michael I Latz. Mechanosensitivity of a rapid bioluminescence reporter system assessed by atomic force microscopy. *Biophys. J.*, 108(6):1341–1351, March 2015.
- [178] Penelope M Tsimbouri, Peter G Childs, Gabriel D Pemberton, Jingli Yang, Vineetha Jayawarna, Wich Orapiriyakul, Karl Burgess, Cristina González-García, Gavin Blackburn, Dilip Thomas, Catalina Vallejo-Giraldo, Manus J P Biggs, Adam S G Curtis, Manuel Salmerón-Sánchez, Stuart Reid, and Matthew J Dalby. Stimulation of 3D osteogenesis by mesenchymal stem cells using a nanovibrational bioreactor. *Nat. Biomed. Eng.*, 1(9):758–770, September 2017.
- [179] Paweł Uruski, Agnieszka Sepetowska, Corinna Konieczna, Martyna Pakuła, Michał Wyrwa, Akylbek Tussupkaliyev, Andrzej Tykarski, Justyna Mikuła-Pietrasik, and Krzysztof Książek. Primary high-grade serous ovarian cancer cells are sensitive to senescence induced by carboplatin and paclitaxel in vitro. *Cell. Mol. Biol. Lett.*, 26(1):44, October 2021.
- [180] Jo Vandesompele, Katleen De Preter, Filip Pattyn, Bruce Poppe, Nadine Van Roy, Anne De Paepe, and Frank Speleman. *Genome Biol*, 3(7):research0034.1, 2002.
- [181] Alexei Verkhratsky and Ole H Petersen. Principles of the ca²⁺ homeostatic/signalling system. In *Neuromethods*, Neuromethods, pages 1–11. Humana Press, Totowa, NJ, 2010.
- [182] Kyle H Vining and David J Mooney. Mechanical forces direct stem cell behaviour in development and regeneration. *Nat. Rev. Mol. Cell Biol.*, 18(12):728–742, December 2017.
- [183] Joris Vriens, Bernd Nilius, and Thomas Voets. Peripheral thermosensation in mammals. *Nat. Rev. Neurosci.*, 15(9):573–589, September 2014.
- [184] Wolfgang Wagner, Simone Bork, Patrick Horn, Damir Kronic, Thomas Walenda, Anke Diehlmann, Vladimir Benes, Jonathon Blake, Franz-Xaver Huber, Volker Eckstein, Petra Boukamp, and Anthony D Ho. Aging and replicative senescence have related effects on human stem and progenitor cells. *PLoS One*, 4(6):e5846, June 2009.

- [185] Andrew B Waight, Bjørn Panyella Pedersen, Avner Schlessinger, Massimiliano Bonomi, Bryant H Chau, Zygy Roe-Zurz, Aaron J Risenmay, Andrej Sali, and Robert M Stroud. Structural basis for alternating access of a eukaryotic calcium/proton exchanger. *Nature*, 499(7456):107–110, July 2013.
- [186] Chong Wang and Hui Liu. Factors influencing degradation kinetics of mRNAs and half-lives of microRNAs, circRNAs, lncRNAs in blood in vitro using quantitative PCR. *Sci. Rep.*, 12(1):7259, May 2022.
- [187] Jiao Wang, Yong-Xin Sun, and Jiliang Li. The role of mechanosensor piezo1 in bone homeostasis and mechanobiology. *Dev. Biol.*, 493:80–88, January 2023.
- [188] W Wang, X Yang, V J Cristofalo, N J Holbrook, and M Gorospe. Loss of HuR is linked to reduced expression of proliferative genes during replicative senescence. *Mol. Cell. Biol.*, 21(17):5889–5898, September 2001.
- [189] Yuanqi Weng, Fei Yan, Runkang Chen, Ming Qian, Yun Ou, Shuhong Xie, Hairong Zheng, and Jiangyu Li. PIEZO channel protein naturally expressed in human breast cancer cell MDA-MB-231 as probed by atomic force microscopy. *AIP Adv.*, 8(5):055101, May 2018.
- [190] George M Whitesides. The origins and the future of microfluidics. *Nature*, 442(7101):368–373, July 2006.
- [191] Wikipedia contributors. Purinergic receptor. https://en.wikipedia.org/w/index.php?title=Purinergic_receptor&oldid=1246644588, September 2024. Accessed: NA-NA-NA.
- [192] Wikipedia contributors. Real-time polymerase chain reaction. https://en.wikipedia.org/w/index.php?title=Real-time_polymerase_chain_reaction&oldid=1264684449, December 2024. Accessed: NA-NA-NA.
- [193] Wikipedia contributors. Stem cell. https://en.wikipedia.org/w/index.php?title=Stem_cell&oldid=1256159332, November 2024. Accessed: NA-NA-NA.
- [194] Jessamine P Winer, Paul A Janmey, Margaret E McCormick, and Makoto Funaki. Bone marrow-derived human mesenchymal stem cells become quiescent on soft substrates but remain responsive to chemical or mechanical stimuli. *Tissue Eng. Part A*, 15(1):147–154, January 2009.
- [195] Yabin Wu, Daisy W J van der Schaft, Frank P Baaijens, and Cees W J Oomens. Cell death induced by mechanical compression on engineered muscle results from a gradual physiological mechanism. *J. Biomech.*, 49(7):1071–1077, May 2016.
- [196] Bailong Xiao. Mechanisms of mechanotransduction and physiological roles of PIEZO channels. *Nat. Rev. Mol. Cell Biol.*, 25(11):886–903, November 2024.

- [197] Peng Xie, Mingxuan Gao, Chunming Wang, Jianfei Zhang, Pawan Noel, Chaoyong Yang, Daniel Von Hoff, Haiyong Han, Michael Q Zhang, and Wei Lin. SuperCT: a supervised-learning framework for enhanced characterization of single-cell transcriptomic profiles. *Nucleic Acids Res.*, 47(8):e48, May 2019.
- [198] Jie Xu, Jayanti Mathur, Emilie Vessières, Scott Hammack, Keiko Nonomura, Julie Favre, Linda Grimaud, Matt Petrus, Allain Francisco, Jingyuan Li, Van Lee, Fu-Li Xiang, James K Mainquist, Stuart M Cahalan, Anthony P Orth, John R Walker, Shang Ma, Viktor Lukacs, Laura Bordone, Michael Bandell, Bryan Laffitte, Yan Xu, Shu Chien, Daniel Henrion, and Ardem Patapoutian. GPR68 senses flow and is essential for vascular physiology. *Cell*, 173(3):762–775.e16, April 2018.
- [199] Tao Xu, Wanqing Yue, Cheuk-Wing Li, Xinsheng Yao, and Mengsu Yang. Microfluidics study of intracellular calcium response to mechanical stimulation on single suspension cells. *Lab Chip*, 13(6):1060–1069, March 2013.
- [200] Tie Yang, Francesca Bragheri, and Paolo Minzioni. A comprehensive review of optical stretcher for cell mechanical characterization at single-cell level. *Micromachines (Basel)*, 7(5):90, May 2016.
- [201] Xuzhong Yang, Chao Lin, Xudong Chen, Shouqin Li, Xueming Li, and Bailong Xiao. Structure deformation and curvature sensing of PIEZO1 in lipid membranes. *Nature*, 604(7905):377–383, April 2022.
- [202] Kira Young, Elizabeth Eudy, Rebecca Bell, Matthew A Loberg, Tim Stearns, Devyani Sharma, Lars Velten, Simon Haas, Marie-Dominique Filippi, and Jennifer J Trowbridge. Decline in IGF1 in the bone marrow microenvironment initiates hematopoietic stem cell aging. *Cell Stem Cell*, 28(8):1473–1482.e7, August 2021.
- [203] Jin Yu, Jiazhong Shi, Yue Zhang, Yi Zhang, Yaqin Huang, Zhiwen Chen, and Jin Yang. The replicative senescent mesenchymal stem / stromal cells defect in DNA damage response and anti-oxidative capacity. *Int. J. Med. Sci.*, 15(8):771–781, 2018.
- [204] Wojciech Zakrzewski, Maciej Dobrzyński, Maria Szymonowicz, and Zbigniew Rybak. Stem cells: past, present, and future. *Stem Cell Res. Ther.*, 10(1):68, February 2019.
- [205] Jun Zhang, Sheng Yan, Dan Yuan, Gursel Alici, Nam-Trung Nguyen, Majid Ebrahimi Warkiani, and Weihua Li. Fundamentals and applications of inertial microfluidics: a review. *Lab Chip*, 16(1):10–34, January 2016.
- [206] Qiucen Zhang and Robert H Austin. Applications of microfluidics in stem cell biology. *Bio-nanoscience*, 2(4):277–286, December 2012.
- [207] Qiancheng Zhao, Heng Zhou, Shaopeng Chi, Yanfeng Wang, Jianhua Wang, Jie Geng, Kun Wu, Wenhao Liu, Tingxin Zhang, Meng-Qiu Dong, Jiawei Wang, Xueming Li, and Bailong Xiao.

Structure and mechanogating mechanism of the piezo1 channel. *Nature*, 554(7693):487–492, February 2018.

- [208] Taifeng Zhou, Bo Gao, Yi Fan, Yuchen Liu, Shuhao Feng, Qian Cong, Xiaolei Zhang, Yaxing Zhou, Prem S Yadav, Jiachen Lin, Nan Wu, Liang Zhao, Dongsheng Huang, Shuanhu Zhou, Peiqiang Su, and Yingzi Yang. Piezo1/2 mediate mechanotransduction essential for bone formation through concerted activation of NFAT-YAP1- β -catenin. *Elife*, 9, March 2020.